Sheffield Hallam University

A Sheffield Hallam University thesis
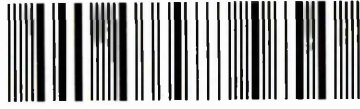
ProQuest Number: 10694123

ProQuest 10694123

Thermo-Elastic-Plastic Analysis for Elastic Component under High Temperature Fatigue Crack Growth Rate

Mohammed Ali Nasser Ali

A thesis submitted in partial fulfilment of the requirements of
Sheffield Hallam University

for the degree of Doctor of Philosophy

August 2013

This thesis is dedicated to the Unknown Soldier (My Wife) and to the living memory of my dad and mum.

Acknowledgements

I would like to express my sincere gratitude to the Ministry of High Education and Scientific Research, Government of Iraq for providing financial support throughout all the period of this research project.

I am indebted to my supervisor, Dr. Syed T. Hasan for his invaluable support and guidance during this research project, and his continuous encouragement and advice while this thesis was being prepared. Without his guidance this work could not have been completed.

I am grateful to all the technical staff in the mechanical laboratory, workshop and the computer laboratory for their help and support during this research work.

Finally, I am indebted to my wife and family for their understanding and support me.

MOHAMMED ALI NASSER ALI

August 2013

Preface

This thesis is presented as part of the requirements for the fulfilment of the degree of Doctor of Philosophy from Sheffield Hallam University, UK. The reports of research and work carried out by the researcher were supervised by Dr. Syed T. Hasan from the Faculty of Arts, Computing, Engineering and Science at Sheffield Hallam University, from October 2009 to August 2013.

MOHAMMED ALI NASSER ALI

August 2013

Abstract

The research project presents a fundamental understanding of the fatigue crack growth mechanisms of AISI 420 martensitic stainless steel, based on the comparison analysis between the theoretical and numerical modelling, incorporating research findings under isothermal fatigue loading for solid cylindrical specimen and the theoretical modelling with the numerical simulation for tubular specimen when subjected to cyclic mechanical loading superimposed by cyclic thermal shock.

The experimental part of this research programme studied the fatigue stress-life data for three types of surface conditions specimen and the isothermal stress-controlled fatigue testing at 300 °C - 600 °C temperature range. It is observed that the highest strength is obtained for the polished specimen, while the machined specimen shows lower strength, and the lowest strength is the notched specimen due to the high effect of the stress concentration. The material behaviour at room and high temperatures shows an initial hardening, followed by slow extension until fully plastic saturation then followed by crack initiation and growth eventually reaching the failure of the specimen, resulting from the dynamic strain ageing occurred from the transformation of austenitic microstructure to martensite and also, the nucleation of precipitation at grain boundaries and the incremental temperature increase the fatigue crack growth rate with stress intensity factor however, the crack growth rate at 600 °C test temperature is less than 500 °C because of the creep-fatigue taking place.

The theoretical modelling presents the crack growth analysis and stress and strain intensity factor approaches analysed in two case studies based on the addition of thermo-elastic-plastic stresses to the experimental fatigue applied loading. Case study one estimates the thermal stresses superimposed sinusoidal cyclic mechanical stress results in solid cylinder under isothermal fatigue simulation. Case study two estimates the transient thermal stresses superimposed on cyclic mechanical loading results in hollow cylinder under thermal shock in heating case and down shock cooling case. The combination of stress and strain intensity factor theoretical calculations with the experimental output recorded data shows a similar behaviour with increasing temperature, and there is a fair correlation between the profiles at the beginning and then divergence with increasing the crack length. The transient influence of high temperature in case two, giving a very high thermal shock stress as a heating or cooling effects, shifting up the combined stress, when applied a cyclic mechanical load in fraction of seconds, and the reputations of these shocks, causing a fast failure under high thermal shock stress superimposed with mechanical loading.

Finally, the numerical modelling analyses three cases studied were solved due to the types of loading and types of specimen geometry by using finite element models constructed through the ANSYS Workbench version 13.0. The first case is a low cyclic fatigue case for a solid cylinder specimen simulated by applying a cyclic mechanical loading. The second is an isothermal fatigue case for solid cylinder specimen simulated by supplying different constant temperatures on the outer surface with cyclic mechanical loading, where the two cases are similar to the experimental tests and the third case, is a thermo-mechanical fatigue for a hollow cylinder model by simulating a thermal up-shock generated due to transient heating on the outer surface of the model or down shock cooling on the inner surface with the cyclic mechanical loading. The results show a good agreement with the experimental data in terms of alternative stress and life in the first case. In case two results show the strain intensity factor is increases with increasing temperature similar to the theoretical solution due to the influence of the modulus of elasticity and the difference in life estimation with the experimental output record is related to the input data made of theoretical physical properties and the experimental stress-life data.

CONTENTS

NOMENCLATURE

SYMBOLS

α	thermal expansion coefficient, $^{\circ}C^{-1}$
γ	constant
ε_f	fracture ductility
ϵ	strain
ϵ_p	plastic strain
ϵ_z	axial strain
θ	transient temperature distribution, $^{\circ}C$
λ_i	Bessel function positive roots.
ν	Poisson's ratio
ρ	density, Kg/m^3
σ	stress, MPa
σ_θ	hoop stress, MPa
$\sigma_{\theta1}, \sigma_{\theta2}, \sigma_{\theta3}$	partial hoop stresses, MPa
$\sigma_{\theta-th.}$	thermal hoop stress, MPa
σ_a	stress amplitude, MPa
$\sigma_{comb.}$	combined stress, MPa
σ_{ct}	crack tip stress, MPa
σ_f	fracture strength, MPa
σ_m	mean stress, MPa
σ_{max}	maximum stress, MPa
$\sigma_{mech.}$	mechanical stress, MPa
σ_{min}	minimum stress, MPa
σ_{TVM}	thermal von-Mises stress, MPa
σ_r	radial stress, MPa
$\sigma_{r1}, \sigma_{r2}, \sigma_{r3}$	partial radial stresses, MPa
$\sigma_{r-th.}$	thermal radial stress, MPa
σ_{UTS}	ultimate stress, MPa
σ_{xx}	x-axis stress, MPa
σ_{ys}	yield strength, MPa
σ_{yy}	y-axis stress, MPa

σ_z	axial stress, MPa
$\sigma_{z1}, \sigma_{z2}, \sigma_{z3}$	partial axial stresses, MPa
$\sigma_{z-th.}$	thermal axial stress, MPa
σ_{zz}	z-axis stress, MPa
$\tau_{xy}, \tau_{yz}, \tau_{zx}$	plain stresses, MPa
v	y-axis unit displacement vector
φ	phase shift angle
$\Delta\epsilon_e$	elastic strain range
$\Delta\epsilon_p$	plastic strain range
$\Delta\epsilon_t$	total strain range
$\Delta\sigma$	stress range, MPa
Δl	distance between the voltage leads, mm
ΔK_ϵ	strain intensity factor range, $\sqrt{mm}$
ΔK	stress intensity factor range, $MPa\sqrt{mm}$
ΔK_{th}	thermal stress intensity factor range, $MPa\sqrt{mm}$

NOTATION

a	inner radius, mm
b	outer radius, mm
b_0, b_1, b_2	regression parameters
c	crack length, mm
c_i	crack growth, mm
c_p	specific heat, J/ Kg°C
d	notch inner diameter, mm
$\frac{dc}{dN}$	crack growth rate
$e_{xx}, e_{yy}, e_{zz}, e_{xy}, e_{yz}, e_{zx}$	element strains
f	frequency, Hz
i	bessel function roots order
k	thermal conductivity, W/m.°C
m	constant
n	monotonic strain hardening exponent

n'	cyclic strain hardening exponent
p	parabola order
r	radius, mm
r_p	plastic zone radius, mm
t	time, sec
th	hollow cylinder wall thickness, mm
u	x-axis unit displacement vectors
v	volume, m^3
x, y, z	coordinates
A	amplitude ratio or cross sectional area
A_1, A_2, A_{3i}	constants
$A_0 - -A_{23}$	rigid body translations of the element
B_1, B_2, B_{3i}	constants
C	material dependent constant
CAD	computer aided design
CPU	central processing unit
CT	combat specimen type
D	coefficient of diffusion or gauge length outer diameter
DCPD	direct current electrical potential drop
E	modulus of elasticity, GPa
EL	elongation
F	heat flux, J
$F\left(\frac{a}{b}, \frac{c}{th}\right)$	geometry factor for hollow cylinder
$F\left(\frac{a}{b}\right)$	geometry factor for solid cylinder
FE	finite elemnets
FEA	finite element analysis
FEM	finite element method
F_z	z-axis force component
G_I	elastic energy release rate of mode I
H	coefficient of surface heat transfer, W/m^2K
I	current, Amp
I_{in}	inlet current, Amp

I_{out}	outlet current, Amp
IF	isothermal fatigue
$IP - TMF$	in phase thermo-mechanical fatigue
J	J-integral factor
J_0, J_1	Bessel's functions
K	strength coefficient
K_ϵ	strain intensity factor, $\sqrt{mm}$
K_I	mode I stress intensity factor, $MPa\sqrt{mm}$
K_{Ic}	final fracture stress intensity factor, $MPa\sqrt{mm}$
K_{max}	maximum stress intensity factor, $MPa\sqrt{mm}$
K_{min}	minimum stress intensity factor, $MPa\sqrt{mm}$
L	length, m
LVDT	linear variable differential transformer
N	number of cycles, cycle
$OP - TMF$	out of phase thermo-mechanical fatigue
Q	relevant quantity
R	load ratio
RA	reduction area
R_e	specific resistivity of the material, ohm.m
T	temperature, °C
T_a	inner surface temperature, °C
T_b	outer surface temperature, °C
T_r	temperature distribution at r position, °C
$T(r, t)$	temperature distribution at time and position, °C
T_m	melting temperature, °C
T_0	initial temperature, °C
TMF	thermo-mechanical fatigue
V	potential energy
Vol	voltage, volt
Vx	specimen output voltage, volt
Vy	reference output voltage, volt
W	size parameter

Y	shape function of (c/w)
Y_0, Y_1	Bessel's functions
2D	two dimension
3D	three dimension

LIST OF FIGURES

LIST OF TABLES

CHAPTER ONE

1- INTRODUCTION

1.1 Introduction:

The expectation of an increase in the world-wide demand for energy in the twenty-first century has encouraged the international community to consider ways to meet energy needs while maintaining and improving the environment. This has naturally led to improving the power generation industries such as the fission nuclear reactors and conventional fossil-fired power generation systems, dealing with components, which are subjected to higher loads at temperatures elevated than before, due to the increasing requirements regarding weight, performance and exhaust gas emission, such power generation can be produced without the environmental effects that accompany the use of coal or petroleum products. Although renewable energy sources offer the possibility of clean energy, there are challenges concerning the economic efficiency and reliability, whereas the economic reliability of the power generation has been demonstrated by the systems operating today. Rather than relying on the present generation of power industries, an international collaboration is directed toward developing a new generation that will produce abundant, reliable and inexpensive energy under safe environmental conditions [1].

Stainless steels are widely used in power generation industries. Operating experience with the various grades of stainless steels over several decades has generally been excellent. Nevertheless, stress corrosion failures have been reported in few cases. The first ferritic/martensitic steels were used for conventional power-generation applications in the 1920s. The 2¼Cr-1Mo steel, designated by ASTM as Grade 22, was introduced in the 1940s and it is still widely used today. Along with Grade 22, 9Cr-1Mo (T9) composition and 12Cr (AISI 410) which was an early development, the additional chromium was added for corrosion resistance. Since then, there has been a continual push to increase operating temperatures of conventional fossil-fired power-

1

generation systems. This has led to the development of several "generations" of steels with improved elevated-temperature strengths. In the nuclear power generation, the ferritic/martensitic steels were first considered for elevated-temperature in-core application (cladding, wrappers, and ducts) for fast reactors in the 1970s, because of their excellent thermal properties and irradiation resistance (low swelling) relative to austenitic stainless steels, and for fusion reactors. In the 1980s, they were developed by the steel industry for use in conventional power-generation systems and in the petrochemical industry. Since then, steel technology has advanced, and it is of interest to examine the evolution of the elevated-temperature steels for use in those industries since the 1980s [1-2].

The next power generation will, in many cases, have been operating conditions well beyond those of earlier designs. As with most new technologies or technological advances, success often hinges on materials available to meet the new operating conditions. One of the challenging conditions for engineers and designers of structural and material selection should be considered when the industrial component material is subjected to higher loads at an elevated temperature. Considerable research effort has been concentrated on high temperature fatigue over the last years, since thermal fatigue is an area of concern in design. The heating and cooling cycles during start-up and shut down operations cause thermal stresses that often occur in combination with mechanical loads. For example, in power generation plant boilers and heat exchanger where steam generating pipe work and control valves employ thick sections, and where liquid metal cooling is used for fast reactors, thermal fluctuations promote thermal shock conditions. Furthermore, the fatigue crack growth due to thermal shock loading constitutes a problem for turbine blades, pressure-vessel, valves, pipes and in-cores for nuclear reactors such as cladding, wrappers and ducts all of which suffer non-steady temperatures.

Thermal fatigue can be defined as failure under repetitive application of thermal stresses resulting from the rate of temperature changes. It may have different meanings to the problem, depending on their previous training, current interests and professional responsibilities. The work may concern a small part of the problem seeking highly specific answers, whether it deals with the understanding of fatigue crack initiation, or the determination of the design life of components [3]. The thermal fatigue cycle consists of two types, thermo-mechanical and thermal shock fatigue. Thermo-

2

mechanical Fatigue (TMF) refers to the process of fatigue damage under simultaneous changes in temperature and mechanical strain. Fatigue damage at high temperatures develops as a result of inelastic deformation where the strains are non-recoverable. Therefore, thermo-mechanical fatigue damage is complex, as it may accumulate over a range of temperatures and strains under both steady-state and/or transient conditions. Thermal shock usually refers to cases in which a body experiences sudden changes in temperature due to either a change in external environment or to internal heat generation [4].

1.2 Aims of the Research:

This thesis reports the concerns for the development of a fundamental understanding of the fatigue crack growth mechanisms of AISI 420 martensitic stainless steel, based on:

1- The comparative analysis of the theoretical and numerical modelling, incorporating research findings under isothermal fatigue loading for solid cylindrical specimen.

2- The comparative analysis of the theoretical modelling with the numerical simulation for tubular specimen when subjected to cyclic mechanical loading superimposed by cyclic thermal shock loading.

1.3 Objectives of the Research:

The objectives of this research are to produce a comparative analysis of the material behaviour under low cycle fatigue and isothermal fatigue, improving to the transient thermal shock fatigue, based on three modelling solutions:

1- Experimental work:

   ➤ Study the fatigue life of the material at room temperature for different surface conditions types of specimens.

3

➢ Study the fatigue crack growth rate of the material at 300 - 600 °C temperature ranges.

2- Empirical Modelling Solution:

➢ Develop an empirical modelling solution for a solid cylinder specimen under isothermal fatigue based on the experimental properties and boundary conditions.

➢ Develop an empirical modelling solution for a hollow cylinder under up and down shock fatigue cases.

3- Numerical Modelling Solution:

➢ Simulate the fatigue life of the material at room temperature, similar to the experimental low cycle fatigue test.

➢ Simulate the fatigue life of the material under high temperature ranges, similar to the experimental isothermal fatigue tests.

➢ Simulate the up and down shock fatigue cases, similar to the empirical modelling cases.

1.4 Approach of the Research:

This research studies compares between the experimental fatigues testing of AISI 420 martensitic stainless steel, the thermo-elastic-plastic empirical modelling solutions under thermo-mechanical induced stresses which initiate fatigue cracks and provide the driving force for crack propagation, based on the adding of the elastic-plastic thermal stress to the mechanical applied stress, utilizing the experimental mechanical properties and boundary conditions, and the numerical modelling solutions using ANSYS Workbench version 13.0 software based on the similarity to the experimental testing and empirical modelling cases.

1.5 Summary of Thesis Contents:

This thesis serves by an eight chapters as a brief description of the methodology of the fatigue and fracture mechanics with literature review in Chapter Two, where the material selections with the experimental testing and modification design techniques are detailed in Chapter Three. The empirical modelling solutions in details for all cases are produced in Chapter Four, while the numerical modelling simulations are produced in chapter five. The experimental results with discussion are described in Chapters Six and Seven. Finally, the conclusion and the future work in Chapter Eight.

CHAPTER TWO

2- LITERATURE REVIEW

2.1 Introduction:

High temperature fatigue has been investigated for a long time. It is difficult to cover all the published literature related to failure under elevated temperature in this short review due to different issue of the studies. However, as related to the present work, a brief historical background is offered with particular consideration given to the problems of isothermal and thermal shock fatigue specifically to fatigue crack growth due to the steady state and rapid thermal transient interacting with the failure process concerning the material AISI 420 stainless steel or other martensitic alloys.

This chapter serves as a brief description of the fatigue and fracture mechanics and the types of fatigue due to steady and unsteady loadings of high temperature and mechanical loads along with the numerical modelling solution for similar studies.

2.2 Fatigue Failure Mechanisms:

Fatigue failure under balanced cycling conditions takes place by the initiation and growth of one or more cracks until specimen separation occurs. In general, nucleation takes place at a free surface, and the crack grows in three stages, as illustrated in Figure 2.1. Stage I growth is an extension of the initiation process (the initiation crack length being of the order of $10\mu m$) and takes place along a crack tip shear plane. The extent of such growth is usually of the order of a few grain diameters. Stage II growth is normal to the applied stress and is controlled by the continuum response of the material. Finally, when the local crack tip deformation is of the order of the material in homogeneities, static fracture, e.g. voids growth, contributes to crack advance and leads to final failure, Stage III, [5]. The fractional area of fracture surface demonstrated in Fig. 2.1a and devoted to the various stages of failure depends on the applied strain level. At high levels, Stage II covers almost the entire fracture surface, whilst for low levels Stage I

begins to dominate. Stage III only occupies a significant area for high strain level tests on less ductile materials.

A crack in a solid can be stressed in three different modes, as illustrated in Fig. 2.2. Normal stresses to give rise to the (opening mode) or mode I loading, where the displacements of the crack surfaces are perpendicular to the plane of the crack. In-plane shear results in mode II or (sliding mode) the displacement of the crack surfaces is in the plane of the crack. The (tearing mode) or mode III is caused by out-of-plane shear. The superposition of the three modes describes the general case of loading and the most important mode is technically Mode I.

2.2.1 Fatigue Crack Initiation:

Fatigue crack initiation in a ductile metal is a consequence of reversed plasticity within a grain on a metallurgical feature scale of 10^{-3}mm. Surface grains are weakest; they deform plastically at the lowest stress, and this leads to the production of a micro-crack within a grain. Such microplasticity, due to slip within grains, can occur at stresses much lower than the tensile yield stress. The slip can take place only on certain crystallographic planes within a grain. Resistance to crack initiation depends strongly on surface roughness, residual stress and environment, all of which are difficult to control [6].

Several equivalent models have been proposed to explain the initiation of fatigue cracks by local plastic deformation. The Wood's model exposed in Fig. 2.3 reveals that during the rising-load part of the cycle, slip occurs on a favourably oriented slip plane. In the falling-load part slip, takes place in the reverse direction on a parallel slip plane, since slip on the first plane is inhibited by strain hardening, and by oxidation of the newly created free surface giving rise to an extrusion or an intrusion in the metal surface. An intrusion can grow into a crack by the continued plastic flow during subsequent cycles. If the fatigue loading is a cyclic tension-compression this mechanism can still work since the plastic deformation occurring at increasing load will give rise to residual compressive stresses during load release [7].

7
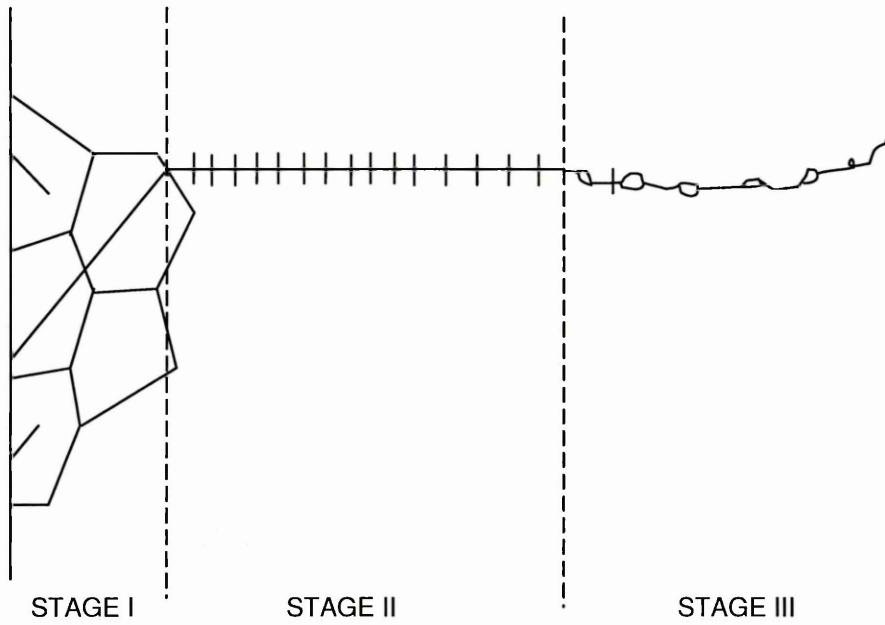
a) Fatigue crack growth propagation across a specimen section
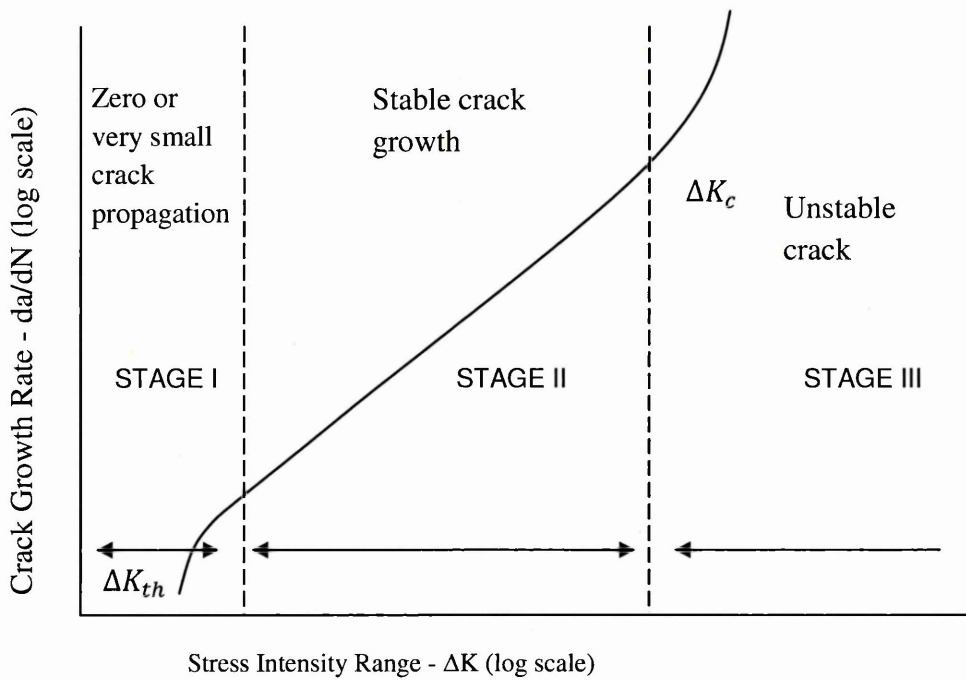
b) Crack growth rate pattern

Figure 2.1 Fatigue crack growth stages.

Mode I   Mode II   Mode III

Opening mode   Sliding mode   Tearing mode
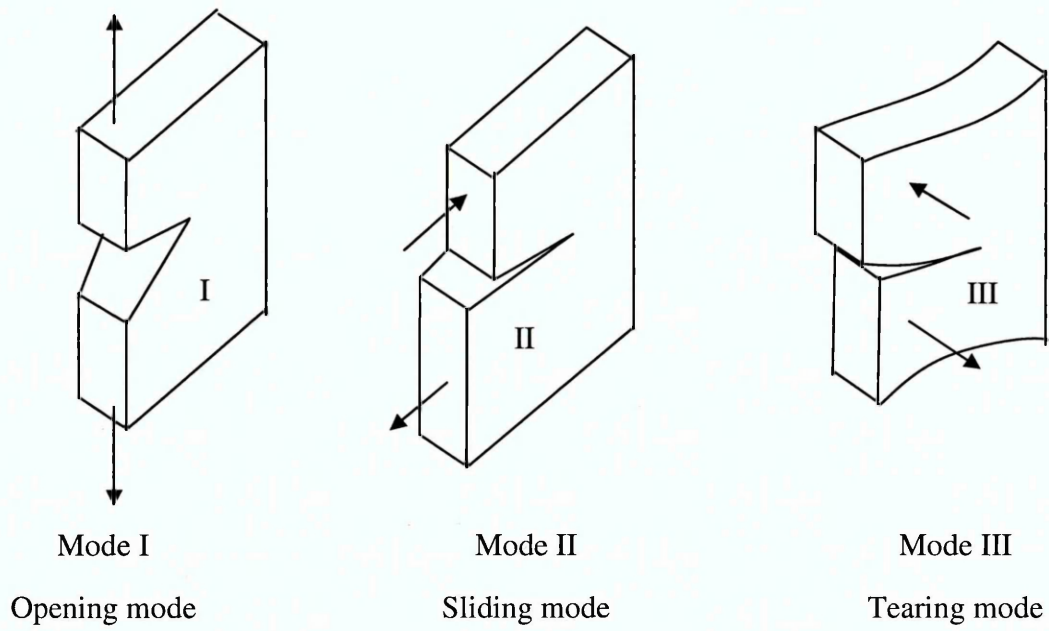
Figure 2.2 The three crack modes of loading.
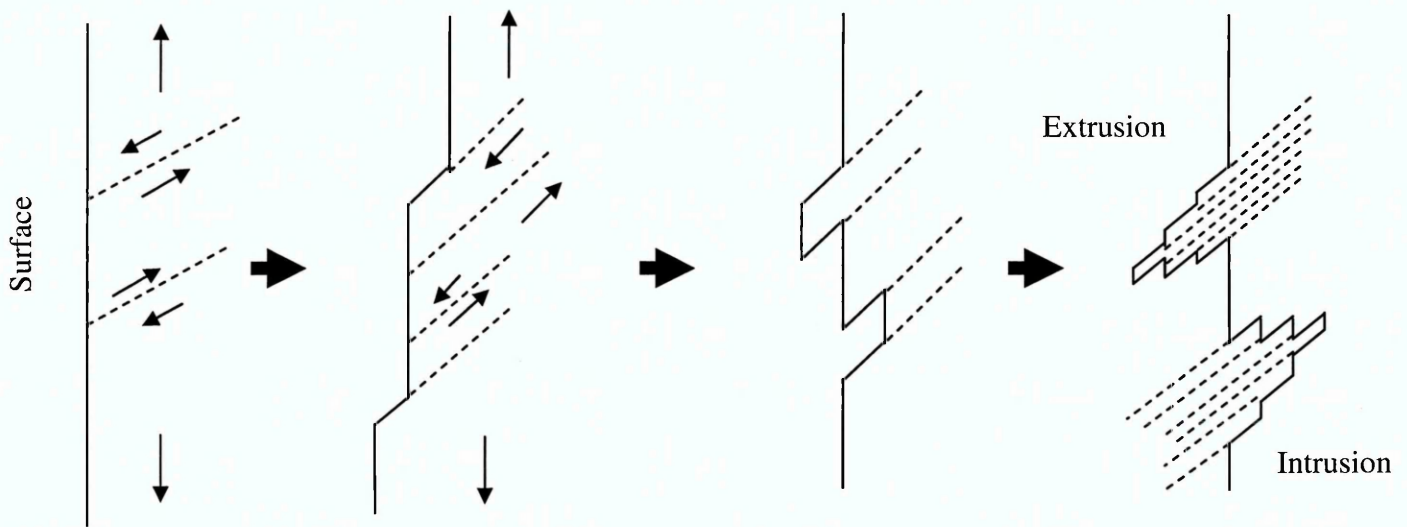
Figure 2.3 Wood's model for fatigue crack initiation.

2.2.2 Fatigue Crack Propagation:

In the metal fatigue literature, the terms fatigue crack propagation and fatigue crack growth are both used for the increase in size of a fatigue crack. A Stage I crack becomes a Stage II crack. When it reaches a critical length, it changes direction and propagates normal to the maximum principal tensile stress. The critical length is strongly dependent on microstructural features and on stress conditions and it varies widely. It is usually less than 0.25mm and typically, around 0.02 mm. After the transition, a Stage II crack propagates through the majority of the cross section. More descriptive terms for Stage I and II, microcrack and macro-crack respectively, are sometimes used [6].

A model of Stage II crack propagation was presented by Tomkins [8] in 1968. This region is the primary region of growth for fatigue cracks. Moreover, Tomkins model demonstrates a repetitive deformation of crack tips through applied cyclic loads. The model is illustrated in Fig. 2.4, where a fully compressed crack, Fig. 2.4a, is loaded through a tension/compression cycle. On increasing the load through the tensile cycle the crack opens with $45°$ shear bands creating a plastic flow ahead of the crack tip, (Fig. 2.4b). At the tensile strain limit, Fig. 2.4c, shear decohesion of the material occurs by these bands producing new crack surface. On the compressive reversal of loading the crack tip closes without recohesion of the new crack surface, (Fig. 2.4d). On returning to full compression a deformation of new surface occurs in the form of a ripple. Under repeated cyclic loading these ripples are repeated with each cycle producing the familiar fatigue crack surface effects of striations.

2.2.2.1 Factors Affecting Fatigue Crack propagations:

There are different types of factors affecting the fatigue crack propagation which can be classified into the following categories:

I- Microstructure of the material:

The effect of the microstructure depends on the grain structure, average grain size and microstructural flaws, which have a significantly high influence on the fatigue life and the crack growth. For example, a material with large grain size would exhibit a

10

a) Fully Compressed

b) Increasing Tension

Flow
Bands

c) Strain Limit

New crack
surface generated
by decohesion

d) Compressive strain reversal

e) Fully Compressed
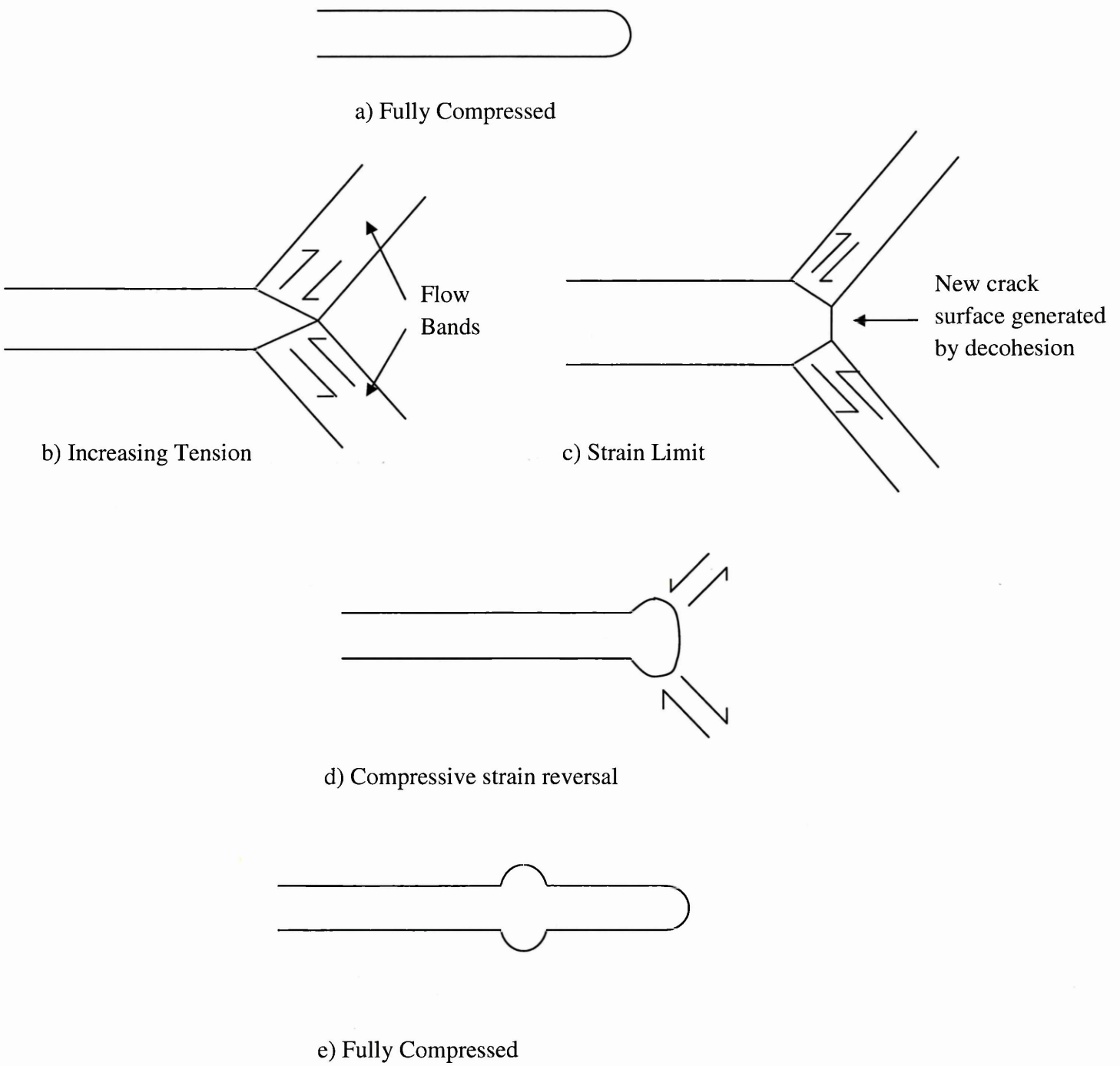
Figure 2.4 Shear de-cohesion model for Stage II crack propagation.

lower fatigue life limit, in comparison with smaller grain size when cycled at an ambient temperature: however, at a high temperature (in the creep range of metals) the coarse-grained materials appear to exhibit better fatigue properties [9].

II- Processing Techniques:

The effect of processing techniques such as forging, rolling and extrusion produce directional properties in the materials due to the grain orientation. For that the fatigue life is specifically increased in the oriented direction and it is lower in the transverse direction. Besides, heat treatment, case hardening, cold and hot working, surface coating, platting, cladding, etc. can all influence the fatigue life and the crack growth due to the residual stress production [9].

III- Load Spectrum:

The actual service loading may be a very complex-one due to the history, magnitude, sign, and rate of loading, which significantly influence the fatigue life and consequently the crack propagation rate [9].

IV- Geometry of the component:

The effect of the geometry is produced by surface finish, notches, welds, connections, and thickness where the surface finish has a significant influence on crack initiation. The geometric surface discontinuities in components such as holes, notches and joints are sources of stress (or strain) concentration and are often the site of crack initiation [9].

V- Temperature:

The fatigue crack growth mechanism at high temperature is a complicated process to study. The important factors influencing the crack growth process are the possibility of

creep or creep-fatigue interaction, thermal ageing effects, thermo-mechanical effects and the environmental interaction [10].

Rising temperatures affect the slip character of the material, reduce grain boundary strength and accelerate oxidation. The combined effect of these processes is to speed up the fatigue crack propagation. Several materials obtained a fatigue limit above a certain temperature; the fatigue limit is considerably reduced, which means that the material can no longer be used at higher temperatures [11]. Intergranular crack growth rate was studied by Bown, et al., [12] at a particularly high temperature in a vacuum under static load, and the same behaviour was reported for martensitic alloys at different temperature ranges in air [13].

VI- Environment:

A corrosive environment causes degradation of the material, the most common visible effect being pitted or surface roughness (etching). These notch-like regions act as stress raisers and are generally the sites of crack initiation. Thus, one needs to shorten the crack nucleation stage and to increase the crack growth rate. The increase in temperature reduces the fatigue resistance of the material; thus increasing the crack propagation [9]. The high temperature fatigue failure studies concern themselves with the great effect on the environment which represents an important factor in the various regions of the crack growth rate curve. Several types of environmental effects on the crack growth rate curve are identified below:

a- The reduction or elimination of ΔK_{th} and an overall enhancement of the crack growth rates until high ΔK levels are reached, at which the purely mechanical contribution to crack growth predominates [14].

b- An additional enhancement of crack growth rates owing to monotonic, sustained load fracture during the tensile part of the stress cycle. This behaviour is typical for fatigue in liquid environment that causes stress corrosion [15].

c- The sustained load caused by the gaseous environment usually hydrogen, [16], [17].

d- The overall enhancement of the crack growth rate explained in some instances by local corrosion on the crack surfaces, [18].

The influence of the air and vacuum environment on the fatigue crack growth plays a very significant role where the fatigue lifetimes are reduced in air compared to the vacuum [17].

VII- Oxidation:

The influence of oxygen is more pronounced as the temperature is increased. A suggested mechanism is the embrittlement of grain boundaries due to oxygen penetration. This embrittlement is explained in terms of pinning the grain boundaries due to the existence of oxides and small cavities. During cyclic loading at a high temperature, the lack of grain boundary mobility may lead to intergranular cracking [9]. The model depicted in Fig. 2.5 is described by a monolayer of oxygen or an oxide layer form rapidly on the freshly formed slip step exposed in air during a tension cycle. In the compression part of the cycle, the slip reverse takes place on the same plane, and some of the freshly absorbed oxygen is drawn into the body of the crystal in the form of dissolved atoms. During the next cycle, this process is repeated and more oxygen is supplied to the crystal which could then diffuse along the slip band. Additionally, the chemisorptions of oxygen in, and near the slip band causes weakening in the persistent slip bands of the crystal eventually leading to crack [9].

The work represented by Fournier et al [19-21] for 9Cr–1Mo Martensitic Steel, has concluded that the presence of the oxide layer filling the cracks leads to faster propagation. This layer thickness increases with the high strain in tension and compression. The oxide composition strongly depends on the environment, temperature and the exact chemical composition of the steel, where the effective behaviours concerned are the oxidation morphology and the oxidation kinetics.

VIII- Creep-Fatigue:

Creep of materials is classically associated with time-dependent plasticity under a fixed stress at an elevated temperature, often greater than roughly 0.5 Tm, where Tm is the absolute melting temperature [22]. It is one of the principal damage mechanisms for materials operating at an elevated temperature. It can produce larger strain deformation, stress relaxation, and crack initiation and growth. The combination of high temperature

14

(below the melting point of the metal) and high stresses in the material make it susceptible to creep, and the interactions of creep and fatigue can seriously influence the properties and fatigue life of the materials. Fatigue-creep interactions occur by the propagation of fatigue crack into cavitate materials producing a reduction in endurance.
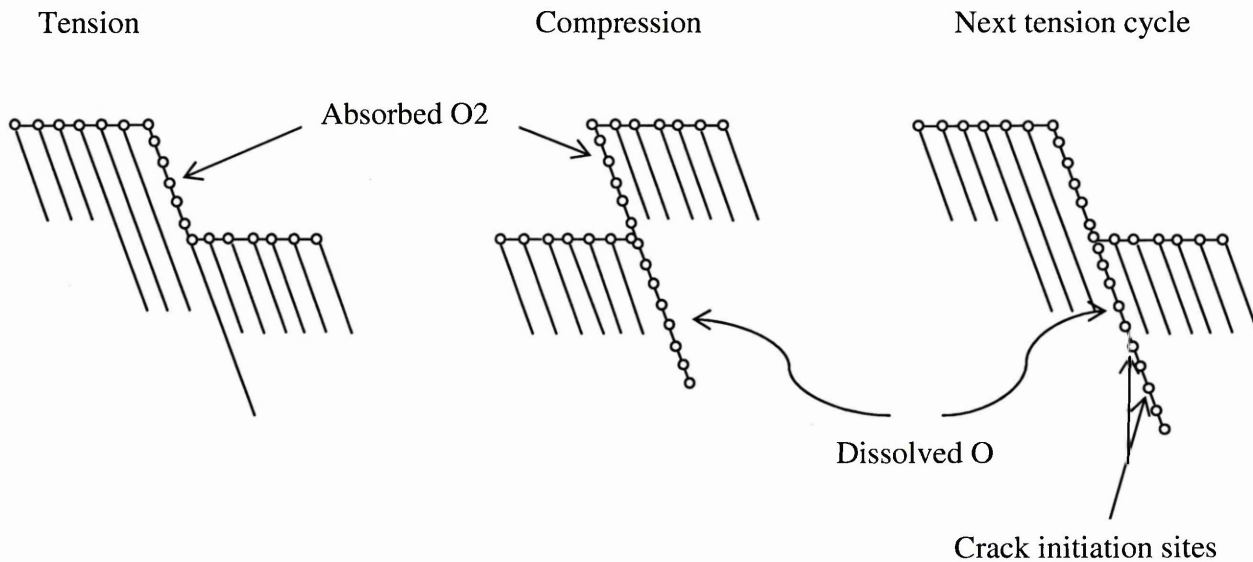
Figure 2.5 Oxidation mechanism assisted stage I crack growth.

Studies [19-20] conducted in 2008 pointed out that the true creep-fatigue is a stronger lifetime reduction factor, compared to the usual stress relaxation fatigue under tensile holding period. The compressive holding periods are more deleterious than the tensile ones where the lifetime fatigue is shorter. This difference is more pronounced for the low strain ranges. The two studies stated above are consistent in identifying the physical mechanisms responsible for damage based on the interaction between fatigue, creep and oxidation mechanisms. Fournier et al., [21], [23] proposed a model for creep-fatigue lifetime prediction depending on these two mechanisms for martensitic alloys.

2.2.3 Unstable and Fast Fracture:

The Stage III has been generally identified as a region of rapid growth close to instability in a specimen in which crack tip microscopic fracture events such as ductile void age contribute to the overall growth rate [5].

The primary mechanism of ductile fracture is due to nucleation of microscopic voids, either at dislocation pile ups, points of severe deformation, or around the interface of particle inclusions. These voids grow in size ahead of the crack tip where the stress/deformation field is greatest, increasing in concentration until they coalesce to create larger voids or separate completely to form further crack surface. As with brittle fracture, ductile fracture can occur by a trans-granular or inter-granular fracture as illustrated in Fig. 2.6 where, the trans-granular fracture in ductile structural materials is caused by overloading depending on the constraint; it failed by a process called micro-void coalescence [14]. The inter-granular fracture results from a continuous fracture load or from the deficiency of ductility in the materials due to the segregation of the embrittling elements, particles and precipitates to the grain boundaries as is the case with temper-embrittle steels [14]. This depends on the amount of slip planes that are introduced in the material structure; the more the slip planes, the more dislocation pile ups that occur at grain boundaries; therefore, greater energy is required to initiate void growth and crack propagation. Consequently, face centred cubic materials have more slip planes than the body centred cubic; they are more likely to be fractured by inter-granular processes. At high temperatures, creep effects can also be present. These processes can combine to generate complex fracture processes.

Ferritic and austenitic steels demonstrate a range of fracture processes. Austenitic steels can specifically fracture under low loading for a long time by inter-granular processes. However, at high temperature trans-granular creep fracture dominates. This can, however, be attributed to inter-granular fracture. If inclusion or precipitations are present at the grain boundaries, fracture will occur due to their effect as a stress raiser [24] while, in the martensitic steel, the fatigue rupture mainly initiates on inclusion for low temperature or oxide crack at higher temperature; it always propagates trans-granularly [25].

16

σ, ε

σ, ε

Intergranular Fracture

Transgranular Fracture

σ, ε

σ, ε

σ, ε

Void Nucleation
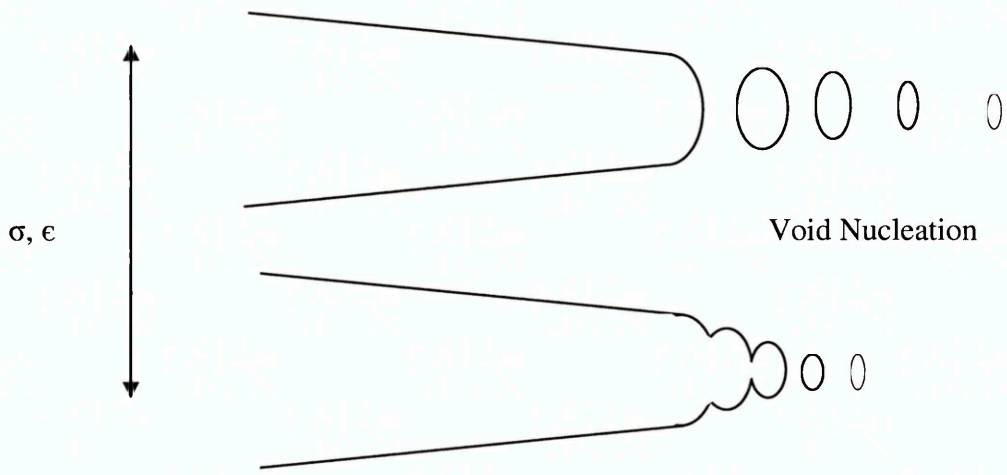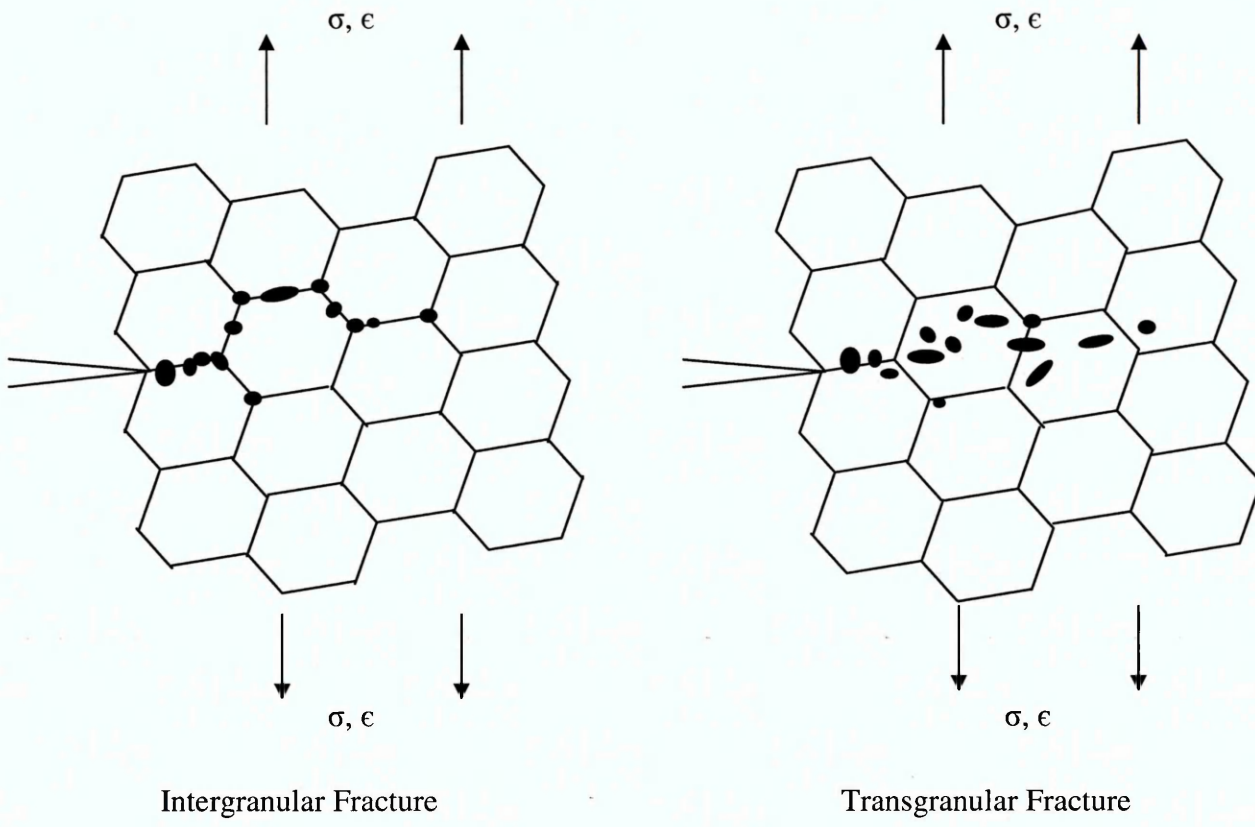
Figure 2.6 Micro-mechanisms of Fracture.

17

2.3 Fracture Mechanisms:

The Design engineer should consider the fact that there is always a certain possibility of risk that a structure may fail, and the probability of such a failure should be kept at an acceptably low level. Fracture mechanics methods help the designer to predict how fast cracks will grow and how fast the residual strength will decrease.

Conventional engineering design criteria are usually based on tensile strength, yield strength and buckling stress of structures. These criteria are adequate for many engineering applications, but they are insufficient when there is likelihood of cracks.

Fracture mechanics have developed into two distinct fields: Linear Elastic and Elastic-Plastic crack tip analysis. Linear Elastic, deals with elastic crack tip stress fields. The fundamental parameter of Linear Elastic Fracture Mechanics (LEFM) theory, the stress intensity factor K_I, may be derived from the classical Griffith theory of fracture [7], or more directly from knowledge of the local stress distribution ahead of a crack as,

$$K_I = \sigma_{ct}.\sqrt{\pi.c} \tag{2.1}$$

To consider the size and geometry of the component, a dimensionless quantity (Y) can be introduced in the above equation, which is a shape function of (c/W), crack length (c) and a size parameter (W),

$$K_I = Y\sigma\sqrt{\pi c} \tag{2.2}$$

The solutions for several (Y) factors are given in stress intensity factor handbooks. Similarly solution for the stress intensity factors for mode II and III crack growth can be so obtained [7].

The application of cyclic loads (either thermal or mechanical. Or combination of both) can produce fatigue crack growth, even though the maximum load is lower than that required to exceed the appropriate (K_{IC}) value for final fracture with monotonically increasing load. Thus, under cyclic conditions, the range of stress intensity factor ΔK can be a useful parameter for the correlation of fatigue crack growth.

An empirical relation between the cyclic crack propagation or growth rates $(\frac{dc}{dN})$ and cyclic stress intensity factor range, ΔK was given by Paris; it is known as the Paris Law [22],

$$\frac{dc}{dN} = C\,(\Delta K)^m \tag{2.3}$$

where,

$$\Delta K = K_{max} - K_{min} \tag{2.4}$$

Here, K_{max} and K_{min} are the values of the opening mode I stress intensity factor, calculated from the maximum and minimum stress during the fatigue cycle.

Elastic-Plastic Fracture Mechanics (EPFM) methods extend fracture behaviour beyond the elastic regime, but they may have a limitation on their range of applicability, as is the case with LEFM. EPFM is generally applied to solve fracture problems in two ways, either by searching for characterizing parameters or by attempting to describe the elastic-plastic deformation field in detail, in order to find a criterion for local failure. Several theoretical contributions have been made to predict fatigue crack propagation rates. Generally, these theories are divided into three groups [26]; they are either:

1) Based on damage or strain accumulation at the crack tip or they

2) Consider a critical crack tip opening displacement as the crack advancing criterion.

More recent theories invoke an energy criterion with crack tip process zone; for example, the J-integral, crack opening displacement (COD), plastic zone size $\left(r_p\right)$ and the strain intensity factor (K_ϵ).

19

J-Integral:

It is a mathematical expression of a line or surface-type integral that encloses the crack front from one crack surface to the other; it is used to characterize the local stress-strain field around the crack front. The J-Integral specifies the plastic stress and strain intensity in a manner similar to that whereby the K parameter in LEFM represents the stress intensity of the surrounding elastic field in the crack vicinity. That depends on stress, strain, crack size, and the geometry of the crack and body [27]. The physical significance of J under monotonic loading is considered a measure of the intensity of the crack tip strain field for elastic-plastic materials. The J-Integral is defined, along a contour around the crack tip by the change in potential energy for a virtual crack extension (dc) [7];

$$J = -\frac{\partial V}{\partial c} \tag{2.5}$$

Crack Tip Opening Displacement (CTOD):

It is a measure of the opening displacement mode of the crack face or a measure of the plastic strain at the crack tip. Several values of this parameter can be calculated from the load displacement records related to such characteristics as unstable cleavage fracture during and after ductile tearing, maximum load condition, first pop-in at brittle crack extension, and the onset of stable crack extension [27].

The general equation of the crack tip opening displacement is [7]:

$$\text{CTOD} = \frac{G_I}{\gamma \sigma_{ys}} = \frac{K_I^2 \left(1 - \nu^2\right)}{E \, \gamma \sigma_{ys}} \tag{2.6}$$

Strain Intensity Factor:

The growth of short cracks has been analysed using a strain intensity factor in high strain fatigue tests conducted with controlled strain limits. Boettner et al., (1965) [28] proposed that for room temperature fatigue of copper, at relatively high strains, crack growth rates can be described by the relation,

20

$$\frac{dc}{dN} \propto \Delta \epsilon_p^2 . c \qquad (2.7)$$

And

$$\Delta K_\epsilon = \Delta \epsilon_p \sqrt{\pi c} \qquad (2.8)$$

Solomon, [29] in 1972, proposed a range of pseudo strain intensity factors as,

$$\Delta K_\epsilon = \Delta \epsilon_t \sqrt{\pi c} \qquad (2.9)$$

Where, $\Delta \epsilon_t -$ is the total strain range given by;

$$\Delta \epsilon_t = \Delta \epsilon_p + \Delta \epsilon_e \qquad (2.10)$$

where, $\Delta \epsilon_e \ and \ \Delta \epsilon_p$ are the elastic and plastic strain ranges respectively.

Equations (2.8) and (2.9) are almost the same at high plastic strain and some improvement can be made by using equation (2.9) when the elastic strain component becomes larger. Haigh and Skelton [30] in a study carried out in 1978 derived a strain intensity parameter to describe cyclic crack opening displacement in both high strain and liner elastic fatigue at room and elevated temperature as,

$$\Delta K_\epsilon = \left(\Delta \epsilon_p + \frac{1}{2} \Delta \epsilon_e \right) \sqrt{\pi c} \qquad (2.11)$$

Whereby the term $\left(\Delta \epsilon_p + \frac{1}{2} \Delta \epsilon_e \right)$ describes the strain range for which the crack was open.

The strain intensity approach was based on an equivalent elastic strain range that works well for fatigue crack growth in conditions whereby the environment and the creep have little effect [10].

2.4 Low Cycle Fatigue:

Most machinery and structures in service do not operate under a constant load and stress. In fact, these loads and stresses are constantly changing. A good example of this is a rotating shaft such as the axle of a railroad car. The bending stresses change from tension to compression as the axle rotates. This constant change in stress can cause fatigue failure which suddenly fractures the material. The process that leads to fatigue failure is the initiation and growth of cracks in the material. Fracture occurs when the crack grows so large that the remaining un-cracked material can no longer support the applied loads.

Knowledge of the fatigue behaviour of materials at low endurance is required for economic and long life design. Low cycle fatigue of metals can be defined as failure resulting from cycles of loading comparatively less than about 10^4 cycles [31] and it is classified into isothermal fatigue and thermal fatigue.

Low cycle fatigue phenomena began to gain attention. Until World War II little attention was paid to the low cycle range, and most of the existing fatigue results were for high cycles only. Then it was realized that for some pressure vessels, pressurized fuselages, mechanisms for extending landing gears and controlling wing flaps, missiles, spaceship launching equipment, etc. only a short fatigue life was required [32]. Today many components in heat exchanger, gas and steam turbines, nuclear reactors and aircraft industries employ stresses appreciably above their yield stresses, which may be due to, for example, start-up and shut-down of the power plant, or the taking-off and landing of an aircraft. The frequency of cycling has usually different orders of magnitude and waveform depending on the experience life.

At high temperature the material deformation process is complex; it involves the addition of a number of thermally activated processes including grain boundary sliding, dislocation climb, etc. [33], and when the time factor is combined with high temperature, creep and environmental interactions may play an important part in the failure process.

Investigators have proposed several methods of analysis to study the failure of different materials under high strain low cycle fatigue at high temperature variables. To the best knowledge of the author, there are few studies that particularly deal with AISI

420 martensitic stainless steel; most studies focus on different types of Martensitic stainless steel.

Numerous studies are conducted on strain controlled fatigue; for instance, Song et al., [34], analysed the cyclic softening observation employing a strain-controlled uniaxial push–pull low-cycle fatigue tests at room temperature and 600 °C; he discovered a cellular dislocation in 12Cr–WMoV martensitic stainless steel lath, and a high effect of the deformation density due to dynamic recovery under cyclic deformation at high temperature. Roessle et al., [35] undertook a study comparing monotonic deformation, cyclic deformation and strain-controlled fatigue properties of several steels used in the ground vehicle industry, obtaining a correlation between fatigue limit, ultimate strength, fatigue life, hardness and strain-life curves estimation relationship from the monotonic tensile properties. Earlier in 2010, B. Fournier et al., [23] tested three types of the 9-12%Cr martensitic steel family under pure fatigue and creep fatigue at 550 °C conditions compared to P91 steel; the experimental lifetimes are very close and the observation of the damage mechanisms remain valid for these three steel types. Other studies conducted by Barsom on the service life prediction, in 1971 [36] displayed the relationship equations between the fatigue crack growth rates in different types of steel with the stress intensity factor range that can be defined by a single equation precisely meeting the engineering purposes.

Modern testing facilities have helped, in producing data close to the actual service conditions. It is difficult to design a test that takes into account all the possible factors contributing to plastic deformation; examples of some of the more important ones are: (a) load cycling, (b) mechanical strain cycling, (c) thermal strain cycling and (d) the effect of environment. Under actual service conditions, most components, if not all, experience a combination of all these loading effects. Furthermore, in the early experiments, data was generated under the individual loading conditions and, with appropriate methods of analysis; the life of the component was predicted. However, it is possible now to study high temperature fatigue behaviour under a combination of loading sequences and environments with advanced technology [10].Thus, the study of the low cycle fatigue at high temperature is a useful starting point for the present study once the parameters that control fatigue failure can be readily monitored and quantified in analysis, especially since many components are known to fail by thermo-mechanical stressing over hundreds of thousands of cycles.

2.5 Isothermal Fatigue:

Isothermal fatigue (IF) is the simplest form of cyclic fatigue operating at a constant and uniform temperature. Cyclic loading may be applied externally or during operation of plant when alternative stresses due to vibration can cause fatigue. Indeed, other more complicated forms of cyclic loading sometimes referred to a single representative isothermal temperature. Therefore, more complex methods of evaluation requirement demand economic climate and high competition for accurate component specification in life as well as in performance.

Many investigators have concerns regarding the isothermal fatigue which studies the behaviour of the materials subjected to cyclic high temperatures. Others have used isothermal fatigue data to find out whether a relationship exists with the study of thermal shock fatigue crack growth behaviour in different materials. Usually it is assumed that maximum temperature of the thermal shock cycle is more damaging than the average temperature. Therefore, for correlation purposes, isothermal fatigue studies are normally performed at the maximum temperature of the thermal shock cycle [10]. Many studies are carried out on different types of martensitic stainless steel materials. Some investigators focus on the effects of the structured deformation, as a strain ageing, softening behaviour or damaging at temperature ranges. Armas et al., [37] studied the dynamic strain ageing effects in a low cyclic fatigue stress response of type AISI 420 stainless steel in the temperature range 300- 823K; they observed a short initial hardening stage followed by a saturation period independent of test temperature; it is vulnerable to failure and a cyclic softening at all temperatures. The damage effect was considered an effective factor by Gerard et al., [38] who studied the influence of temperature damage on 12Cr martensitic stainless steel. They noted that the fatigue damage was controlled by two types of mechanisms depending on the plastic strain range mechanisms; they are the thermally activated mechanism and the non-thermally activated one. The contribution of the thermally activated mechanism increases when the plastic strain range decreases. Lindau et al., [39], [40] found out that the fatigue life reduction can be understood by the time evolution of the irradiation induced hardening, when they studied the damage ratio under strain-controlled post irradiation and in-beam fatigue loading under simultaneous irradiation temperature.

24

The dependence of the cyclic softening behaviour of the martensitic stainless steel with temperature changes is a significant factor to be considered by other investigators. Kanazawa et al., (1979) [41] analysed the cyclic softening observation of two kinds of martensitic stainless steel at room temperature and at 400-600 °C ranges; the cyclic softening behaviour was observed at each test temperature and the temperature and the material dependences of low cycle fatigue life for a given plastic strain range coincide qualitatively with the dependences of the reduction in area in a tensile test. However, the dependences cannot be explained quantitatively by the equations of Coffin or Manson. Bernhart, [25] found out a cyclic softening without stabilization; the higher the initial strain amplitude, the more the material softens. The level of the plastic strain amplitude at half-life was found to be only dependent on the initial total strain, but the evolution rate is temperature dependent. Zhang et al., [42] analysed two hot working martensitic tool steels commonly used in forging industry under isothermal and thermo-mechanical fatigue conditions at a temperature range of 200-550 °C; they demonstrated the influence of the temperature, strain amplitude, strain rate and initial hardness on the cyclic softening behaviour. The isothermal and thermo-mechanical fatigue cyclic softening is observed to be rapid in the first stage but it soon flattens out. The same authors, [43] and [44], focused on the mechanisms involved in the softening of another tempered martensitic steel type under isothermal fatigue at different hardness levels at room to high temperature ranges. A sharp ageing is also observed even during the short time of the sample heating and temperature stabilisation stage before the fatigue test starts and the cyclic softening intensity increases with testing temperature from 300 to 600 °C, but the maximal softening intensity occurs at room temperature. Negesha et al., [45], studied the low cyclic fatigue behaviour of tempered modified ferritic steel and martensitic steel at different strain amplitude and temperature range of 300-873 °C. They noticed initial brief hardening in the first few cycles, followed by a continuous and gradual softening regime that ended in stress plateau that resulted into the specimen failure. The fatigue life decreased as the temperature increased; that could be attributed to oxidation-fatigue interaction. Later, Fournier et al., [46], proposed a model based on the physical mechanisms describing the microstructural recovery (corresponding to a decrease of the dislocation density and sub-grain coarsening) observed experimentally. They also presented very good predictions and extrapolations of the cyclic softening effect observed in uniaxial tension-compression loadings for strain ranges larger than 0.3%. Stress–relaxation and creep behavior are correctly predicted for high stress.

Further detailed investigations are made to assess the creep fatigue interaction behaviour of different types of martensitic steel. Fournier et al., [19-21, 23], analysed the creep fatigue and oxidation mechanism of modified martensitic steel at high temperature. No creep or any type of creep damage was observed, except very close to the fracture surface; they suggested that it might be due to viscoplastic deformation rather than diffusion process, whereas oxide layer is observed in the compression creep fatigue holding period which is mainly subjected to tension stresses conversely for the tensile holding period. Fournier et al., [47], compared the cyclic behaviour of advanced ferritic-martensitic steels under fatigue and creep fatigue at high temperature; they displayed all observed cyclic softening effect linked to the coarsening of the sub-grains and laths and to the decrease of the dislocation density. These changes of the microstructure led to a drastic loss in creep strength for all the materials under study. However, due to a better precipitation state, several materials optimized for their creep strength still exhibit good creep resistance after cyclic softening. Mannan et al., [48], found out the effects of several time-dependent processes such as creep, oxidation, phase transformations and dynamic strain ageing depending on strain rate and temperature. It is reported that dynamic strain ageing enhances the stress response and reduces ductility. It localizes fatigue deformation, enhances fatigue cracking and reduces fatigue life. High-temperature oxidation accelerates trans-granular and inter-granular fatigue cracking. Other researchers focus on the physically based empirical modelling and on different martensitic steels to study the creep fatigue properties such as, Hyeong-Yeon Lee et al., [49]. Fournier et al., [20, 21, 23] proposed the interaction between fatigue, creep and oxidation damage model, On the other hand, Zhang [42] predicted an isothermal based upon the comparison of the experimental results. This model is useful to explain some experimental results such as the increase in strain softening when the strain rate decreases during isothermal testing, as well as the relation between the mean stress and the temperature range or the cyclic softening with strain amplitude in an isothermal condition.

Crack growth behaviour is also examined by several researchers. BOWEN et al., [50], identified the crack growth at low stress intensities, a low ductility type of inter-granular fracture; it is controlled by the dynamic segregation of sulphur to crack-tip regions. While at high stress intensities, the mechanism of fracture changes to inter-granular micro-void coalescence is controlled by the distribution of sulphides. This is

26

when the micro mechanisms of high-temperature crack growth in martensitic steel have been studied in vacuum, under static loading at 500 °C. Kim et al., [13], examined the microstructural mechanism of the fatigue crack growth behaviour of reduced activation ferritic/martensitic steel at room temperature and at 400 °C. Machined and welded specimens revealed that the fatigue crack growth rate at 400 °C is significantly higher than at room temperature, slightly higher in welding than in machined specimen due to the finer lath structure of moderately tempered martensitic phase when the stress intensity factor range is normalized by Young's modulus. This means that the difference of crack growth rates between room temperature and 400 °C primary results from the difference of Young's modulus. Kuei-Chang Hsu et al., [51], investigated the fatigue crack growth behaviour for 17-4 PH martensitic precipitation-hardening stainless steel, in three heat-treated conditions at temperatures ranging from 300 to 500 °C; the findings indicated that the fatigue crack growth rates increased with the temperature, except for conditions A and H900 which were tested at 500 °C and the exceptions could be attributed to an in-situ precipitate-coarsening effect during the test. The earlier work of NOGAMI et al., [52], considered the improvement of fatigue life assessment method by investigating the crack growth behaviour under low cycle fatigue for reduced activation ferritic/martensitic steel. They found out that the crack growth rate could be estimated using the total strain range and the surface crack length by introducing the concept of the normalized crack growth rate.

2.6 Thermal Fatigue:

Thermal fatigue may be defined as failure due to the rate of temperature changes and the alternating exposure at higher and lower temperatures influencing the life of a material. Thermal fatigue can be known by many different names; creep fatigue, thermal shock, craze cracking, thermal rupture, thermal strain fatigue, thermal stress fatigue and high temperature fatigue [26]. It can be broadly divided into two categories:

I- Stresses can that arise in the absence of thermal gradients due to the expansion and contraction of mechanically restrained structures [5].

II- Stresses that are produced from rapid changes in temperature; for instance, thermal gradient may cause different expansion through the section of the component.

The process may be illustrated with an example. If a solid body is at high temperature and then it is suddenly cooled to room temperature, due to the rapid change in surface temperature, thermal gradients will be set up in the body, which leads to transient strains and associated stresses. The process of transient temperature variation in a body is commonly termed as thermal shock fatigue. Thermal shock of this type is always associated with fast heating or cooling rates. However, it is not necessary that the thermal stresses experienced in a structure are the result of differential rate of heating and cooling cycles. They may be experienced in a uniformly heated structure, if the free expansion of the body is suppressed by external constraints, thereby setting up compressive stresses. This leads to isothermal fatigue.

The majority of service loads involving thermal fatigue are substantially less complicated than those of mechanical loading situations, since thermal fluctuations are generally the result of machine start-up and shut-down. Elevated or even sub-zero temperatures are often held at an approximate constant whereby the start-up and shut-down of the system invariably causes most of the damage. Figure 2.7 shows the basic representations of the thermal load cycle. Turbine blades in a gas generator are prone to the scenario shown in Figure 2.7a, whereby the rise and fall in demand require the start-up and shut-down of further generators. A similar pattern would be observed in Figure 2.7b (turbine blades in a jet engine) whereby the take-off and landing expose the blades to a large increase in temperature whilst the flight time incurs a steady-state and overall lower temperature [24].

A basic understanding of the thermal fatigue problem is an essential preliminary to the complete solution of superimposed thermal and mechanical fatigue problems.

2.6.1 Thermal Shock:

We cannot predict that a material has been sufficiently well chosen for its performance at elevated temperatures; hence, the cycles shown in Fig. 2.7a and b, become a case of primary damage due to the huge changes in temperature over a period of time. Indeed, some situations experience this kind of cycle. Fig. 2.7c exhibits such an event by cooling systems in liquid metal fast breeder reactors using molten sodium as a coolant following thermal fluctuations that vary rapidly and heat the extractor [24].

Thermal Shock usually refers to cases whereby a body experiences sudden changes in temperature due either to a change in external environment or to internal heat generation. It is the transient feature of the temperature distribution that distinguishes thermal shock from ordinary conditions of static or slowly varying thermal stress [4]. In other words, it occurs when a thermal gradient causes different parts of an object to expand by different amounts. This differential expansion can be understood in terms of stress or of strain, equivalent. At some point, this stress overcomes the strength of the material, causing a crack to form. If nothing stops this crack from propagating through the material, it will cause the object's structure to fail. Thermal shock events primarily take place at elevated temperatures. As such the up-shock event (increasing temperature) is much more common as a repeating cycle than the down shock (decreasing temperature) event. This is due to cooling rate commonly left to natural cooling by conduction and/or convection. However, as mentioned previously the less common down shock events take place in extreme environments.

Rapid heating and cooling are incurred during the start-up and shutdown of chemical and nuclear reactors and steam and gas turbines. In nuclear reactors, thermal fatigue may occur in fuel elements and in pressure-vessel walls as a result of plastic strain and associated stresses arising from the thermal gradients set up during the repeated start-up of the reactor or on emergency shutdown. Moreover, the flame-tubes and blades of aircraft gas turbines are liable to thermal fatigue cracking, particularly as a result of the high transient temperatures induced at fuel-ignition.

The behaviour of brittle and ductile materials under thermal shock is similar to that of ordinary isothermal mechanical conditions. Brittle fracture tends to occur as a shattering of the specimen when multiple small cracks or craze cracking becomes unstable. Griffith's brittle fracture theory holds that instability occurs when the elastic energy released in the crack exceeds the energy required to create new surfaces. Conversely, ductile behaviour can be analysed by modifying the surface energy term to include the energy for local plasticity around the crack tip. This may prove to be somewhat more complicated for thermal shock analysis since localized tensile and compressive stresses are set up, as well as plastic deformation, not solely due to the crack tip stress static [24]. Properties such as specific heat and conductivity, which do not enter directly into consideration for thermal stresses under known conditions of temperature, become important in thermal-shock applications because these properties

determine the temperature gradients, and the rate of change of the gradients, which in turn, govern strains and strain rates. Some materials are more sensitive than others to stress gradients or to strain rate; hence, thermal shock may rank materials differently than slowly applied thermal stress [4].

Many considerable progressive studies are undertaken in recent years on different materials to understand the variables that govern such behaviours. Although a great deal of information exists in the literatures about the relative performance of various materials under certain conditions of thermal cycling (the gradual type and the rapid type that can be classed as thermal shock), the test conditions are frequently not sufficiently well defined to permit analysis on the basis of fundamental variables or the temperatures are excessively high compared to the use temperature of the material. For this reason much of the available data must be regarded as being specifically applicable only under test conditions imposed rather than utilized for more generalized comparisons. Still, it is useful to compile some of the more recently obtained data as a partial guide to material selection in design and as a starting point for the development of additional data for materials of interest in special applications [4].

The current research presented an empirical solution to analyse the thermal shock fatigue under heating and cooling conditions, more detailed explanation are provided in Chapter Four. Some investigators gave interesting insights on the martensitic stainless steel highlighting different effective variables of the thermal fatigue behaviour. Lin et al., [53-54] illustrated the effect of the residual stress decrease with an increase in the thermal fatigue cycle number. This is because the formation of the crack relieves the residual stresses of specimen due to solidification structure difference at low thermal fatigue cycle; additionally, the density of cracks on near fusion line is higher than that of the centreline. Also, the retained ferrite becomes a harmful factor for crack propagation tendency because too much ferrite content in AISI 420 martensitic matrix may result in a lower strength structure and the crack can propagate easily. Mitrokhovich, [55] studied the thermal fatigue of low-carbon martensitic steel and compared its resistance to thermal erosion with that of a conventional die steel. Akdogan et al., [56] analysed the heat transfer and material behaviour of the thermally cycled mould martensitic stainless steel used in glassware production.
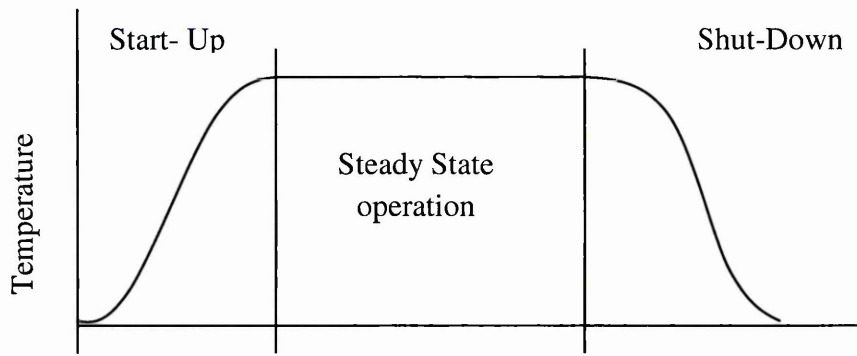
(a) One Cycle Time Period [Power
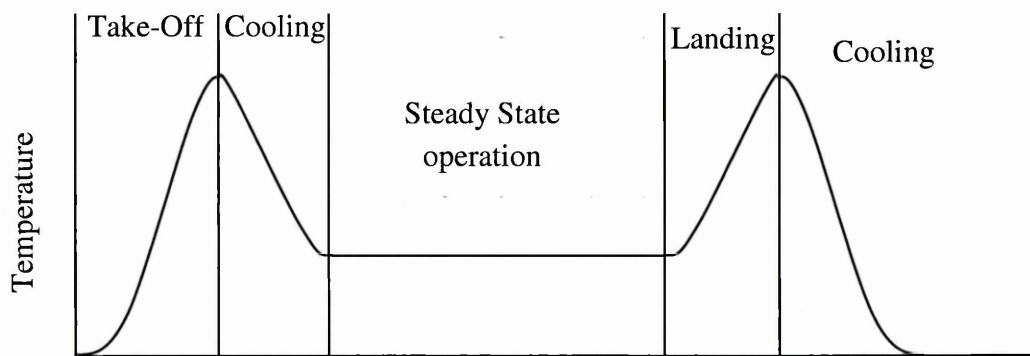
(b) One Cycle Time Period [Jet Engine]
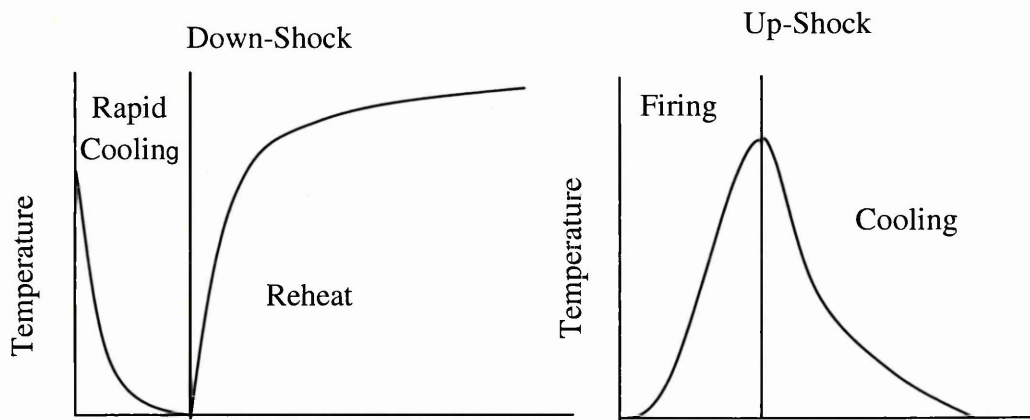
(c) One Cycle Time Period
[LMFBR/Gas Turbine]

One Cycle Time Period
[Gun Barrel]

Figure 2.7 Typical thermal loading cycles.

31

2.6.2 Thermo-mechanical Fatigue:

Thermo-Mechanical Fatigue (TMF) is a variation of mechanical fatigue of materials where heating and cooling cycles are applied to test a material added to a mechanical cyclic loading. The temperature cycles have, in most cases the same frequency as the loading cycles, but different phase shifts. If the phases shift $\varphi = 0^\circ$ the TMF tests are called In-Phase tests where the maximum mechanical strain occurs at the maximum temperature of the cycle. If the phase shift is $\varphi = 180^\circ$ the TMF tests are called Out-of-Phase where the maximum mechanical strains coincide with the minimum temperature as shown in Fig. 2.8. For special testing parameters, the phase shift can be applied between $360^\circ > \varphi > 0^\circ$, to fit the real requirements for the tested material in later application fields [57].

Thermo-mechanical fatigue also refers to the process of fatigue damage under simultaneous changes in temperature and mechanical strain. Fatigue damage at high temperatures develops as a result of inelastic deformation where the strains are non-recoverable. Therefore, TMF damage is complex, as it may accumulate over a range of temperatures and strains under both steady-state and/or transient conditions.

It can contribute to the accumulation of TMF damage in various kinds of equipment, such as jet engines, land-based turbines for power generation, heat-exchangers and pressure vessels. For example, during straight and level flight, aircraft jet engines (or steady operation of power generation turbines) have essentially constant temperatures and imposed loads, where steady-state creep (and the environment) is the primary damage mechanisms. During take-off and landing of the aircraft engine or start-up and shut-down for power generation turbines; however, the transient demand for more power output induces load and temperature changes, which thus impose fatigue damage. Furthermore, the damage modes may interact in a TMF cycle in ways that are never encountered in conventional fatigue testing, which makes life prediction under TMF conditions, particularly challenging. Nevertheless, techniques have been proposed, validated, and introduced into practices that provide reasonable assessment of remaining life.

Life prediction in the TMF regime is particularly important in high-temperature turbines (jet engines and land-based turbines), the power-generation industry (both conventional and nuclear), and in the automotive industry, to name a few.
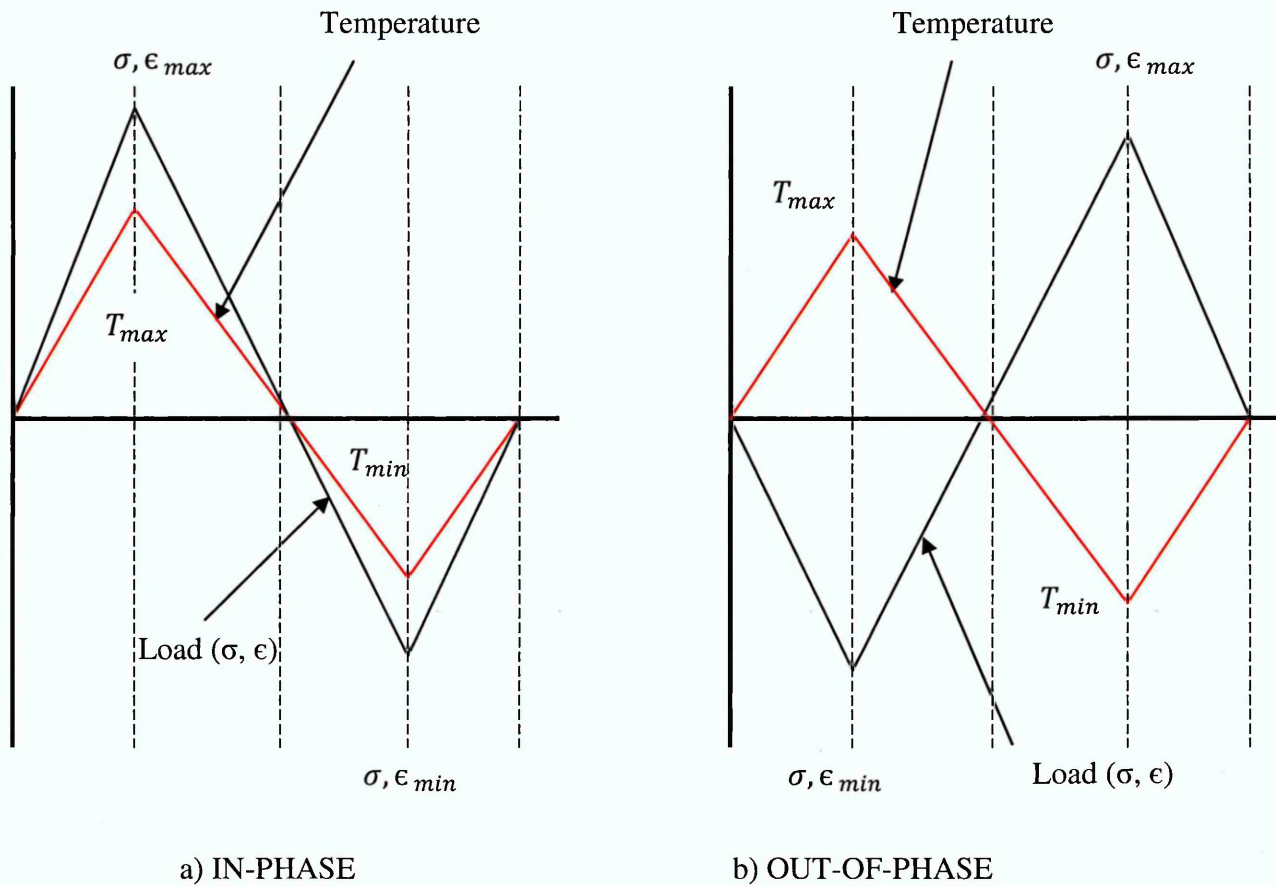
Figure 2.8 Thermo-mechanical loading cycles.

Significant advances can be made by combining mechanical studies with increasingly sophisticated finite-element thermal stress analysis. Development of more refined engineering-based models should result in less reliance on component simulation, which is subject to some uncertainty. It has been customary to characterize materials in terms of their fatigue properties, (including creep, fatigue, environment properties) and to compute the life of components such as turbine blades using experimental data and models that implicitly or explicitly describe damage evolution as a function of the numbers of cycles. While such experimental and analytical information is essential for life prediction, it is not always sufficient.

The present work addresses the eliminations of the effect on the environment specially the corrosion effect due to the high resistance property of this type of material. To the best of the researcher's knowledge, there is no specific research that focuses on

33

the material studied in this project, but some scholars studied the different types of martensitic steel. Mannan et al., [48] studied compression and the difference between high temperature low cycle fatigue caused by different times and thermo-mechanical fatigue for austenitic and martensitic steel materials; they noted that the effect of dynamic strain aging raise the stress response and reduce ductility and that the high-temperature oxidation accelerates trans-granular and inter-granular fatigue cracking in modified 9Cr–1Mo steel. Besides, they suggested that the thermo-mechanical fatigue (TMF) studies are closer to the actual service conditions. Nagesha et al., [58] compared the In-phase and Out-of-phase thermo-mechanical fatigue with isothermal under different temperature ranges, for 9Cr-1Mo ferritic martensitic steel; they discovered that fatigue life prediction under isothermal cycling at the maximum temperatures compared to both in-phase and out-of-phase thermo-mechanical fatigue cycling, leading to a life variation sequence; IF < OP-TMF < IP-TMF. Zhang et al., [42] formulated a cyclic anisothermal constitutive model with internal variables to understand and explicate experimental results such as the increase in strain softening when strain rate decreases in isothermal testing, as well as the relations between mean stress and temperature range or cyclic softening with strain amplitude under anisothermal conditions.

2.7 Fatigue Mechanisms and Numerical Analysis:

Nowadays, finite element (FE) theory and assessment is widely accepted and employed in industry for problem solving in areas of automobile suspension, chassis design and static, thermal, elastic and elastic-plastic stress analysis. Though the theory of finite element is complex, it possesses a foundation that can help tackle engineering problems. It is this aspect which makes it capable of programming into a versatile tool for modern engineers to advance their capabilities.

Much work was conducted in the 1970's to expand the applicability of finite element (FE) to fracture mechanics and life prediction whilst also using it as a tool to test and assess the standard recommendations of fracture toughness testing. Efforts were also made to further understand the various parameters such as fatigue life and damage, crack initiation and the determination of stress intensity factors.

34

The fatigue life is an important factor to assess the durability of the designed parts. Studies have been made on the evaluation of the fatigue life using finite element methods (FEM). Dietz et al., [59] presented a new method to predict the fatigue lifetime of a railway bogie under dynamic loads, based on a combination of frequency domain and time domain calculations, which allows lifetime prediction with reduced computational effort. The method is implemented on concurrent engineering software environment together with a computer aided design (CAD), a finite-element-method (FEM) and a multi-body system program to demonstrate the possibility to perform fatigue lifetime calculations without simulating the whole time-span of vehicle life. Mahmood et al., [60] disclosed that the accumulated fatigue damage model and the employed stochastic method are able to simulate the fatigue damage progress in a wind turbine composite blade. Similarly, MOVAGHGHAR et al., [61] studied the wind turbine blade performing a dynamic analysis with a full 3-D finite element method using ANSYS software; the study revealed that the calculated life of the analysed blade could meet the design requirement. Firat et al., [62] highlighted a numerical simulation of radial fatigue damage assessment of metallic automotive components and its application, based on the local strain approach in conjunction with linear elastic FE stress analyses. They observed that the fatigue test cycles prediction of using damage parameter is conservative and considerably close to actual test cycles for all camber angles. Furthermore, variations in cyclic damage values appeared to be insignificant. Initiation assessment is also very problematic as it is highly dependent on the minute features, like the microstructure and surface roughness. In 2010, Glodez et al., [63] performed a numerical simulation of crack-initiation with ABAQUS, using a plug-in that was written specially for handling micro-crack nucleation and coalescence, by introducing segmented slip bands, where micro-cracks nucleate in multiple stages. This demonstrated a reasonably good correlation with experimental testing, but it still has some deficiencies. Hongxia Yua et al., [64] used the explicit dynamic solver to analyse bolted steel connections. Comparing the results with those from static analysis and tests gives satisfactory predictions of the responses of steel connections up to post-failure deformations.

2.7.1 Thermal Fatigue Numerical Simulation:

Studying the effect of temperature on failure behaviour supported by the finite element method has taken a step further applying different thermal fatigue estimate models. In 2003, Yang et al., [65] produced FE analyses of the fatigue life when cyclic out-of-plane deformation applied on a printed circuit board (PCB) assembly inside a thermal chamber by twisting the PCB mechanically. The combined effects of the mechanical deformation and the coefficient of thermal expansion (CTE) mismatch of different materials accelerate the failure of solder joints, so as to reduce the reliability testing time of the PCB assembly; it achieved a good correlation between the simulation and the test results. Che et al., [66] inquired about the thermal cycling and thermal shock loads simulated in FE analysis to study the temperature ramp rate effects on fatigue life for PBGA components with Sn-3.8Ag-0.7Cu solder joints. Based on test results, the outermost ring elements averaging method gave better results compared to the mean time to failure.

Recently, numerical solution is significantly concerned with thermal fatigue life estimation and failure analysis. CLA′ UDIO et al., [67] made a life prediction comparison between a FE technique and experimental test for a gas turbine disc subjected to high temperature. The FEM results obtained are in very close agreement with the experimental data for the disc. Even when considering that the propagation life for the disc was measured using a beach mark technique and errors in the experimental data, the solutions are quite close. Likewise, Revel et al., [68] investigated experimental data and the 3-D numerical simulation of the thermal loads and of the associated stresses for continuous casting rollers used in the steel industry; the analysis was conducted by the thermal loading of a cylinder with dimensions of one fifth of the real cylinder. The numerical simulation is carried out to evaluate strain and stress levels induced by thermal loading using the finite element method, in order to numerically estimate thermal loading with the highest accuracy optimized with industrial process.

Some research studies focus on the estimation of the stress intensity factor by using FE method to study the crack initiation and growth under the effect of thermal fatigue. Donald et al., [69] produced a FEA model that could approximate a growing and arresting crack in the hot spot specimen. The model yields a very reasonable estimate of fatigue crack growth through the hot spot as well as potential arrest distance based on

36

the stress intensities developed at each crack length. Nam Le et al., [70] developed an effective analytical approach that depended on the weight function method and on the Duhamel's principle to estimate the time-dependant stress intensity factor of a plate with an edge crack submitted to thermal cyclic loading. The assessment with ABAQUS numerical simulation gave a very close agreement.

2.7.2 Thermo-Mechanical Fatigue Numerical Simulation:

Recently, more efforts are exerted to utilize the finite element methods to studying the fatigue life and the influential stresses of different components and devices under thermal and mechanical loads interactions. The fatigue life estimation of power devices investigated by Shinohara et al., [71-72] proposed an electrical-thermal–mechanical analysis of the solder layer during thermal cycling, based on the finite element method. The objective is to verify the calculation accuracy of this fatigue life evaluation method of a power device, to demonstrate how the mesh resolution affects the fatigue life evaluation. Concerning the solder joints, Yung-Chuan Chiou [73] modified an analysis process to study the effects of inter-metallic compound (IMC) growth on the fatigue life of the solder balls for flip-chip plastic ball grid array packages under thermal cycling test conditions, carrying out a series of non-linear finite element analyses to simulate the stress/strain history at the critical locations, and then to predict the fatigue life. He demonstrated that the solder joint fatigue life decreased as the IMC thickness increased and that the predicted thermal fatigue life of lead rich solders based on the effects of IMC growth is apparently smaller than that which does not consider the IMC growth in the reliability analysis.

The fatigue life prediction under high temperature effect is reported by Shang et al., [74]; it has not been dealt previously regarding the thermo-mechanical behaviour of the SPF die. The thermo-mechanical, time-dependent, elastic–plastic creep behaviour of a representative tool in a high-temperature superplastic forming press is simulated using a sequential finite element-based heat transfer and mechanical stress analysis approach; it is validated against laboratory measurements. The short-duration of minor cycles, associated with blank and part insertion and removal, had a predominant effect on die life, due to high temperatures and low material yield stress leading to significant cyclic plastic strains and thermally induced residual stresses and creep strain accumulation

during the rapid residual stress relaxation. Earlier, similar work was reported by Deshpande et al., [75]; it predicted the thermo-mechanical life-limiting of a large SPF tool under realistic forming conditions using elastic-plastic-creep FE analyses. A plastic strain along the exposed sides (top edges) of the tool while opening the press shows a crack initiation leading to ratchetting phenomenon, based on uniaxial ductility exhaustion. This gives shorter life than the creep-fatigue prediction methodology, based on a bi-linear strain-range partitioning method to combine creep and fatigue damage.

Some researchers examine the thermal and thermo-mechanical stresses resulting from the applying load in order to predict the fatigue life of the components. Rodriguez et al., [76] produced a thermal mechanical finite element model to investigate the thermal stresses in the adhesive back bonds of the in-surface mounted structures and to examine the effects of thermal fatigue on soft solder interfaces in conventional power modules such as gate bipolar transistors modules. Chen et al., [77] presented a three-dimensional thermo-mechanical model based on finite element analysis to study the thermal history and thermo-mechanical process in the butt-welding of aluminium alloy and to validate the efficiency of the model by experimental values. They maintained that the high stress is located in the region extending down from the crown to the mid-thickness of the weld. Moreover, the prediction reveals that fixturing releases the welded plates that affect the stress distribution of the weld. Terriault et al., [78] produced an 1D bilinear model program, through the USERMAT procedure in ANSYS, to present the mechanical and thermal hysteresis for actuated devices made of shape memory alloys. The model is validated through isothermal tensile testing; a good agreement with experimental results is exposed.

Other numerical simulations related to the thermal shock fatigue problems are developed by Kang et al., [79]; it is a three-dimensional thermo-elastic-plastic finite element program that investigates the dimensional change and stress distribution according to the carbon content and variations of the temperature and the volume fraction of each phase generated within the steel specimen during the quenching process. It was discovered that numerically obtained values were in good agreement with the experimental results available in the literature in terms of temperature and stress distributions. Panda et al., [80] modelled the temperature and thermal stress distribution in the sample using the finite element software on the thermal shock and thermal fatigue behaviour of alumina. The findings of the research studies proved that

the fatigue life sharply decreased with an increase in initial crack length or by increasing the temperature difference of the fatigue cycles. Tomba et al., [81-82] estimated the temperature and thermal stress distributions during air impinging using finite element analysis for cordierite disks obtained by slip casting and sintering at 1,450 °C for 2 h. The calculated cordierite thermal stresses were assessed by experimental data.

2.8 Summary:

The literature reviews studies have been made focusing on the behaviour of different types of martensitic stainless steels at room temperature and high temperature ranges under strain-controlled fatigue testing, analysed the cyclic softening and strain ageing described by initial hardening in the first few cycles followed by gradual softening.

This present research provide the fatigue crack growth rate data at high temperature using AISI 420 martensitic stainless steel under stress-controlled fatigue testing, correlated with developed empirical modelling solution and numerical modelling simulation employing ANSYS software.

CHAPTER THREE

3- MATERIAL AND EXPERIMENTAL WORKS

3.1 Materials:

The AISI 420 martensitic stainless steel is similar to low alloy or carbon steel, having a structure the same as the ferritic steel. Its structure is body centred cube (bcc) and it is classed as a hard Ferro-magnetic group. Grade 420 is high carbon high hardness martensitic steel, where the strength obtained by heat treatment depends on the carbon content of the alloy. An increase in the carbon content raises the strength and hardness potential but decreases ductility and toughness. Its best hardness and corrosion resistance is achieved when the metal is hardened and surface grounded or polished.

The development of elevated-temperature ferritic/martensitic steels began in 1920s with the introduction of Cr-Mo steels for conventional power-generation applications. The 2.25Cr-1Mo steel, designated by ASTM as Grade 22, was introduced in the 1940s and it is still widely used today. Along with Grade 22, 9Cr–1Mo (Grade 9), a Fe–9.0Cr–1.0Mo–0.6Si–0.45Mn–0.12C composition, it was an early development; the additional chromium was added for corrosion resistance. Since then, there has been a continual push for increased operating temperatures of conventional fossil-fired power-generation systems. This led to the development of several generations of steels with improved elevated-temperature strengths. Steels beyond the zero generation contained mainly 9–12% Cr for improved corrosion and oxidation resistance for elevated-temperature operating conditions [1]. The first generation, in addition to increased chromium, involved primarily the addition of the carbide formers, vanadium and niobium, to T22 and T9 compositions to add precipitate strengthening. For the second generation (developed in 1970–1985) carbon, niobium, and vanadium were optimized, nitrogen (0.03–0.05%) was added, and the maximum operating temperature increased to 593 °C. The third generation of steels was developed based on the previous generation, primarily by the substitution of tungsten for some of the molybdenum,

although boron and nitrogen were also utilized. They were developed and introduced in the 1990s for 620 °C operations with 105 h creep rupture strengths at 600°C of 140 MPa. Finally, the next generation of steels is being developed at present, where the intention is to push operating temperatures to 650 °C. These fourth-generation steels differ from the previous generation primarily by the use of up to 3.0% cobalt; they have projected 105 h creep-rupture strengths at 600 °C of 180 MPa [1]. Ferritic/martensitic steels considered for fast reactors in the 1970s, and for fusion reactors in the 1980s were developed by the steel industry for use in conventional power-generation systems and in the petrochemical industry. Since then, steel technology has advanced, and it is of interest to examine the evolution of the elevated-temperature steels for use in those industries since the 1980s [1]. The next power generation (both conventional and nuclear) plants will, in many cases, have been operating conditions well beyond those of earlier designs. As with most new technologies or technological advances, success often hinges on materials available to meet the new operating conditions. In Europe, much of the development effort is on a EUROFER oxide-dispersion-strengthened (ODS) steels composition that will be produced as martensitic steel because of its composition. Recently, the Japanese nuclear cycle development institute, which has been in existence since 1987, concentrated on martensitic ODS steel based on the F82H composition [83].

The selection of AISI 420 martensitic stainless steel in this present research study is made, due to the low cost of this material compared to the austenitic type and all research attention has been focussed on studying the high temperature fatigue behaviour of AISI 316 austenitic or 9Cr martensitic stainless steel; this type is not considered due to its high hardness and low toughness properties, while the power generation plants utilize this type of material in many of its components, like turbine blades, pressure vessels and valve parts. This project focuses on the high temperature operating conditions of AISI 420 martensitic stainless steel. The composition of AISI 420 martensitic stainless steel, typical composition of two common types of steels used in power generation industry. They are MANET I, nominally Fe-0.14C-0.4Si-0.75Mn-10.8Cr-0.75Mo-0.2V-0.15Nb-0.009B-0.02N-0.9Ni and HT9, nominally Fe-0.2C-0.4Si-0.6Mn-12Cr-1Mo-0.5W-0.25V-0.5Ni (all compositions in wt %), the typical physical properties used in this research are displayed in Tables 3.1 and 3.2.

Table 3.1 The Chemical composition of AISI 420 martensitic stainless steel.

Grade	C	Mn	Si	P	S	Cr	Mo	Ni
420	0.14	0.74	0.38	0.028	0.021	11.55	0.03	0.23

* Testing values in accordance with in house procedures for spark OES techniques introduced by Sheffield Testing Laboratories.

Table 3.2 Physical properties for annealed grade 420 martensitic stainless steel.

Properties	AISI 420
Density (Kg/m^3)	7800
Specific Heat (J/ Kg. K) at T (0-100 °C)	460
Thermal Conductivity (W/m. K) at (20-100 °C)	24.9
Coefficient of Thermal Expansion (cm/cm/°C) at T (0 - 100 °C) at T (0 - 315 °C) at T (0 - 538 °C) at T (0 - 650 °C)	10.3×10^{-6} 10.8×10^{-6} 11.7×10^{-6} 12.2×10^{-6}
Melting point (°C)	1455 - 1510

* Values supplied from (MatWeb, MATERIAL PROPERTY DATA) website.

Martensitic stainless steels are commonly used for manufacturing components with excellent mechanical properties and moderate corrosion resistance, so that they can work under high and low temperatures. Unlike other stainless steels, their properties could be changed by heat treatment; hence these types of steels used for wide ranges of applications, like power generation industry as in steam generators and nuclear reactors [84]. The martensitic stainless steel is not as corrosion-resistance as the austenitic but it is extremely strong and tough, as well as highly machine-able, wear-resistance and can be hardened by heat treatment for best corrosion resistance is achieved when the metal

is hardened, surface grounded or polished. Typical application areas are: pump components, turbine blades, piston rods, shafting fittings, steel balls, bolts, nuts, nozzles, pressure vessels, valve parts, glass and plastics processing tools, cutlery, dental and surgical instruments, seats for oil well pumps, offshore platforms for oil extraction, separating screens and strainers, springs, shears, and wear surfaces.

3.2 Specimen Design and Preparation:

Three standard geometry specimens used for different type of testing were carried out in this programme. The material used was the AISI 420 martensitic stainless steel supplied in the form of bars 32.5 mm in diameter.

The gauge portion of the specimen in a thermo-mechanical fatigue (TMF) test should be under ideal conditions, with constant gauge-volume and cross-section area. Therefore, the geometry of the specimen should not affect the resulting cyclic stress and lifetime behaviour, e.g. due to stress in-homogeneities, undesired stress gradient, etc. The specimen geometry should provide a uniform cross section of the gauge portion, and the shape should be chosen in such a way that the uniform distribution of stresses, strain and temperatures in the gauge length be ensured.

The geometry of the specimen design is chosen to minimize the risk of buckling in compression and to avoid failure initiation at the transition radius, allowing the extensometer to measure the strain without interference or slippage; moreover, the parallel length of the specimen has to be longer 20% than the extensometer gauge length. However, it must not exceed the gauge length plus the width of the gauge length in order to reduce the risk of failure outside the extensometer and the ratio between the parallel lengths over gauge length chosen with respect to an optimization of the axial temperature profile. The cross-sectional area within the gripping section should be at least two times the cross-sectional area within the gauge section, in order to avoid fracture in the gripping section [57]. Machining of the specimen may produce residual stresses in the surface region, which can (especially in the case of brittle materials) affect the TMF test results. Residual stresses may be caused by temperature gradients, which occur during machining, inhomogeneous plastic deformation of the near-surface regions during machining or by micro-structural alteration. Their influence is less marked in tests on ductile materials and in TMF tests with relatively high maximum

temperatures, because in these cases the residual stresses are, to large extent, relaxed upon preliminary thermal cycling [26].

The types of the samples for the different tests are explained below:

3.2.1 Tensile Test Specimen Design:

The tensile test specimen is machined as received raw material depending on the standards of the validated Code-of-Practice for strain controlled TMF testing [57], with due consideration for the extensometer fixing location, the real sample image and the geometrical model are shown in Figs 3.1 and 3.2.
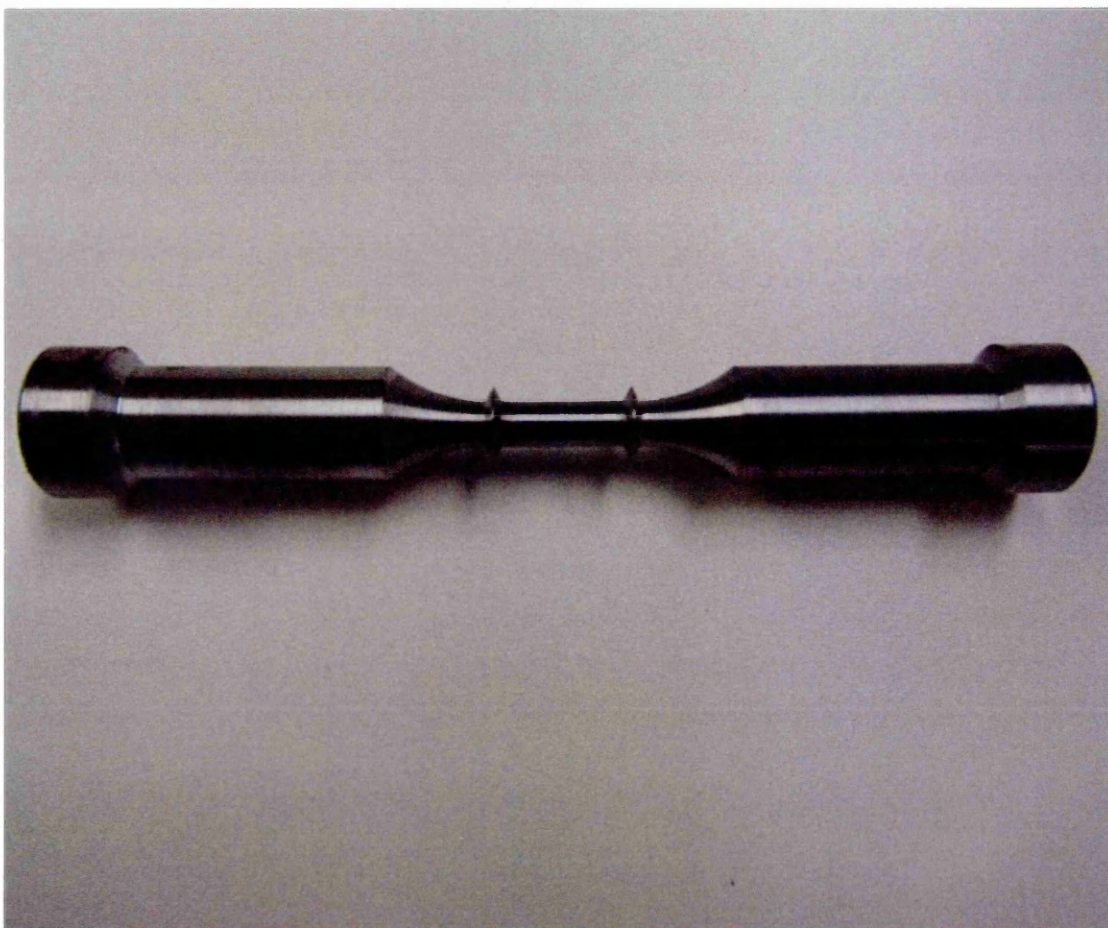
Figure 3.1 The real image of the machined tensile test solid cylinder specimen.
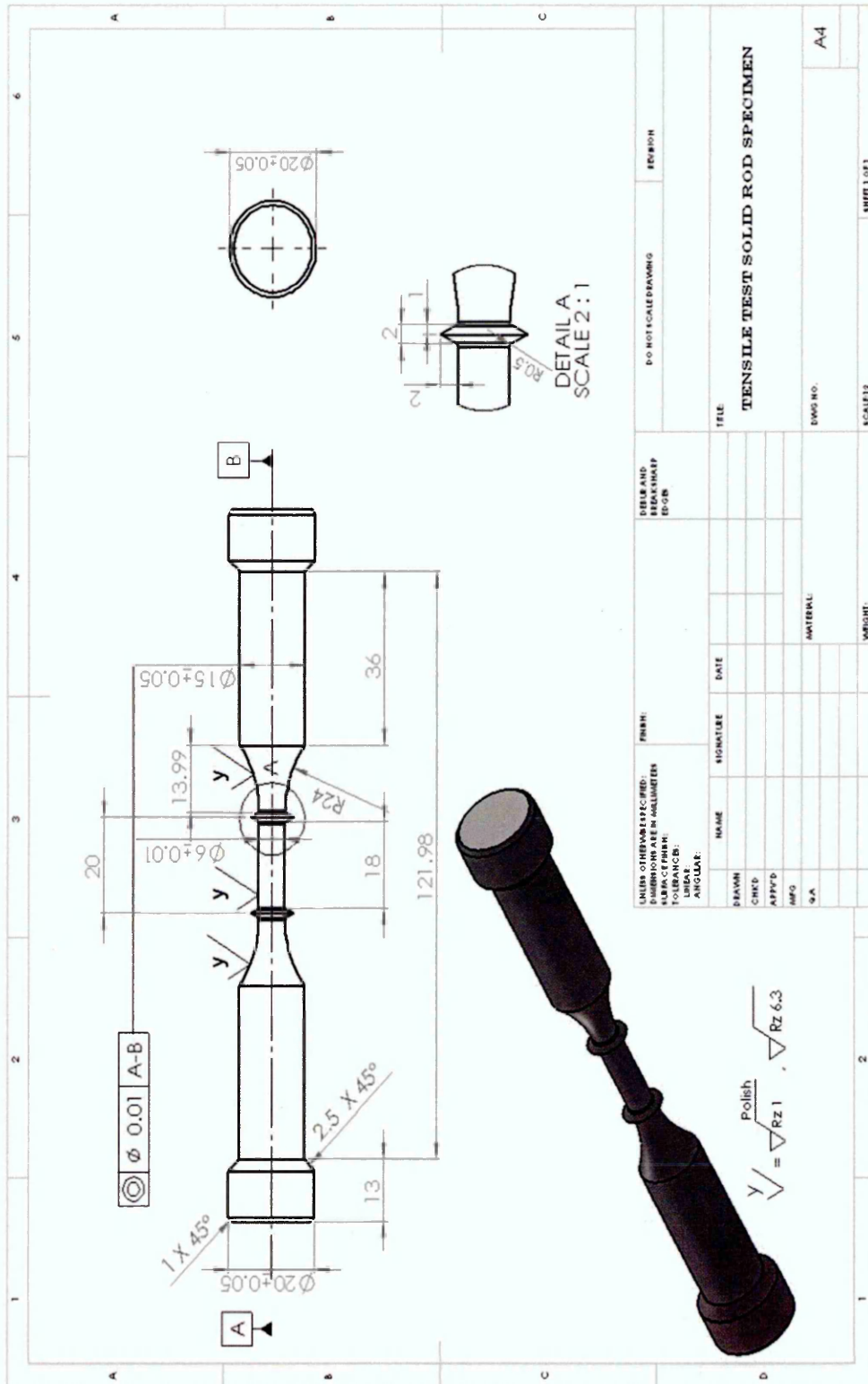
Figure 3.2 The tensile test solid cylindrical specimen.

3.2.2 Low Cyclic and Isothermal Fatigue Test Specimen Design:

Three types of the fatigue samples manufactured forms, as received row material is based on solid cylindrical specimens (machined, polished and notched), which are detailed as follows:

I- Machined and Polished Specimen:

The low cyclic and Isothermal fatigue test specimens are machined a rod as received row material depending on the standards of the validated Code-of-Practice for strain controlled TMF testing [57], without extensometer fixation location and M3 screw hole made for the current supply connection of the Direct current potential drop (DCPD) for crack growth monitoring device.

To avoid premature surface crack initiation along the gauge length part of the specimen due to the surface roughness, a primary fine grinding was performed with 1000 grade silicon carbide paper, and then final polishing executed with 1 micron paste, with screw ended made for the polished specimen type, to be used in another testing machine, both real images and the geometrical model are shown in Figs 3.3 to 3.6.

Figure 3.3 The real image of the low cyclic fatigue machined specimen.

46

Figure 3.4 The low cyclic and isothermal fatigue test machined solid cylindrical specimen.

Figure 3.5 The low cyclic fatigue test polished solid cylindrical specimen.
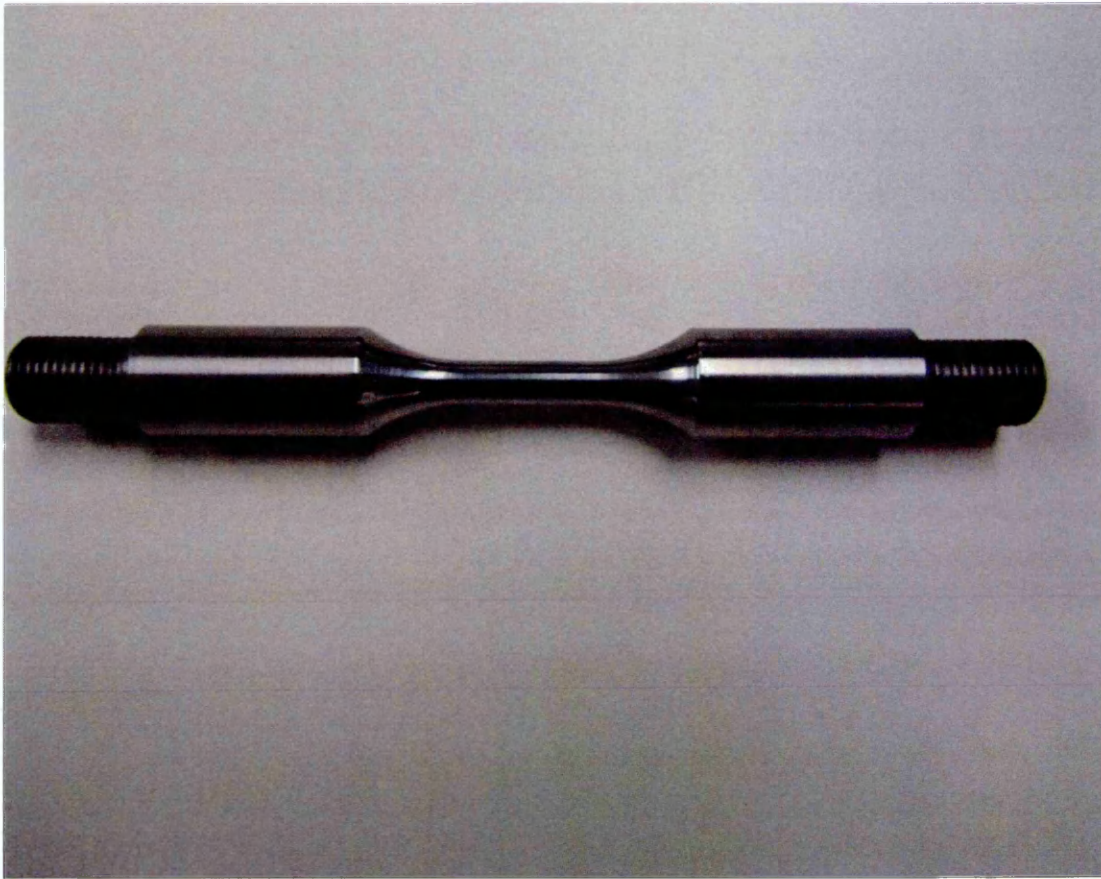
Figure 3.6 The real image of low cyclic fatigue polished specimen.

II- Notched Specimen:

To investigate the difference between already cracked samples with no cracked, a fatigue test was carried out. The notched specimen, screw ended is made according to the (D/d) ratio of the E602-03, ASTM test method [85], the geometrical model and real image are shown in Figs 3.8 and 3.9.
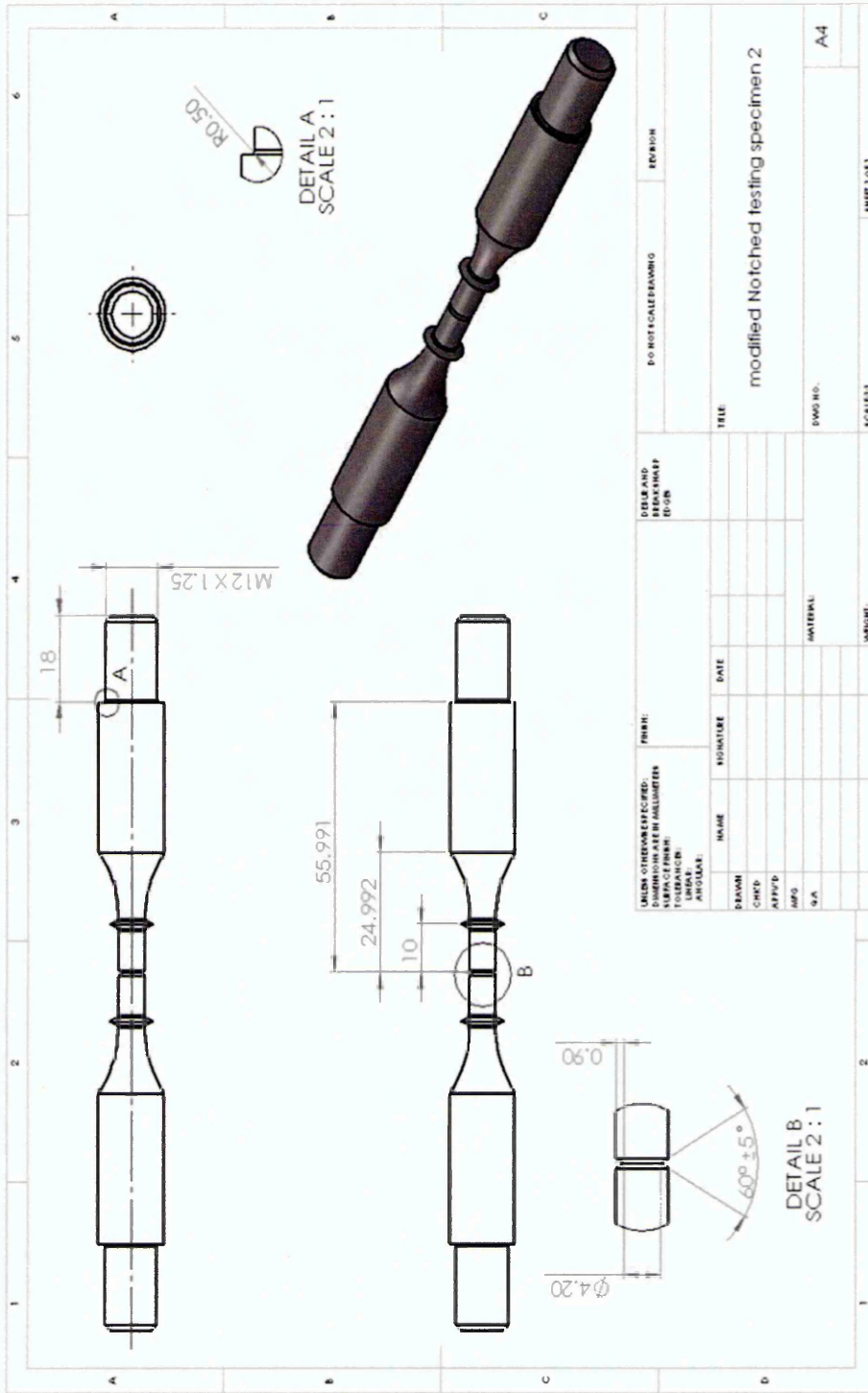
Figure 3.8 The low cyclic test notched solid cylindrical specimen.

Figure 3.9 The real image of low cyclic fatigue notched specimen.

3.3 Tensile Tests:

A study of the material response under simple tension is an important step in the process of understanding the mechanics of material, and generating input data for low cyclic and isothermal fatigue tests. Tensile tests at room temperate and high temperature at different temperature level had been carried out. According to the high temperature test, the specimen stays for 15 minutes for temperature settled, which gives a difference temperature (25 – 50 °C) less due to the convection heat transfer effects of the gap between the specimen and the furnace liner. Engineering stress-strain diagrams of AISI 420 stainless steel at room and high temperatures are presented in Figs 3.10.and 3.11. According to the experimental work of the obtained data for the ultimate tensile

strength and the 0.2 per cent offset yield strength which is apparent at high temperatures, the ultimate tensile strength decreases with the temperature increase and the yield strength decreases with the temperature increase while at 550 °C, the yield strength increased and then decreased with the further temperature increase. The temperature range between 425°C and 525°C must be avoided owing to embrittlement at 475°C [86]. This is more significantly clear when it displayed the effect of the elevated temperature on elongation and the reduction in area for AISI 420 stainless steel is exhibited in Fig 3.12.

This steel is a harden-able stainless steel containing high chrome. In the quenched and tempered condition, its attributes may be numbered as a good tensile strength, good corrosion resistance to air and fresh water as well as to other mildly aggressive chemicals. It is generally supplied hardened and tempered either in tensile range 700 – 800 MPa (condition R), or in the tensile range 770 – 930 MPa (condition S).
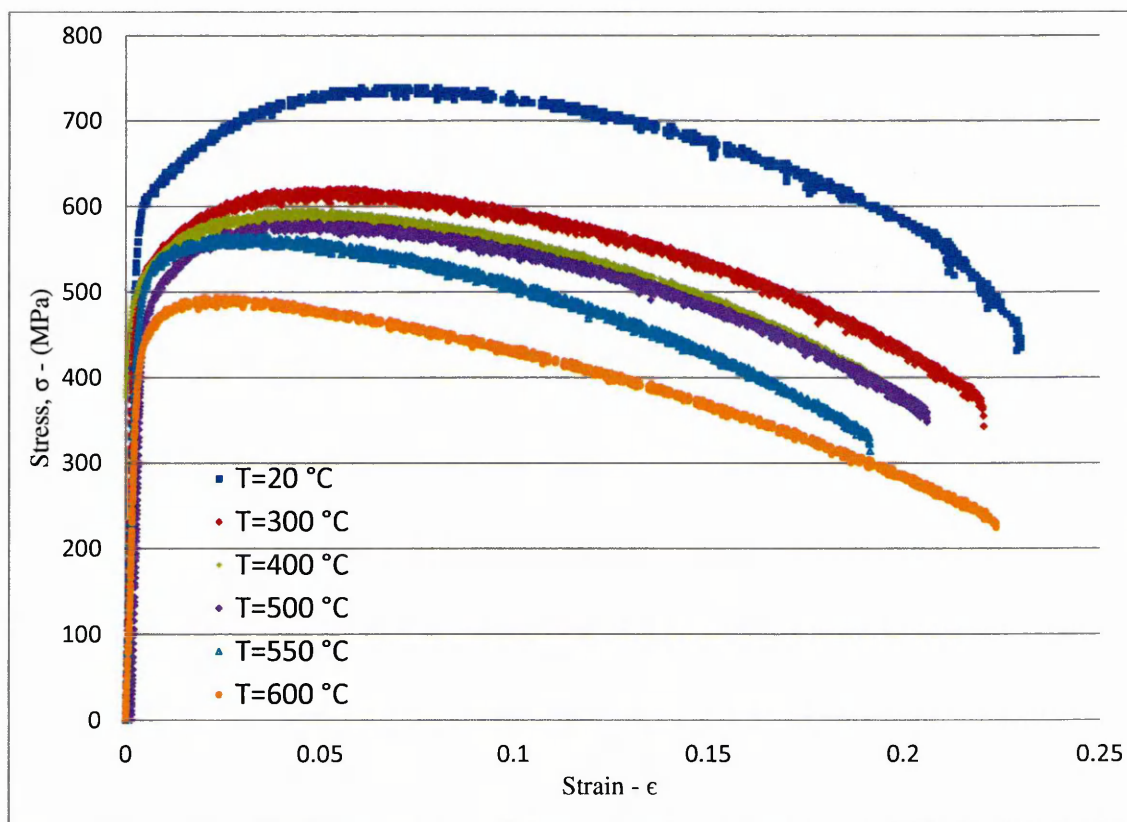
Figure 3.10 Engineering stress-strain diagrams of AISI 420 stainless steel at room and elevated temperatures.
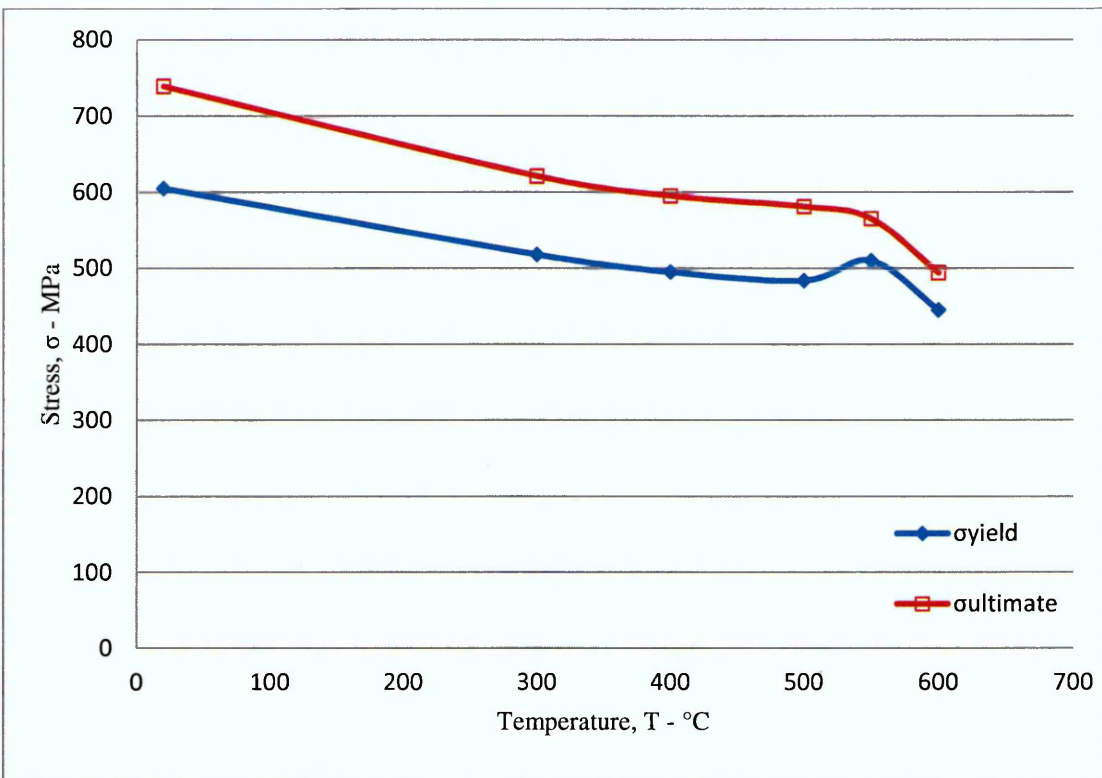
Figure 3.11 The yield and ultimate strength of the AISI 420 material with temperature.
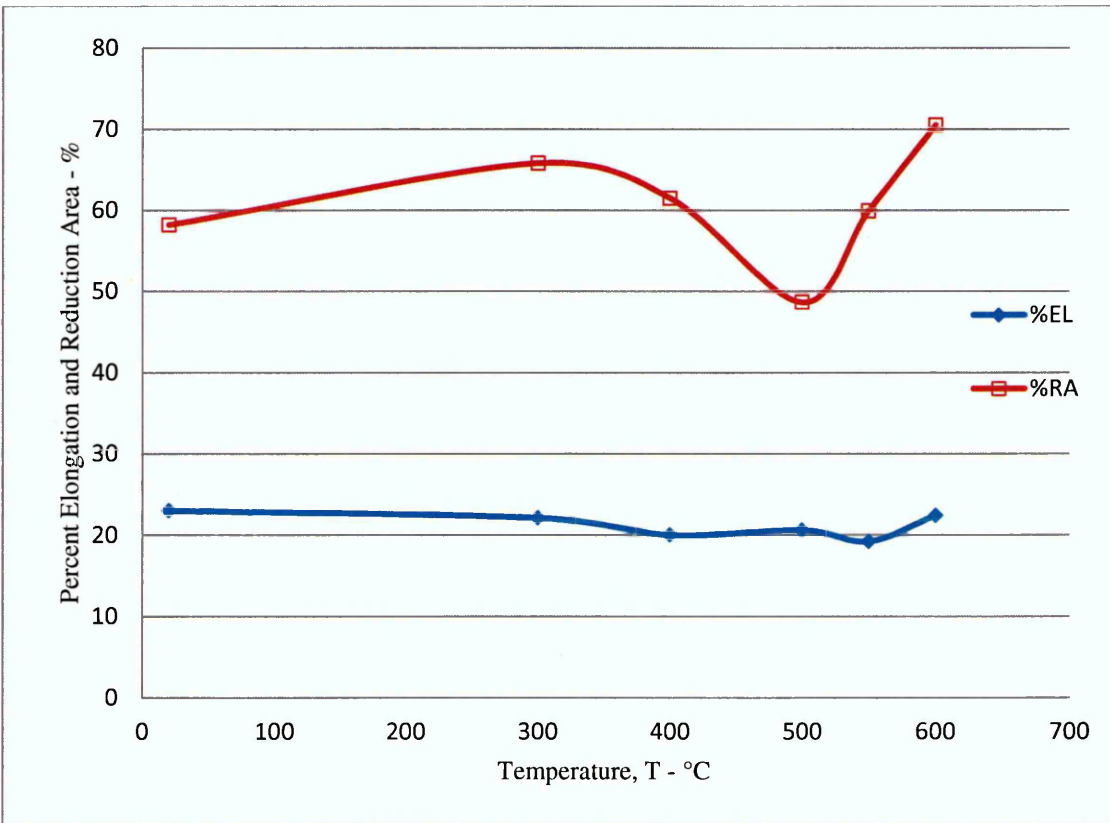
Figure 3.12 Effect of elevated temperature on total elongation and reduction in area.

The engineering stress-strain properties at high temperature are presented in Table 3.3.

Table 3.3 The engineering stress - strain properties at elevated temperatures.

Property	20 °C	300 °C	400 °C	500 °C	550 °C	600 °C
Ultimate tensile strength σ_{UTS} - (MPa)	739	621	595	581	565	494
0.2% tensile yield strength σ_{ys} - (MPa)	605	518	495	484	510	445
Modulus of elasticity E - (GPa)	132.38	121.6	193.36	78.06	100	87.08
Elongation - %EL	23	22.1	20	20.6	19.2	22.4
Reduction in Area - %RA	58.18	65.77	61.46	48.64	59.89	70.48

3.4 True Stress - Strain Property and Strain Hardening:

For each metal, there is a range of potential strength or hardness, which can be achieved by cold working, annealing, heat treating, etc. If a metal is initially soft, it will cyclically harden; if it is initially hard, it will probably soften [87]. The initial state is reflected by the monotonic strain hardening exponent, n. For most metals subjected to cyclic loadings, the value of the cyclic strain hardening exponent, n', lies between 0.1 and 0.2. Consequently, if n is initially low (a "hard" metal), the expected cyclic behaviour would be for n' to increase. On the other hand, an initially high n (a "soft" metal) would indicate that n' will decrease [87].

The monotonic strain hardening exponent, n, is defined as the slope of the true stress - strain curve ($\log \sigma - \log \epsilon_p$) as shown in Fig. 3.13, and the equation of the strain hardening exponent is exhibited below, Fig. 3.14.

$$n = \left[(\log \sigma_f - \log \sigma)/(\log \epsilon_f - \log \epsilon)\right] = \left[(\log \sigma_f/\sigma)/(\log \epsilon_f/\epsilon)\right] \qquad (3.1)$$

The true stress that causes a true plastic strain to the unity can be expressed by the equation:

$$\sigma = K \, \epsilon_p{}^n \qquad (3.2)$$

The true plastic strain properties are listed in Table 3.4.

Table 3.4 The true plastic stress - strain properties.

property	Remarks
True fracture strength - σ_f - (MPa)	850
True fracture ductility - ϵ_f	0.094
Strain hardening exponent - n	0.0936
Strength coefficient - K - (MPa)	1000
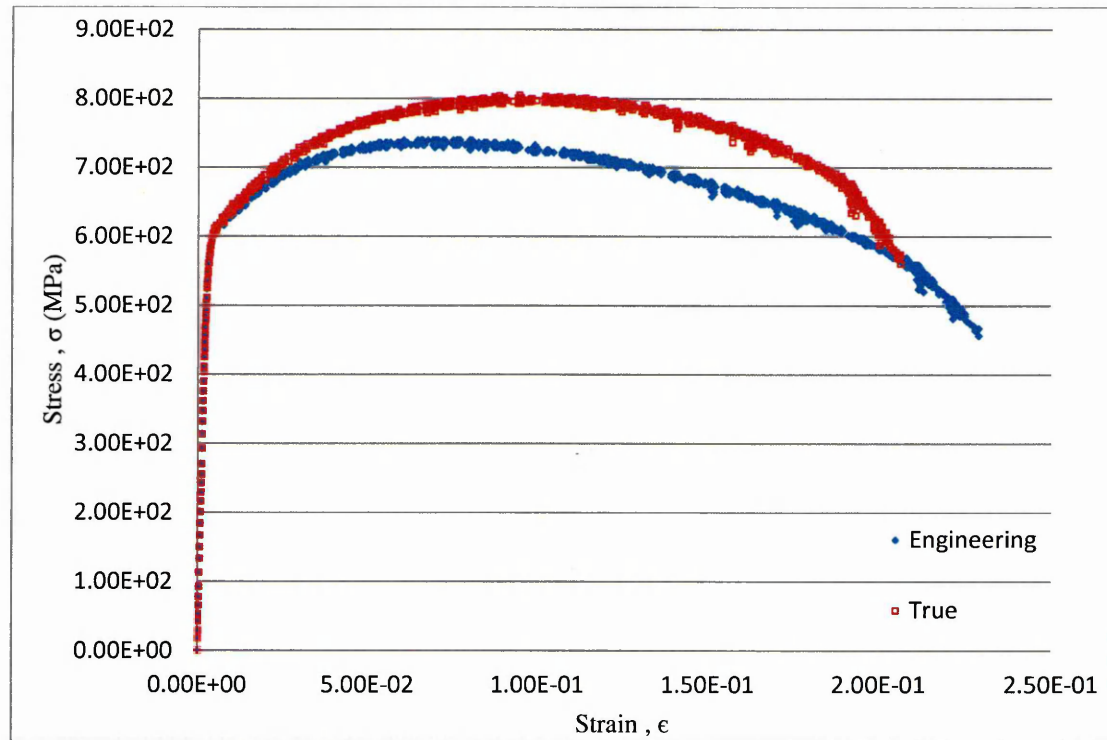
Figure 3.13 The true and engineering stress - strain curves of AISI 420 stainless steel at room temperature.

55
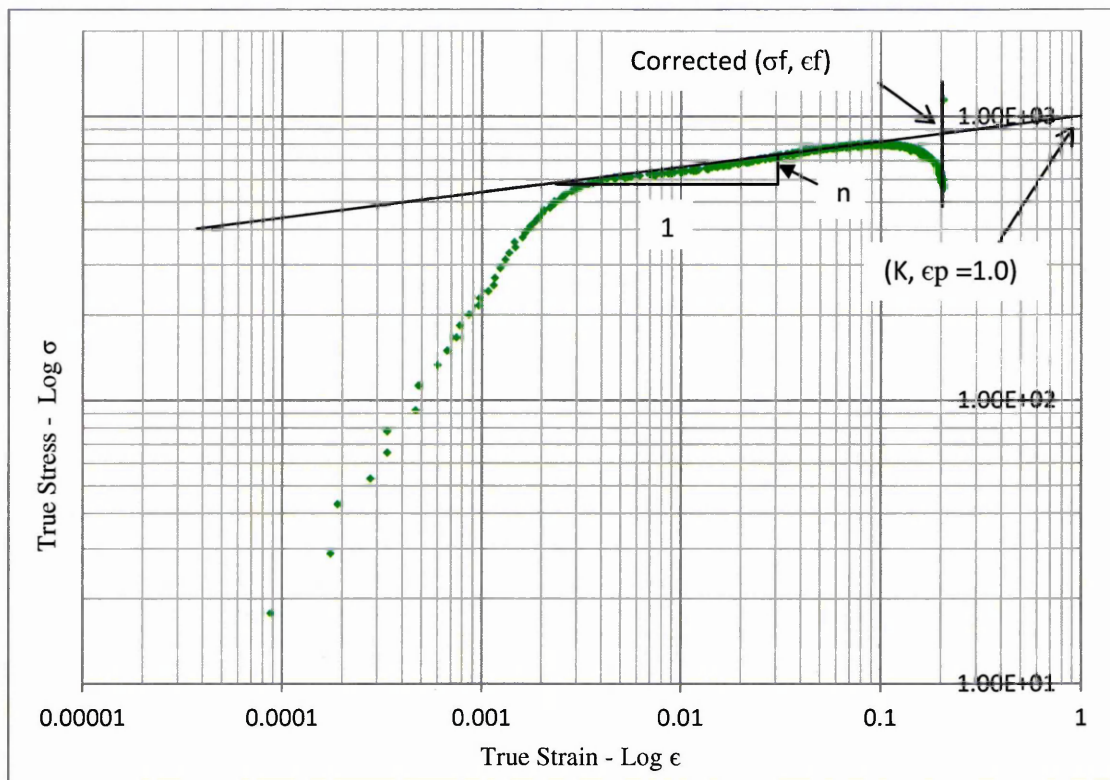
Figure 3.14 The relation between the true stress, strain and the monotonic strain hardening exponents.

3.5 Fatigue Life (S – N) Tests:

Three series of uniaxial low cyclic fatigue tests at room temperature were carried out, the first on the machined specimen, the second on the polished specimen and the third on the notched specimen. Tests on the different types of specimens were conducted to establish the compatibility and reliability of data generated and to analyse the effect of stress concentration induced due to specimen machining surface roughness and also, already, cracked samples. The nominal stress is required to cause a fatigue failure in number of cycles. These test results data can be illustrated as a curve graph of cyclic stress range versus number of cycles to failure. The data is received from cycling smooth (machined or polished) or notched specimens until failure. The procedure is to test the first specimen at a high range stress where failure is expected in a fairly short number of cycles, after that the test is decreased in percentage for each succeeding specimen until specimens do not fail in the specified numbers of cycles, which is usually taken in this research study at least 10^7 cycles. The highest stress at which a

56

runout (non-failure) occurs is interpreted as the fatigue threshold. In this research, the non-failure tests are usually terminated after about ($5 \times 10^6 - 12 \times 10^6$) cycles.

The stress versus number of cycles (S-N) fatigue data collected in the laboratory is generated using a ratio-reversed stress cycle. However, actual loading applications usually involve a mean stress on which the oscillatory stress is superimposed, as shown in Fig. 3.15. The following definitions are used to define a stress cycle with range, alternating and mean stress.
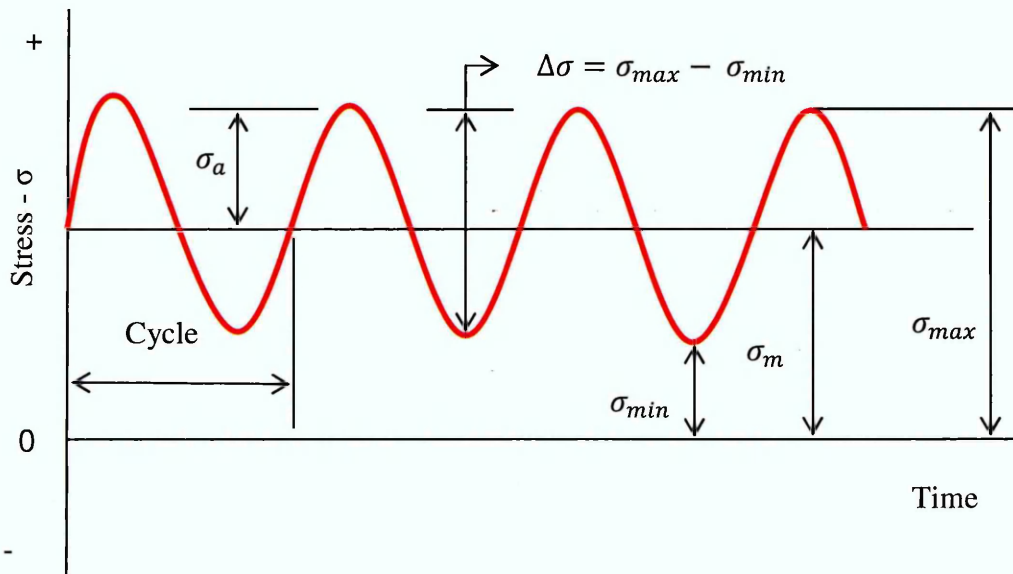
Figure 3.15 Typical cyclic loading parameters.

The stress range is the algebraic difference between the maximum and minimum stress in a cycle:

$$\Delta\sigma = \sigma_{max} - \sigma_{min} \tag{3.3}$$

The stress amplitude is one-half the stress range:

$$\sigma_a = \frac{\Delta\sigma}{2} = \frac{\sigma_{max} - \sigma_{min}}{2} \tag{3.4}$$

The mean stress is the algebraic mean of the maximum and minimum stress in the cycle:

$$\sigma_m = \frac{\sigma_{max} + \sigma_{min}}{2} \tag{3.5}$$

Two ratios that are often defined for the representation of mean stress are the stress or load ratio R and the amplitude ratio A:

$$R = \frac{\sigma_{min}}{\sigma_{max}} \tag{3.6}$$

$$A = \frac{\sigma_a}{\sigma_m} = \frac{1 - R}{1 + R} \tag{3.7}$$

In this present research study, a ratio-reversed loading type is conducted; it is called tension-tension cycle with R-ratio of 0.1, which is the minimum stress; it is equal to 0.1 times the maximum stress. This is often used for aircraft components testing. The sine wave spectra cyclic loading of the specimen was carried out in all fatigue tests, by setting the maximum and minimum load of the cycle in the input program of the servo hydraulic machine to maintain a fixed R-ratio, for a 5 Hz cyclic test frequency. Cyclic maximum and minimum loads could be monitored on the output screen of the servo hydraulic machine computer. The cyclic stress range versus number of cycles to failure is illustrated in Tables (3.5, 3.6 and 3.7) for different types of specimens.

Table 3.5 The stress versus number of cycle's data used for the machined specimen.

Machined Specimen		
Test No.	Stress Range, Δσ, (MPa)	Number of Cycles, (cycle)
SN13	605	65212
SN7	544.5	152728
SN11	517.275	5225926
SN8	490.05	12007424

Table 3.6 The stress versus number of cycle's data used for the polished specimen.

Polished Specimen		
Test No.	Stress Range, $\Delta\sigma$, (MPa)	Number of Cycles, (cycle)
PSN1	605	355760
PSN2	544.5	5438976
PSN3	490.05	9815040

Table 3.7 The stress versus number of cycle's data used for the notched specimen.

Notched Specimen		
Test No.	Stress Range, $\Delta\sigma$, (MPa)	Number of Cycles, (cycle)
NSN1	605	6839
NSN2	544.5	9204
NSN3	363	42914
NSN4	121	5533440

3.6 Isothermal Fatigue Tests:

When a tensile test is applied on the material at different temperatures, it is clear that the yield strength is reduced with an increase in the temperatures due to the softening and material ductility increase. But when the material is subjected to cyclic mechanical loading at constant temperature, it becomes more complex and it is frequently assumed that the higher temperature cycles will inflict more damage than those at lower range.

In this research, a cyclic mechanical loading (stress range) equal to the yield stress or slightly exceeds it is applied to the solid cylindrical specimen at selected high temperatures leaving it for 30 minutes to soak with the temperature range less than approximately (20 – 30 °C) due to the convection heat transfer effect of the gap

between the furnace liner and the specimen in order to study the fatigue crack growth under uniaxial loading conditions. The details of the isothermal fatigue tests are presented in Table 3.8. The main objectives of conducting this experiments was to observe the crack growth behaviour of the AISI 420 stainless steel under different high thermal loading conditions, and to correlate the isothermal fatigue data with the theoretical and numerical modelling calculated results.

Table 3.8 The Isothermal Fatigue Test Results.

Test No.	Temperature (°C)	Cyclic Stress Range (MPa)	No. of Cycles (cycle)	R- ratio	Frequency (Hz)
MIF300	300	518	139032	0.1	5
MIF400	400	540	86360	0.1	5
MIF500	500	493.7	149520	0.1	5
MIF600	600	448.675	7150	0.1	5

3.7 Testing Facilities:

Testing was carried out on two MAYES uniaxial machines, different in size and specimen gripping design type. According to the tests conditions requirements, furnaces were assembled and used with one of the machines to perform the elevated temperature tensile and isothermal fatigue tests.

3.7.1 Loading Controlled:

The servo hydraulic machine controlled the load applied in the tests by sine spectra for 5Hz cycle test frequency achieving the load ratio, $R = \frac{\sigma_{min}}{\sigma_{max}}$ in fixed magnitude of 0.1. The numbers of the cycles are recorded in the machine computer output screen together with the extension displacement of the specimen due to the live position of the grip which is recorded. The difference between the two servo hydraulic machines employed is the size and the type of the specimen gripping. The first small machine used the screw grip with the screw end specimens; the other big machine with the split grip type is used with the button head specimen. The photos of the servo hydraulic machines are exposed in Fig. 3.16 and 3.17.

Figure 3.16 The small servo-hydraulic testing machine with screw grip type.

Figure 3.17 The big servo-hydraulic testing machine with split grip type.

3.7.2 Strain Measurement:

An axial extensometer displayed in Fig. 3.18 is employed in the tensile tests of this research; it is spring-loaded on to ridges made at the ends of the specimen gauge length, using a spring outside the furnace in case of elevated temperature tests. The

displacement measured is transferred by means of rods outside the furnace, usually to a linear variable differential transformer (LVDT). To minimise the effects of bending in the specimen, the mean strain were determined for the two LVDTs positioned diametrically opposite each other on the specimen/loading rod chain [88].
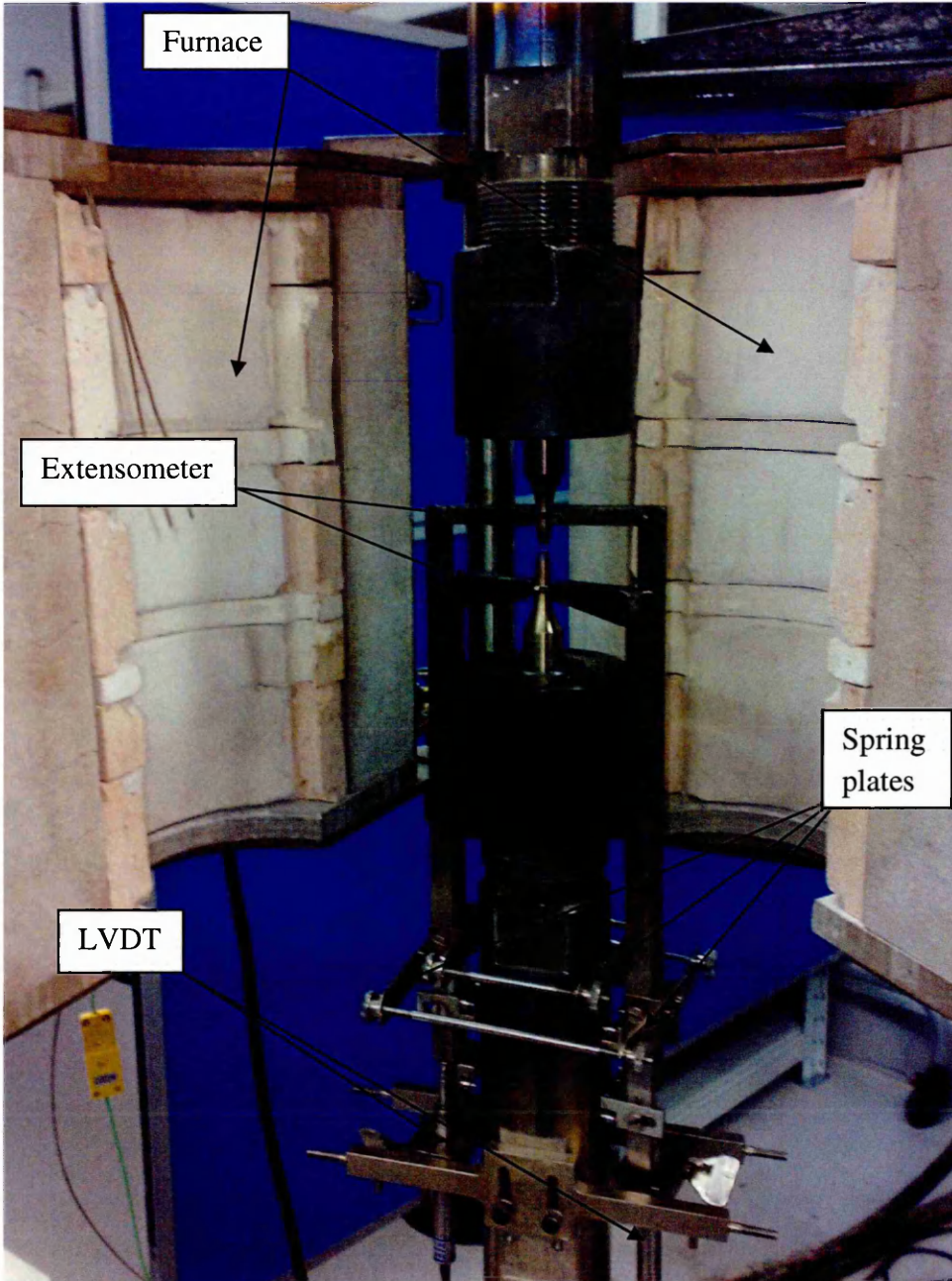
Figure 3.18 The image of the used axial extensometer in the tensile tests.

3.7.3 Heating System:

To achieve the primary requirements of the heating system for the high temperature tensile and fatigue tests, one has to produce the required temperature uniformly along the specimen and to maintain this condition for the duration of the test. Electrical muffle furnace was used in this research for testing. Electrical resistance coils were embedded in the refractory mouldings defining the cylindrical shape of the heating space. The heater assembly is encased in refractory insulation and the whole is contained in a robust metal case. For testing work, there are three windings defining a central zone which is employed in the present tests along with two outer zones. The muffle furnace is a book form type, with consists of two longitudinally divided half cylinders hinged together as revealed in Figs. 3.18 and 3.21. This type allows a high degree of access to the specimen-grip-extensometer and the crack growth measurement arrangements.

3.7.4 Crack Growth Monitoring:

In this research, the crack initiation and propagation measurement have been made by utilizing the Matelect DCM-2, direct current electrical potential drop (DCPD) device. The electric potential method is based on the fact that there will be a disturbance in the electric potential field related to any discontinuity in a current carrying body; the magnitude of the disturbance depends directly on the size and shape of the discontinuity. For the present test piece geometry, a constant direct current of 5 Amperes (Amp.) was selected to pass through the specimen during the test, and the resultant change in electrical potential between two points on the specimen was monitored as a function of crack depth.

The simplest implementation of the potential drop method requires four electrical connections for two specimens, one as a reference (constant), which is outside the furnace and testing machine and the other as a testing specimen (variable). In the present laboratory tests, the current connection leads, which are made of 80/20 nickel-chrome alloy wire, size 2 mm with 0.33ohm/m resistance at room temperature were screwed on the specimen by means of solid nickel ring terminals; the voltage leads that are made of 80/20 nickel-chrome alloy wire with 0.913mm size and 1.64 ohm/m

resistance are spot welded diagonally in a distance (4 – 5 mm) outer the gauge length (in the slop section to avoid fracture in the welding position), between the current leads. The appropriate placing utilized is shown in Figs.3.19 to 3.21.
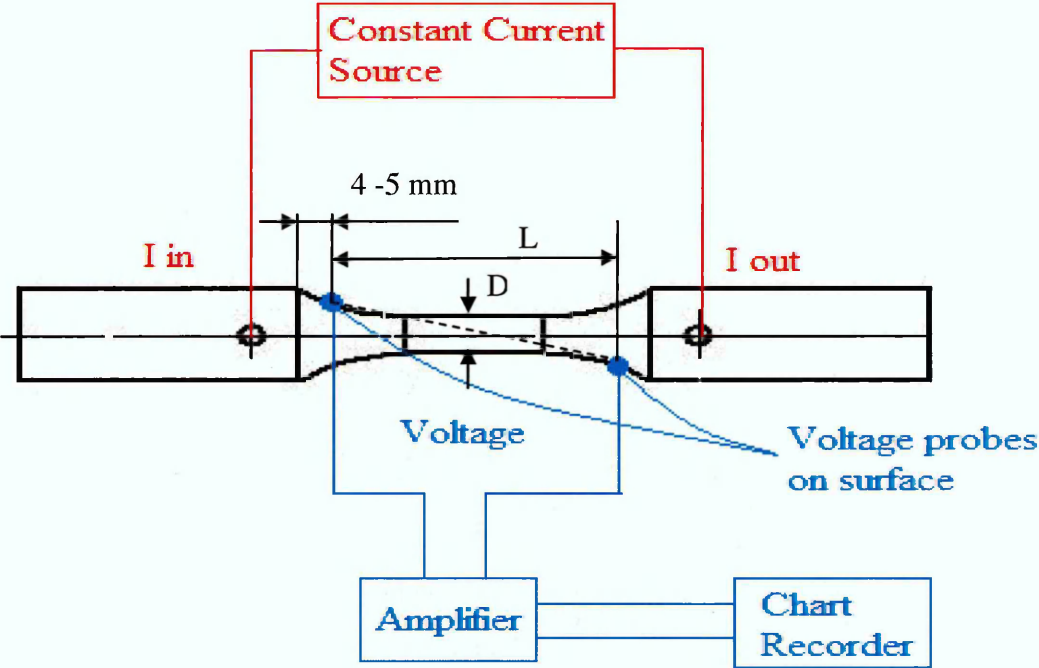
Figure 3.19 Schematic diagram of the DCPD placed connections.
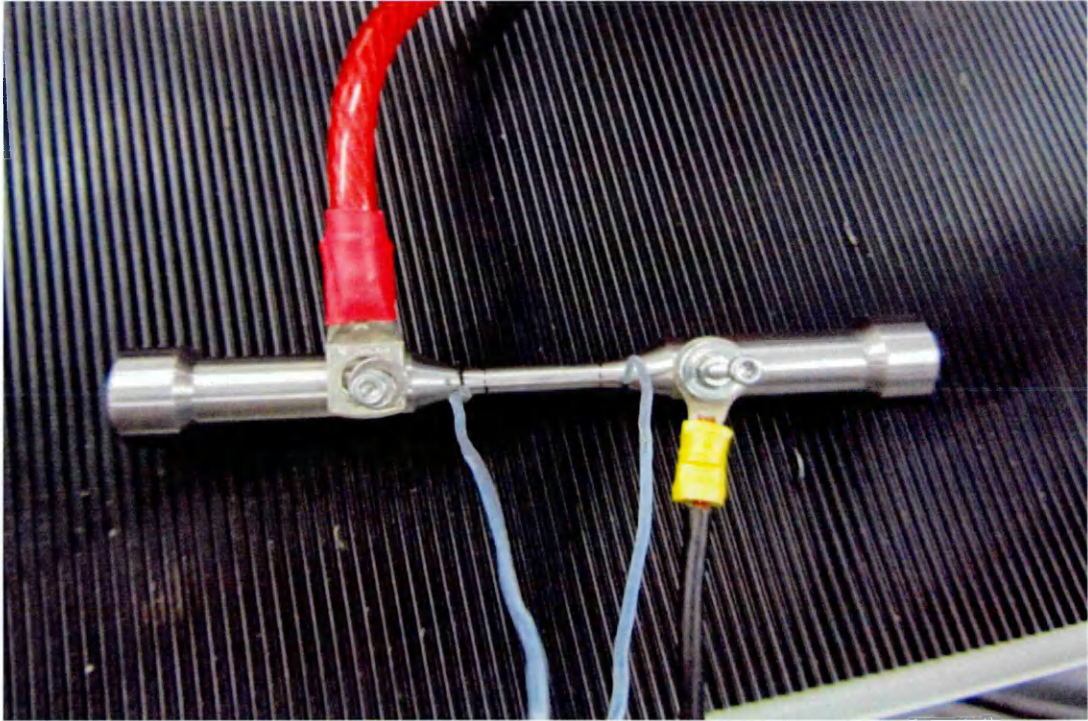
Figure 3.20 The DCM-2 DCPD connections with the reference specimen.
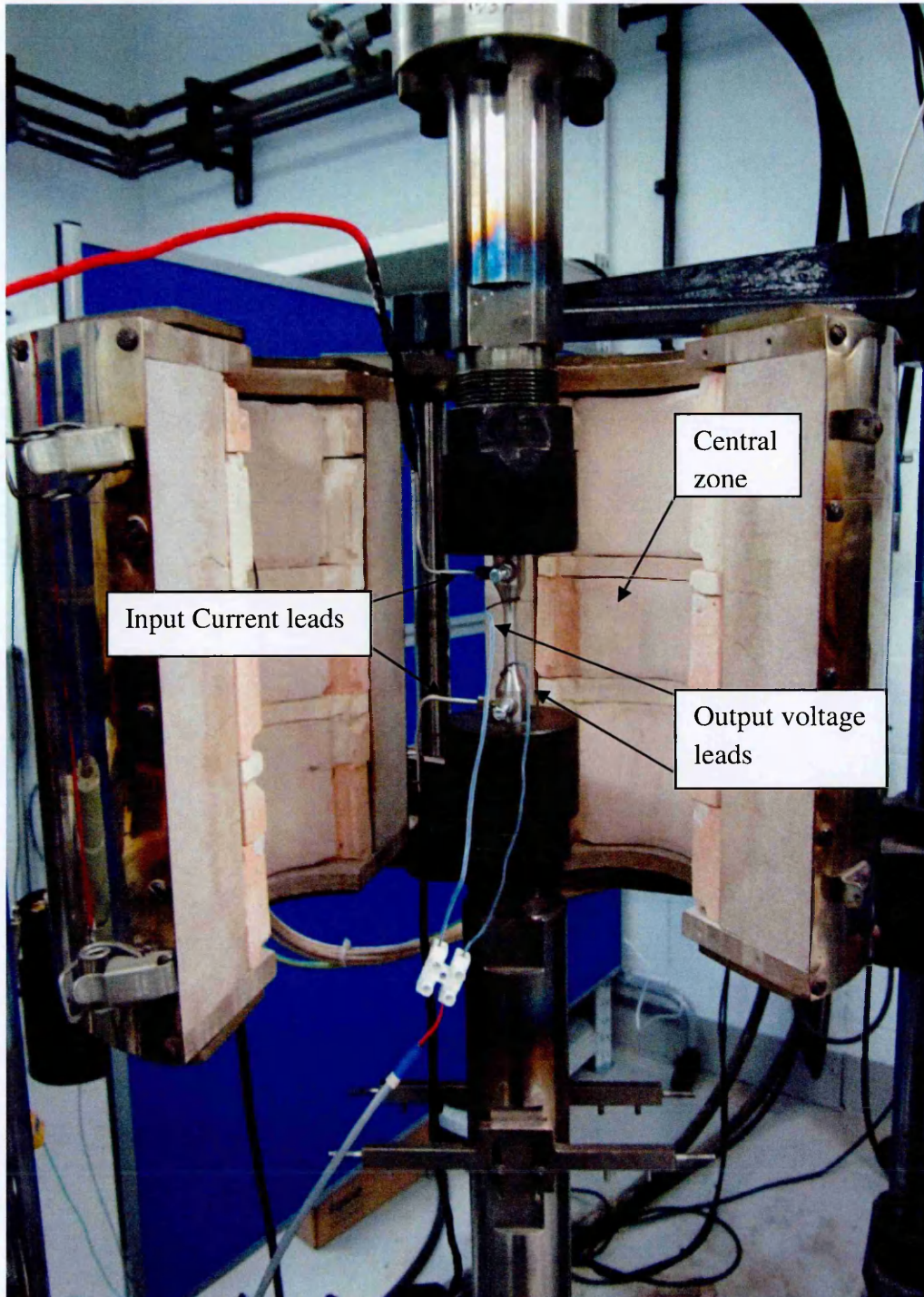
Figure 3.21 The image of the book form muffle furnace used in the tests with the DCM-2 DCPD device with the specimen connections.

The DCPD device is operated by supplying a constant current passing through the free load specimen called reference, which is used as a standard; then, it is used continuously through the tested specimen. The resultant output voltage ratio between the Specimen (x) and the reference (y) was measured. This technique is utilized quantitatively, by a calibration curve fitting equation related to the potential change to the crack depth of the material type. This equation is found by many repeated test. The DCPD device layout and the real image are shown in Figs.3.22 to 3.24.
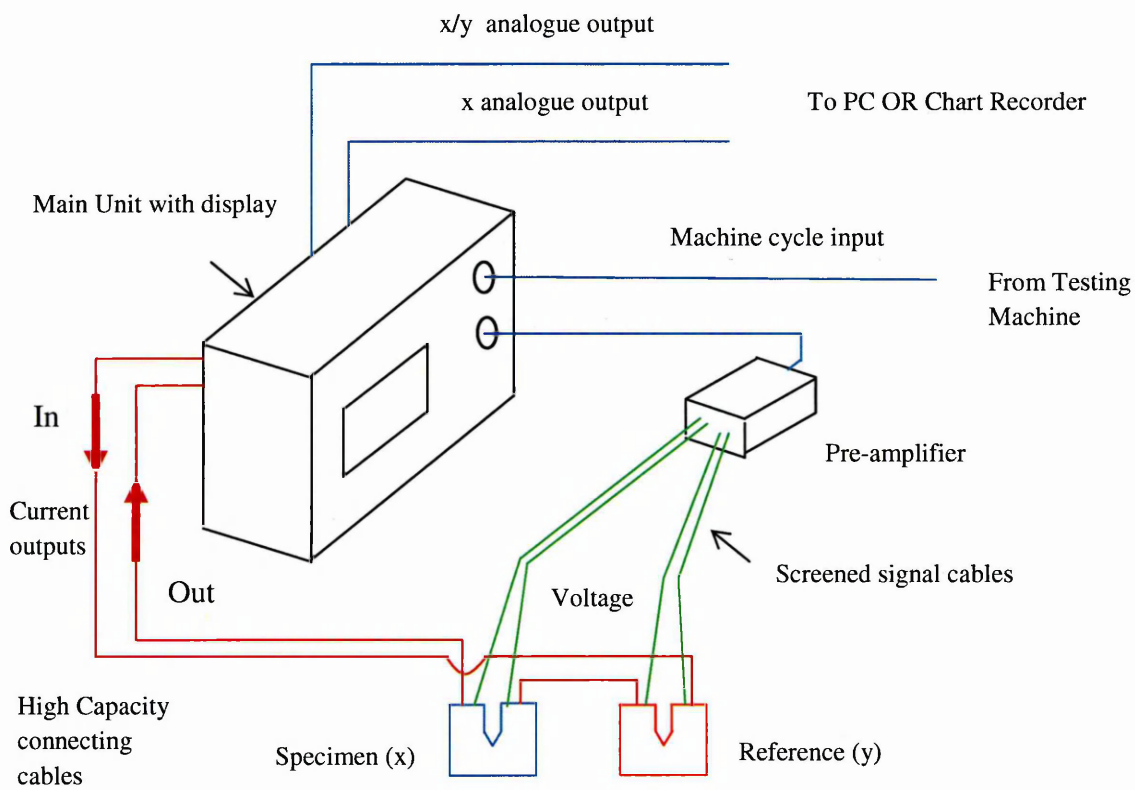
Figure 3.22 Schematic diagram of a typical DCPD test configuration.

Program displays input and output data

DCPD Machin

Specimen

Connections

Reference

Figure 3.23 The real image of the DCPD device with connections.

Calibration Equation

Specimen Voltage Reading

Reference Voltage Reading

Measured Ratio

Current Supply

Crack length

Crack length with time graph

Figure 3.24 The program data display of the DCPD device.

68

3.7.4.1 DCPD Calibration:

Calibration depends on the particular test-piece geometry (diameter/length) and the distance between the positioning of the current input leads and the potential measurement probes, displaying the current-voltage basis relationship for electrical conductivity materials, which is found to be fixed and similar in all the tests; it can be described by the equation.

$$Vol = \frac{4R_e.\Delta L.I}{\pi.D^2}$$

(3.8)

where;

Vol: is the Voltage.

R_e: is the specific electrical resistivity depending on the material type.

ΔL: is the distance between the output voltage leads.

I: is the current.

D: is the specimen gauge length diameter.

The aim of the calibration is to find out the potential behaviour equation of the conductive material depending on the current supply and the crack depth (which means the change in resistance). The equation is created by conducting a fatigue crack test but in the opposite direction, that means supplying a constant current, which uses 5 Amp. in the tests passing through the reference and specimen cutting the specimen in particular measured depth and recording the result output voltage ratio data at each depth. The same sequence is repeated until the specimen is separated or until it becomes very thin. From the recorded voltage ratio data and the measured cutting depth (crack depth), the resultant curve is plotted; the curve fitting equation was found. It is used as a calibration equation for testing the material utilized in the DCPD device to measure the crack depth when applying the real fatigue test. The plot and equation of the crack depth simulation with the output ratio is presented in Fig.3.25.

$$y = 35.192x^5 - 273.94x^4 + 850.3x^3 - 1319.1x^2 + 1028.2x - 320.72$$
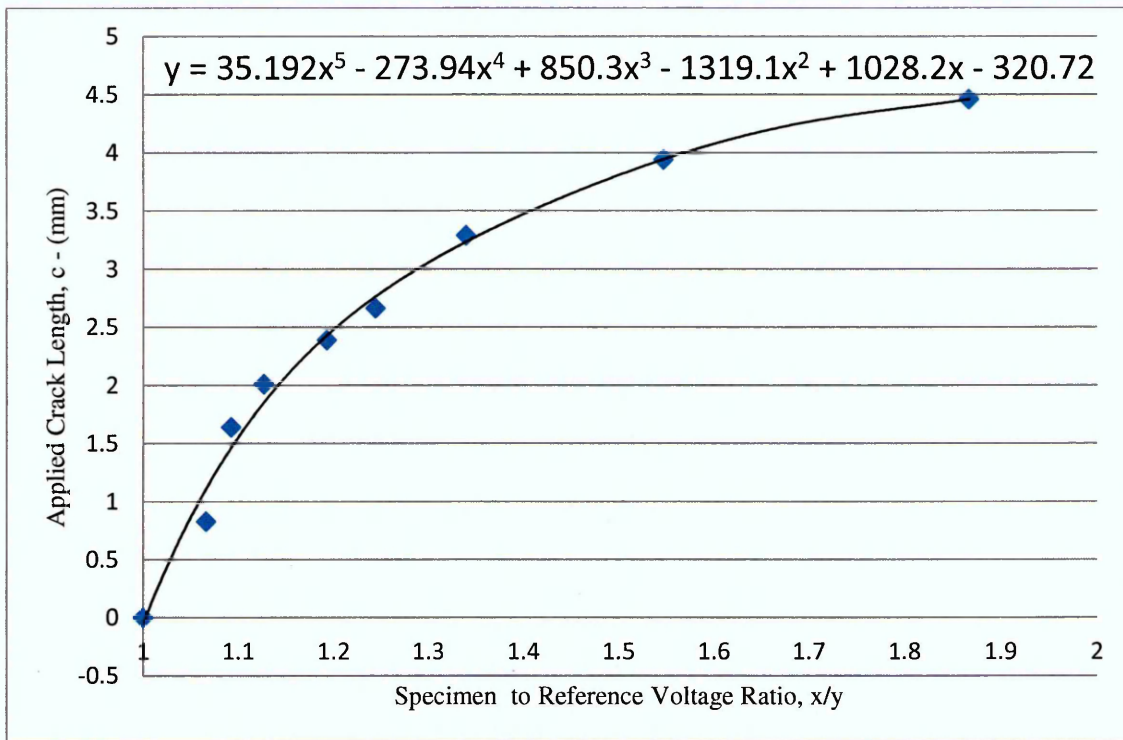
Figure 3.25 The calibration curve fitting equation of the conducting material utilized in DCPD device.

3.7.4.2 Error Factors Affecting on the DCPD Reading:

The accuracy of the crack growth rate measurements obtained using the DCPD method is limited by a number of error factors. These error factors which are characteristic of those encountered in the measurement of very low resistances arise from the following sources as a witness in laboratory testing:

I) The resistance of a stainless steel specimen is typically a few micro-ohms that provide a direct measure of the resistance of the specimen then for accurate measurement of crack length; it is essential to reduce the current to the minimum as it is used in test 5 Amp.

II) The dynamic extension and compression of the specimen is due to the applied cyclic loading (tension and compression load phase). Regarding the direct constant current supplied, it obtains a significant variation in the recording data due to the changes in length between the potential voltage leads positions; this is the reason to present a zigzag profile. This occurred because of missing synchronization between the cyclic

70

loadings of the servo-hydraulic machine with the recording program of the DCPD device. For that reason, the selection of the maximum recorded data is made for all the behaviour profiles of the tested specimens in the crack growth curve fitting and calculations data; for example, the isothermal fatigue test at 600 °C is shown in Fig 3.26.
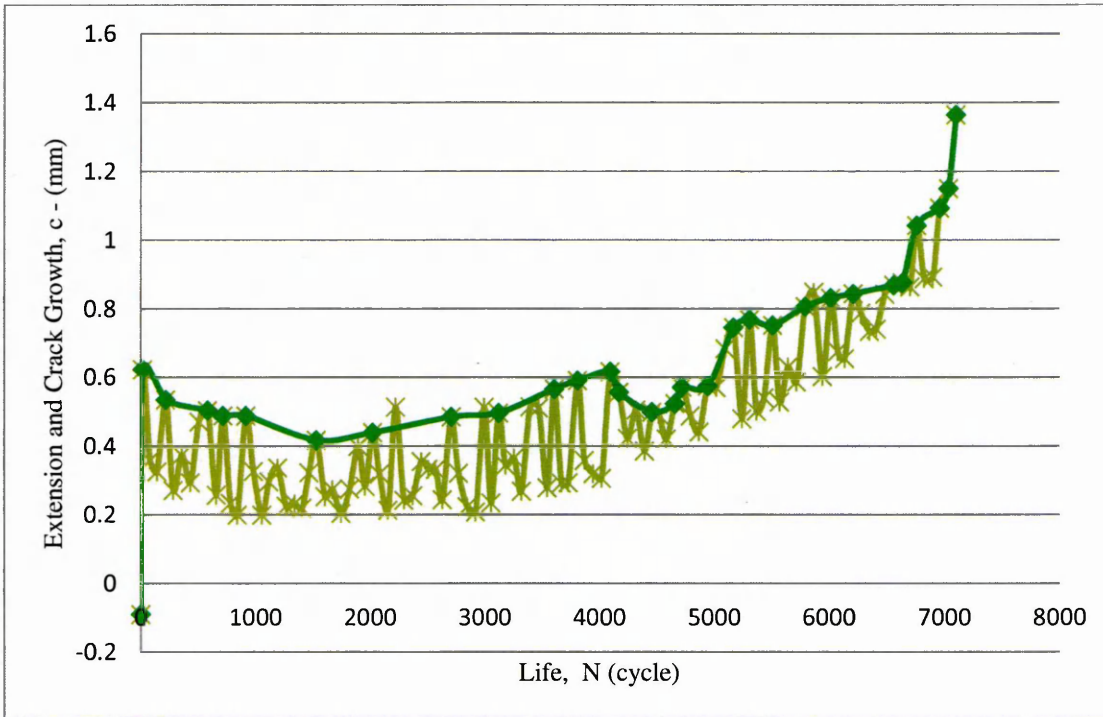
Figure 3.26 The real zigzag output and the selected data of the 600 °C test behaviour profile.

III) Because of the free running (continuous) reading of the DCPD device, the timing shift which is developed by the recording data by the DCPD device takes about 1.6 sec in one period reading. During this period, the applied cyclic load on the cyclic loading machine is doing a 5cycle/sec; this causes a shift and oscillation in reading because of the change in the length by the tension or compression of the specimen, subsequent to the length between the voltage measured points leads of the DCPD, that is the reason of not having smooth recording of the data.

IV) The computer program coupled with the DCPD device takes 15 sec to do one record, which work as a filter but due to a long delay, the records are affected by the cyclic position saved in peak or trough levels.

71

V) The most significant and often overlooked error is caused by the temperature, where the coefficient of resistance of steel is about $5 \times 10^{-3} \ K^{-1}$. The error caused by a 5 K change in temperature can therefore amount to 2.5% [89]. Furthermore, the temperature increased the ductility of the testing specimen; it was behind all the flaws mentioned earlier. Specially, the length between the voltage lead.

3.8 Fatigue Crack Growth Rate Test Results Calculations:

The rate of mode I crack growth is determined by subjecting fatigue cracked or uncracked specimen, to constant amplitude cyclic loading. The incremental in crack length is recorded along with the corresponding number of elapsed load cycles acquiring stress intensity (K_I), crack length (a), and cycle count (N) data during the test. The data was monitored using a DCPD technique, and the crack growth rate was determined by the incremental polynomial method using a least squares curve fitting of a second order parabola joining groups of seven crack length readings, to get the crack propagation, and to find the crack growth rate, by differentiation to give the extension per cycle. A modified Matlap program for solid cylinder specimen illustrated in appendix A, was modified based on the ASTM test method for the constant-load-amplitude fatigue crack growth rate [90].

The crack growth calculation can be possibly solved by two methods: I) the secant method or point-to-point calculation, and II) the incremental polynomial method. Both methods are known to give approximately the same average growth rate response. However, the secant method often results in the increased scattering in growth rate relative to the incremental polynomial method, since the latter numerically smooth's the data [90].

The incremental polynomial method was selected to compute crack growth rates, which involved fitting a second order polynomial (parabola) to sets of (2p+1) successive data points, where for our calculation, a Matlap program is made with the value of p =3, which is seven points, it was selected to deal with a solid cylinder specimen. The form of the equation for the local fit is as follows:

$$c_i = b_0 + b_1 \left(\frac{N_i - C_1}{C_2}\right) + b_2 \left(\frac{N_i - C_1}{C_2}\right)^2 \qquad (3.9)$$

where;

$$-1 \le \left(\frac{N_i - C_1}{C_2}\right) \le +1 \qquad for \quad i-p \; \le j \; \le i+p \qquad (3.10)$$

And b_0, b_1 and b_2 are the regression parameters that are determined by the least squares method over the range $c_{i-p} \le c \le c_{i+p}$. The value c_i is the fitted value of crack length at N_i. The parameters;

$$\left. \begin{aligned} C_1 &= \left(\frac{N_{i-p} + N_{i+p}}{2}\right) \\[2em] C_2 &= \left(\frac{N_{i-p} - N_{i+p}}{2}\right) \end{aligned} \right\} \qquad (3.11)$$

and

are used to scale the input data, thus avoiding numerical difficulties in determining the regression parameters. The read and measured crack growth data of a test utilized in room temperature is presented in Fig. 3.27 showing the slow increase of crack length primarily then the sharp one at the end and the isothermal fatigue test data conducted in the temperature range of 300 to 600 °C; they will be presented in Chapter six.

The rate of crack growth at N_i is obtained from the derivative of the above parabola, (Eq. 3.9), which is given by the following expression:

$$\left(\frac{dc}{dN}\right)_{c_i} = \left(\frac{b_1}{C_2}\right) + \frac{2\, b_2\, (N_i - C_1)}{C_2^2} \qquad (3.12)$$

The fatigue crack growth rate curve is found by presenting the data I terms of the growth rate per cycle of loading from Eq. 3.12, versus the fluctuation of stress intensity

factor at the tip of the crack; the value of crack length c_i is obtained from the regression calculation (Eq.3.9) used to calculate the stress intensity factor range.
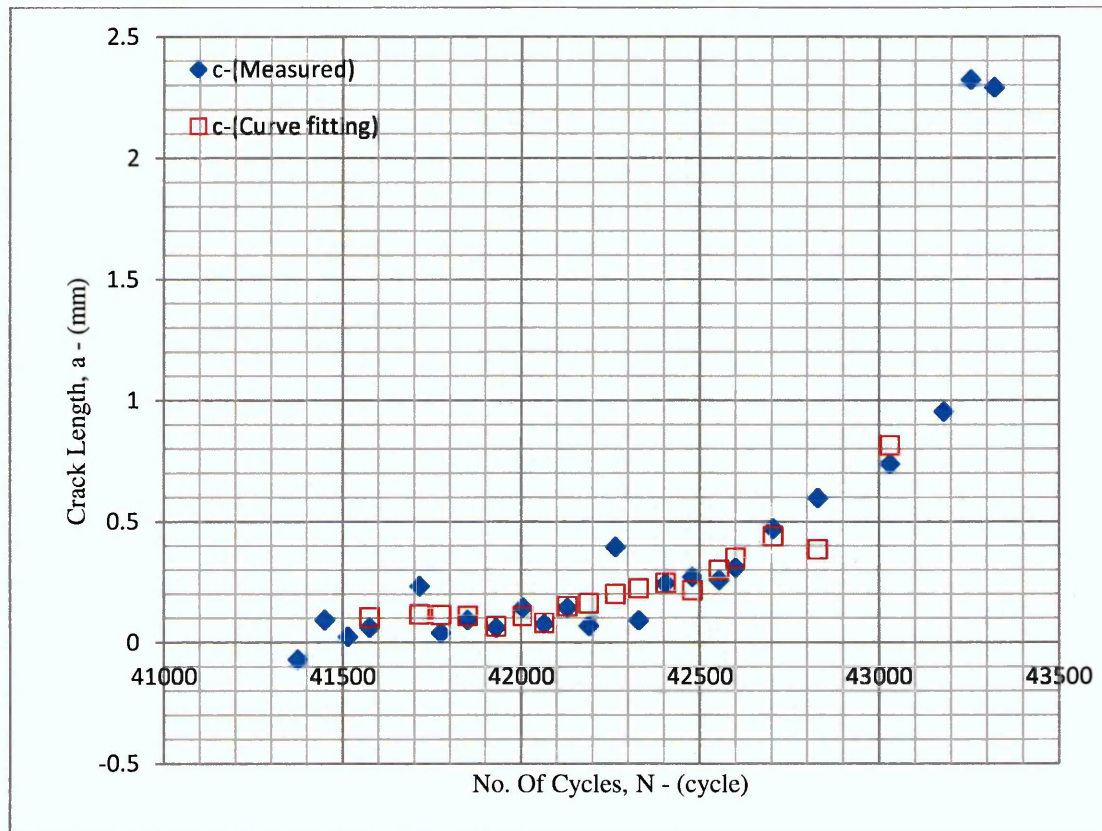
Figure 3.27 The read and measured crack growth data.

3.9 Stress Intensity Factor Calculation:

A room temperature fatigue test and isothermal test conducted in the temperature range of 300 to 600 °C, (to be discussed in Chapter Six), for a solid cylinder were carried out under controlled sinusoidal cycling at 5 Hz with R-ratio of 0.1. The stress intensity factor for a crack subjected to cyclic mechanical stresses at constant temperatures was calculated by the following relationship [91]:

$$K_I = \sigma \sqrt{\pi c} \ \ F\left(\frac{c}{r}\right) \tag{3.13}$$

74

The geometry factor $F\left(\frac{c}{r}\right)$ is a function, given by Tada [91], for uncracked solid cylinder under tension and approximated by the following polynomial expression:

$$F\left(\frac{c}{r}\right) = \frac{1}{(1 - {}^{c}/_{r})^{3/2}} \left\{1.122 - 1.302 \frac{c}{r} + 0.988 \left(\frac{c}{r}\right)^2 - 0.308 \left(\frac{c}{r}\right)^3\right\} \qquad (3.14)$$

This function has an accuracy of 15 FOR ($\frac{c}{r} \leq 0.6$).

Fatigue crack growth under linear elastic conditions is primarily governed by the stress intensity factor range experienced by a crack. Besides, if reversed loading is applied to the specimen, the compressive half of the stress cycle contributes little to crack growth since the crack faces are pushed together to make a closure. Therefore in calculating the stress intensity factor range (ΔK), the following rules were applied as,

$$\sigma_{min} > 0 \qquad then \qquad \Delta K = K_{max} - K_{min} \qquad (3.15)$$

where, K_{max} is the maximum positive stress intensity factor in the applied stress cycle and K_{min} is the minimum stress intensity factor. However, with R-ratio of 0.1, negative stresses were not included in this series of tests. The fatigue crack growth rate versus the calculated stress intensity factor range for fatigue test at room temperature is represented in Fig.3.28.

When the crack growth rate to number of cycles is plotted against the stress intensity factor range, both scales being logarithmic, the equation of the crack growth rate of this work material is based on Paris Law [7], which describes the slope of the stage II of the fatigue crack propagation behaviour of the material, through the information derived from the fatigue crack growth test represented as follows:

$$\frac{dc}{dN} = C\,(\Delta K)^m \qquad (3.16)$$

75
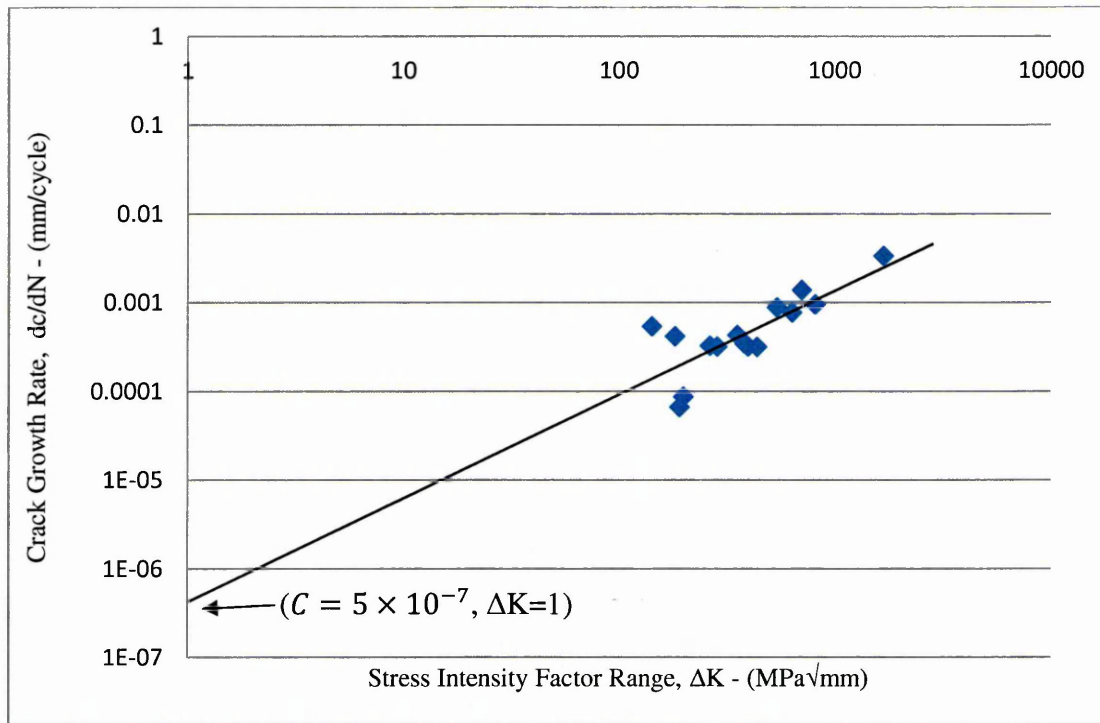
Figure 3.28 The fatigue crack growth rate of AISI420 martensitic stainless steel.

The constant C is equal to $\frac{dc}{dN}$ at the intersection point of the slop with Y-axis $(\frac{dc}{dN})$, at (log (ΔK) =1), and the exponent m is defined as the slope of the $(\log(\frac{dc}{dN}) - \log(\Delta K))$ curve, which is:

$$m = \left[\left(\log\left(\frac{dc}{dN}\right)_2 - \log\left(\frac{dc}{dN}\right)_1\right) / (\log(\Delta K)_2 - \log(\Delta K)_1)\right] = \left[\frac{\log\frac{\left(\frac{dc}{dN}\right)_2}{\left(\frac{dc}{dN}\right)_1}}{\log\frac{(\Delta K)_2}{(\Delta K)_1}}\right] \quad (3.17)$$

The crack growth rate equation of this work material is:

$$\frac{dc}{dN} = 5 \times 10^{-7} \, (\Delta K)^{1.161} \quad (3.18)$$

3.10 Modified Thermo-Mechanical Fatigue Test Techniques:

In a thermo-mechanical test, the temperature is cycled either in-phase or out-of-phase with the applied mechanical strain or stress in a completely controlled manner with a fast response. This is a much more difficult test to carry out at that temperature to accurately cycled, thermal and mechanical loads synchronized. The merits of the test are that deformation and rupture data can be obtained under conditions, which are close to service conditions. A Thermo-mechanical test facility was designed to assist studies of the growth of cracks under repeated severe cooling shocks. This facility enables three types of test to be performed: I) an isothermal fatigue test, in which the specimen is maintained at a constant temperature, and an alternating mechanical load is applied, II) an In-phase thermo-mechanical fatigue test, where the phase of cycling loads of temperature and alternating mechanical applied load are the same, and III) an Out-of phase thermo-mechanical fatigue test, where the phase of cycling loads of temperature and alternating mechanical applied loads are the opposite.

According to the test conditions required, modifications to the thermo-mechanical test machine were made to carry out a thermo-mechanical fatigue test which provided transient down shock cooling control by transient circulation of cooling fluid through the testing specimen. The modifications are described in two parts, as follows:

3.10.1 Modified System Cooling Layout Design:

The operation of the new development design of thermo-mechanical machine is by circulating oil in two ways through the machine: the first transient way involves injecting oil in the specific measured, and controlled by the electrical valve (solenoid) passing inside the grips of the machine then through the testing hollow cylinder specimen. The second way is by the oil continually flowing to the upper and lower grips of the machine for grip cooling. The two ways are connected to pass the oil to the filter and later to the radiator for cooling by the water and fan, finally to achieve continuous circulating, the oil is pumped again. The system layout is shown in Fig.3.29.

3.10.2 Modified Specimen Gripping Design:

Assembling the parts of the combined grip device for the threaded end hollow cylinder specimen was designed not just to transmit the imposed cyclic forces without backlash, but also to ensure the alignment of specimen axis and its axis. Moreover, the grip is based on generating cyclic temperature loading by controlling the flow of the coolant oil inside the bore of the hollow cylindrical specimen. The grips are designed either to water, force air or oil cooled in order to allow quick cyclic stabilization of the longitudinal temperature distribution within the gauge length of the testing specimen and to provide stable thermal conditions during the experiment, the working diagram is illustrated in Fig. 3.28 and the parts and assemblies in Figs 3.30 to 3.40.
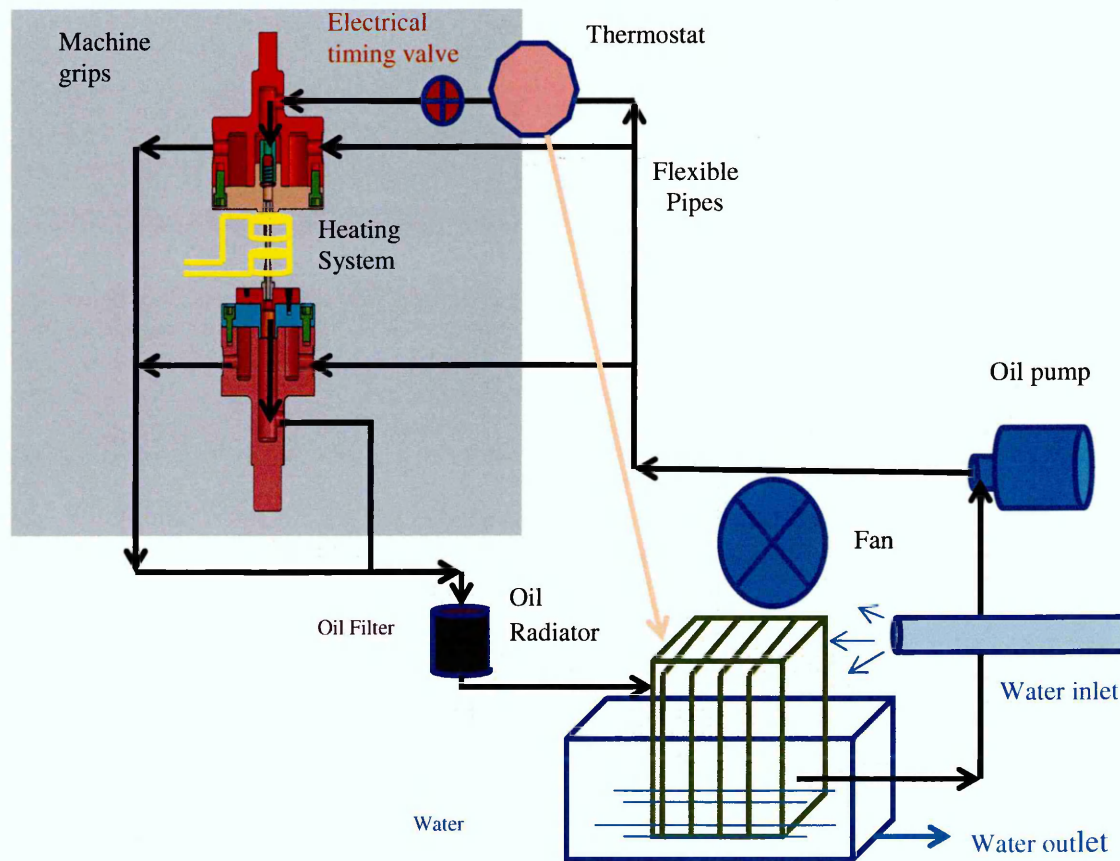
Figure 3.29 The working diagram of the modified thermo-mechanical fatigue testing machine.

Figure 3.30 The design of upper grip body.

Figure 3.31 The design of the valve body for the upper.

Figure 3.32 The design of the valve insert of the upper grip.

Figure 3.33 The design of the upper cover of the upper grip.

Figure 3.34 The assembly of the valve components with the cover of the upper grip.

Figure 3.35 The upper grip total assembly.

This part must
checked with the machine base

M52
60
1 X 45°
M20
150
25
70
Ø35

SECTION A-A

Ø80
60
R5
R10
90
90
Ø40
M20
A
A

Ø116
Ø176
R73
Ø99

Figure 3.36 The design of the lower grip body.

85

Ø146

Ø80

15

30

20

1 X 45°

1 X 45°

Ø36

45

SECTION A-A

M8 x8

R12.50 x8

Ø16.50 x8

Ø28

Ø176

A

A

Lower grip cover

new lower grip cover 2

A4

SHEET 1 OF 1

DO NOT SCALE DRAWING

Figure 3.37 The design of the lower grip cover.

Figure 3.38 The design of the lower grip cover adapter.

Grip adapter

M16 L-Ker screw

Grib body

M8 L-Ker screw

Grip cover

SECTION C-C
SCALE 1:2

C

C

Lower grip assembly

new lower grip assembly 2

Figure 3.39 The total assembly design of the lower grip.

Figure 3.40 The total assembly design of the upper and lower grip with specimen.

CHAPTER FOUR

4- THERMO-MECHANICAL MODELLING

4.1 Empirical Modelling:

The crack growth analysis, stress and strain intensity factor approaches are analysed and presented as case studies.

Case one presents the analysis of the estimated thermal stresses superimposed on sinusoidal cyclic mechanical stress results in the solid cylinder under isothermal fatigue simulation on the crack growth. Case two analyses the estimated transient thermal stresses superimposed on cyclic mechanical loading results in the hollow cylinder under thermal shock in heating case and down shock cooling case.

Case one calculation depends on the same experimental thermal and mechanical loading to assess the link between the two studies. Thermo-Elastic-Plastic analysis data of the two cases are obtained by the series of calculation as follows:

➢ Temperature distribution calculation.

➢ Thermal stresses calculation.

➢ Elastic-Plastic stress calculation.

➢ Thermo–Mechanical stress calculation.

➢ Stress and Strain Intensity Factor calculation.

4.2 Temperature Distribution Calculation:

To analyse the two types of cylinders subjected to transient thermal loading in isothermal loading, heating and down shock cooling cases, a temperature distribution is estimated. It evaluates the thermal stresses induced by the thermal loading assuming that the material is uniform, homogeneous and isotropic. Furthermore, the temperature

distribution varies only with the radial coordinate through the cylinder wall, and the cylinder is initially at a uniform temperature in which results vary with the position of the wall thickness and time.

The transient temperature distributions for the solid cylinder is subjected to constant thermal loading at the outer surface; a hollow cylinder geometric model is also subjected to thermal loading during heating or re-heating and down shock cooling cases are given by employing the solution of the general conduction heat equation given by:

$$\frac{\partial \theta_{(r,t)}}{\partial t} = D \left(\frac{\partial^2 \theta_{(r,t)}}{\partial r^2} + \frac{1}{r} \frac{\partial \theta_{(r,t)}}{\partial r} \right), \quad a < r < b, \quad t > 0. \tag{4.1}$$

where

$$\theta_{(r,t)} = T_{(r,t)} - T_0 \tag{4.2}$$

T_0 is the initial temperature of the cylinder corresponding to zero time and stress state and $T_{(r,t)}$ is the temperature distribution at time t and r position through the wall thickness. Also, D is the coefficient of diffusion (i.e., $D = \frac{k}{\rho.cp}$; k, ρ, cp are being the thermal conduction coefficient of the cylinder material, the mass density, and the specific heat).

Carslaw and Jaeger [92] proposed model for solid and hollow cylinder making use of the application of Laplace transformation in a cylindrical region and the Bessel function of the first and second kinds with the boundary conditions of each case studied. In this model, four Bessel function roots are used to give an acceptable stability for the solutions, Nied and Erdogan [93], calculated the transient thermal stress for hollow elastic cylinder fast cooled from inside obtaining Laplace transformation for the solution using the first four roots ($i = 1,...,4$) while Cho et al [94], introduced an elasto-dynamic solution for the thermal shock stresses in thick cylinder subjected to sudden thermal loading using Laplace transformation with Bessel function and Hankel transform by employing the first ten roots ($i = 1,...,10$).

4.2.1 Solid Cylinder Model:

Many investigators have dealt with the infinite long solid cylinder under different loading conditions. Ishikawa, [95], studied the theoretical transient thermal stresses when the surface is subjected to a sudden temperature drop after a sudden temperature rise. Molina and Trujillo, [96], estimated the thermal stresses when a constant heat flux is applied to its surface employing hyperbolic heat conduction model. Zhao et al, [97], presented an analysis of transient thermo-mechanical study for a solid cylinder material under rapid exposure to connective medium of different temperatures, obtaining the analytical solution formula by using the separation of variables method. Aouadi, [98], studied the thermoplastic-diffusion interactions when applying a thermal shock on the solid cylinder surface employing the Laplace transformation and numerical Laplace inversion in the solution.

The present work reports the outer surface of the solid cylinder which is subjected to constant temperature and the initial temperature assumed to be at a selected temperature range.

The general boundary condition is:

$$\theta_{(b,t)} = T_{(b,t)} - T_0 = T_b \qquad (4.3)$$

$T_b = 300, 500 \text{ and } 600\,°C, \quad r = b, \quad t > 0.$
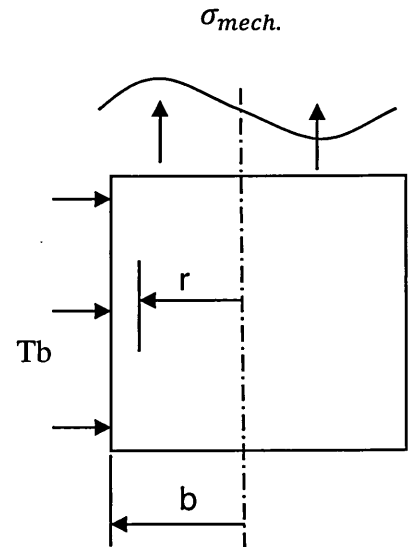
The solution of Equation (4.1) gives, the temperature distribution through the solid cylinder wall, in this case, it is:

92

$$\theta_{(r,t)} = T_b \cdot \left(1 - \frac{2}{b} \sum_{i=1}^{\infty} e^{-D.\lambda_i^2.t} \cdot \frac{J_0(r.\lambda_i)}{\lambda_i.J_1(b.\lambda_i)} \right) \qquad (4.4)$$

where;

λ_i are the positive roots of the equation:

$$J_0(b.\lambda_i) = 0 . \qquad (4.5)$$

During the isothermal boundary conditions, temperature gradients are introduced across the solid cylinder specimen that resulting in thermal stresses that varies with both time and position through the specimen.

Figs. 4.1 to 4.3 shows the temperature distribution calculated through the solid cylinder wall during different time intervals at (300 °C, 500 °C and 600 °C) outer supplied temperature. The temperature profiles dropped from outer surface reaching the minimum, when it is closes with the cylinder centre line, this temperature will rise with the increase in the outer surface supplied temperature and time interval reaching the steady equalized to the outer surface temperature. Figs. 4.4 to 4.6 show the calculated temperature distribution with time at selected radii to present the behaviour and the timing period for the temperature distribution to become steady at each radius. Also the temperature at the outer surface was constant at all-time which indicates a satisfactory agreement with the boundary conditions.
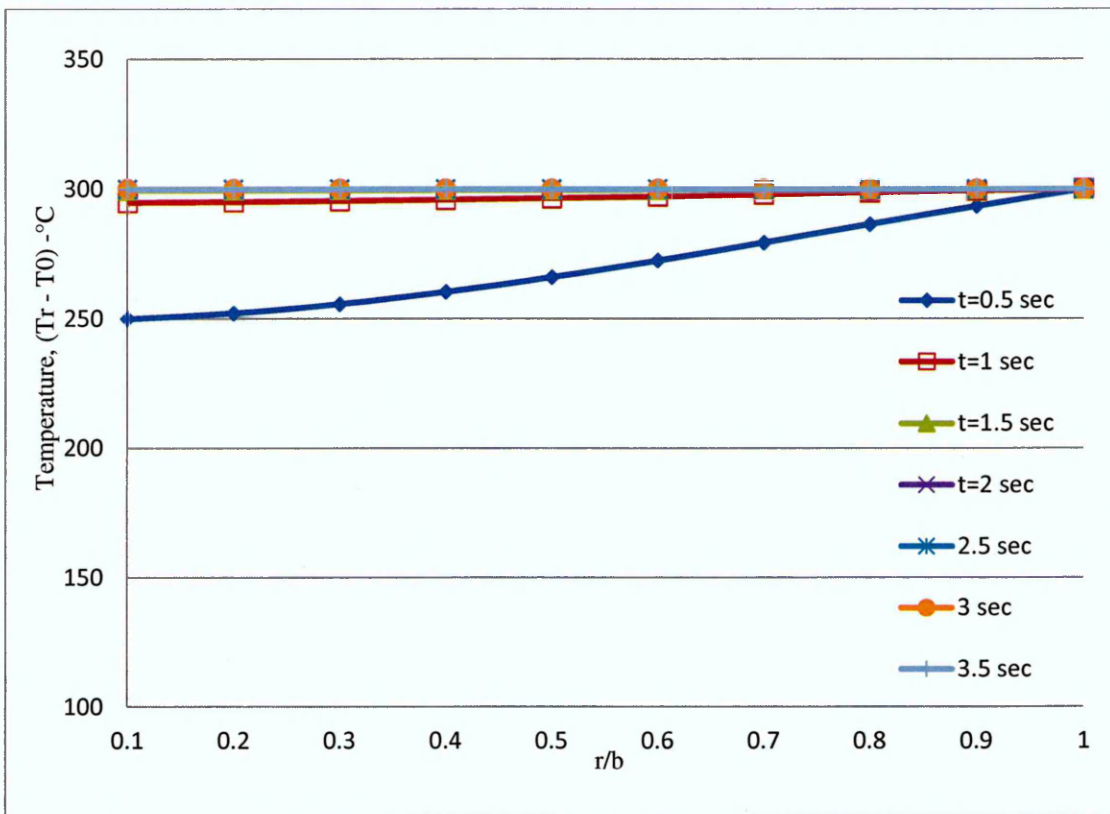
Figure 4.1 The temperature distribution through the solid cylinder wall at different times subjected to Tb = 300 °C.
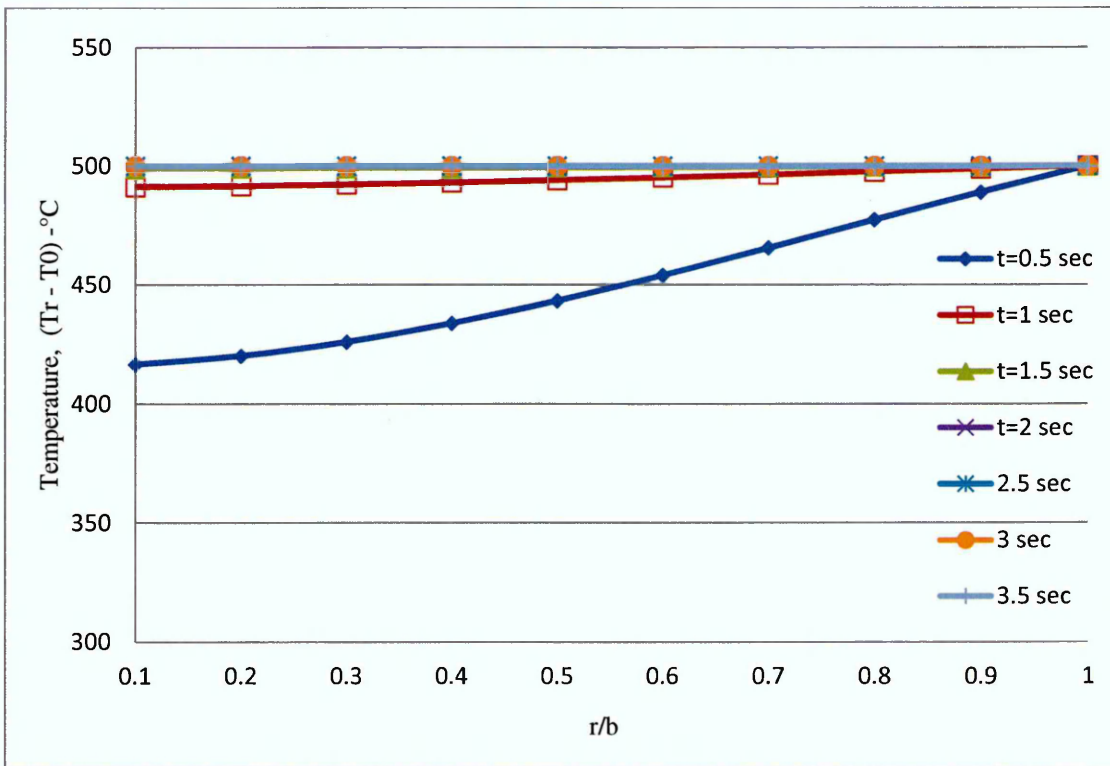
Figure 4.2 The temperature distribution through the solid cylinder wall at different times subjected to Tb = 500 °C.
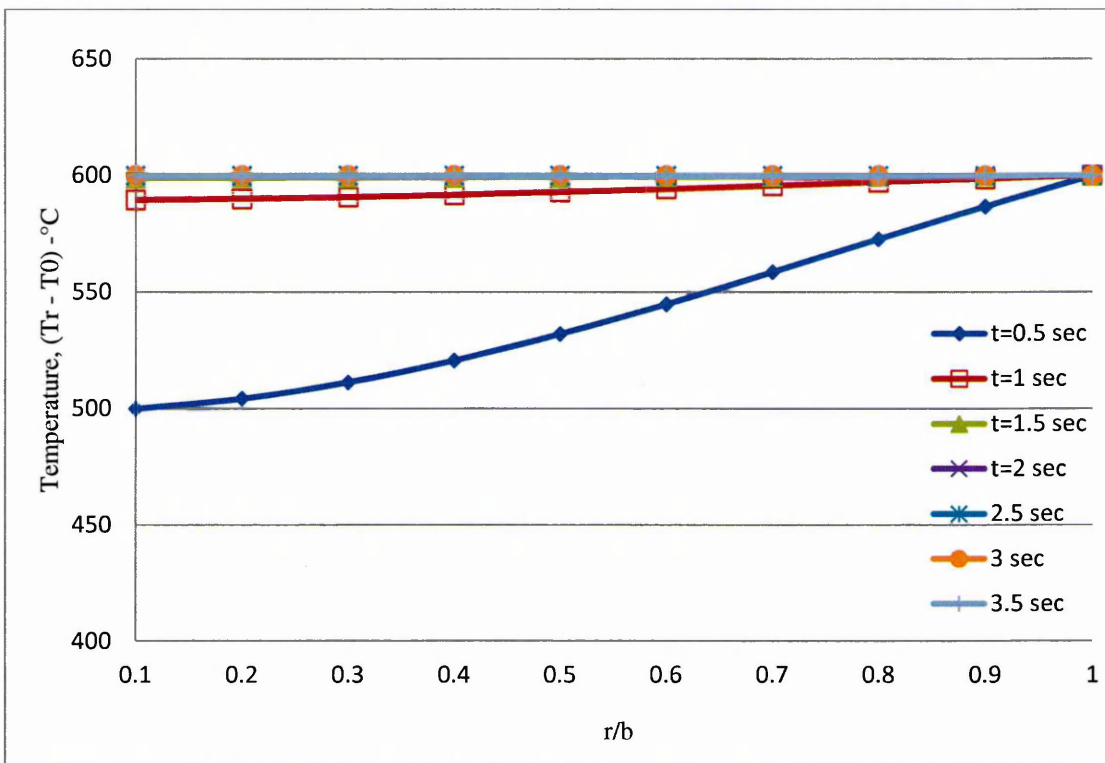
Figure 4.3 The temperature distribution through the solid cylinder wall at different times subjected to Tb = 600 °C.
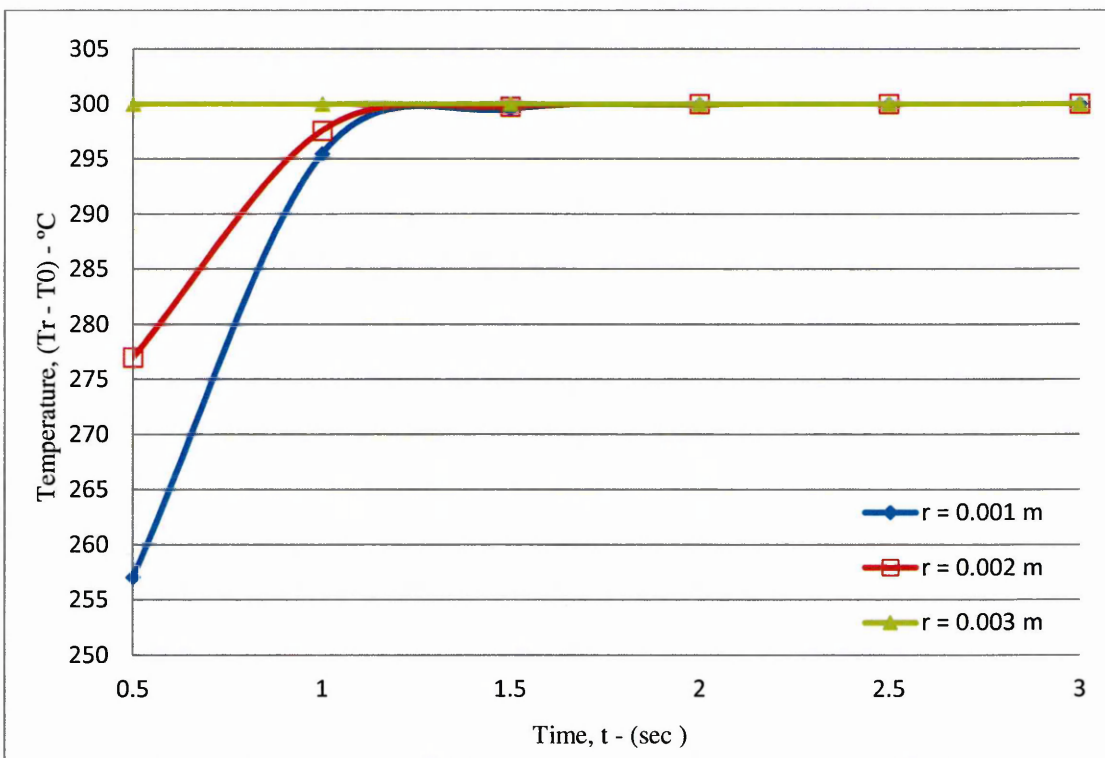
Figure 4.4 The temperature distribution with time at selected radii by supplying Tb = 300 °C.
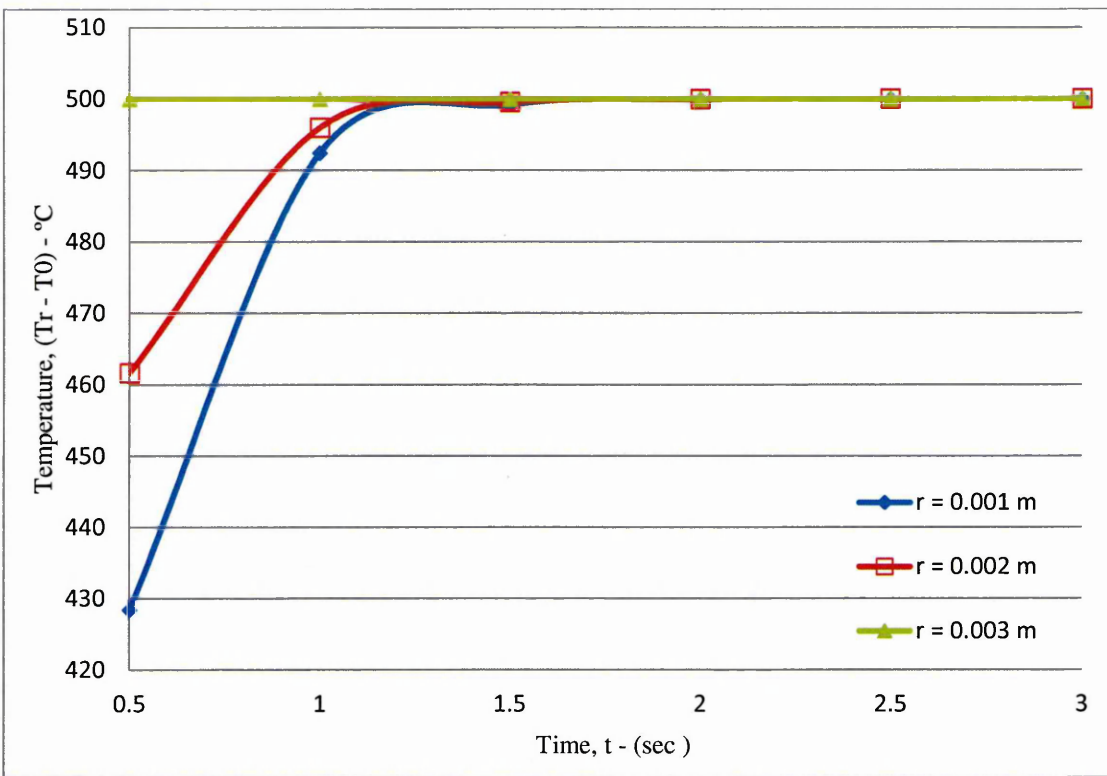
Figure 4.5 The temperature distribution with time at selected radii by supplying Tb = 500 °C.
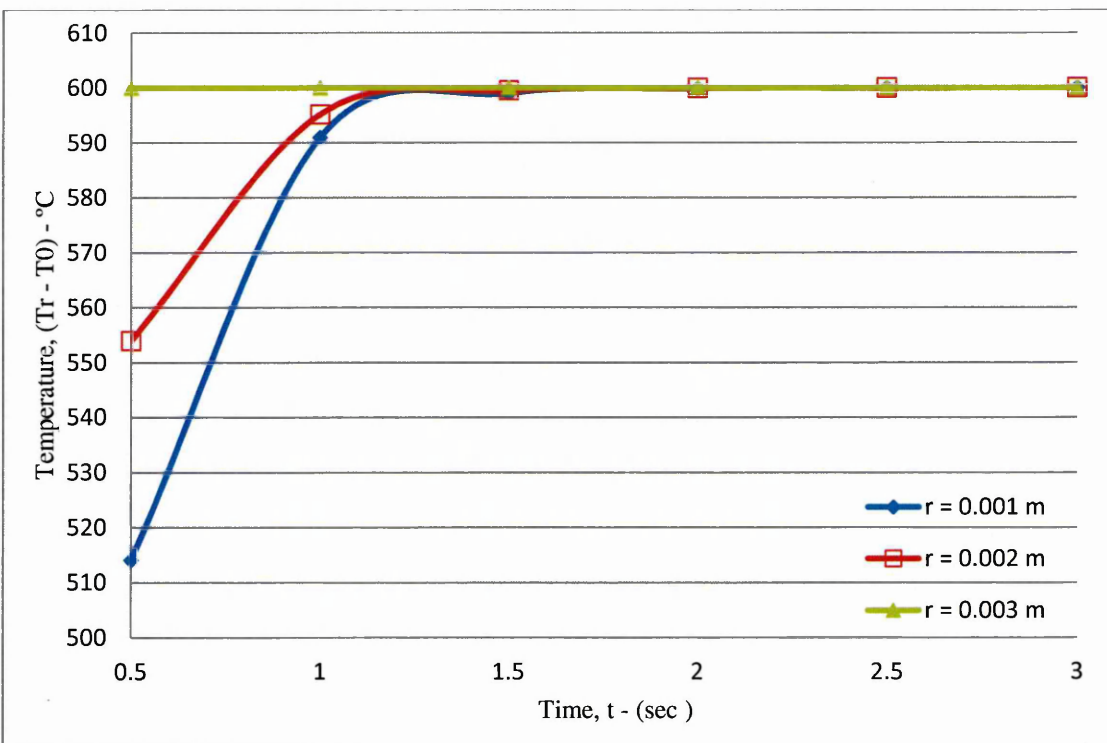
Figure 4.6 The temperature distribution with time at selected radii by supplying Tb = 600 °C.

96

4.2.2 Hollow Cylinder Model:

Work has been carried out on the hollow cylinder with different case studies. Radu et al. [99], presented a set of analytical solutions using a finite Hankel transform and Bessel functions with several new features developed for the field of temperature and thermal stresses in a hollow cylinder affected by a sinusoidal transient thermal loading at the inner surface. Additionally, Kardomateas [100, 101], exposed the stresses and displacement in an orthotropic hollow circular cylinder applying a thermal load on the boundary surface employing Carslaw and Jaeger solution for temperature in terms of Bessel function and using Hankel expansions. Jabbari et al., [102,103], utilized a thick hollow cylinder made of functionally graded materials under one or two dimensional steady-state temperature distribution with general thermal and mechanical boundary conditions using the method of Navier equation. Ehteram et al., [104], presented a theoretical solution for the transient thermal stress in a two layered isotropic hollow cylinder with un-similar temperature in the circumferential direction whereas Clayton, [105], studied the experimental and analytical damage of the temperature and stress in reactor structural components subjected to a thermal shock using the Carslaw and Jaeger transient temperature solution.

A- Heating or Re-heating Case:

In this case the outer surface of the hollow cylinder is subjected to heating flux and the inner surface is kept at a constant temperature (600 °C).

The general boundary conditions are:

$$\theta_{(a,t)} = T_{(a,t)} - T_0 = T_a = 600\,°C \quad ,r = a\,, \ t > 0. \quad (4.6)$$

$$\frac{\partial\,\theta_{(b,t)}}{\partial r} = \frac{\partial\,T_{(b,t)}}{\partial r} = \frac{F}{k} \qquad ,r = b \ , \ t > 0 \qquad (4.7)$$
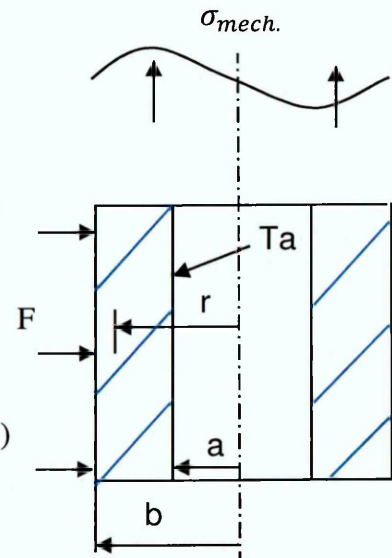
The distribution of temperature through the shell wall in this case is:

$$\theta_{(r,t)} = A_1 + A_2 \ln\frac{r}{a} + \sum_{i=1}^{\infty} A_{3i} \cdot [\, J_0\,(r\,\lambda_i).Y_0(a\,\lambda_i) - Y_0(r\,\lambda_i).J_0\,(a\,\lambda_i)\,] \qquad (4.8)$$

where;

A_1, A_2, A_{3i} are constant shown in Appendix B. and λ_i are the positive roots of the equation below, where $(i = 1, ..., 4)$ are chosen:

$$[J_0\,(a\,\lambda_i) \cdot Y_1(b\,\lambda_i) - Y_0\,(a\,\lambda_i) \cdot J_1(b\,\lambda_i)\,] = 0 \qquad (4.9)$$

Fig. 4.7 presents the temperature distribution through the hollow cylinder when supplying an induction heating flux at the outer surface and the inner surface controlled to be at constant temperature 600 °C. The temperature profiles have been drawn for different time intervals. Fig. 4.8 presents the temperature distribution through the hollow cylinder wall with time at selected radii. The maximum temperature will be at the outer surface facing the supplied heating flux and at the beginning of the time due to the heating flux shock then equalized. Also the inner radius temperature is constant matching the controlled temperature at 600 °C in the boundary conditions.

98
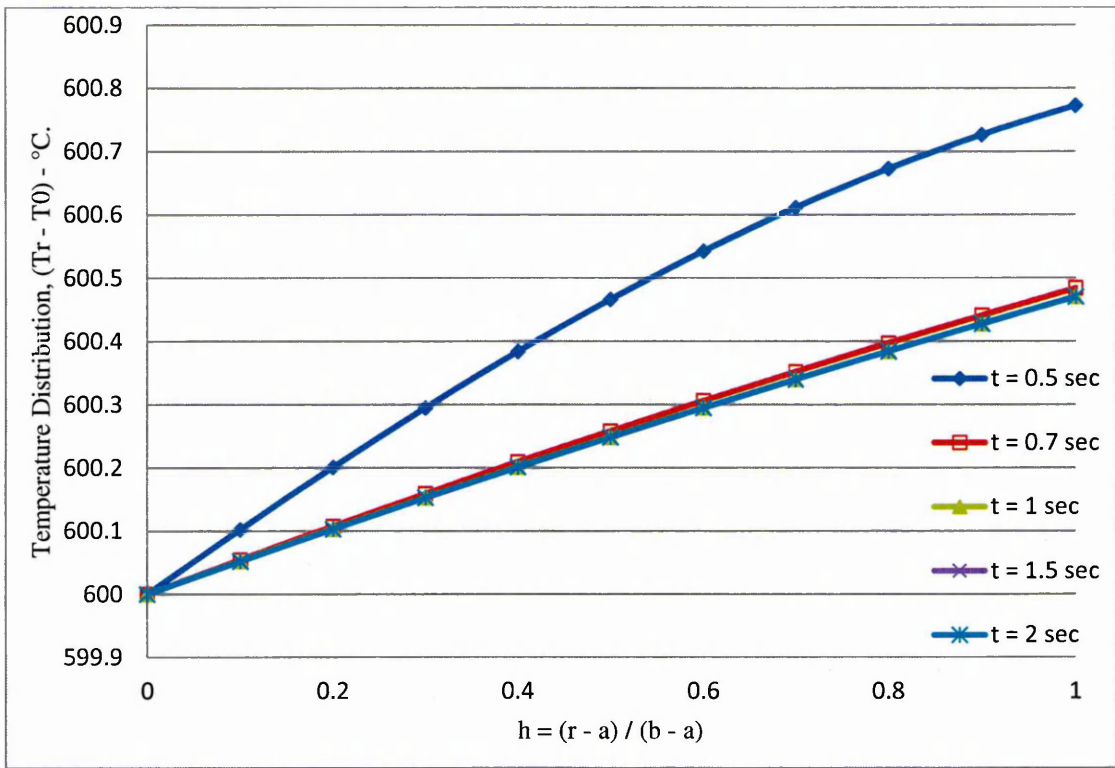
Figure 4.7 The temperature distribution through the hollow cylinder wall at different times in the heating case.
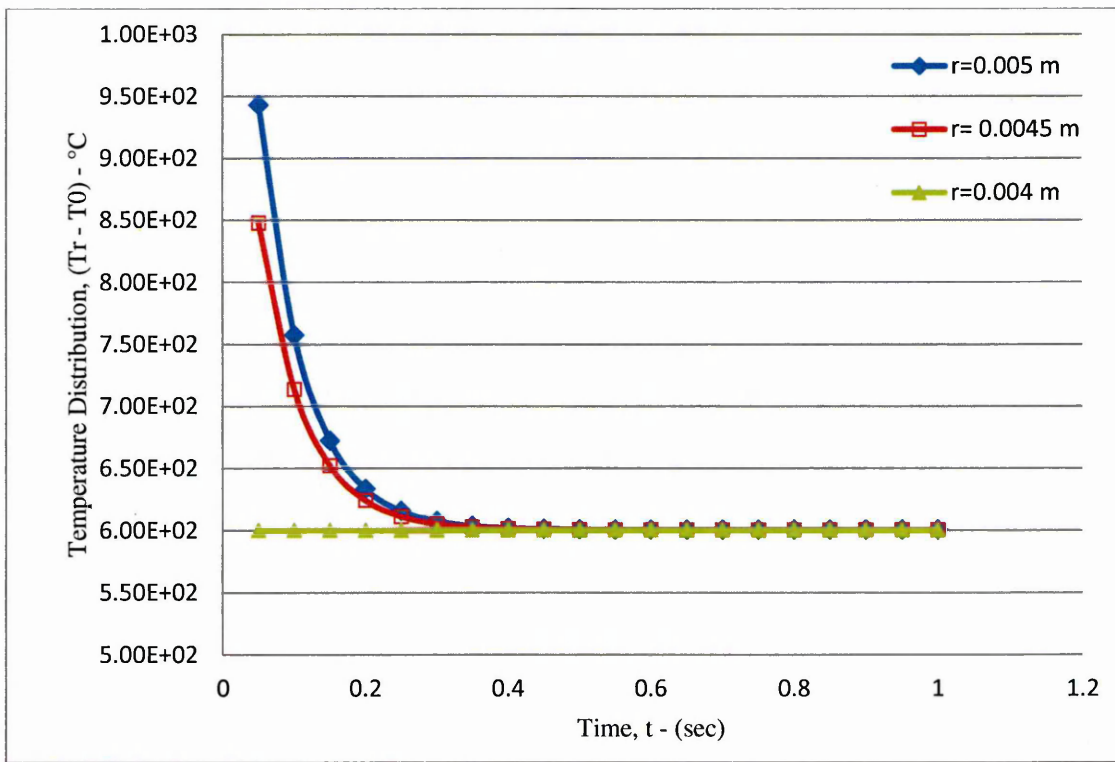
Figure 4.8 The temperature distribution through the hollow cylinder wall with time at selected radii in the heating case.

99

B- Down Shock Cooling Case:

The outer surface of the hollow cylinder will be controlled at constant temperature, and the inner surface will be down shock cooled by forced air, and the initial temperature is assumed to be at room temperature.

The initial and general boundary conditions are:

$$\frac{\partial\,\theta_{(a,t)}}{\partial r} = \frac{\partial\,T_{(a,t)}}{\partial r} = -\frac{H}{k}\,(T_a - T_{air})\qquad ,r = a\,,\ t > 0 \qquad (4.10)$$

$$\theta_{(b,t)} = T_{(b,t)} - T_0 = T_b \qquad ,r = b\ ,t > 0 \qquad (4.11)$$
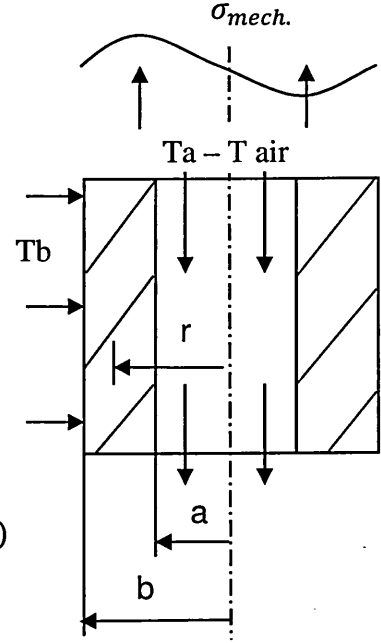
The distribution of temperature through the shell wall in this case is:

$$\theta_{(r,t)} = B_1 + B_2 \ln\frac{r}{b} + \sum_{i=1}^{\infty} B_{3i}\,[\,J_0\,(r\,\lambda_i).Y_1(a\,\lambda_i) - Y_0(r\,\lambda_i).J_1\,(a\,\lambda_i)\,] \qquad (4.12)$$

where;

H is the coefficient of surface heat transfer when the inner surface is exposed to cooling by forced air depending on the air velocity and the diameter of the pipe and B_1, B_2, B_{3i} are constant as exposed in Appendix B. Also, λ_i are the positive roots of the equation where $(i = 1, ... ,4)$, as follows:

$$[J_1\,(a\,\lambda_i)\,.\,Y_0(b\,\lambda_i) - Y_1(a\,\lambda_i)\,.J(b\,\lambda_i)\,] = 0 \qquad (4.13)$$

100
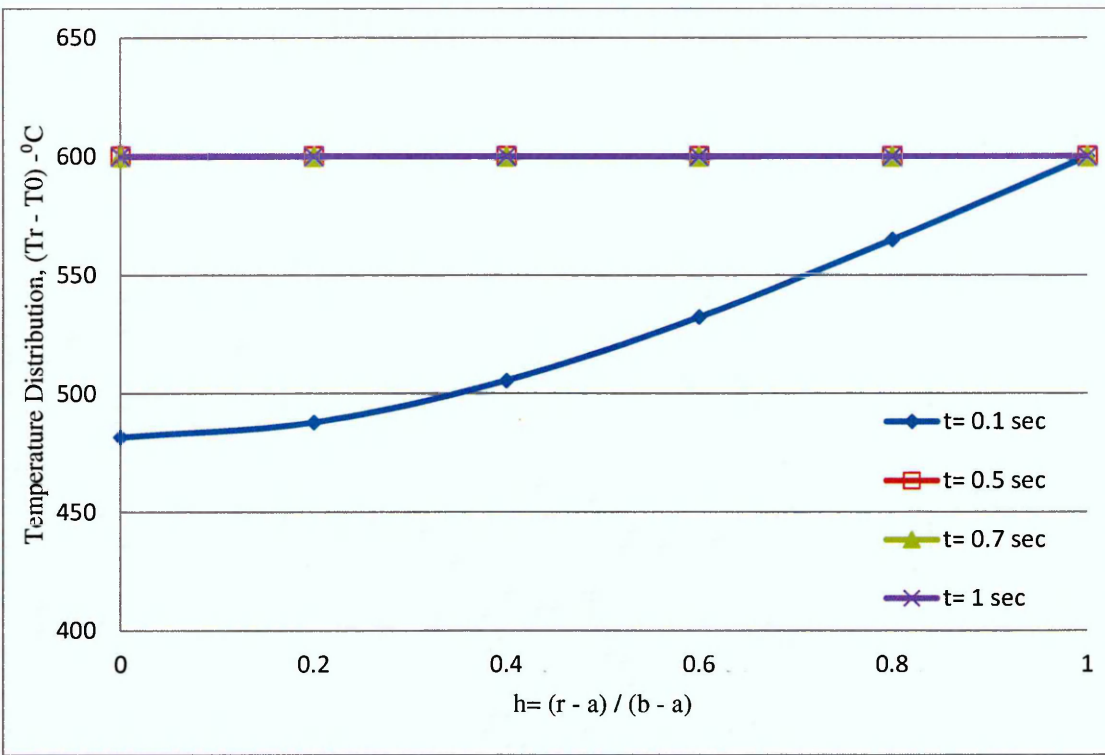
Figure 4.9 The temperature distribution through the hollow cylinder wall at different times in the down shock cooling case.
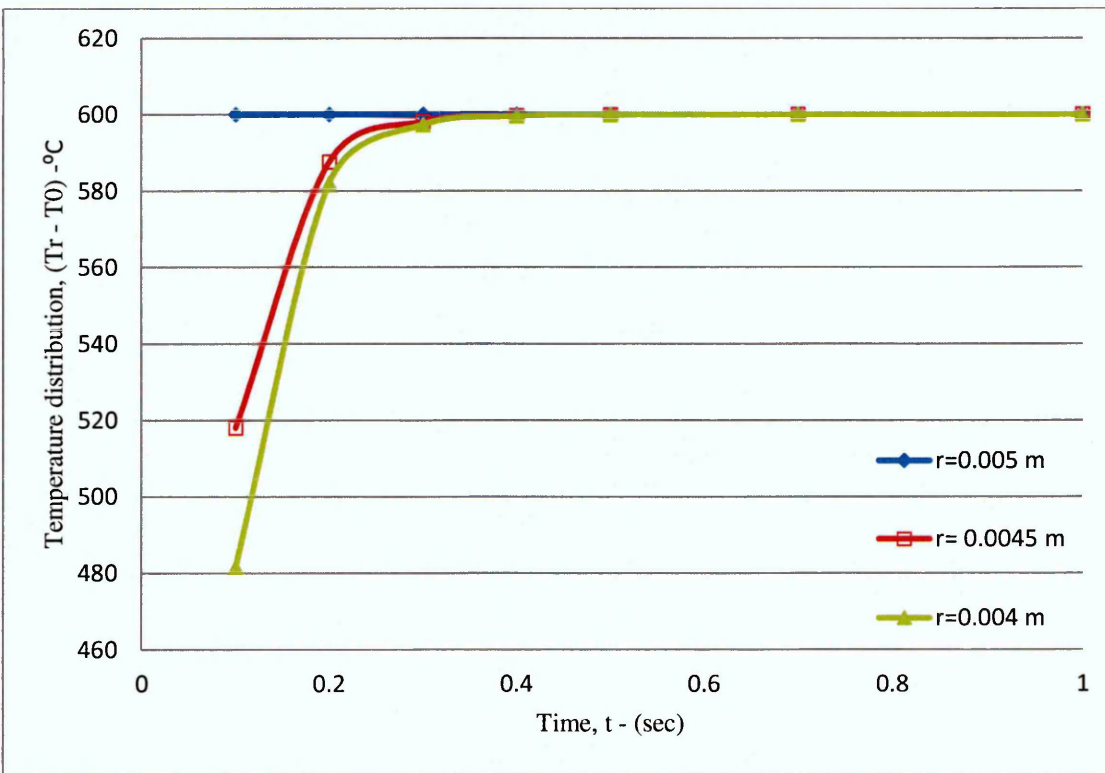
Figure 4.10 The temperature distribution through the hollow cylinder wall with time at selected radii in the down shock cooling case.

101

Fig. 4.9 illustrates the temperature distribution through the hollow cylinder wall when supplying a transient cooling at the inner surface. The temperature profiles show the decreasing path through the wall which rises with time to be steady and equal to the outer surface temperature. Fig. 4.10 illustrates the behaviour of the temperature distribution with time at selected radii. The profiles show the significant drop due to rapid cooling at 0.1 second which then achieves steady temperature with the passage of time.

4.3 Thermal Stresses Calculation:

An elastic relation for resultant thermal stresses have been established by Timoshenko and Goodier, 1970, [106]; it is later applied to long circular solid and hollow cylinders due to non-symmetrical temperature distribution under zero axial strain ($\epsilon_z = 0$).

The general thermal stresses formulas for the cylindrical region in plain strain is given by:

$$\sigma_{r-th} = \frac{\alpha E}{1 - \nu} \frac{1}{r^2} \left(\frac{r^2 - a^2}{b^2 - a^2} \int_a^b \theta_{(r,t)} \, r \, dr - \int_a^r \theta_{(r,t)} \, r dr \right). \qquad (4.14)$$

$$\sigma_{\theta-th} = \frac{\alpha E}{1 - \nu} \frac{1}{r^2} \left(\frac{r^2 + a^2}{b^2 - a^2} \int_a^b \theta_{(r,t)} \, r \, dr + \int_a^r \theta_{(r,t)} \, r \, dr - \theta_{(r,t)} . r^2 \right). \qquad (4.15)$$

$$\sigma_{z-th} = \frac{\alpha E}{1 - \nu} \left(\frac{2\nu}{b^2 - a^2} \int_a^b \theta_{(r,t)} \, r \, dr - \theta_{(r,t)} \right). \qquad (4.16)$$

where;

a = 0, at the solid cylinder case.

4.3.1 Solid Cylinder:

From the substitutions of the temperature distribution of the solid cylinder case in the general formulas, the thermal stress estimation is given below; useful integration details are shown in Appendix B.

$$\sigma_{r-th} = \frac{\alpha \, E \, T_b}{1-v} \cdot \sum_{i=1}^{\infty} \frac{C1}{\lambda_i} \cdot \left[\frac{J_1(r.\lambda_i)}{r} - \frac{J_1(a.\lambda_i)}{b} \right]. \tag{4.17}$$

$$\sigma_{\theta-th} = \frac{\alpha \, E \, T_b}{1-v} \cdot \sum_{i=1}^{\infty} \frac{C1}{\lambda_i} \cdot \left[\lambda_i \cdot J_0(r.\lambda_i) - \frac{J_1(r.\lambda_i)}{r} - \frac{J_1(a.\lambda_i)}{b} \right]. \tag{4.18}$$

$$\sigma_{z-th} = -\alpha \, E \, T_b \cdot \left[1 + \frac{1}{1-v} \sum_{i=1}^{\infty} \frac{C1}{\lambda_i} \cdot \left[\frac{2v}{b} \cdot J_1(a.\lambda_i) - \lambda_i \cdot J_0(r.\lambda_i) \right] \right]. \tag{4.19}$$

where;

$$C1 = \frac{2}{b} \cdot e^{-D \lambda_i^2 t} \frac{1}{\lambda_i \cdot J_1(b.\lambda_i)}. \tag{4.20}$$

Figs. 4.11 to 4.13 show the thermal radial stress distribution through the solid cylinder wall at different time intervals. The profiles show the maximum tension stress in the position close to the centre line, for the cylinder; it is reduced rapidly with time reaching zero which is equal to the outer surface stress. Additionally, the higher supplied temperature gives higher thermal radial stress in the core of the cylinder. The profiles of the thermal radial stress distribution along with time taken at different selected radii, show that the maximum tension stress at the radius closes to the cylinder centre line (r = 0 m) and rapidly decreases with time reaching to zero. Also, at the outer surface, the radial stress is constant, equal to zero, as shown in Figs. 4.14 to 4.16.
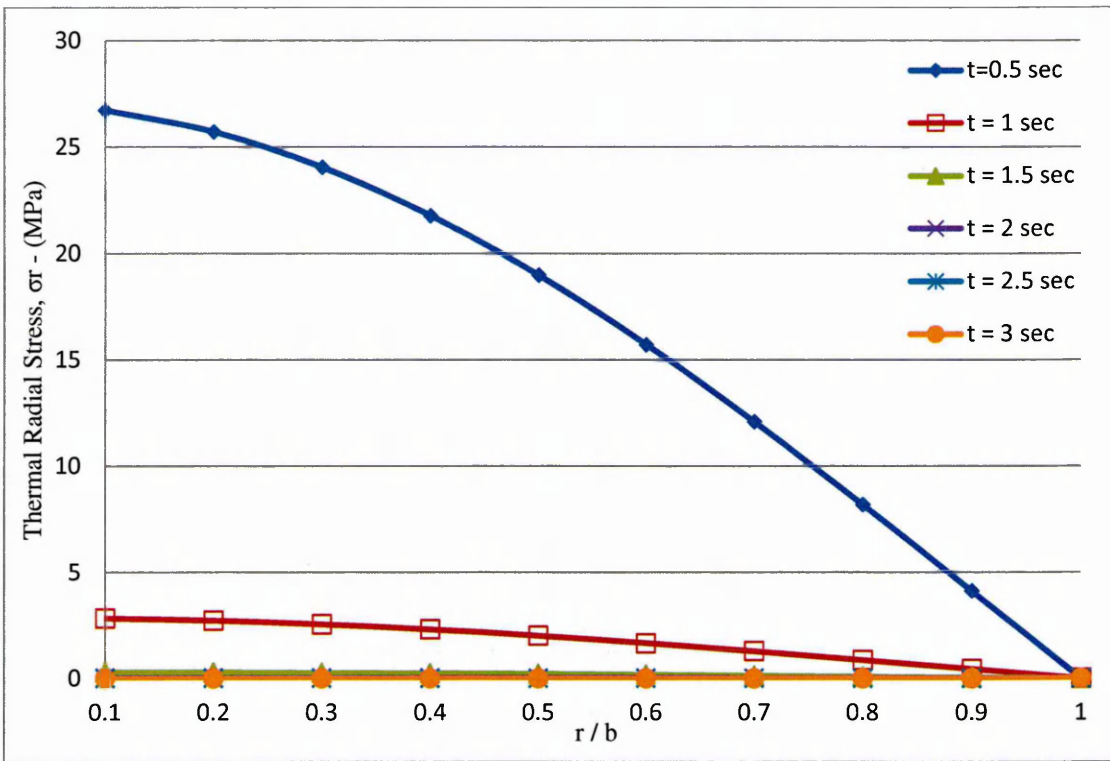
Figure 4.11 The thermal radial stress distribution through the solid cylinder wall at different times by supplying Tb = 300 °C.
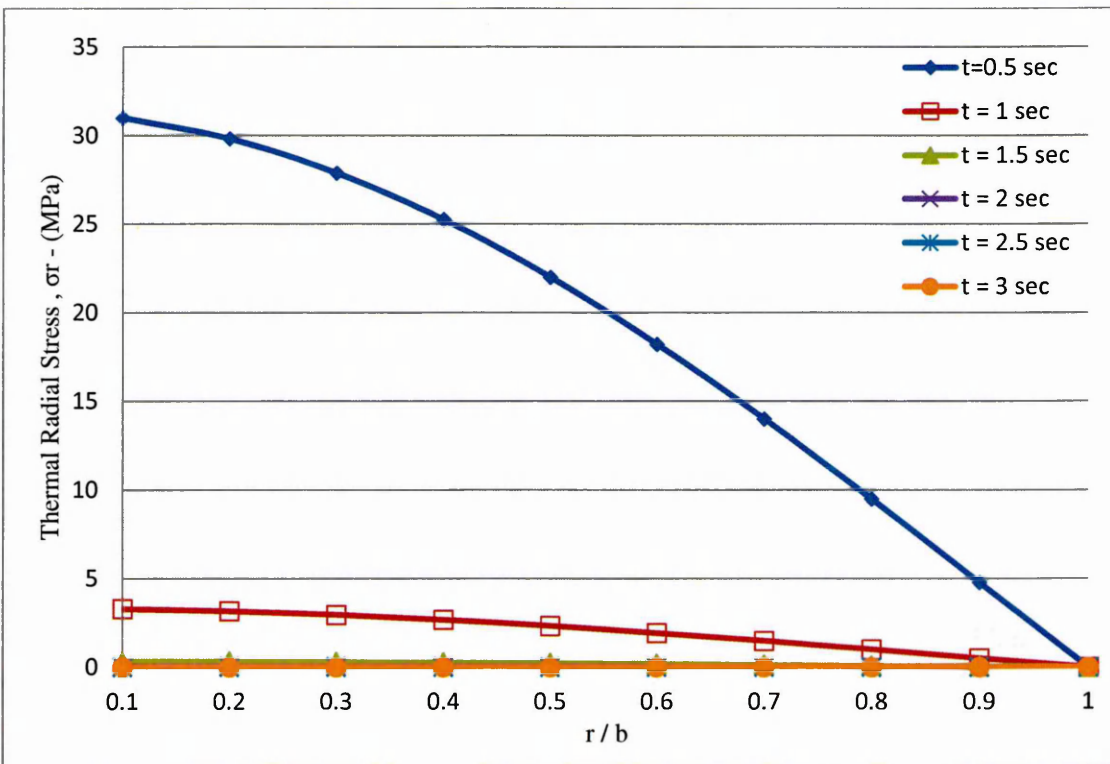
Figure 4.12 The thermal radial stress distribution through the solid cylinder wall at different times by supplying Tb = 500 °C.

104
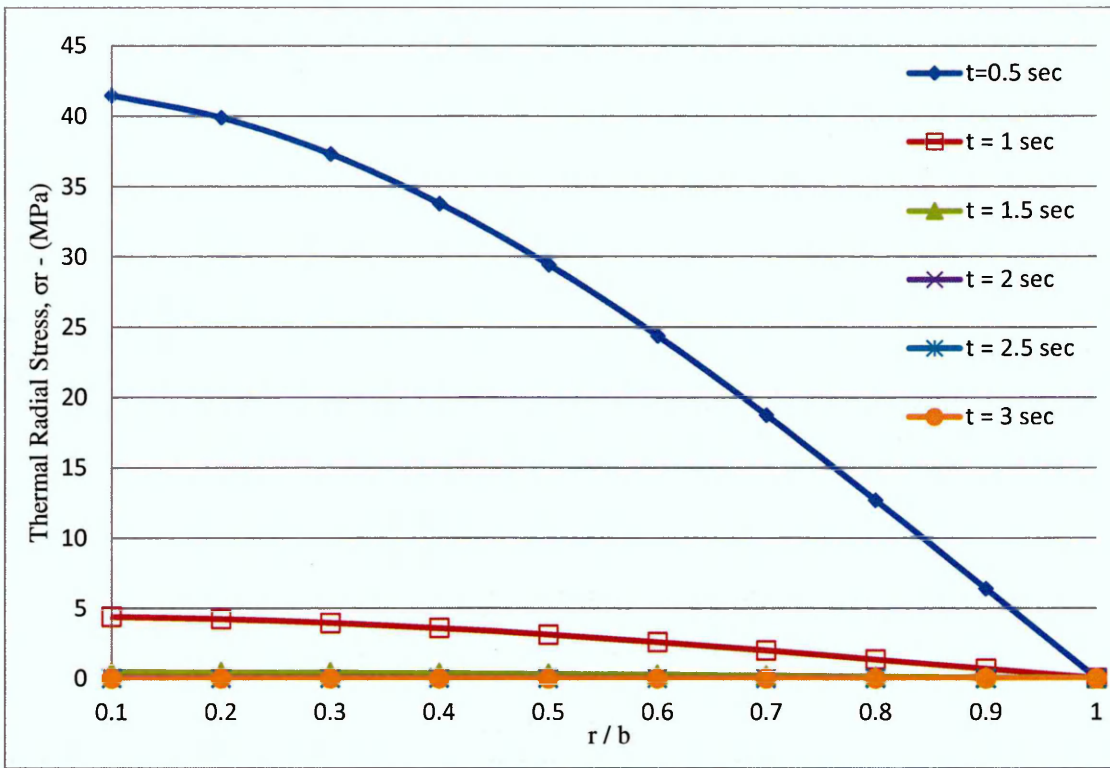
Figure 4.13 The thermal radial stress distribution through the solid cylinder wall at different times by supplying Tb = 600 °C.
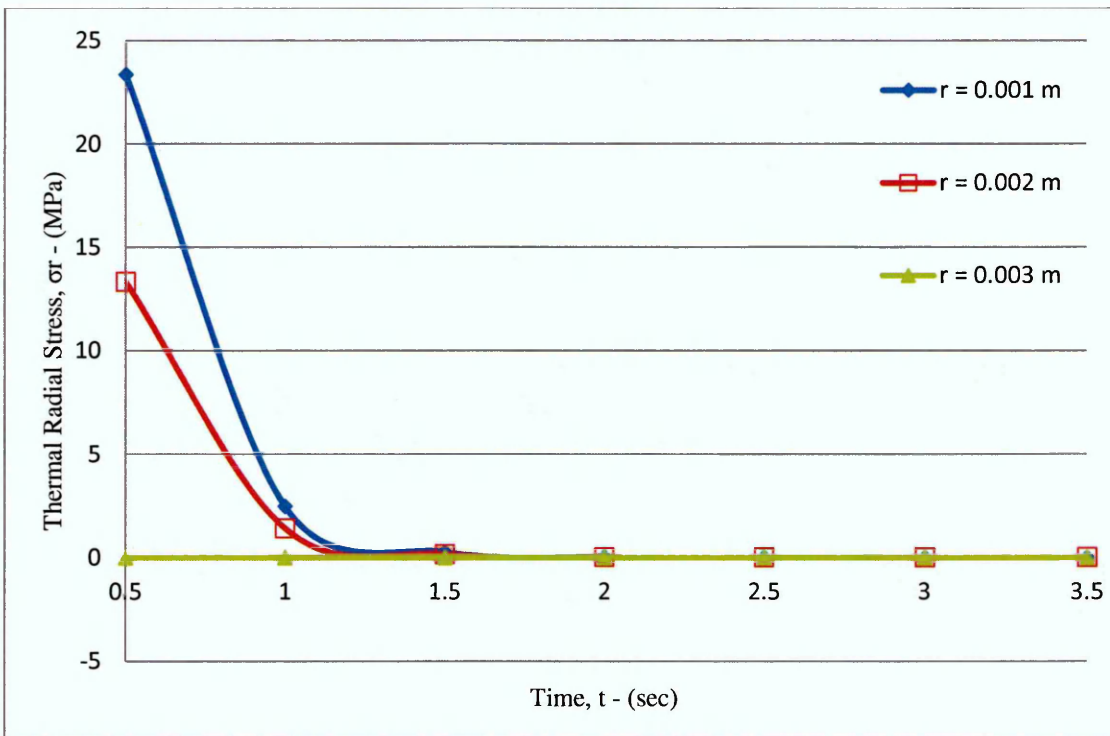
Figure 4.14 The thermal radial stress distribution in the solid cylinder with time at selected radii by supplying Tb = 300 °C.
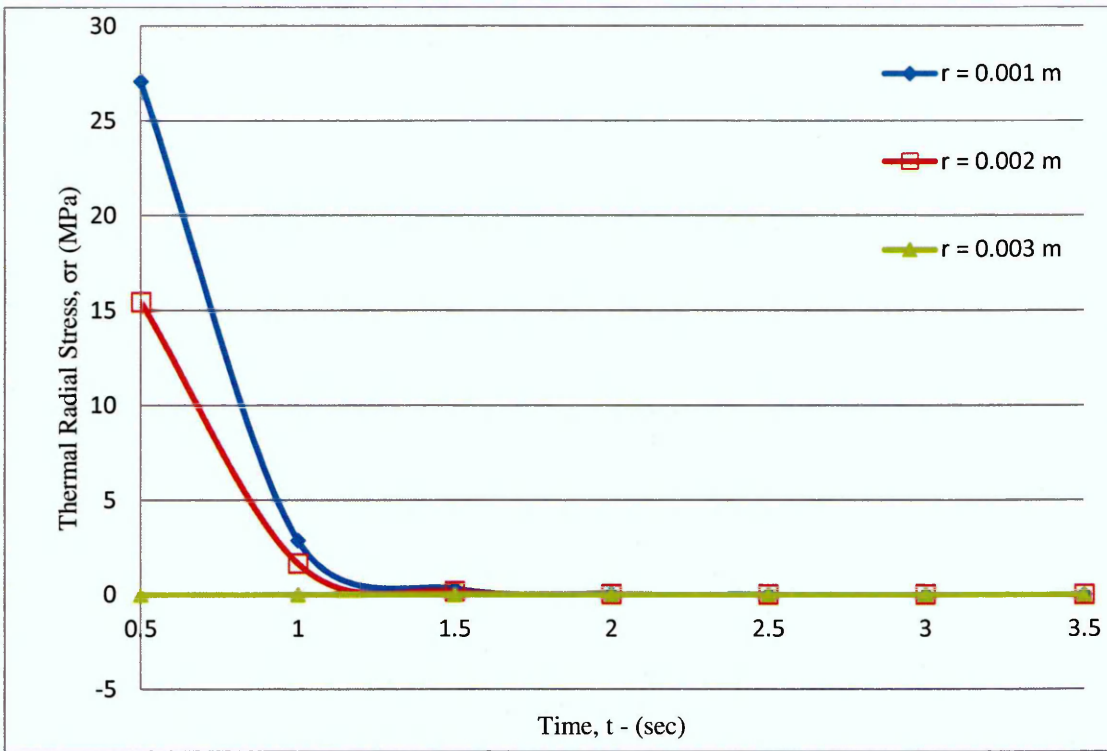
Figure 4.15 The thermal radial stress distribution in the solid cylinder with time at selected radii by supplying Tb = 500 °C.
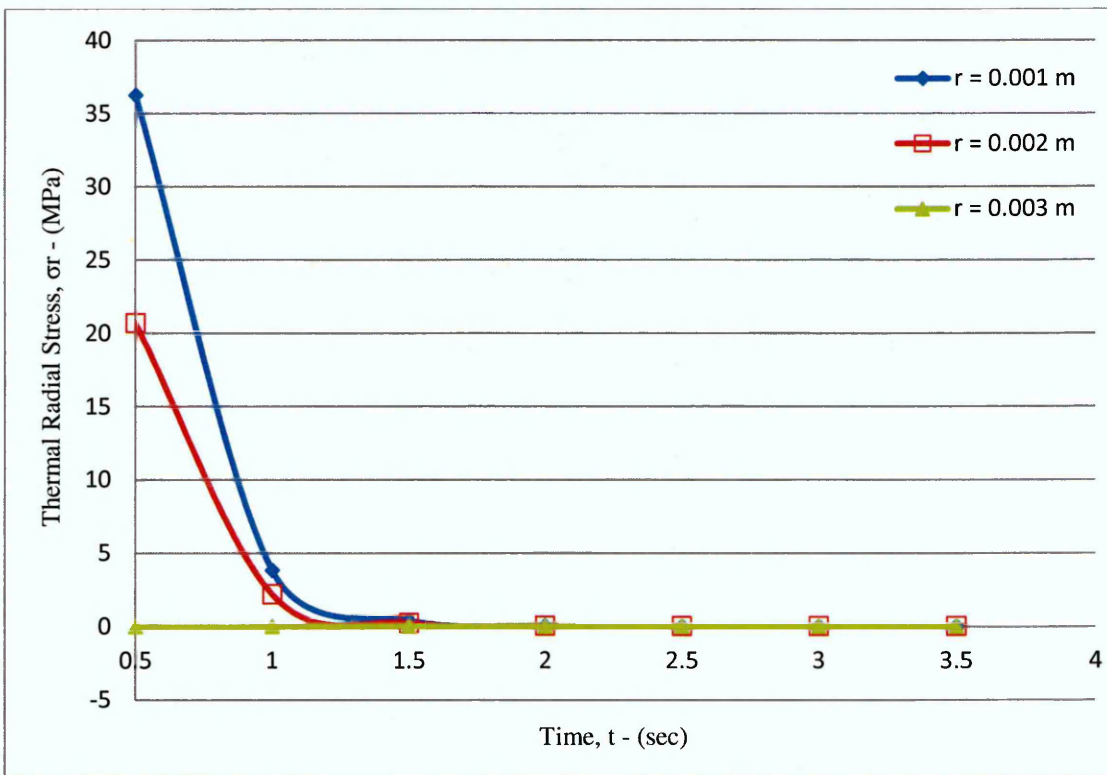
Figure 4.16 The thermal radial stress distribution in the solid cylinder with time at selected radii by supplying Tb = 600 °C.

106

Figs. 4.17 to 4.19 show the thermal hoop stress through the solid cylinder wall at different time intervals. The curves show that at (r/b = 0.54), it is equal to zero at all times, which is an inversion point, the tension stress below the point, the maximum tension hoop stress closes with the centre line (at the centre line goes to infinity) and over the point, the compression stress, where the maximum compression stress was at the outer surface. This stresses were reduced suddenly with time reaching zero. Also, the higher supplied temperature gives the higher tension and compression stress. The curves path is clearer when the thermal hoop stress distribution is drawn with time at selected radii, it then represents the compression stresses at the outer radius (r = 0.003 m), also at (r = 0.002 m) which are over the inversion point; the tension stress at the radius closes to the cylinder centre line, then all are reduced rapidly with time reaching zero during 2 seconds, as shown in Figs. 4.20 to 4.22.
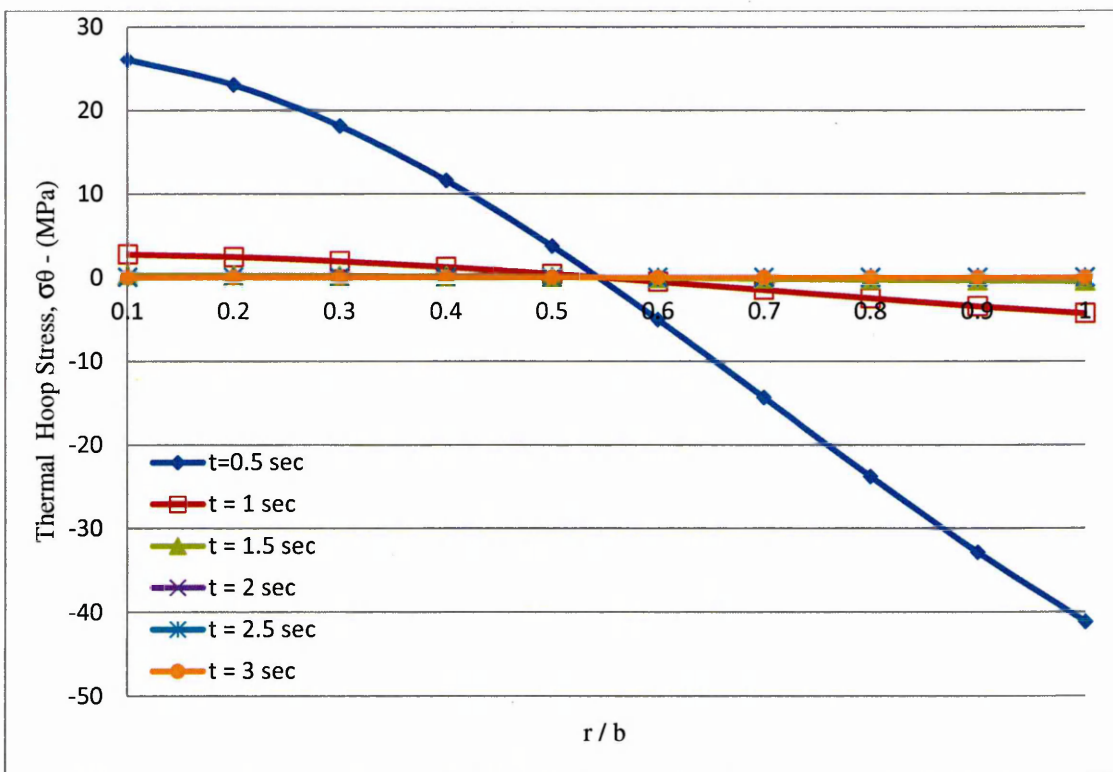
Figure 4.17 The thermal hoop stress distribution through the solid cylinder wall at different times by supplying Tb = 300 °C.
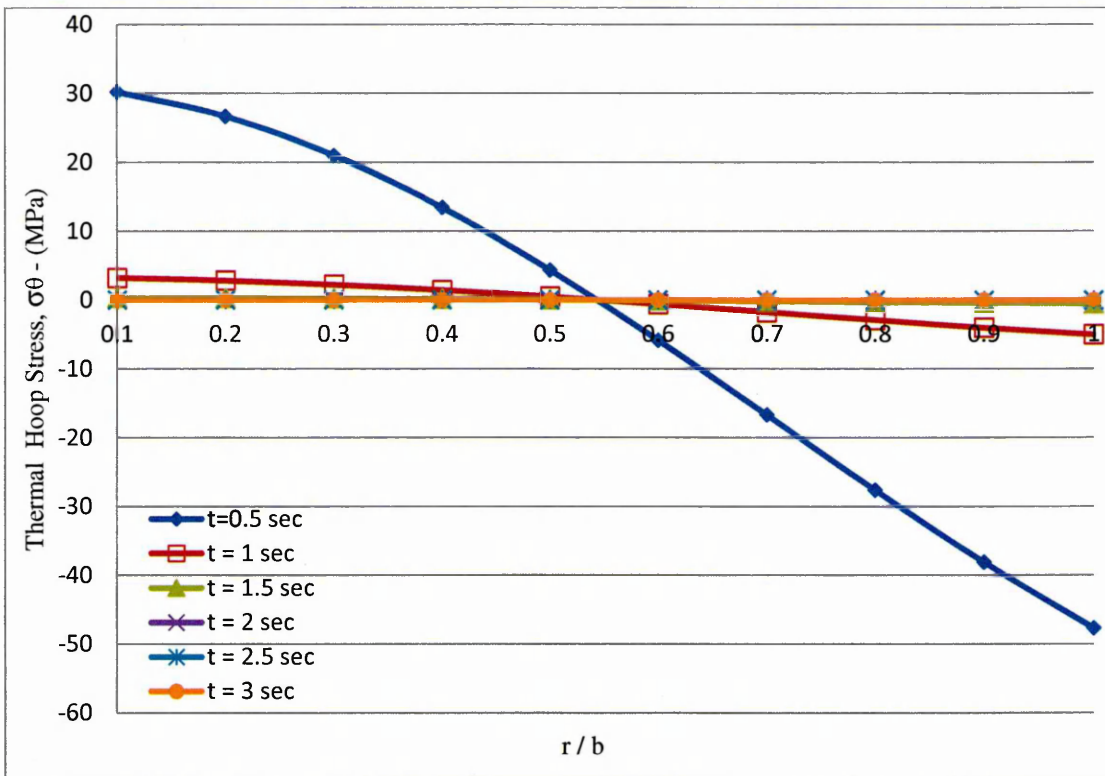
Figure 4.18 The thermal hoop stress distribution through the solid cylinder wall at different times by supplying Tb = 500 °C.
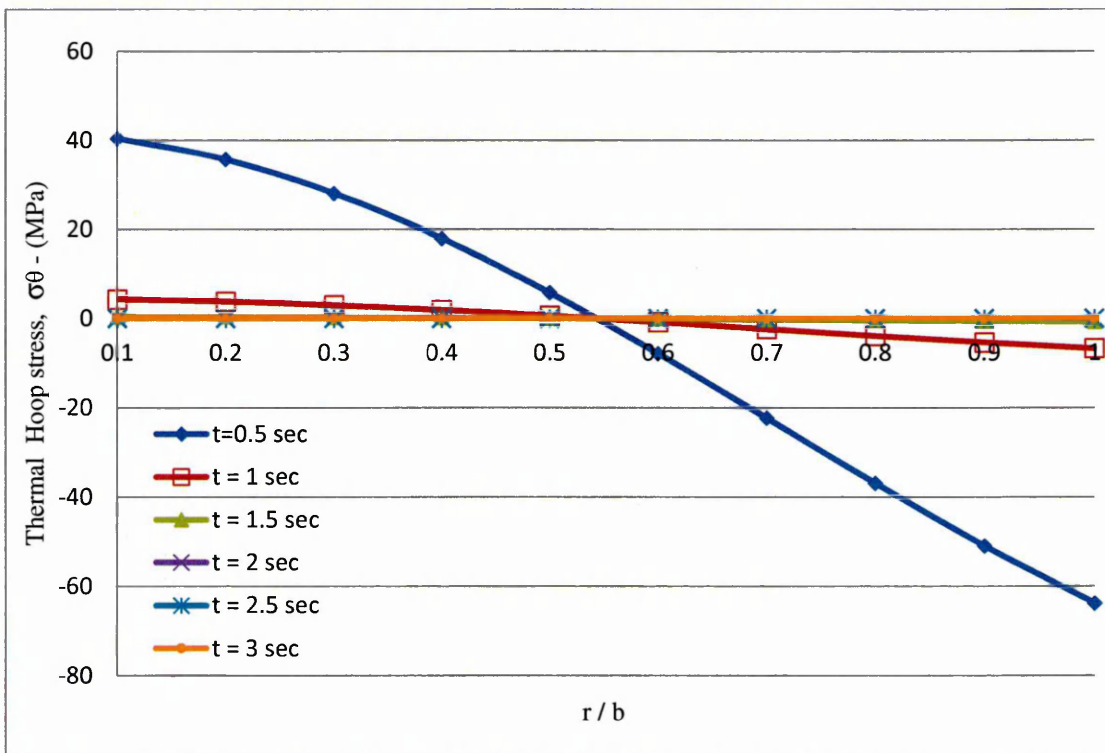
Figure 4.19 The thermal hoop stress distribution through the solid cylinder wall at different times by supplying Tb = 600 °C.
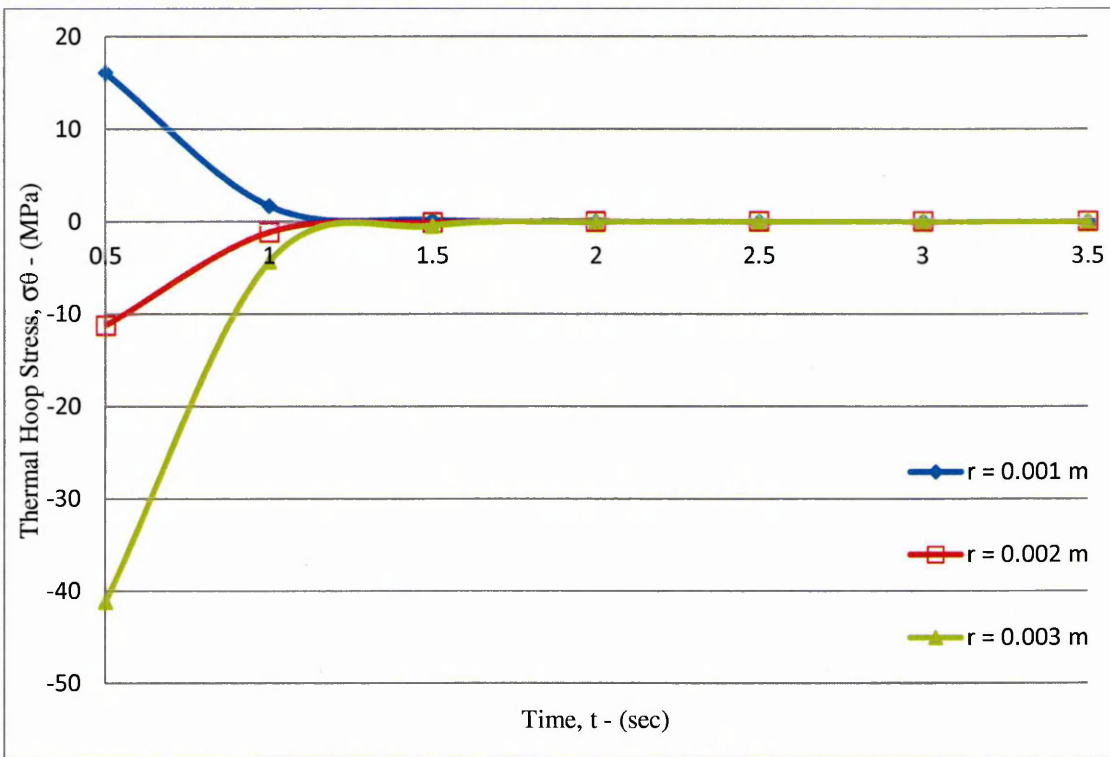
Figure 4.20 The thermal hoop stress distribution in the solid cylinder with time at selected radii by supplying Tb = 300 °C.
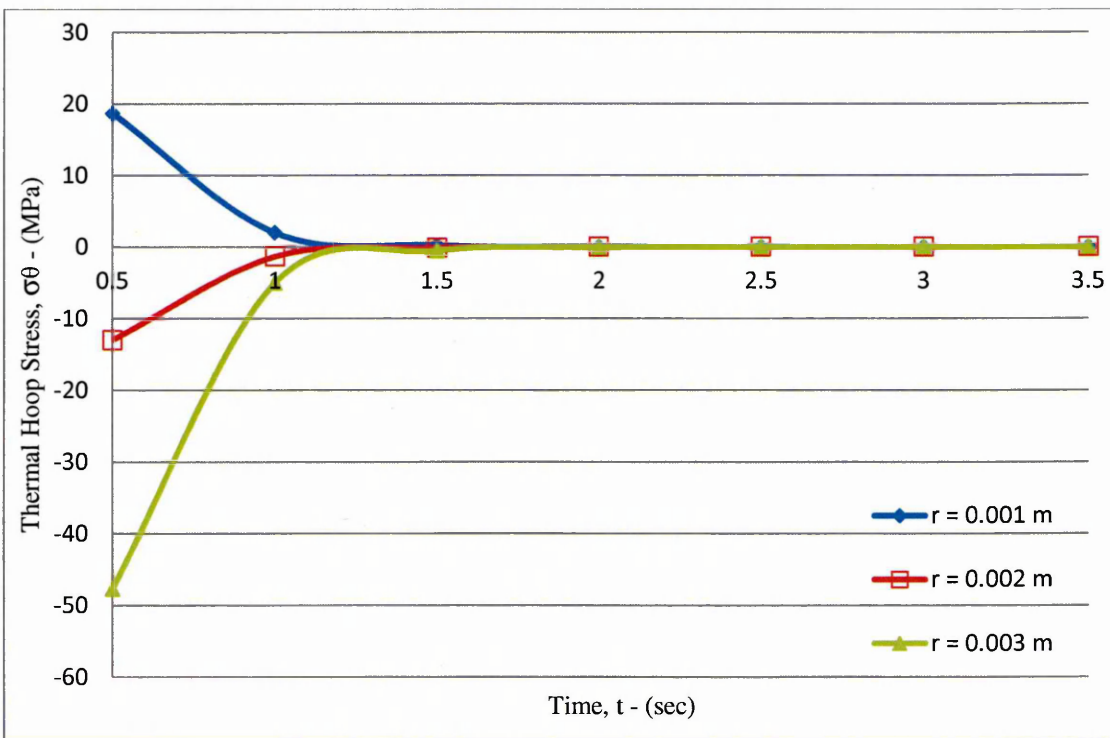
Figure 4.21 The thermal hoop stress distribution in the solid cylinder with time at selected radii by supplying Tb = 500 °C.

109
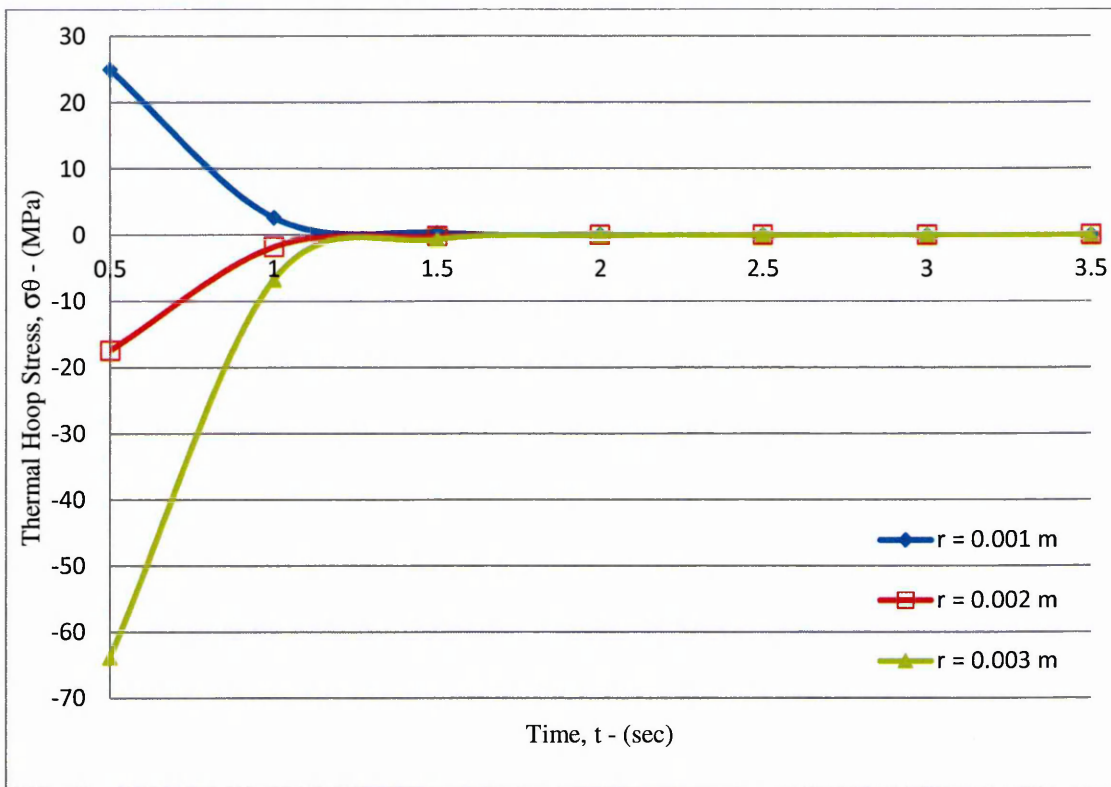
Figure 4.22 The thermal hoop stress distribution in the solid cylinder with time at selected radii by supplying Tb = 600 °C.

The thermal axial stress distribution behaviours are similar to the hoop stresses but all are in compression and the inversion point is shifted to (r/b = 0.9). The minimum stress approaches the cylinder centre line and above the point is the maximum compression stress at the outer surface. Likewise, the higher outer surface supplied temperature increased in the axial stresses (shift the curves up), as shown in Figs. 4.23 to 4.25. In Figs. 4.26 to 4.28, the thermal axial stresses profiles are drawn against time to present clearly the behaviours of the stresses at different radii and the rapid reduction during 2 seconds to the steady state stress equal to (-E α Tb).
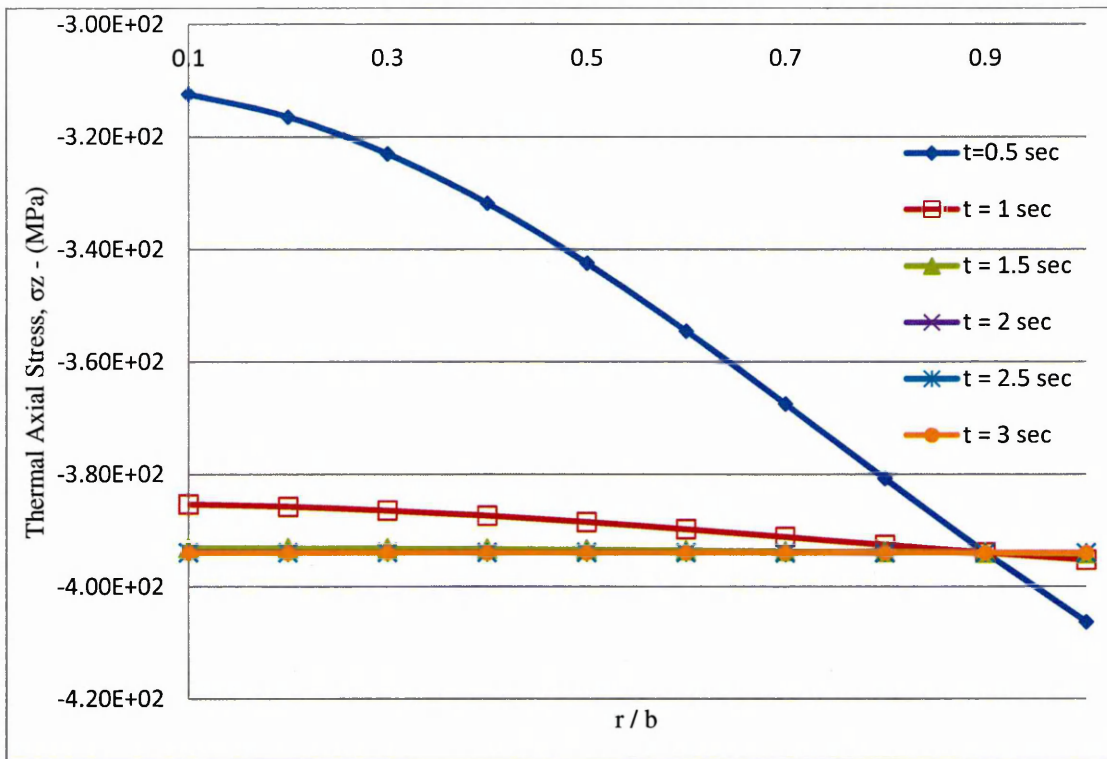
Figure 4.23 The thermal axial stress distribution through the solid cylinder wall at different times by supplying Tb = 300 °C.
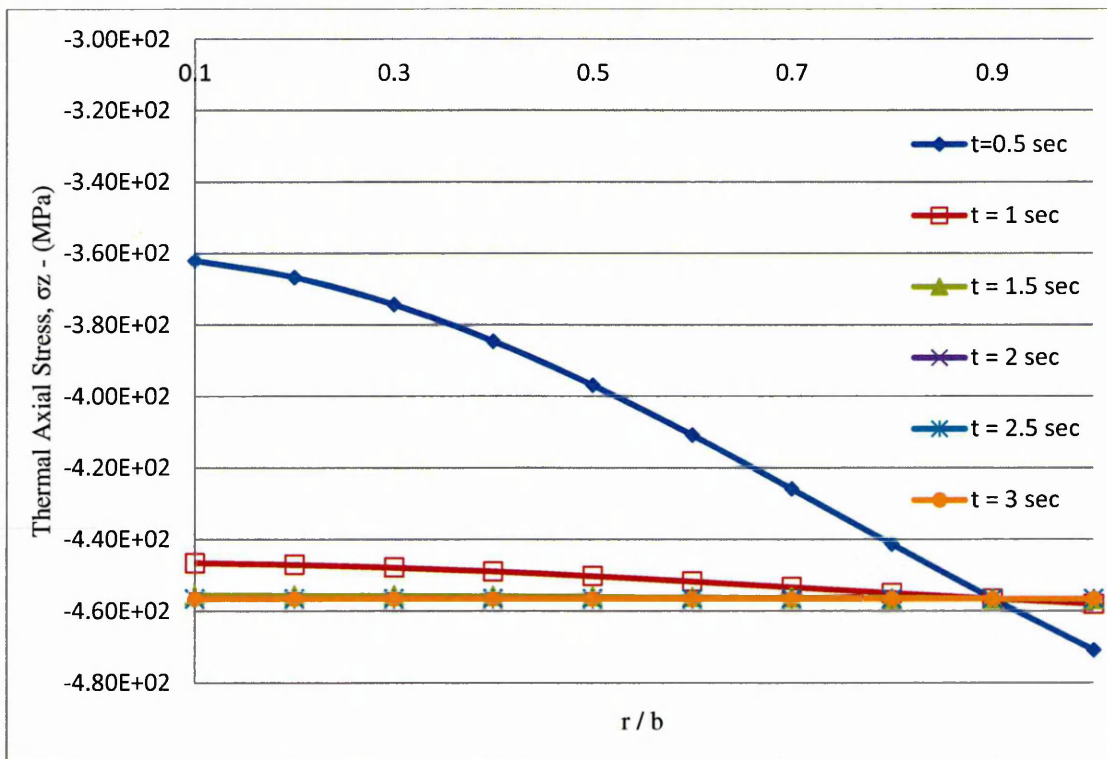
Figure 4.24 The thermal axial stress distribution through the solid cylinder wall at different times by supplying Tb = 500 °C.
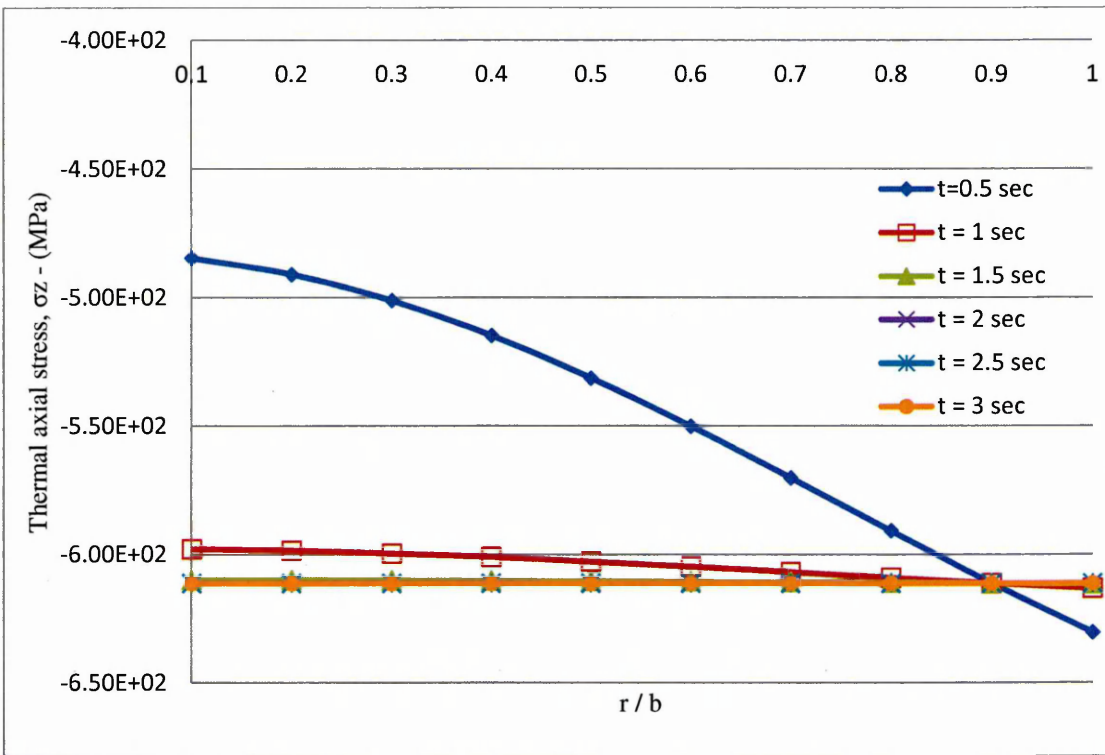
Figure 4.25 The thermal axial stress distribution through the solid cylinder wall at different times by supplying Ta = 600 °C.
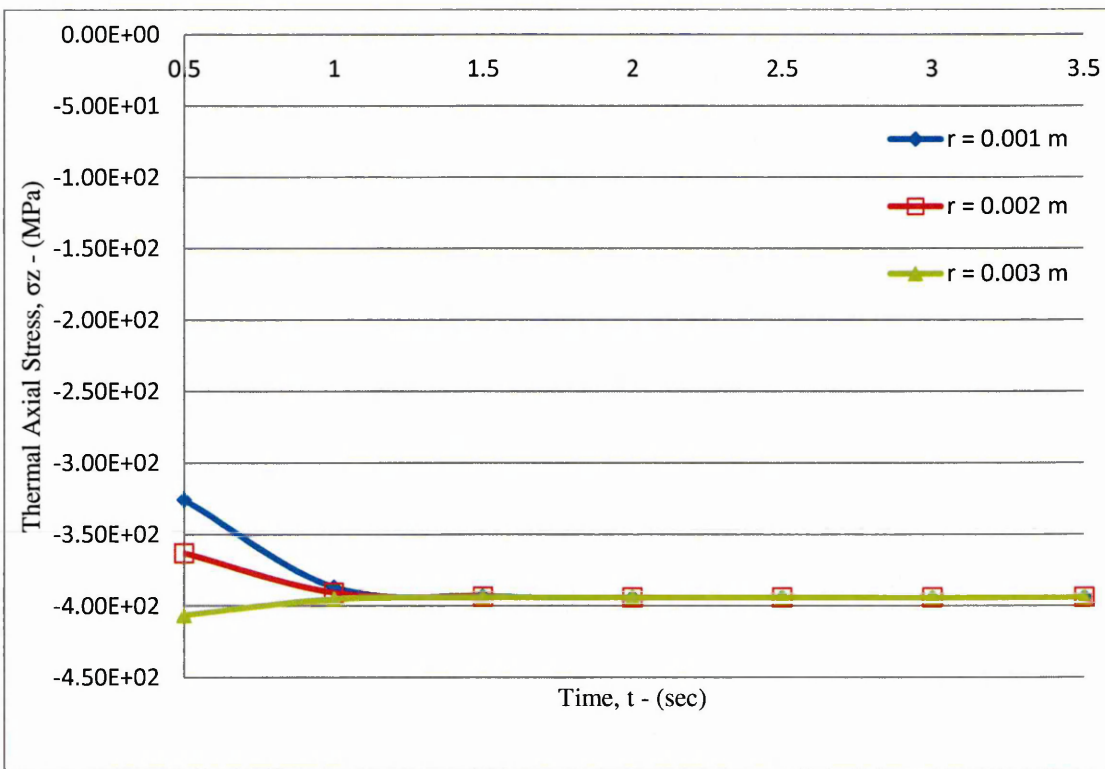
Figure 4.26 The thermal axial stress distribution in the solid cylinder with time at selected radii by supplying Tb = 300 °C.

112
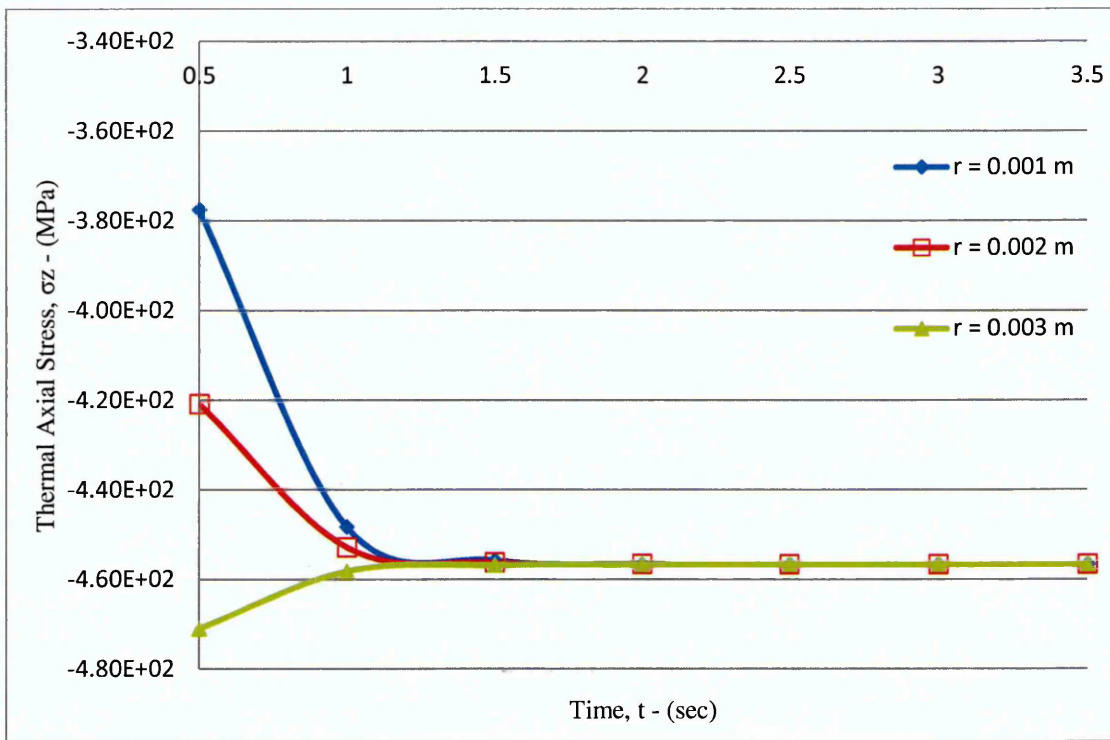
Figure 4.27 The thermal axial stress distribution in the solid cylinder with time at selected radii by supplying Tb = 500 °C.
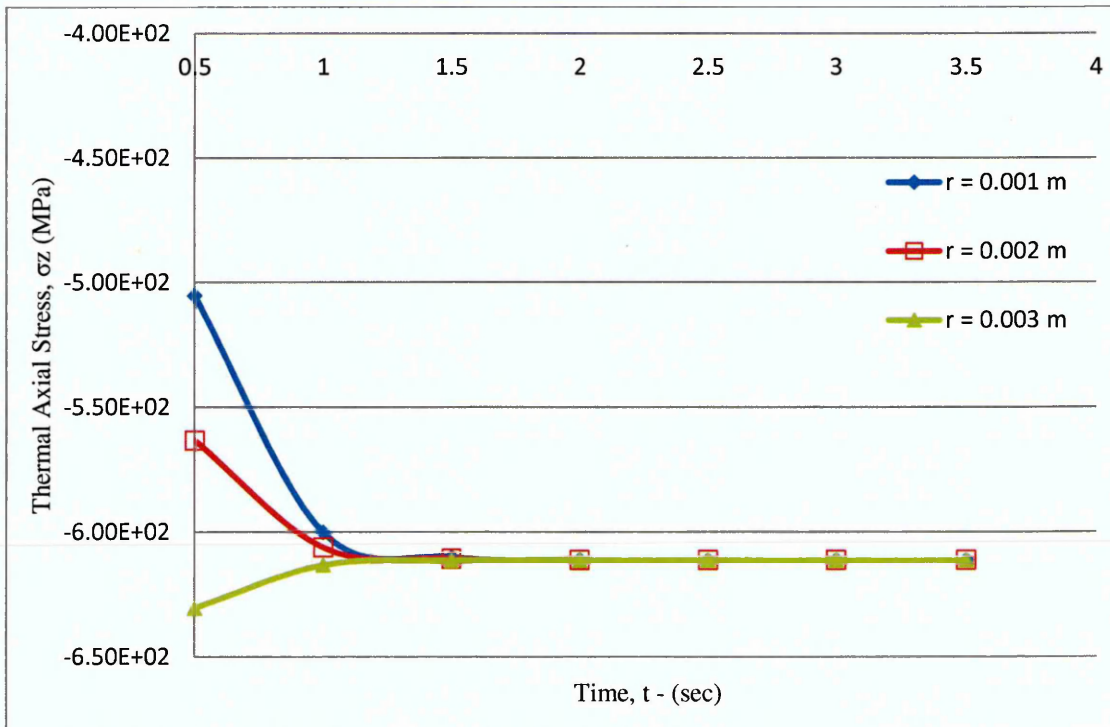
Figure 4.28 The thermal axial stress distribution in the solid cylinder with time at selected radii by supplying Tb = 600 °C.

113

4.3.2 Hollow Cylinder model:

A- Heating or re-heating Case:

The temperature distribution equation is divided into three parts, as

$$
\left.\begin{aligned}
T_1 &= A_1 \\[2mm]
T_2 &= A_2 \ln\frac{r}{a} \\[2mm]
T_3 &= A_{3i}\left[J_0\,(r\,\lambda_i).Y_0(a\,\lambda_i) - Y_0(r\,\lambda_i).J_0(a\,\lambda_i)\right]
\end{aligned}\right\} \tag{4.21}
$$

By the substitutions of the divisions in the general formulas of the thermal stress estimation; it is solved alone as shown below. The useful integration details are shown in Appendix B.

For the radial stress is:

$$
\sigma_{r1} = 0 \tag{4.22}
$$

$$
\sigma_{r2} = \frac{\alpha\,E\;A_2}{2\,r^2(b^2 - a^2).(1 - v)}\left[r^2(b^2 \ln\frac{b}{r} + a^2 \ln\frac{r}{a}) + a^2 b^2 \ln\frac{a}{b}\right] \tag{4.23}
$$

$$
\sigma_{r3} = \frac{\alpha\,E\;A_{3i}}{\lambda_i\,r^2\,(1 - v)}\left[J_0\,(a\,\lambda_i)\left\{\frac{b(r^2 - a^2)}{(b^2 - a^2)}.Y_1(b\,\lambda_i) - r.Y_1(r\,\lambda_i)\right\}\right.
$$

$$
+ Y_0(a\,\lambda_i)\left\{ r\,J_1\,(r\,\lambda_i) - \frac{b(r^2 - a^2)}{(b^2 - a^2)}\;J_1\,(b\,\lambda_i)\right\}
$$

$$
\left.+ \frac{2}{\pi\,\lambda_i}.\frac{(b^2 - r^2)}{(b^2 - a^2)}\right] \tag{4.24}
$$

114

The final radial stress for the heating case is given by:

$$\sigma_r = \sigma_{r1} + \sigma_{r2} + \sigma_{r3} \tag{4.25}$$

The hoop stress is:

$$\sigma_{\theta 1} = 0 \tag{4.26}$$

$$\sigma_{\theta 2} = \frac{\alpha E A_2}{2 r^2 (b^2 - a^2).(1 - v)} \left[r^2 \left\{ b^2 (\ln\frac{b}{r} - 1) + a^2 (\ln\frac{r}{a} + 1) \right\} \right.$$
$$\left. + a^2 b^2 \ln\frac{b}{a} \right] \tag{4.27}$$

$$\sigma_{\theta 3} = \frac{\alpha E A_{3i}}{r^2 (1-v)} \left[J_0 (a \lambda_i) \left\{ \frac{b(r^2 + a^2)}{\lambda_i(b^2 - a^2)} . Y_1(b \lambda_i) - \frac{r}{\lambda_i} . Y_1(r \lambda_i) + r^2 Y_0(r \lambda_i) \right\} \right.$$
$$- Y_0(a \lambda_i) \left\{ \frac{r}{\lambda_i} J_1 (r \lambda_i) + \frac{b(r^2 + a^2)}{\lambda_i(b^2 - a^2)} J_1 (b \lambda_i) \right.$$
$$\left. + \frac{r}{\lambda_i} . J_1 (r \lambda_i) r^2 J_0 (r \lambda_i) \right\} - \frac{2}{\pi \lambda_i^2} . \frac{(b^2 + r^2)}{(b^2 - a^2)} \right] \tag{4.28}$$

The final hoop stress for the heating case is given by:

$$\sigma_\theta = \sigma_{\theta 1} + \sigma_{\theta 2} + \sigma_{\theta 3} \tag{4.29}$$

For the longitudinal stress, it is:

$$\sigma_{z1} = - \alpha E A_1 \tag{4.30}$$

$$\sigma_{z2} = \frac{\alpha E A_2}{(1 - v)} \left[\frac{v}{(b^2 - a^2)} \{b^2 \ln b - a^2 \ln a\} + (1 - v) \ln a - \ln r - \frac{v}{2} \right] \tag{4.31}$$

$$\sigma_{z3} = \frac{\alpha E A_{3i}}{(1 - v)} \left[J_0(a \lambda_i) \left\{ \frac{2 v b}{\lambda_i (b^2 - a^2)} \cdot Y_1(b \lambda_i) + Y_0(r \lambda_i) \right\} \right.$$
$$- Y_0(a \lambda_i) \left\{ \frac{2 v b}{\lambda_i (b^2 - a^2)} J_1(b \lambda_i) + J_0(r \lambda_i) \right\}$$
$$\left. - \frac{4 v}{\pi \lambda_i^2 (b^2 - a^2)} \right] \tag{4.32}$$

The final longitudinal stress for the heating case is given by:

$$\sigma_z = \sigma_{z1} + \sigma_{z2} + \sigma_{z3} \tag{4.33}$$

During the heating case of the hollow cylinder, Fig. 4.29 shows the thermal radial stress distribution through the hollow cylinder wall drawn at different periods. The stress profiles illustrate the maximum compression stress at the inner surface equalized to zero at the outer surface. With time, there is a rapid rise reaching zero at the inner surface and changed to maximum tension stress in the middle of the hollow cylinder wall. Also at the present, the thermal radial stress distribution behaviour with time at selected radii is presented in Fig. 4.30, which indicates that the maximum compression stress at the inner radius goes to zero with 1 second. Figs. 4.31 and 4.32 display the thermal hoop stress distribution drawing varying with position through the wall and time. The stress profiles illustrate that the maximum tensile stress occurred at the inner surface turned to compression stress at the outer surface; it is rapidly reduced to be steady-state profile at 1 second. The thermal axial stress distribution with radius and time is shown in Figs. 4.33 and 4.34. The figures are all in a compression mode; the maximum stress occurred at the outer surface in the beginning; with time, arrived to a steady-state profile through the hollow cylinder wall.
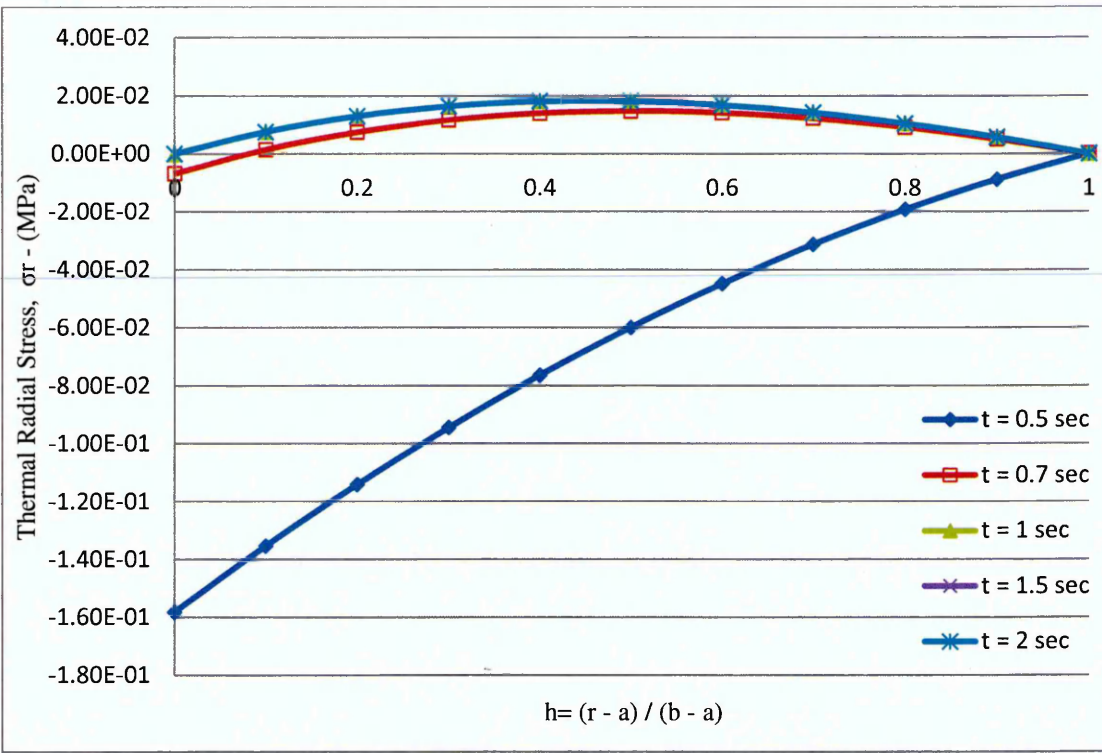
Figure 4.29 The thermal radial stress distribution through the hollow cylinder wall at different times in the heating case.
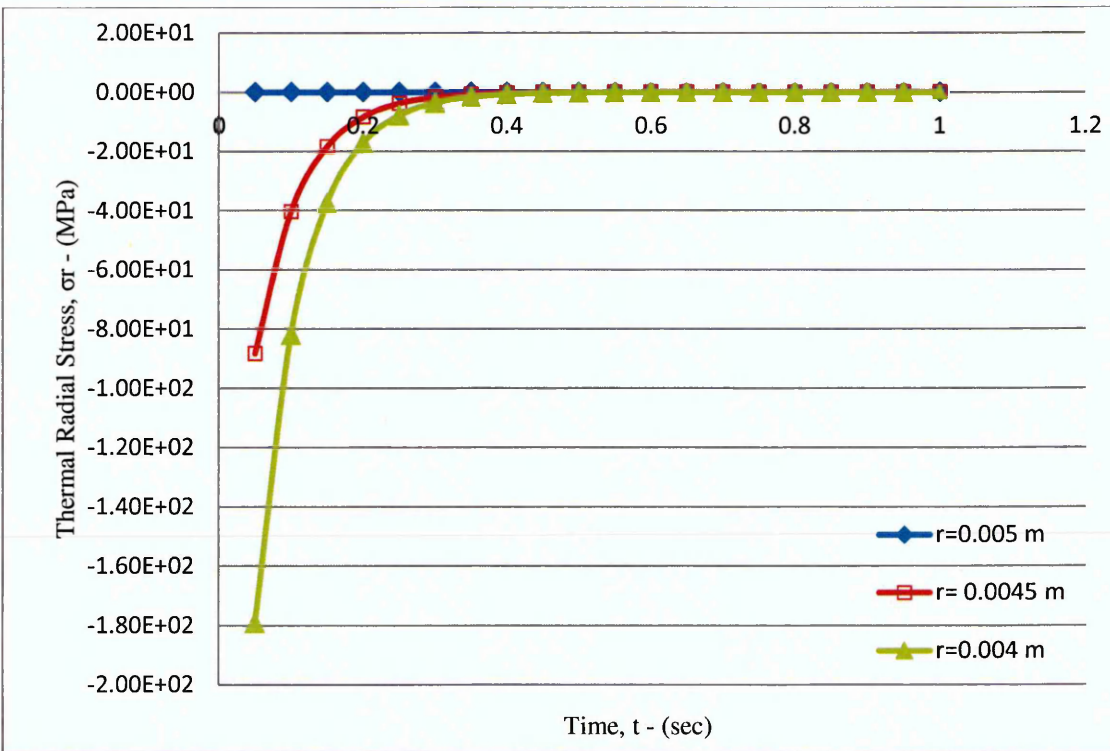
Figure 4.30 The thermal radial stress distribution with time at selected radii in the hollow cylinder heating case.

117
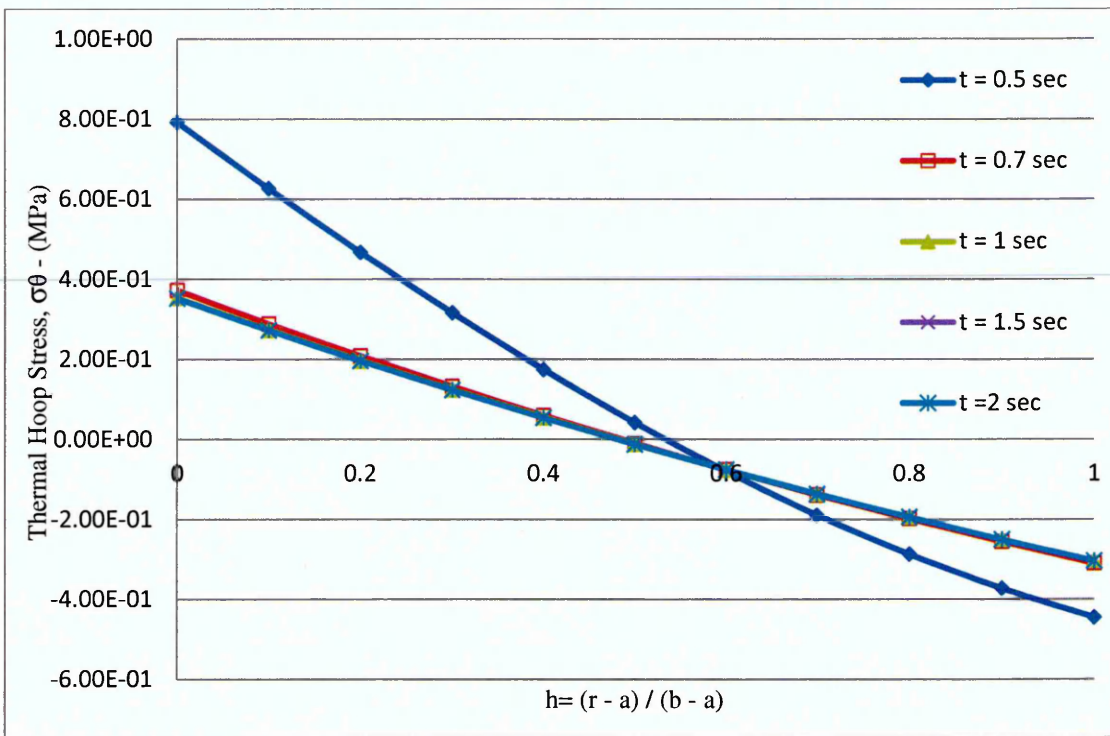
Figure 4.31 The thermal hoop stress distribution through the hollow cylinder wall at different times in the heating case.
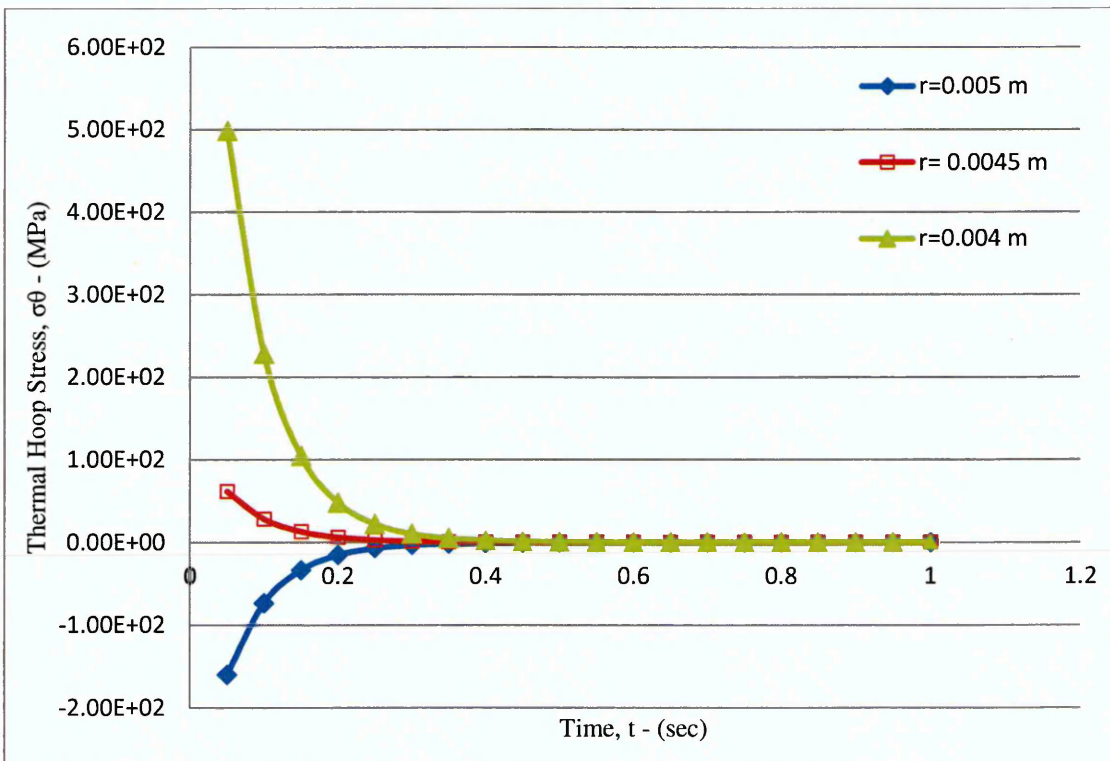
Figure 4.32 The thermal hoop stress distribution with time at selected radii in the hollow cylinder heating case.

118
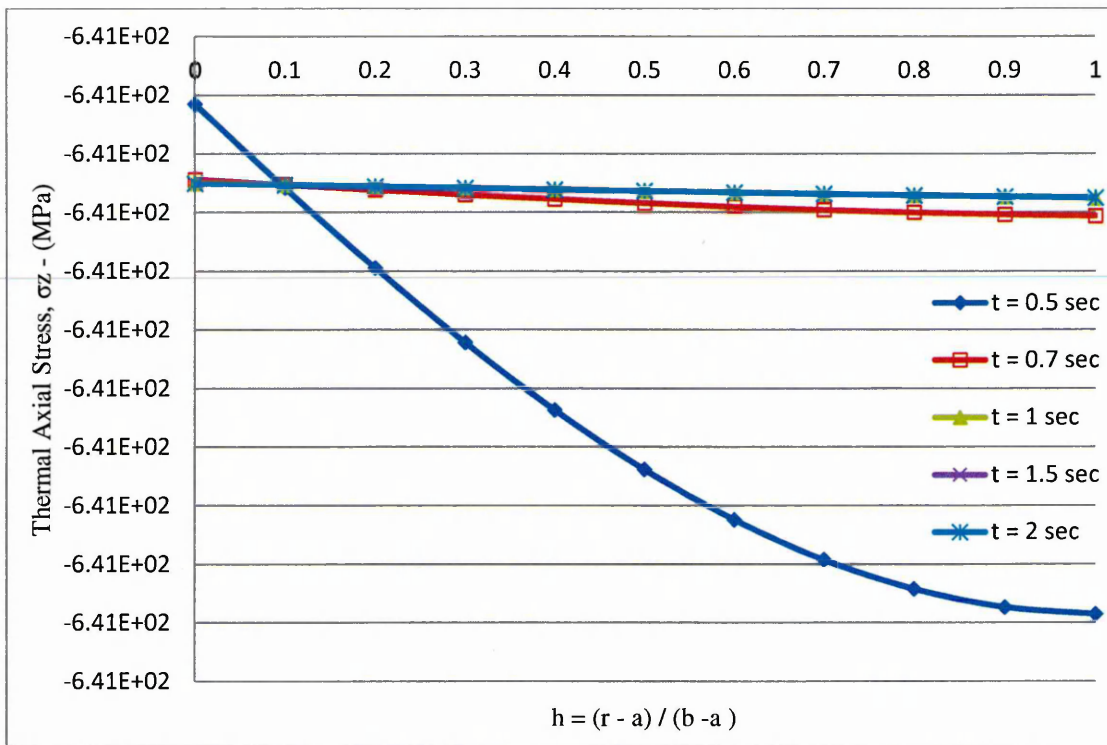
Figure 4.33 The thermal axial stress distribution through the hollow cylinder wall at different times in the heating case.
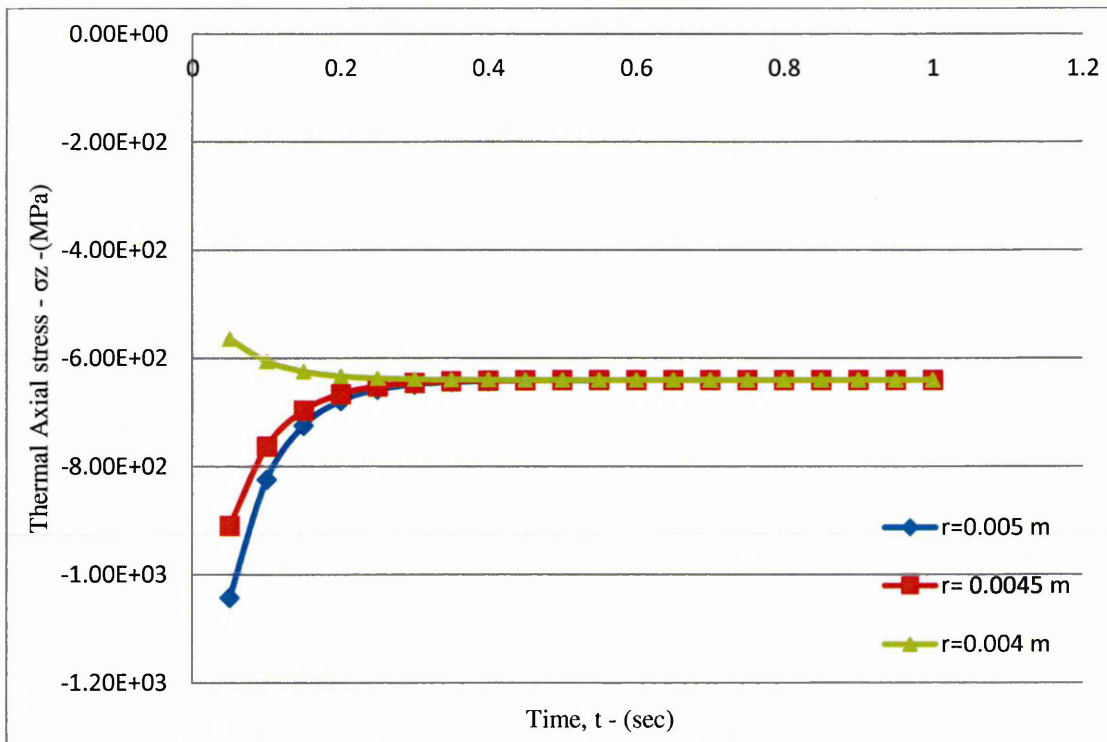
Figure 4.34 The thermal axial stress distribution with time at selected radii in the hollow cylinder heating case.

B- Down shock cooling Case:

The temperature distribution equation is divided into three parts, as;

$$
\left.
\begin{aligned}
T_1 &= B_1 \\
T_2 &= B_2 \ln\frac{r}{a} \\
T_3 &= B_{3i} \left[J_0\left(r\,\lambda_i\right).Y_1(a\,\lambda_i) - Y_0(r\,\lambda_i).J_1(a\,\lambda_i) \right]
\end{aligned}
\right\} \tag{4.34}
$$

Similarly, by the substitutions of divisions in the general formulas of the thermal stresses estimation; it is solved separately, (useful integration details are provided in Appendix B).

For the radial stress is:

$$
\sigma_{r1} = 0 \tag{4.35}
$$

$$
\sigma_{r2} = \frac{\alpha\,E\,B_2}{2\,r^2(b^2 - a^2).(1-v)} \left[r^2(b^2 \ln\frac{b}{r} + a^2 \ln\frac{r}{a}) + a^2 b^2 \ln\frac{a}{b} \right] \tag{4.36}
$$

$$
\sigma_{r3} = \frac{\alpha\,E\,B_{3i}}{\lambda_i\,r^2\,(1-v)} \left[J_1\left(a\,\lambda_i\right)\left\{ \frac{b(r^2 - a^2)}{(b^2 - a^2)}.Y_1(b\,\lambda_i) - r.Y_1(r\,\lambda_i)\right\} \right.
$$
$$
+ Y_1(a\,\lambda_i)\left\{ r\,J_1\left(r\,\lambda_i\right) \right.
$$
$$
\left. \left. - \frac{b(r^2 - a^2)}{(b^2 - a^2)}\,J_1(b\,\lambda_i)\right\} \right] \tag{4.37}
$$

The final radial stress for the heating case is given by:

$$\sigma_r = \sigma_{r1} + \sigma_{r2} + \sigma_{r3} \tag{4.38}$$

The hoop stress is:

$$\sigma_{\theta 1} = 0 \tag{4.39}$$

$$\sigma_{\theta 2} = \frac{\alpha\, E\, B_2}{2\, r^2\, (b^2 - a^2)\,.\,(1 - v)} \left[r^2 \left\{ b^2 \left(\ln\frac{b}{r} - 1 \right) + a^2 \left(\ln\frac{r}{a} + 1 \right) \right\} \right.$$
$$\left. + a^2 b^2 \ln\frac{b}{a} \right] \tag{4.40}$$

$$\sigma_{\theta 3} = \frac{\alpha\, E\, B_{3i}}{r^2\, (1 - v)} \left[J_1\,(a\,\lambda_i) \left\{ \frac{b(r^2 + a^2)}{\lambda_i(b^2 - a^2)} . Y_1(b\,\lambda_i) + \frac{r}{\lambda_i} . Y_1(r\,\lambda_i) + r^2 . Y_0(r\,\lambda_i) \right\} \right.$$
$$- Y_1(a\,\lambda_i) \left\{ \frac{r}{\lambda_i}\, J_1\,(r\,\lambda_i) + \frac{b(r^2 + a^2)}{\lambda_i(b^2 - a^2)}\, J_1\,(b\,\lambda_i) \right.$$
$$\left. \left. - r^2\, J_0\,(r\,\lambda_i) \right\} \right] \tag{4.41}$$

The final hoop stress for the heating case is given by:

$$\sigma_\theta = \sigma_{\theta 1} + \sigma_{\theta 2} + \sigma_{\theta 3} \tag{4.42}$$

For the longitudinal stress, it is:

$$\sigma_{z1} = -\,\alpha\, E\, B_1 \tag{4.43}$$

$$\sigma_{z2} = \frac{\alpha E B_2}{(1-v)} \left[\frac{v}{(b^2-a^2)} \{b^2 \ln b - a^2 \ln a\} + (1-v) \ln b - \ln r - \frac{v}{2} \right] \qquad (4.44)$$

$$\sigma_{z3} = \frac{\alpha E B_{3i}}{(1-v)} \left[J_1(a \lambda_i) \left\{ \frac{2 v b}{\lambda_i (b^2-a^2)} \cdot Y_1(b \lambda_i) + Y_0(r \lambda_i) \right\} \right.$$
$$\left. - Y_1(a \lambda_i) \left\{ \frac{2 v b}{\lambda_i (b^2-a^2)} J_1(b \lambda_i) + J_0(r \lambda_i) \right\} \right] \qquad (4.45)$$

The final longitudinal stress for the heating case is given by:

$$\sigma_z = \sigma_{z1} + \sigma_{z2} + \sigma_{z3} \qquad (4.46)$$

During the down shock cooling case in the hollow cylinder, Figs. 4.35 and 4.36 show the thermal radial stress distribution varying with radius and time. The profiles indicate that the stress is steady at the inner and outer radius and the maximum compression stress is in the middle of the hollow cylinder wall due to the opposed direction effects of the heating and cooling at two surfaces of the hollow cylinder; this effect vanished rapidly and turns to tension stress with time regarding to the balance between heating and cooling action effects. The thermal hoop stress distribution with the radius and time appears in the tensile mode in the inner surface due to cooling effects and compression in the outer surface due to the heating effects. The maximum hoop stress occurs in the middle of the cylinder thickness and also at the beginning of time; it is then reduced to zero at 0.7 second due to the equalized action of the loadings, as shown in Figs. 4.37 and 4.38. The thermal axial stress distribution with radius and time is illustrated in compression mode; the maximum stress in the inner surface and at the beginning of time but it reduced rapidly to steady-state level with time as shown in Figs. 4.39 and 4.40.
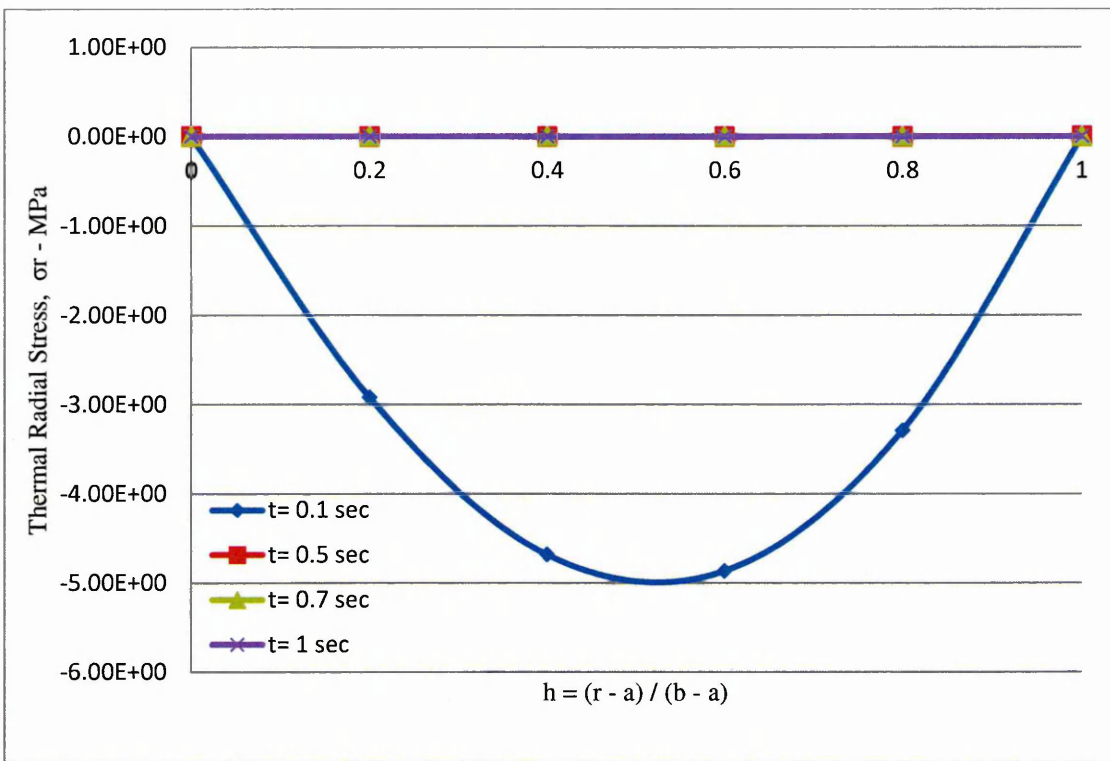
Figure 4.35 The thermal radial stress distribution through the hollow cylinder wall at different times in the down shock cooling case.
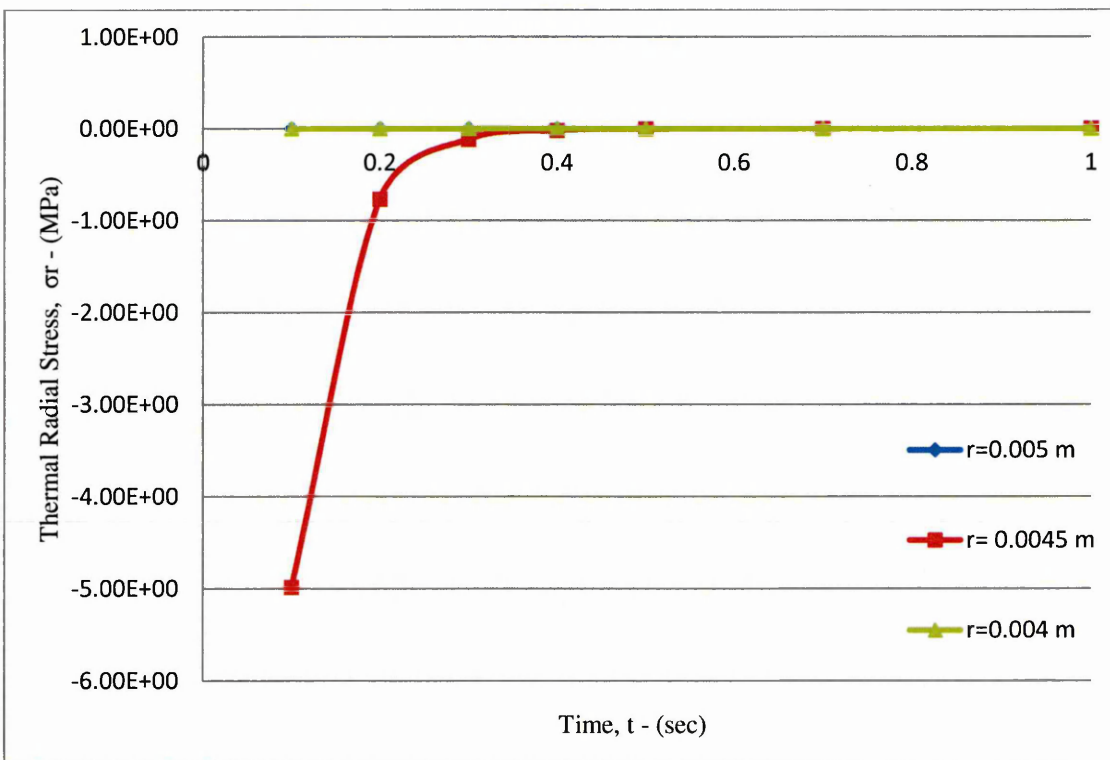
Figure 4.36 The thermal radial stress distribution with time at selected radii in the hollow cylinder down shock cooling case.

123
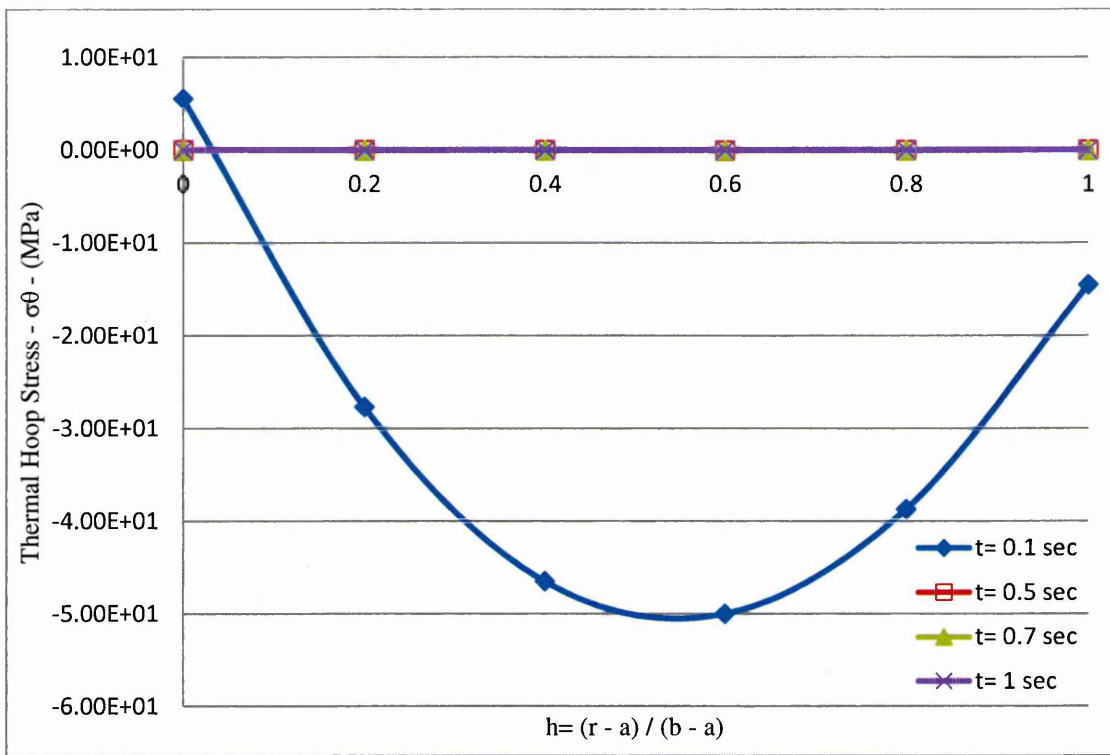
Figure 4.37 The thermal hoop stress distribution through the hollow cylinder wall at different times in the down shock cooling case.
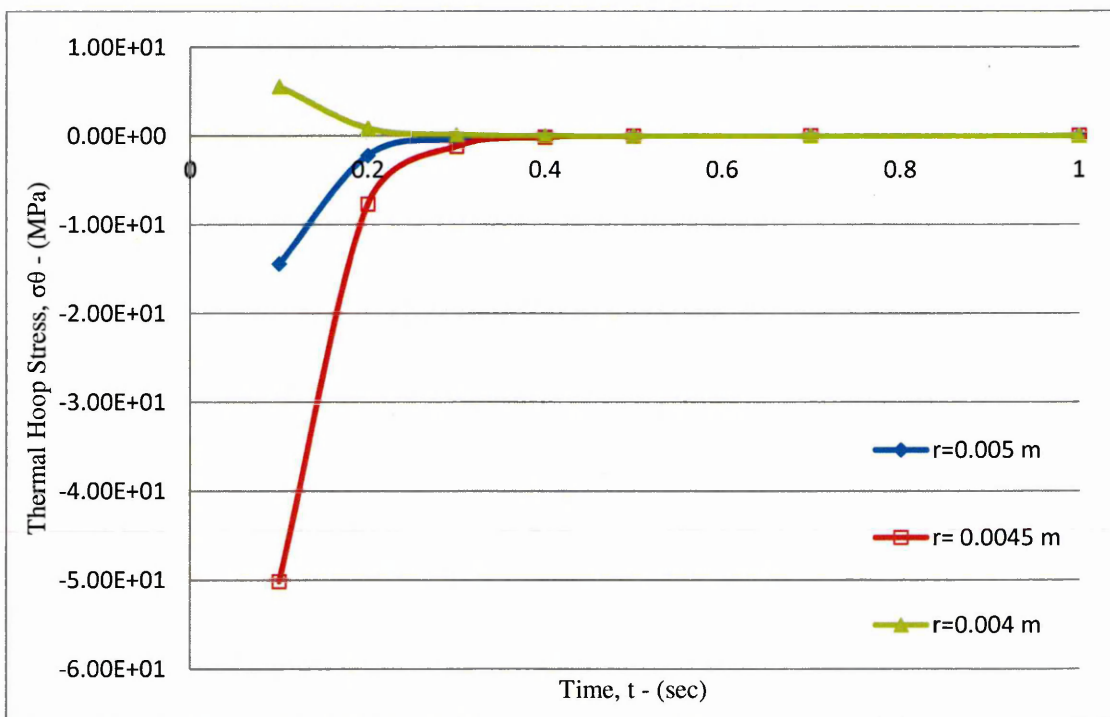
Figure 4.38 The thermal hoop stress distribution with time at selected radii in the hollow cylinder down shock cooling case.

124
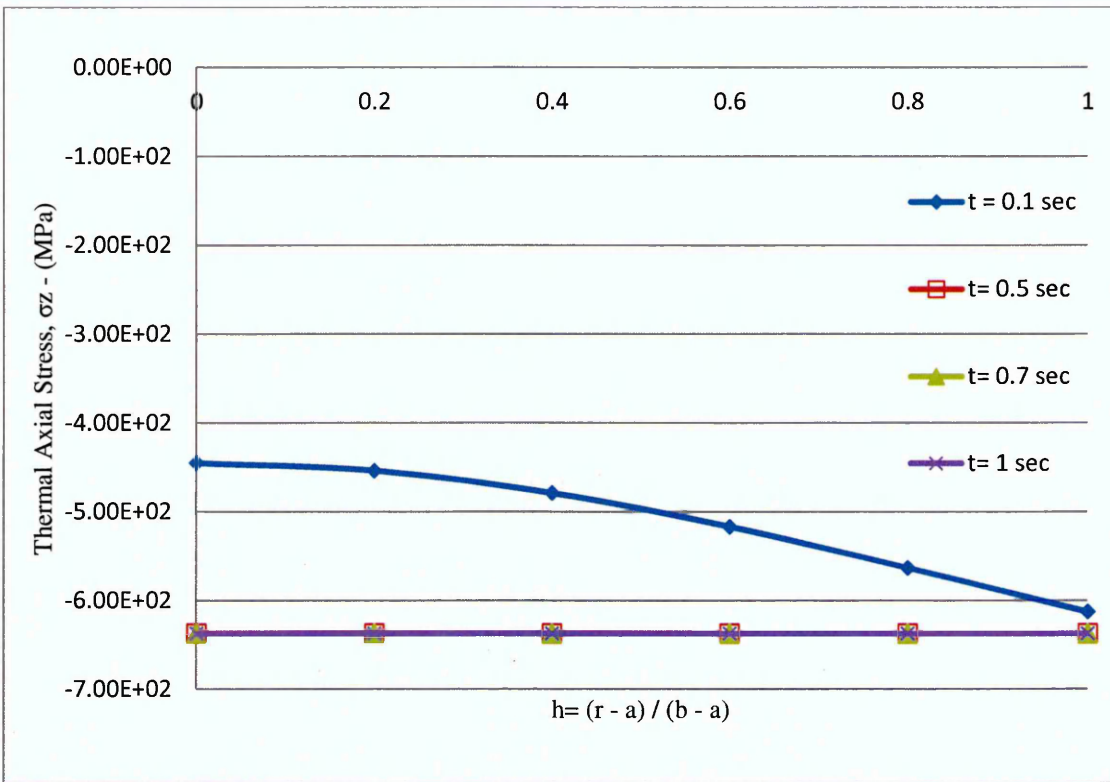
Figure 4.39 The thermal axial stress distribution through the hollow cylinder wall at different times in the down shock cooling case.
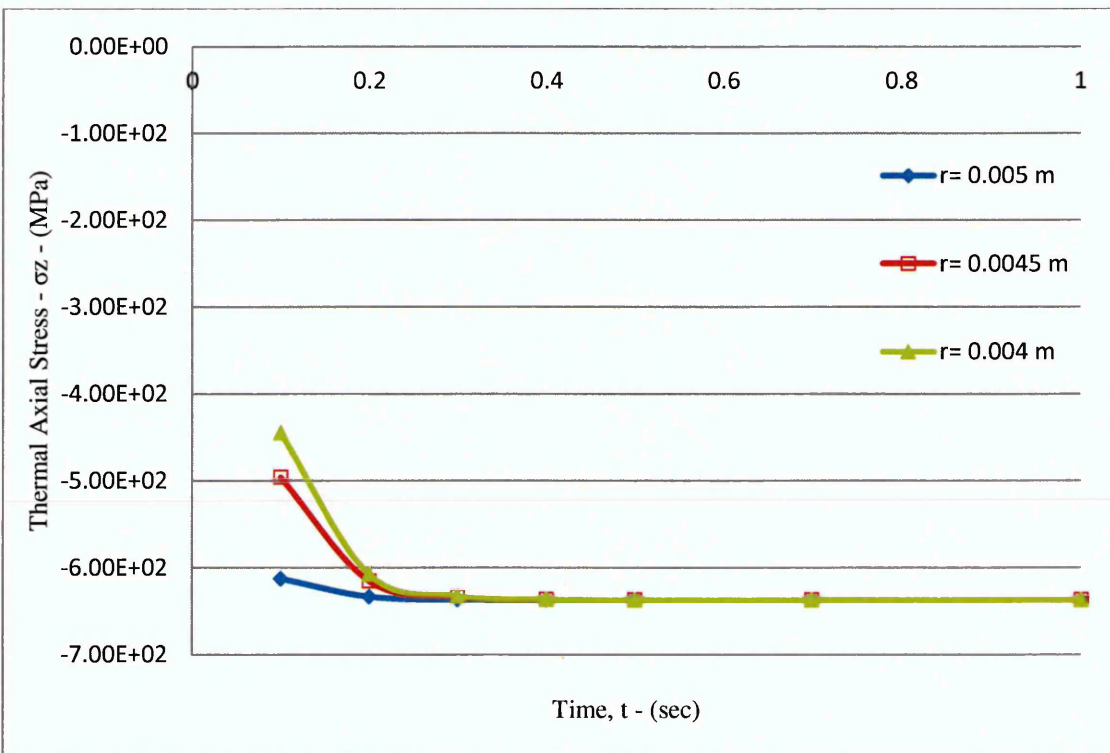
Figure 4.40 The thermal axial stress distribution with time at selected radii in the hollow cylinder down shock cooling case.

125

4.4 Elastic-Plastic Stress Calculations:

The accumulative influence of the thermal stress component is generally a high strain process especially at high temperatures; additionally it increases when combined with mechanical loading. The Elastic-Plastic analysis is introduced by using the Von Mises Plasticity criterion given by:

$$(\sigma_{r-\text{th}} - \sigma_{\theta-\text{th}})^2 + (\sigma_{\theta-\text{th}} - \sigma_{z-\text{th}})^2 + (\sigma_{z-\text{th}} - \sigma_{r-\text{th}})^2 = 2\,\sigma_{TVM}^2 \qquad (4.47)$$

von Mises stress is given by;

$$\sigma_{TVM} = \sqrt{\frac{(\sigma_{r-\text{th}} - \sigma_{\theta-\text{th}})^2 + (\sigma_{\theta-\text{th}} - \sigma_{z-\text{th}})^2 + (\sigma_{z-\text{th}} - \sigma_{r-\text{th}})^2}{2}} \qquad (4.48)$$

In the isothermal fatigue case, the distributions of the elastic-plastic equivalents von Mises stress through the solid cylinder outer surface (outer radius) with time are shown in Fig. 4.41. The overall behaviour of the von-Mises thermal stress starts with high value at the beginning (0.05 sec) due to the thermal shock, then it rapidly decreases reaching to the steady-state at (1 sec). For that reason, the isothermal fatigue study will depend on the steady-state section only. Increasing the temperature has increased the elastic-plastic thermal stress, except at 400 °C where it reaches its higher value due to the high modulus of Elasticity (E) magnitude.

In the transient cases, the distribution of the equivalent elastic-plastic von Mises stress occurred in the inner surface of the hollow cylinder. In the heating case, the maximum thermal up-shock occurs at the start time (0.05 sec), it then decreased reaching to the minimum steady level in the fraction of a second as shown in Fig 4.42. This is due to the high heating flux supplied to the outer surface mentioned before in the boundary conditions. While, the thermal down shock is clearly occurs in the starting time, it then increased reaching to the maximum steady level in fraction of second due to the cooling effects as shown in Fig. 4.43.
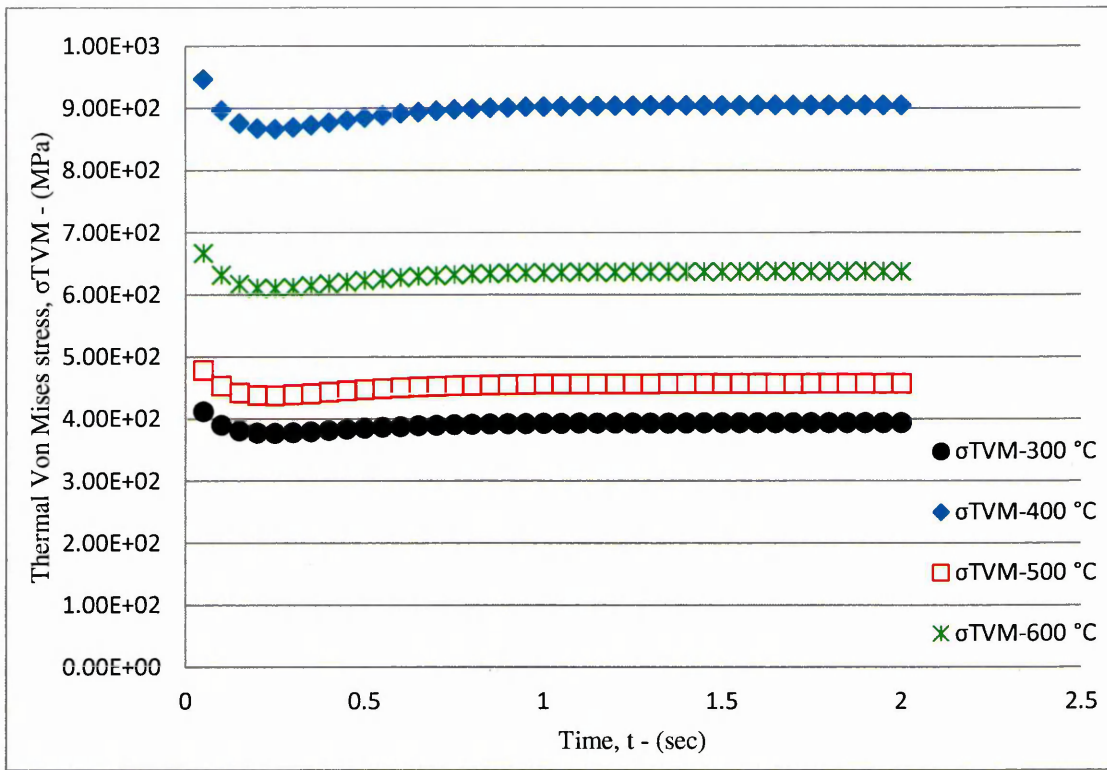
Figure 4.41 The von-Mises equivalent stress distribution with time at the outer surface of the solid cylinder at different temperature levels.
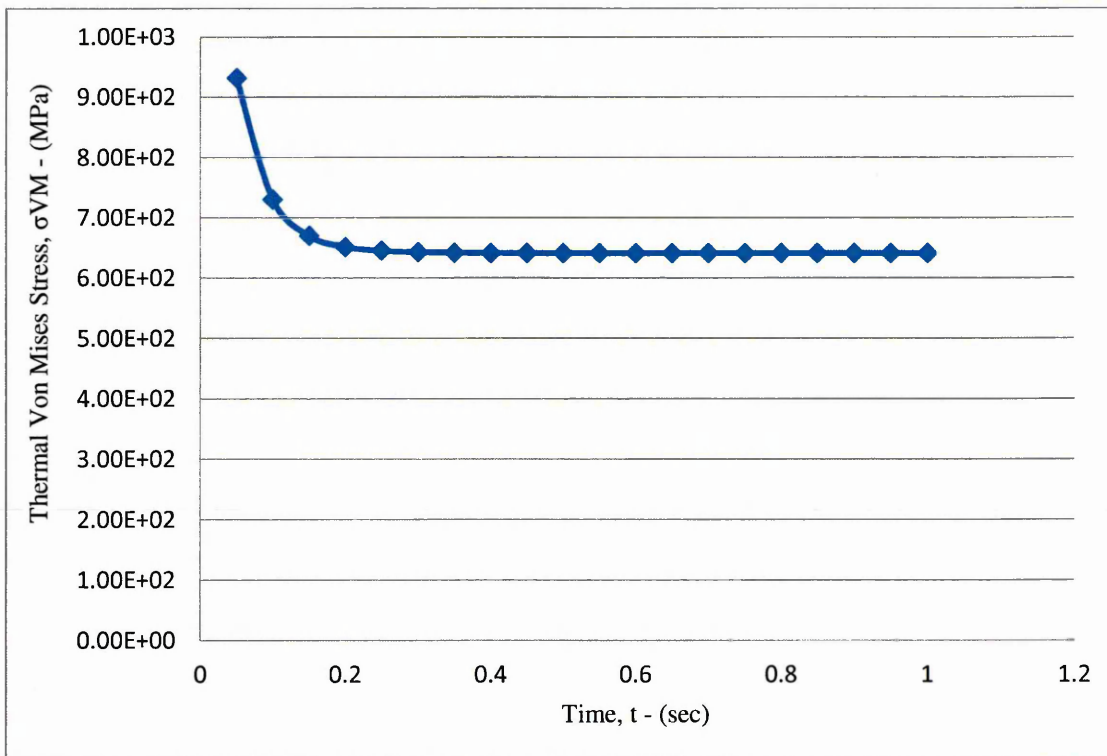
Figure 4.42 The von-Mises equivalent stress distribution with time in the inner surface of the hollow cylinder under heating case.
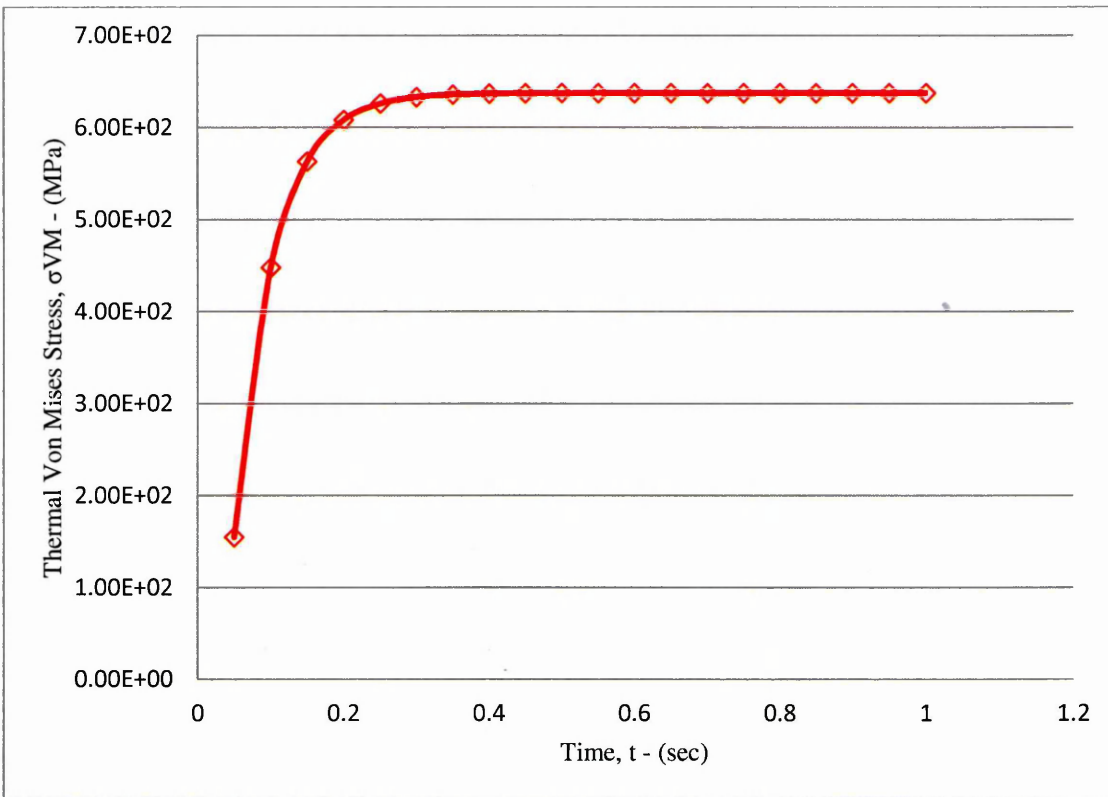
Figure 4.43 The von-Mises equivalent stress distribution with time in the inner surface of the hollow cylinder under cooling case.

4.5 Thermo-Mechanical Stress Calculation:

The mechanical load is formed by employing tension–compression sinusoidal mechanical stresses based on yield stress equal to the stress range and oriented to the axial axis of the cylinder making a ratio of minimum to maximum applied stress $(R = \frac{\sigma_{min}}{\sigma_{max}} = 0.1)$ and using frequency (f = 5 Hz) similar to the experimental test, by using the formulas:

$$\sigma_{mech.} = \frac{\Delta\sigma \cdot (0.55 + 0.45 \cdot \sin(2\pi.f.t))}{(1-R)}. \tag{4.49}$$

128

In this theoretical solution, the assumption of the interaction influence of the thermal stress with the mechanical stress can be described by solving thermal stress in elastic–plastic stress added to the cyclic mechanical loading to estimate the thermo–mechanical combined stress as expressed by the equation:

$$\sigma_{comb.} = \sigma_{TVM} + \sigma_{mech.}.$$ (4.50)

It is difficult to predict the behaviour of the interaction effects of thermo–mechanical loading through the cylindrical coordinates in reality. The distributions of the thermo-mechanical combined stress for all testing temperature in the solid cylinder and hollow cylinder case studies related with time are presented in Figs. (4.44 to 4.46). In the solid cylinder, thermo-mechanical combined stress increased with the increase in the temperature because the effect of the thermal elastic–plastic stress on the cyclic mechanical loading raises the value of the stress effect. Except at 400 °C, the stress value jumped regarding the highly thermal von-Mises and the applying mechanical stress. The cyclic behaviour is dominant on the combined stress profile regarding the constant thermal stress value especially over (1 sec), which is the steady state referred to as isothermal fatigue case. While in the hollow cylinder of the two cases, the effects of the thermal up-shock and down shock at the starting time are showing a significant influence on the combined stress, maximized the stress level in the heating case and minimized it in the cooling case, causing a very high stress range between the maximum and the minimum stress. Therefore, the repeat of these shocks will be a reason of component failure due to thermo-mechanical fatigue.
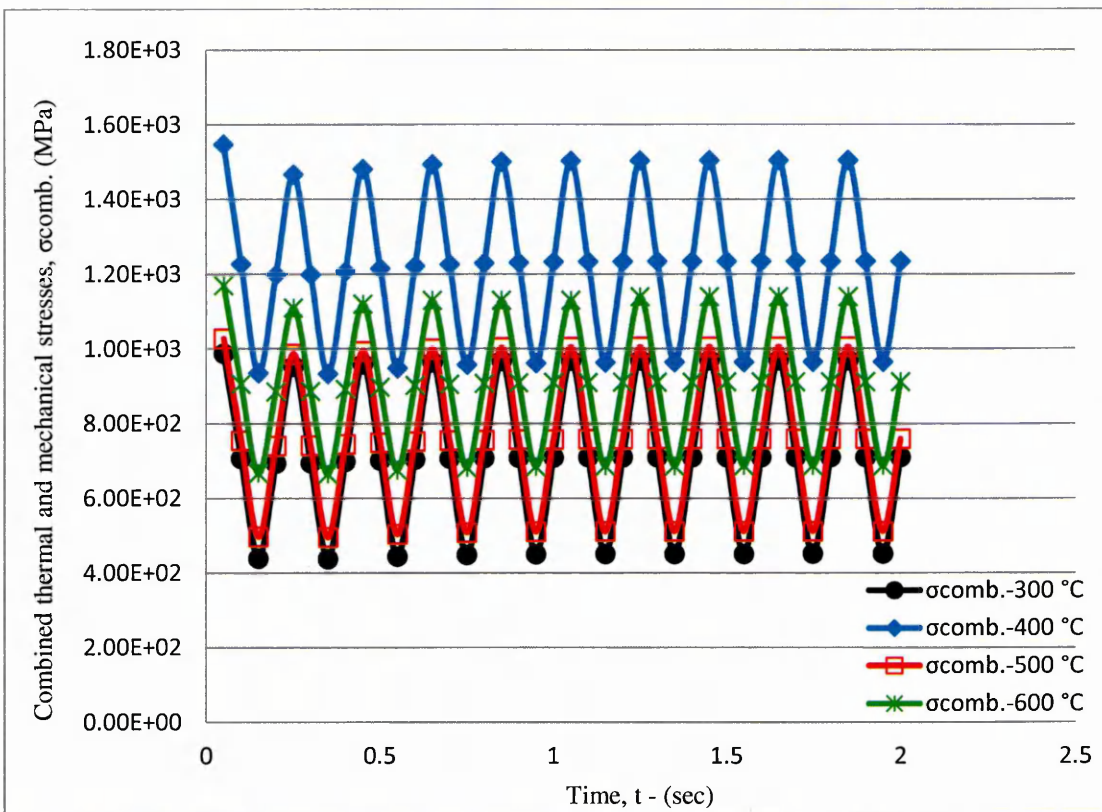
Figure 4.44 The distribution of thermo–mechanical combined stress with time at the outer surface of the solid cylinder.
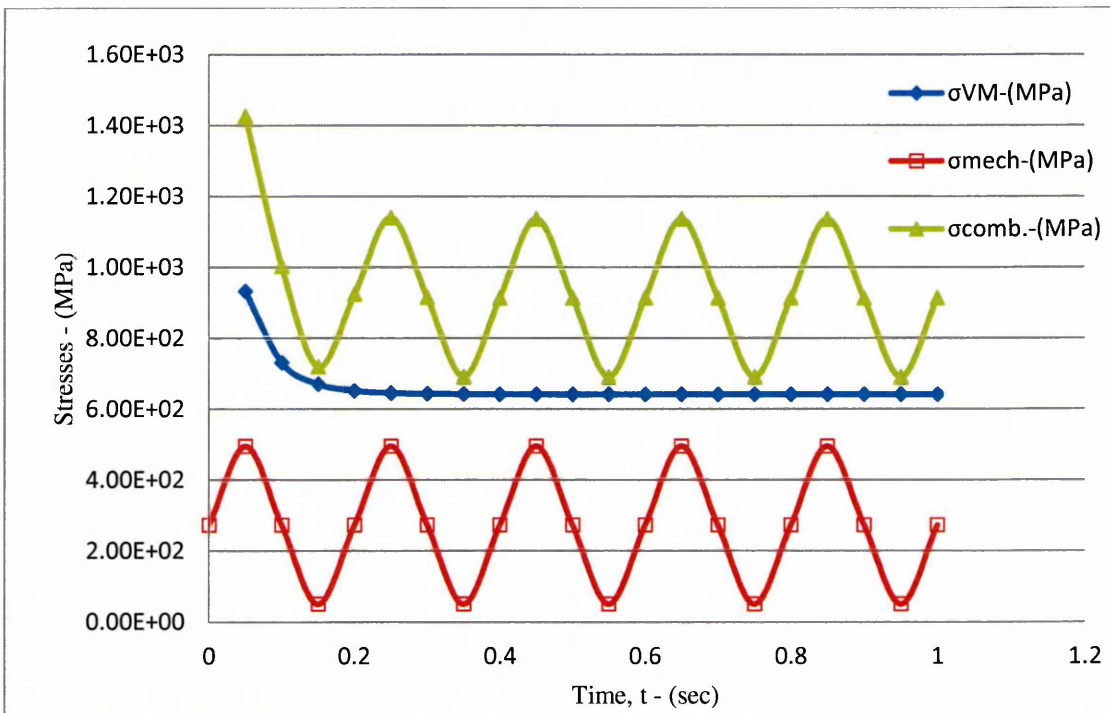
Figure 4.45 The distribution of thermo–mechanical loads with time in the inner surface of the hollow cylinder at heating case.

130
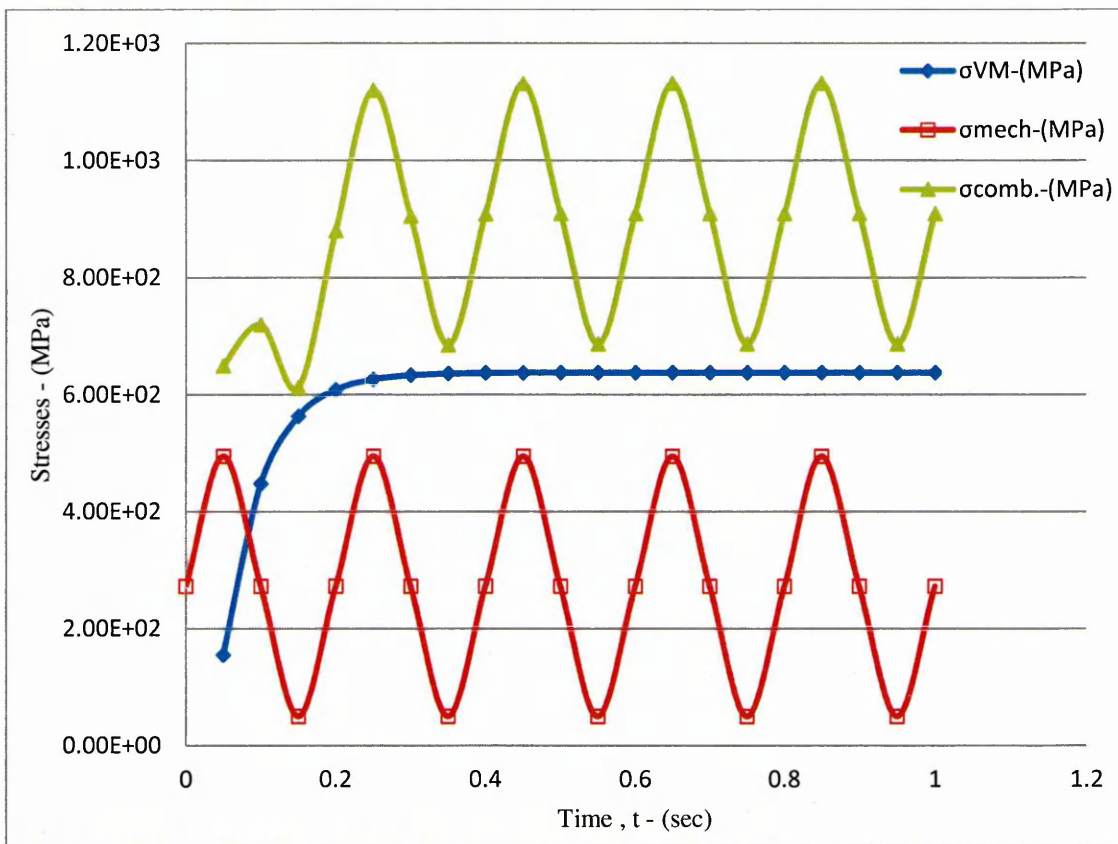
Figure 4.46 The distribution of thermo–mechanical loads with time in the inner surface of the hollow cylinder at cooling case.

4.6 Stress and Strain Intensity Factor Formulation:

Researchers have undertaken specific works on the stress intensity factor calculations with crack depth; they started in the internal surface of a hollow cylinder subjected to transient thermal stresses. Shahani and Nabavi, [107], improved a formula for the evaluation of the transient thermal stress intensity factors assisted by the weight function method for an internal semi-elliptical crack in a thick-walled cylinder subjected to transient thermal stresses. Additionally, Jones, [108], examined the impulse response model to estimate the stress intensity factors in the thermally striped internal surface of a hollow cylinder circumferentially cracked.

In this work, the stress intensity factor has been estimated by employing a formula derived by Tada et al., [91], who induced in a solid cylinder externally circumferential crack under uniaxial tensile stress for the isothermal fatigue case and hollow cylinder internally cracked under uniaxial stress for the thermal shock fatigue cases, through the

131

substitution of the difference between the maximum and minimum combined stress as a thermo-elastic–plastic stress range at that particular crack growth length and the division of the stress intensity factor by the modulus of Elasticity to find the strain intensity factor.

4.6.1 Solid Cylinder Solution:

The stress and strain intensity factor estimation in the solid cylinder isothermal fatigue case is carried out by using the following equations.

$$K_I = \Delta\sigma_{comb.} \sqrt{\pi . c} \; . \; F\left(\frac{c}{r}\right). \tag{4.51}$$

at $r = b$

$$F\left(\frac{c}{b}\right) = \frac{1}{(1 - c/b)^{3/2}}\left\{1.122 - 1.302\frac{c}{b} + 0.988\left(\frac{c}{b}\right)^2 - 0.308\left(\frac{c}{b}\right)^3\right\}. \tag{4.52}$$

$$K_\epsilon = \frac{K_I}{E}. \tag{4.53}$$

The distribution of the stress and strain intensity factors as a result of the combined stress range against the crack growth in the isothermal case for different temperature levels are shown in Figs. (4.47 and 4.48). The profiles illustrate the increment of the stress intensity factor with crack propagation through the solid cylinder wall and the decrease with the increasing temperature, except at 400 °C which is maximized due to the highly thermal and mechanical stresses. Also the curves give an indication that the theoretical estimation of the material behaviour is bounded by the maximum stress that occurred at 400 °C and the minimum at 600 °C. While the strain intensity factor also increased with crack propagation but it not always increases with the rising temperature. This is because of the effect of the modulus of Elasticity of the material on the profiles, which is clear significantly, especially at 400 °C and the strain intensity is bounded between the maximum at 500 °C and 400 °C.
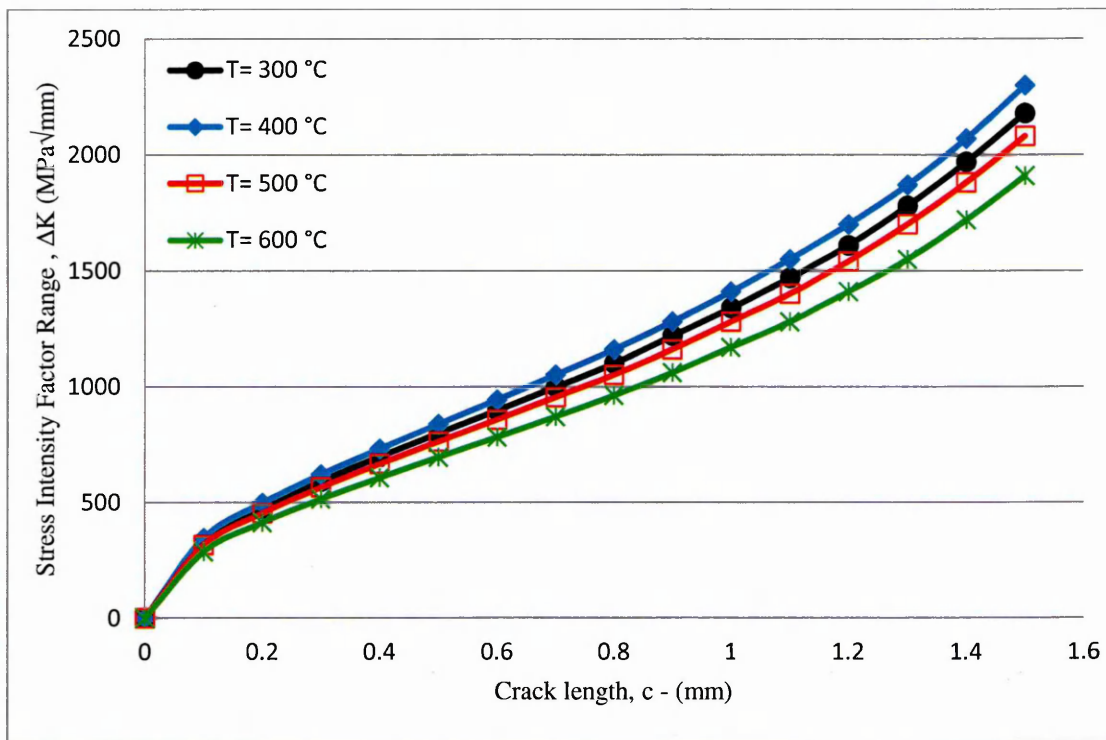
Figure 4.47 The distribution of the stress intensity factor range with crack length in the isothermal fatigue simulations.
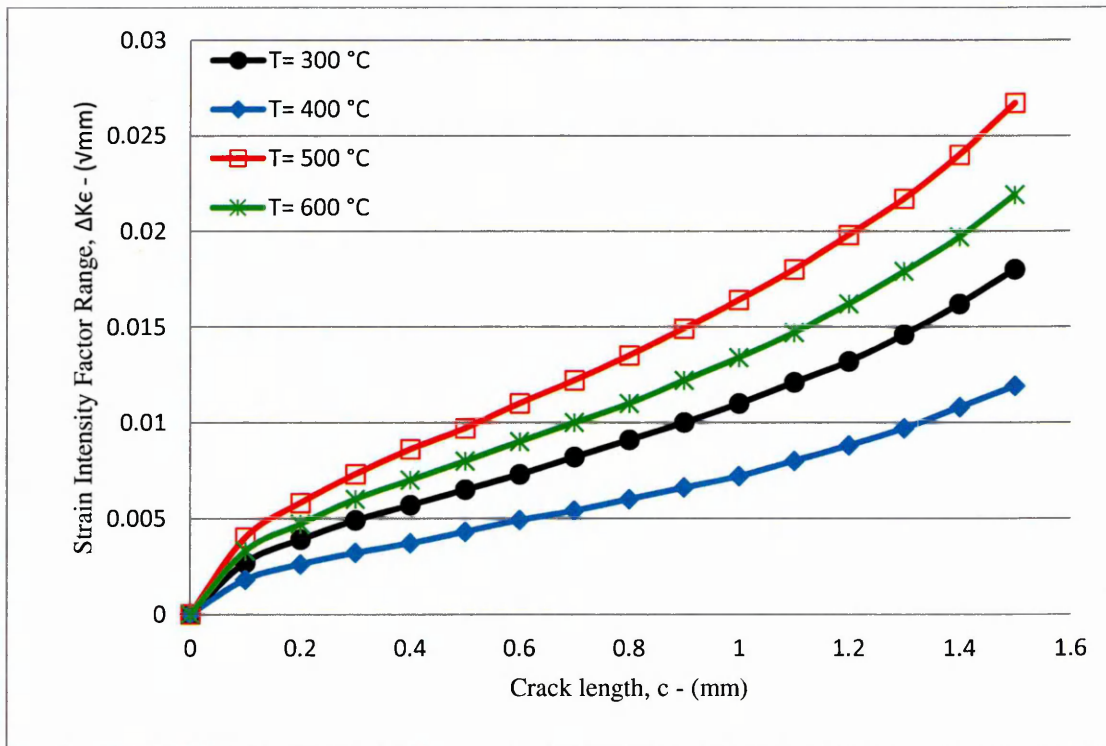
Figure 4.48 The distribution of the strain intensity factor range with crack length in the isothermal fatigue simulations.

4.6.2 Hollow Cylinder Solution:

The stress and strain intensity factor estimation in the hollow cylinder thermal shock heating and down shock cooling fatigue cases is performed by the following equations.

$$K_I = \Delta\sigma_{comb.} \cdot \sqrt{\pi.c} \cdot F\left(\frac{a}{b}, \frac{c}{th}\right). \tag{4.54}$$

$$F\left(\frac{a}{b}, \frac{c}{th}\right) = \frac{\left\{-2.4229\left(^{c}/_{th}\right)^3 + 2.41\left(^{c}/_{th}\right)^2 - 0.6541\left(^{c}/_{th}\right) + 1.122\right\}}{\sqrt{1-\left(\frac{c}{th}\right)}} \tag{4.55}$$

where;

$$th = b - a$$

$$K_\epsilon = \frac{K_I}{E}. \tag{4.56}$$

In the hollow cylinder under heating and down shock cooling cases, the distribution of the stress and strain intensity factors resulting from using combined elastic-plastic stress range with the ratio of the crack growth to the hollow cylinder wall thickness are shown in Figs. (4.49 to 4.52). The range of the stress and strain intensity factors profiles rapidly increased at the start indicating the high influence of the thermal shock; it is then gradually increased. The effect of the heat flux in the heating case is high, raising the curves in this case over the down shock cooling case.
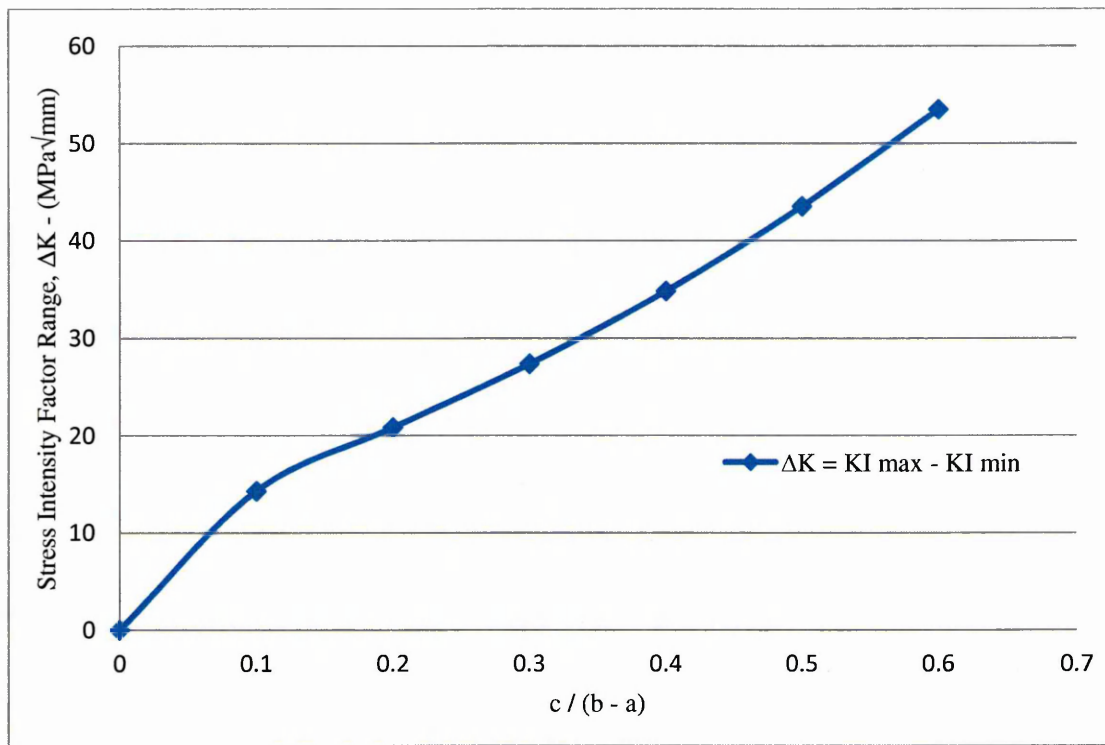
Figure 4.49 The distribution of the stress intensity factor range with crack growth ratio to the hollow cylinder wall thickness in the heating case.
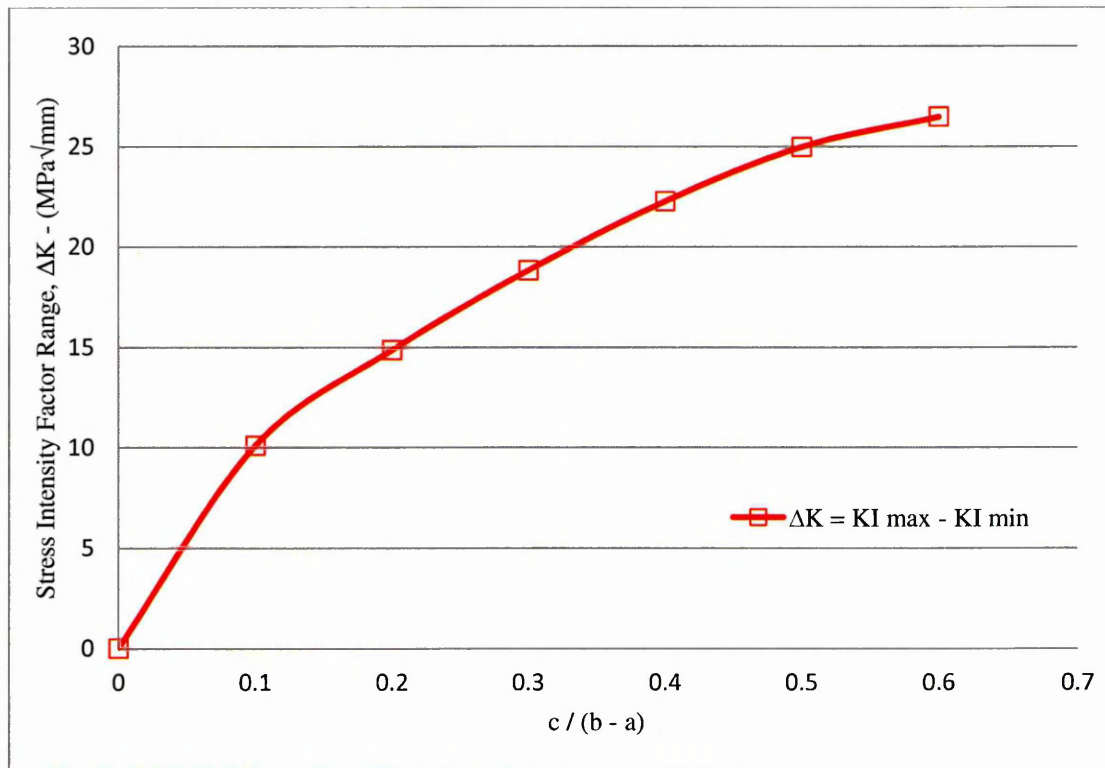
Figure 4.50 The distribution of the stress intensity factor range with crack growth ratio to the hollow cylinder wall thickness in the cooling case.

135
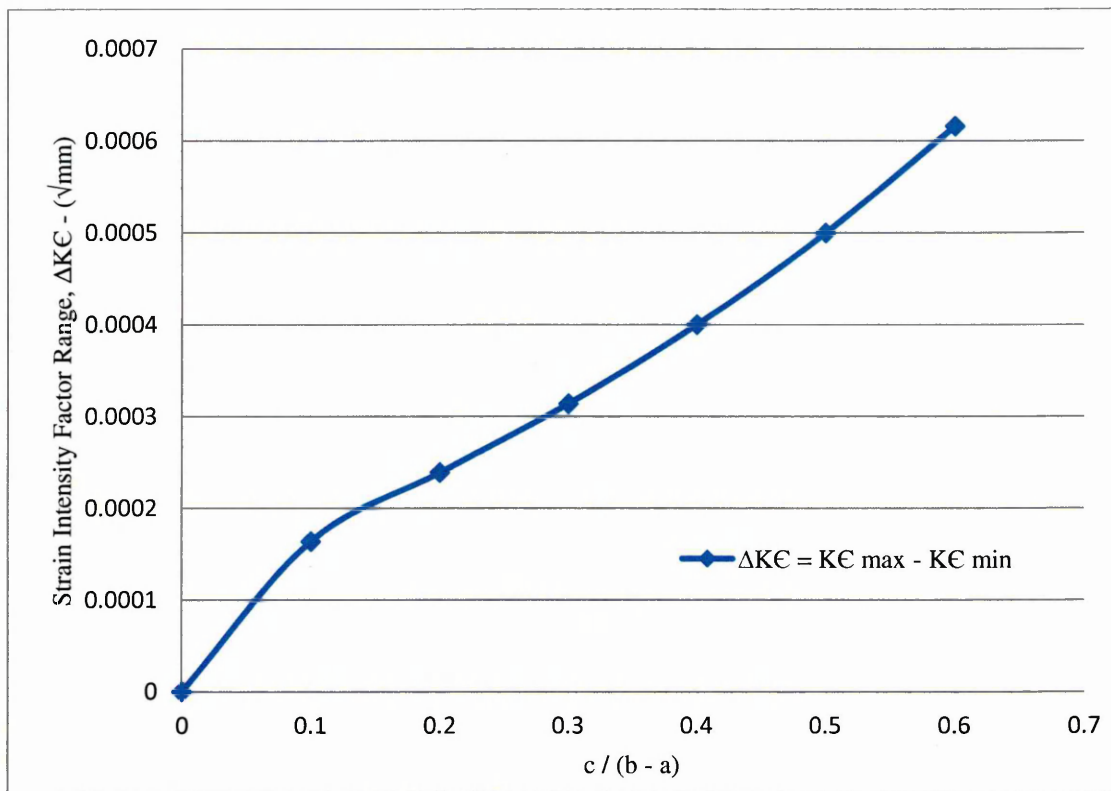
Figure 4.51 The distribution of the strain intensity factor range with crack growth ratio to the hollow cylinder wall thickness in the heating case.
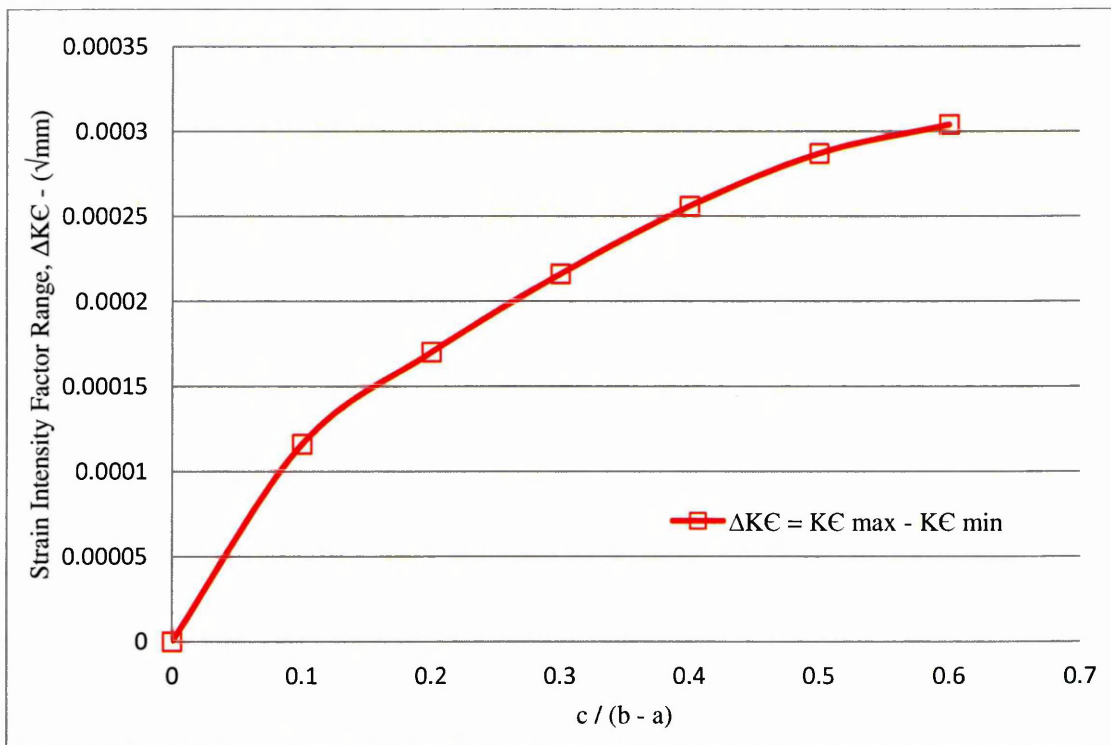
Figure 2.52 The distribution of the strain intensity factor range with crack growth ratio to the hollow cylinder wall thickness in the cooling case.

CHAPTER FIVE

5- NUMERICAL MODELLING

5.1 Introduction:

Finite element methods are techniques for approximating the governing differential equations for a continuous system with a set of algebraic equations relating a finite number of variables [116]. The major finite element analysis (FEA) application is the determination of stresses and temperatures in a component or member in locations where failure is most likely to take place. If the stresses or temperatures exceed allowable or safe limits, the products can be redesigned and then reanalyzed. Analysis can also be diagnostic, supporting interpretation of product failure data; it can be used to assess performance and serve to minimize weight and cost without loss of structural integrity or reliability [117].

In this chapter, three numerical modelling analyses case studies were solved due to the types of loading and types of geometry specimen by using finite element models constructed through the ANSYS Workbench version 13.0. The first case is a low cyclic fatigue case for a solid cylinder specimen simulated by applying a cyclic mechanical load at one end of the specimen toward the cylinder axis. The second is an isothermal fatigue case for solid cylinder specimen simulated by supplying different constant temperatures on the outer surface with cyclic mechanical load at the end of the specimen, where the two cases are similar to the experimental tests and the third case, is a thermo-mechanical fatigue for a hollow cylinder model by simulating a thermal up-shock generated due to transient heating on the outer surface of the model or down shock cooling on the inner surface to the cyclic mechanical loading.

ANSYS is a general objective finite element modelling software package for numerical solution of mechanical problems, which are regarded as linear or non-linear static/dynamic structural analysis, heat transfer and fluid dynamics, as well as

electromagnetic and acoustic problems. Fatigue was initially presented as a new facility in version 6.0. It was intended to give useful information to the engineering designer when fatigue is introduced. Fatigue results can have a convergence attached. Currently, a stress - life approach has been adopted for conducting the fatigue analysis as well as calculating the mean stress and loading conditions.

The general methodology for numerical analysis simulation has classically been performed as follows:

1- Pre-processing stage.

2- Simulation and Solution stage.

3- Post-Processing stage.

5.2 Pre-processing stage:

The behaviour of a phenomenon in a system depends upon the geometry of the system, the property of the material and the boundary, initial and loading conditions. For an engineering system, the geometry can be very complex. Furthermore, the boundary conditions can also be complicated. Therefore, it is very difficult to solve the governing differential equation via analytical means. In practice, most of the problems are solved employing numerical methods. ANSYS program has many finite-element analysis capabilities, ranging from a simple linear static analysis to a complex nonlinear transient dynamic analysis. It is important to remember that ANSYS does not assume a system of units for intended analysis. In the present numerical simulations cases, the preparation of model analysis needs to be attempted as two separate appropriate analysis types: thermal (in steady state and transient thermal loading) and structural (fatigue) analysis, which either works separately in low cyclic fatigue or it is combined with thermal, to produce thermal stresses and thermal fatigue solutions.

The procedure of computational modelling using the finite element method (FEM) consists of four main steps for the pre-processing stage [118]:

1- Creating the model geometry.

2- Mesh Generation.

3- Specification of material property.

4- Specification of boundary (Initial and loading) conditions.

5.2.1 Creating the model geometry:

The ultimate purpose of a finite element analysis is to create an accurate mathematical engineering model; this model contains all the nodes, elements, material properties, real constants, boundary conditions and other features that are utilized to represent the engineering system [119]. The real structure geometry is very complex, it is eventually represented by a collection of elements, and the curves and curved surfaces are approximated by piecewise straight lines or flat surfaces, if linear elements are used. The accuracy of representation of the curved parts is controlled by the number of elements used. Conversely, the more elements, the longer the computational time that is. Hence, due to the constraints on computational hardware and software, it is always necessary to limit the number of elements [120].

Depending on the ANSYS software used, there are three ways to create the finite element geometric models.

i) Direct Generation:

The location of each node and the connectivity of each element are manually defined. Points can be created simply by keying in the coordinates. Lines and curves can be created by connecting the points or nodes. Surfaces can be created by connecting, rotating or translating the existing lines or curves, and solids can be created by connecting, rotating or translating the existing surfaces. Points, lines and curves, surfaces and solids can be translated, rotated or reflected to form new ones.

ii) Solid modelling:

The geometry of the shape of the model is described by the boundaries; it establishes controls over the size and element shape and then instructs the ANSYS program to generate all the nodes and elements automatically, as it's done in the heating and down shock case studies.

139

iii) Importing a model:

As an alternative to creating a model directly in ANSYS, there is a possibility to create a solid geometrical model, firstly, in any preferred computer aided design (CAD) software packages and importing into the ANSYS program, as it's done in the low cyclic and isothermal fatigue cases by using Solid Works 2010 software.

5.2.2 Mesh Generation:

The performance of meshing is discrete the geometry created into small pieces called elements or cells. The discretion means dividing (meshing) the problem domain into small elements or cells using a set of grids or nodes, where the solution within an element can be approximated very easily using simple functions such as polynomials. The solutions for all of the elements provide the solution of the whole problem. Mesh generation is a very important task of the pre-process. It can be a very time consuming task for the analyst, and usually an experienced analyst will produce a more credible mesh for a complex problem.

To generate a mesh of nodes and elements utilized in ANSYS software package, one has to follow the following main steps, [119]:

I) Setting element attributes which include the element type, real constants and material properties.

II) Setting mesh control, where ANSYS provides a large number of mesh controls. Also a free and mapped mesh is appropriate for the analysis. A free and mapped mesh is restricted by constraints of the elements shapes and the mesh pattern. A mapped area mesh contains either only quadrilateral or triangular element, while a volume, mesh contains hexahedron or tetrahedral element. In addition, a mapped mesh typically has a regular pattern, with clear element rows. This type of meshing techniques was utilized in the two simulations due to its simplicity and uniform symmetric geometrical models.

III) Generating the meshing of the solid model.

140

The problem domain has to be meshed properly into elements of specific shapes such as triangles and quadrilaterals. Triangulation is the well-established way to create meshes with triangular elements. It can be made almost fully automated for two-dimensional (2D) planes, and even three-dimensional (3D) spaces, as the basis of tetrahedral and hexahedral three-dimensional (3D) solid elements, where the formulation of three-dimensional elements is straightforward, because it is basically an extension of two dimensional solid elements. Therefore, it is commonly available in most of the pre-processors. The additional advantage of using triangles is the flexibility of modelling complex geometry and its boundaries. In contrast, the accuracy of the simulation results based on triangular elements is often lower than that obtained by quadrilateral elements. Quadrilateral element meshes, however, are more difficult to generate in an automated manner.

In this chapter, two types of three-dimensional solid elements are considered, tetrahedral and hexahedral elements in shape with either flat or curved surfaces. Each node of the element will have three translational degrees of freedom. The element can thus be deformed in all three directions in space.

I- Tetrahedral Element:

The most popular three–dimensional elements are the tetrahedral elements. However, it is occasionally difficult to partition a domain into only elements of this type. For this reason, tetrahedral elements are often combined with hexahedral and pentahedral elements. This element has four surfaces and four nodes each having three degrees of freedom (u, υ and w), making the total degrees of freedom in a tetrahedral element twelve, as shown in Fig. 5.1.

The fundamentals of the displacement vectors are described in many FEM references [121-123]. The variation of each component of displacement with nodes can be assumed in terms of a polynomial, defined by four constants as follows [121]:
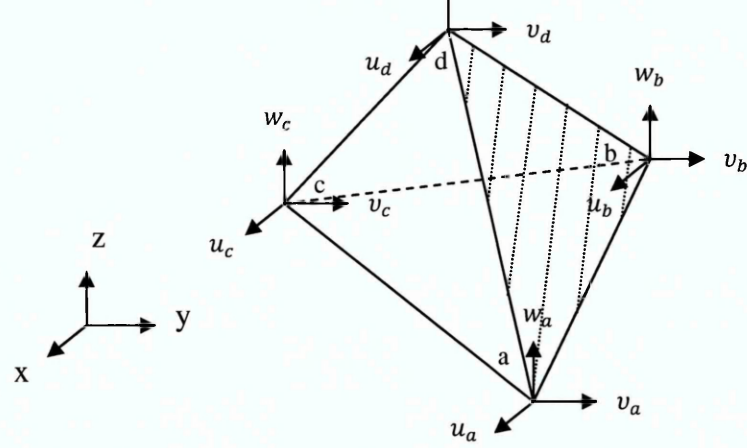
Figure 5.1 A tetrahedral element.

$$u(x, y, z) = A_0 + A_1 x + A_2 y + A_3 z$$

$$v(x, y, z) = A_4 + A_5 x + A_6 y + A_7 z \qquad (5.1)$$

$$w(x, y, z) = A_8 + A_9 x + A_{10} y + A_{11} z$$

Where A_0, A_4 *and* A_8 represent the rigid body translations of the element along the x, y and z axes respectively. Writing these equations in the matrix form:

$$\{U\} = \begin{Bmatrix} u(x, y, z) \\ v(x, y, z) \\ w(x, y, z) \end{Bmatrix} \qquad (5.2)$$

and

$$\{A\} = \{A_0 \quad A_1 \quad \dots \quad A_{10} \quad A_{11}\}^T \qquad (5.3)$$

The nodes displacements are obtained by substituting the coordinates of the nodes into Eqs.5.1 and writing these displacements in the following matrix form:

142

$$\{\mathbf{u}\} = [c]\{A\} \tag{5.4}$$

Where

$$\{\mathbf{u}\} = \{u_{ai} \quad v_{ai} \quad w_{ai} \quad u_{bi} \quad v_{bi} \quad w_{bi} \quad u_{ci} \quad v_{ci} \quad w_{ci} \quad u_{di} \quad v_{di} \quad w_{di}\}^T \tag{5.5}$$

And

$$[c] = \begin{bmatrix}
1 & x_a & y_a & z_a & 0 & 0 & 0 & 0 & 0 & 0 & 0 & 0 \\
0 & 0 & 0 & 0 & 1 & x_a & y_a & z_a & 0 & 0 & 0 & 0 \\
0 & 0 & 0 & 0 & 0 & 0 & 0 & 0 & 1 & x_a & y_a & z_a \\
1 & x_b & y_b & z_b & 0 & 0 & 0 & 0 & 0 & 0 & 0 & 0 \\
0 & 0 & 0 & 0 & 1 & x_b & y_b & z_b & 0 & 0 & 0 & 0 \\
0 & 0 & 0 & 0 & 0 & 0 & 0 & 0 & 1 & x_b & y_b & z_b \\
1 & x_c & y_c & z_c & 0 & 0 & 0 & 0 & 0 & 0 & 0 & 0 \\
0 & 0 & 0 & 0 & 1 & x_c & y_c & z_c & 0 & 0 & 0 & 0 \\
0 & 0 & 0 & 0 & 0 & 0 & 0 & 0 & 1 & x_c & y_c & z_c \\
1 & x_d & y_d & z_d & 0 & 0 & 0 & 0 & 0 & 0 & 0 & 0 \\
0 & 0 & 0 & 0 & 1 & x_d & y_d & z_d & 0 & 0 & 0 & 0 \\
0 & 0 & 0 & 0 & 0 & 0 & 0 & 0 & 1 & x_d & y_d & z_d
\end{bmatrix} \tag{5.6}$$

The strain within the element can be displayed in a matrix form as follows:

$$\{\epsilon\} = [N]\,[c^{-1}] \begin{Bmatrix} u_a \\ v_a \\ w_a \\ u_b \\ v_b \\ w_b \\ u_c \\ v_c \\ w_c \\ u_d \\ v_d \\ w_d \end{Bmatrix} \tag{5.7}$$

Where

$$\{\epsilon\} = \begin{Bmatrix} e_{xx} \\ e_{yy} \\ e_{zz} \\ e_{xy} \\ e_{yz} \\ e_{zx} \end{Bmatrix} = \begin{Bmatrix} \dfrac{\partial u}{\partial x} \\[2mm] \dfrac{\partial v}{\partial y} \\[2mm] \dfrac{\partial w}{\partial z} \\[2mm] \dfrac{\partial u}{\partial y} + \dfrac{\partial v}{\partial x} \\[2mm] \dfrac{\partial v}{\partial z} + \dfrac{\partial w}{\partial y} \\[2mm] \dfrac{\partial w}{\partial x} + \dfrac{\partial u}{\partial z} \end{Bmatrix} \qquad (5.8)$$

And, by differentiating Eqs.5.1 according to the scheme of Eq.5.7, we can demonstrate:

$$[N] = \begin{bmatrix} 0 & 1 & 0 & 0 & 0 & 0 & 0 & 0 & 0 & 0 & 0 & 0 \\ 0 & 0 & 0 & 0 & 0 & 0 & 1 & 0 & 0 & 0 & 0 & 0 \\ 0 & 0 & 0 & 0 & 0 & 0 & 0 & 0 & 0 & 0 & 0 & 1 \\ 0 & 0 & 1 & 0 & 0 & 1 & 0 & 0 & 0 & 0 & 0 & 0 \\ 0 & 0 & 0 & 0 & 0 & 0 & 0 & 1 & 0 & 0 & 1 & 0 \\ 0 & 0 & 0 & 1 & 0 & 0 & 0 & 0 & 0 & 1 & 0 & 0 \end{bmatrix} \qquad (5.9)$$

II- Hexahedral Element:

This element consists of a rectangular parallelepiped shown in Fig.5.2; it has eight nodes located at the corners and six surfaces. The sides are parallel to the reference axes. The study of the properties of this element is facilitated by introducing the non-dimensional coordinates, x', y' and z', defined in matrix form:

144

$$\begin{Bmatrix} x \\ y \\ z \end{Bmatrix} = \begin{bmatrix} h_x & 0 & 0 \\ 0 & h_y & 0 \\ 0 & 0 & h_z \end{bmatrix} \begin{Bmatrix} x' \\ y' \\ z' \end{Bmatrix} \tag{5.10}$$
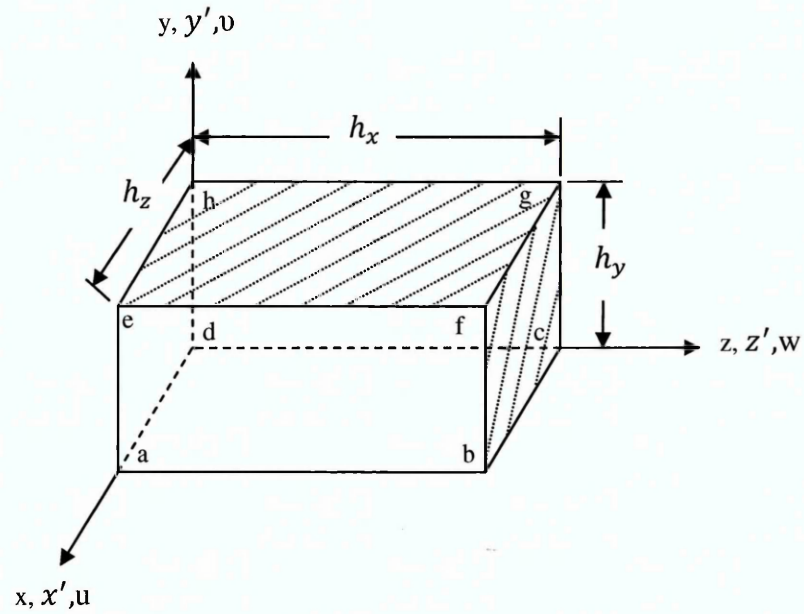
Figure 5.2 A hexahedral element.

The variation of each component of displacement with nodes can be assumed in terms of a polynomial, defined by eight constant as follows:

$$\left.\begin{aligned}
u(x',y',z') &= A_0 + A_1 x' + A_2 y' + A_3 z' + A_4 x'y' + A_5 y'z' + A_6 z'x' + A_7 x'y'z' \\
v(x',y',z') &= A_8 + A_9 x' + A_{10} y' + A_{11} z' + A_{12} x'y' + A_{13} y'z' + A_{14} z'x' + A_{15} x'y'z' \\
w(x',y',z') &= A_{16} + A_{17} x' + A_{18} y' + A_{19} z' + A_{20} x'y' + A_{21} y'z' + A_{22} z'x' + A_{23} x'y'z'
\end{aligned}\right\}$$

$$\tag{5.11}$$

Writing these equations in the matrix form:

145

$$\{U\} = \begin{Bmatrix} u(x',y',z') \\ v(x',y',z') \\ w(x',y',z') \end{Bmatrix}$$

(5.12)

$$\{A\} = \{A_0 \quad A_1 \quad ... \quad A_{22} \quad A_{23}\}^T$$

(5.13)

The nodes displacements are obtained by substituting the coordinates of the nodes into Eqs.5.11 and writing these displacements in the following matrix form:

$$\{\mathbf{u}\} = \{u_{ai} \quad v_{ai} \quad w_{ai} \quad ... \quad u_{hi} \quad v_{hi} \quad w_{hi}\}^T$$

(5.14)

And

$$[c] = \begin{bmatrix} L_1 & M_1 & S_1 \\ L_2 & M_2 & S_2 \\ L_3 & M_3 & S_3 \\ L_4 & M_4 & S_4 \end{bmatrix}$$

(5.15)

In Which

$$\{L_1\} = \begin{Bmatrix} 1 & x'_a & y'_a & z'_a & x'_a y'_a & y'_a z'_a & z'_a x'_a & x'_a y'_a z'_a \\ 0 & 0 & 0 & 0 & 0 & 0 & 0 & 0 \\ 0 & 0 & 0 & 0 & 0 & 0 & 0 & 0 \\ 1 & x'_b & y'_b & z'_b & x'_b y'_b & y'_b z'_b & z'_b x'_b & x'_b y'_b z'_b \\ 0 & 0 & 0 & 0 & 0 & 0 & 0 & 0 \\ 0 & 0 & 0 & 0 & 0 & 0 & 0 & 0 \end{Bmatrix}$$

(5.16a)

$$\{L_2\} = \begin{Bmatrix} 1 & x'_c & y'_c & z'_c & x'_c y'_c & y'_c z'_c & z'_c x'_c & x'_c y'_c z'_c \\ 0 & 0 & 0 & 0 & 0 & 0 & 0 & 0 \\ 0 & 0 & 0 & 0 & 0 & 0 & 0 & 0 \\ 1 & x'_d & y'_d & z'_d & x'_d y'_d & y'_d z'_d & z'_d x'_d & x'_d y'_d z'_d \\ 0 & 0 & 0 & 0 & 0 & 0 & 0 & 0 \\ 0 & 0 & 0 & 0 & 0 & 0 & 0 & 0 \end{Bmatrix}$$

(5.16b)

$$\{L_3\} = \begin{Bmatrix} 1 & x'_e & y'_e & z'_e & x'_e y'_e & y'_e z'_e & z'_e x'_e & x'_e y'_e z'_e \\ 0 & 0 & 0 & 0 & 0 & 0 & 0 & 0 \\ 0 & 0 & 0 & 0 & 0 & 0 & 0 & 0 \\ 1 & x'_f & y'_f & z'_f & x'_f y'_f & y'_f z'_f & z'_f x'_f & x'_f y'_f z'_f \\ 0 & 0 & 0 & 0 & 0 & 0 & 0 & 0 \\ 0 & 0 & 0 & 0 & 0 & 0 & 0 & 0 \end{Bmatrix}$$

(5.16c)

$$\{L_4\} = \begin{Bmatrix} 1 & x'_g & y'_g & z'_g & x'_g y'_g & y'_g z'_g & z'_g x'_g & x'_g y'_g z'_g \\ 0 & 0 & 0 & 0 & 0 & 0 & 0 & 0 \\ 0 & 0 & 0 & 0 & 0 & 0 & 0 & 0 \\ 1 & x'_h & y'_h & z'_h & x'_h y'_h & y'_h z'_h & z'_h x'_h & x'_h y'_h z'_h \\ 0 & 0 & 0 & 0 & 0 & 0 & 0 & 0 \\ 0 & 0 & 0 & 0 & 0 & 0 & 0 & 0 \end{Bmatrix}$$

(5.16d)

$$\{M_1\} = \begin{Bmatrix} 0 & 0 & 0 & 0 & 0 & 0 & 0 & 0 \\ 1 & x'_a & y'_a & z'_a & x'_a y'_a & y'_a z'_a & z'_a x'_a & x'_a y'_a z'_a \\ 0 & 0 & 0 & 0 & 0 & 0 & 0 & 0 \\ 0 & 0 & 0 & 0 & 0 & 0 & 0 & 0 \\ 1 & x'_b & y'_b & z'_b & x'_b y'_b & y'_b z'_b & z'_b x'_b & x'_b y'_b z'_b \\ 0 & 0 & 0 & 0 & 0 & 0 & 0 & 0 \end{Bmatrix}$$

(5.16e)

$$\{M_2\} = \begin{Bmatrix} 0 & 0 & 0 & 0 & 0 & 0 & 0 & 0 \\ 1 & x'_c & y'_c & z'_c & x'_c y'_c & y'_c z'_c & z'_c x'_c & x'_c y'_c z'_c \\ 0 & 0 & 0 & 0 & 0 & 0 & 0 & 0 \\ 0 & 0 & 0 & 0 & 0 & 0 & 0 & 0 \\ 1 & x'_d & y'_d & z'_d & x'_d y'_d & y'_d z'_d & z'_d x'_d & x'_d y'_d z'_d \\ 0 & 0 & 0 & 0 & 0 & 0 & 0 & 0 \end{Bmatrix}$$

(5.16f)

$$\{M_3\} = \begin{Bmatrix} 0 & 0 & 0 & 0 & 0 & 0 & 0 & 0 \\ 1 & x'_e & y'_e & z'_e & x'_e y'_e & y'_e z'_e & z'_e x'_e & x'_e y'_e z'_e \\ 0 & 0 & 0 & 0 & 0 & 0 & 0 & 0 \\ 0 & 0 & 0 & 0 & 0 & 0 & 0 & 0 \\ 1 & x'_f & y'_f & z'_f & x'_f y'_f & y'_f z'_f & z'_f x'_f & x'_f y'_f z'_f \\ 0 & 0 & 0 & 0 & 0 & 0 & 0 & 0 \end{Bmatrix}$$

(5.16g)

$$\{M_4\} = \begin{Bmatrix} 0 & 0 & 0 & 0 & 0 & 0 & 0 & 0 \\ 1 & x'_g & y'_g & z'_g & x'_g y'_g & y'_g z'_g & z'_g x'_g & x'_g y'_g z'_g \\ 0 & 0 & 0 & 0 & 0 & 0 & 0 & 0 \\ 0 & 0 & 0 & 0 & 0 & 0 & 0 & 0 \\ 1 & x'_h & y'_h & z'_h & x'_h y'_h & y'_h z'_h & z'_h x'_h & x'_h y'_h z'_h \\ 0 & 0 & 0 & 0 & 0 & 0 & 0 & 0 \end{Bmatrix}$$

(5.16h)

$$\{S_1\} = \begin{Bmatrix} 0 & 0 & 0 & 0 & 0 & 0 & 0 & 0 \\ 0 & 0 & 0 & 0 & 0 & 0 & 0 & 0 \\ 1 & x'_a & y'_a & z'_a & x'_a y'_a & y'_a z'_a & z'_a x'_a & x'_a y'_a z'_a \\ 0 & 0 & 0 & 0 & 0 & 0 & 0 & 0 \\ 0 & 0 & 0 & 0 & 0 & 0 & 0 & 0 \\ 1 & x'_b & y'_b & z'_b & x'_b y'_b & y'_b z'_b & z'_b x'_b & x'_b y'_b z'_b \end{Bmatrix}$$

(5.16i)

147

$$\{S_2\} = \begin{Bmatrix} \begin{pmatrix} 0 & 0 & 0 & 0 & 0 & 0 & 0 & 0 \\ 0 & 0 & 0 & 0 & 0 & 0 & 0 & 0 \\ 1 & x'_c & y'_c & z'_c & x'_c y'_c & y'_c z'_c & z'_c x'_c & x'_c y'_c z'_c \\ \\ 0 & 0 & 0 & 0 & 0 & 0 & 0 & 0 \\ 0 & 0 & 0 & 0 & 0 & 0 & 0 & 0 \\ 1 & x'_d & y'_d & z'_d & x'_d y'_d & y'_d z'_d & z'_d x'_d & x'_d y'_d z'_d \end{pmatrix} \end{Bmatrix} \qquad (5.16j)$$

$$\{S_3\} = \begin{Bmatrix} \begin{pmatrix} 0 & 0 & 0 & 0 & 0 & 0 & 0 & 0 \\ 0 & 0 & 0 & 0 & 0 & 0 & 0 & 0 \\ 1 & x'_e & y'_e & z'_e & x'_e y'_e & y'_e z'_e & z'_e x'_e & x'_e y'_e z'_e \\ \\ 0 & 0 & 0 & 0 & 0 & 0 & 0 & 0 \\ 0 & 0 & 0 & 0 & 0 & 0 & 0 & 0 \\ 1 & x'_f & y'_f & z'_f & x'_f y'_f & y'_f z'_f & z'_f x'_f & x'_f y'_f z'_f \end{pmatrix} \end{Bmatrix} \qquad (5.16k)$$

$$\{S_4\} = \begin{Bmatrix} \begin{pmatrix} 0 & 0 & 0 & 0 & 0 & 0 & 0 & 0 \\ 0 & 0 & 0 & 0 & 0 & 0 & 0 & 0 \\ 1 & x'_g & y'_g & z'_g & x'_g y'_g & y'_g z'_g & z'_g x'_g & x'_g y'_g z'_g \\ \\ 0 & 0 & 0 & 0 & 0 & 0 & 0 & 0 \\ 0 & 0 & 0 & 0 & 0 & 0 & 0 & 0 \\ 1 & x'_h & y'_h & z'_h & x'_h y'_h & y'_h z'_h & z'_h x'_h & x'_h y'_h z'_h \end{pmatrix} \end{Bmatrix} \qquad (5.16l)$$

The strain within the element can be displayed in a matrix form as follows:

$$\{\epsilon\} = [N]\,[c^{-1}] \begin{Bmatrix} u_a \\ v_a \\ w_a \\ u_b \\ v_b \\ w_b \\ \vdots \\ u_g \\ v_g \\ w_g \\ u_h \\ v_h \\ w_h \end{Bmatrix} \qquad (5.16)$$

148

Where

$$\{\epsilon\} = \begin{Bmatrix} \epsilon_{xx} \\ \epsilon_{yy} \\ \epsilon_{zz} \\ \gamma_{xy} \\ \gamma_{yz} \\ \gamma_{zx} \end{Bmatrix} = \begin{Bmatrix} \dfrac{1}{h_x}\dfrac{\partial u}{\partial x'} \\[2mm] \dfrac{1}{h_y}\dfrac{\partial v}{\partial y'} \\[2mm] \dfrac{1}{h_z}\dfrac{\partial w}{\partial z'} \\[2mm] \dfrac{1}{h_y}\dfrac{\partial u}{\partial y'} + \dfrac{1}{h_x}\dfrac{\partial v}{\partial x'} \\[2mm] \dfrac{1}{h_z}\dfrac{\partial v}{\partial z'} + \dfrac{1}{h_y}\dfrac{\partial w}{\partial y'} \\[2mm] \dfrac{1}{h_x}\dfrac{\partial w}{\partial x'} + \dfrac{1}{h_z}\dfrac{\partial u}{\partial z'} \end{Bmatrix} \tag{5.17}$$

And, by differentiating Eqs.5.11 according to the scheme of Eq.5.17, we can demonstrate:

$$[N] = \begin{bmatrix} 0 & \dfrac{1}{h_x} & 0 & 0 & \dfrac{y'}{h_x} & 0 & \dfrac{z'}{h_x} & \dfrac{y'z'}{h_x} \\[3mm] 0 & 0 & \dfrac{1}{h_y} & 0 & \dfrac{x'}{h_y} & \dfrac{z'}{h_y} & 0 & \dfrac{x'z'}{h_y} \\[3mm] 0 & 0 & 0 & \dfrac{1}{h_z} & 0 & \dfrac{y'}{h_z} & \dfrac{x'}{h_z} & \dfrac{x'y'}{h_z} \\[3mm] 0 & \dfrac{1}{h_x} & \dfrac{1}{h_y} & 0 & \left(\dfrac{x'}{h_y}+\dfrac{y'}{h_x}\right) & \dfrac{z'}{h_y} & \dfrac{z'}{h_x} & \left(\dfrac{x'z'}{h_y}+\dfrac{y'z'}{h_x}\right) \\[3mm] 0 & 0 & \dfrac{1}{h_y} & \dfrac{1}{h_z} & \dfrac{x'}{h_y} & \left(\dfrac{y'}{h_z}+\dfrac{z'}{h_y}\right) & \dfrac{x'}{h_z} & \left(\dfrac{x'y'}{h_z}+\dfrac{x'z'}{h_y}\right) \\[3mm] 0 & \dfrac{1}{h_x} & 0 & \dfrac{1}{h_z} & \dfrac{y'}{h_x} & \dfrac{y'}{h_z} & \left(\dfrac{z'}{h_x}+\dfrac{x'}{h_z}\right) & \left(\dfrac{y'z'}{h_x}+\dfrac{x'y'}{h_z}\right) \end{bmatrix}$$

$$\tag{5.18}$$

The element stiffness matrix, for instance, will be given from the primary matrix forms by:

$$[K_i] = [c^{-1}]^T [\bar{K}] [c^{-1}] \qquad (5.19)$$

where;

$$[\bar{K}] = V.[N]^T [D] [N] \qquad (5.20)$$

$V = \int dx\, dy\, dz$ = Volume of the element type.

$[D]$ = Material property matrix.

5.2.3 Specification of Material Property:

The important aspect of pre-processing in the finite element analysis simulation is the material property requirements, depending on the application and the material selection. In the ANSYS software, different types of material property data sets are stored in the archived material library file; each material property set has reference number and its own library file. If the material is not included in the library as is in the present two cases, the capability of adding a new archive material library file is possible by defining the selected material property data in the ANSYS Main Menu / Material Models, as the data used in the three cases was produced for AISI 420 martensitic stainless steel.

In the fatigue analysis, the fatigue material data is stored as tabular and graphical view as stress versus life points along with the ability for creating the self-generated material fatigue data and the capability to define the mean stress dependent or multiple R-ratio curves, if the data is available.

The relation between the stress and strain in anisotropic material property is found in many finite elements studies [122, 123].

$$[\sigma] = [D]\{\epsilon\} \qquad\qquad (5.21)$$

where;

$$
\begin{bmatrix} \sigma_{xx} \\ \sigma_{yy} \\ \sigma_{zz} \\ \tau_{xy} \\ \tau_{yz} \\ \tau_{zx} \end{bmatrix}
= \frac{E}{(1+v)(1-2v)}
\begin{bmatrix}
1-v & v & v & 0 & 0 & 0 \\
v & 1-v & v & 0 & 0 & 0 \\
v & v & 1-v & 0 & 0 & 0 \\
0 & 0 & 0 & \dfrac{1-2v}{2} & 0 & 0 \\
0 & 0 & 0 & 0 & \dfrac{1-2v}{2} & 0 \\
0 & 0 & 0 & 0 & 0 & \dfrac{1-2v}{2}
\end{bmatrix}
\{\epsilon\}
$$

$$(5.22)$$

5.2.4 Specification of Boundary Conditions:

The models are usually subjected to different service environments and operational conditions during their lives. It is, therefore, important to consider the material type and all possible scenarios of external loads and constraints, which are called boundary conditions. The results of analysis directly depend on the specified loads and constraints which are applied to the geometrical entities as features that are fully associative to geometry and automatically adjust to geometrical changes. The types of loads and constraints available in the simulation depend on the type of the study. They are applied by fixtures which allow zero or non-zero displacements on vertices, edges, or faces for use with static, frequency, buckling, dynamic and nonlinear studies and external loads, which are combined to directional and thermal loading.

The cases studied are made by applying the boundary conditions as a fixtures, external loading and temperature similar to the experimental tests which are carried out in the laboratory by fixing one end of the solid cylindrical specimen with zero displacements in all directions and applying the maximum force of the cyclic tension

151

load on the other end, with and without supplying a constant temperature on the outer surface of the specimen, also a transient heating or cooling thermal shock loading is subjected to the outer and inner surface, respectively in the hollow cylinder specimen.

In the case studied, complete model within element boundaries is subjected to mechanical loading described by body forces and thermal strain due to temperature effects. In general, the mechanical nodal forces for all nodes, corresponding to the x, y and z coordinates are:

$$[F_i] = \begin{Bmatrix} F_1(x,y,z) \\ \vdots \\ F_n(x,y,z) \end{Bmatrix} = [K_i] \{u\} \tag{5.23}$$

These forces are equal to zero at the fixed end and maximum applied load at the loaded end as a mechanical applied load. While the thermal strain due to thermal expansion in an isotropic material, can be simplified.

$$[\epsilon_{th}] = \alpha T \begin{Bmatrix} 1 \\ 1 \\ 1 \\ 0 \\ 0 \\ 0 \end{Bmatrix} \tag{5.24}$$

where; T is a constant temperature in the isothermal fatigue case and a function of time in the transient thermal shock case.

5.4 Simulation and Solution Stage:

A set of discrete simultaneous system equations based on the mesh generation can be formulated using existing approaches. There are many types of approaches for establishing the simultaneous equations. However, the engineering practice has so far shown two approaches that are most often used for solid and complex structures. The

first is based on energy principles, such as Hamilton's principle, the minimum potential energy principle, and so on. The traditional finite element method is established on these principles. The second approach is the weighted residual method, which is also often used for establishing finite element method equations for many physical problems, such as heat transfer problems [120].

When the computational model has been made, it is then fed to a solver to give the solution of the discrete system, simultaneous equations for the nodes of the mesh elements. This is the most computer hardware demanding process. Different software packages use different algorithms depending upon the physical phenomenon to be established. There are two very important considerations when choosing algorithms for solving a system of equations, one is the storage required and the other is the Central Processing Unit CPU time needed. There are two main types of methods for solving simultaneous equations, direct and iterative methods. Commonly used direct methods include the Gauss elimination method and the LU decomposition method. Those methods work well for relatively small equation systems, and also can be coded in such a way as to avoid full assembly of the system matrices in order to save significantly on the storage. Direct methods operate on fully assembled system equations, and therefore demand larger storage space. Iterative methods include the Gauss–Jacobi method, the Gauss–Deidel method, the SOR method, generalized conjugate residual methods, the line relaxation method, and so on. These methods work well for relatively larger systems [120].

The general thermo–elastic–plastic finite element simulation for a body with force and applied temperature, which is a steady state in the isothermal fatigue case and transient in the thermo-mechanical case, to its exterior boundary can be produced by solving the set of equations.

The temperature distribution in terms of the nodal values in the steady-state case can be obtained by the equation.

$$-\nabla^T k \nabla T + Q = 0 \qquad\qquad (5.25)$$

where

$$\nabla = \begin{Bmatrix} \dfrac{\partial}{\partial x} \\[4pt] \dfrac{\partial}{\partial y} \\[4pt] \dfrac{\partial}{\partial z} \end{Bmatrix} \qquad (5.26)$$

Q = a relevant quantity generated by the case boundary condition.

The temperature distribution in terms of the nodal values in the transient case can be obtained by the equation.

$$\frac{\partial T}{\partial t} - \nabla^2 T = 0 \qquad (5.27)$$

The general stress–strain relationship for a three dimensional isotropic body under thermo-mechanical loading is given by:

$$[\sigma] = [D]\{\epsilon\} - [D][\epsilon_{th}] \qquad (5.28)$$

The plastic von Mises stress distribution in terms of the nodal values can be obtained by the equation.

$$\sigma_{VM} = \sqrt{\left((\sigma_x - \sigma_y)^2 + (\sigma_y - \sigma_z)^2 + (\sigma_z - \sigma_x)^2 \right)/2} \qquad (5.29)$$

And the stress and strain intensity factors of nodal by the equations.

$$K_I = \sigma_{VM}\, Y \sqrt{\pi\, \mathbf{u}} \qquad (5.30)$$

$$K_\epsilon = \frac{K_I}{E} \qquad (5.31)$$

The stress life fatigue module analysis is based on the S-N curve, which is experimentally existed as an input data at different mean stress and R-ratio. The determination of the alternating and mean stresses for the applied loading can be measured by taking the applied load as the maximum value of the cyclic loading expressed by the equations.

$$\sigma_a = \sigma_{max} \left(\frac{1-R}{2}\right) \tag{5.32}$$

$$\sigma_m = \sigma_{max} \left(\frac{1+R}{2}\right) \tag{5.33}$$

The expected life of the body under the applied load can be accounted for directly through the interpolation between the material input data [124].

5.5 Post-Processing Stage:

The results generated after solving the system equation usually have to be visualized in such a way that it is easy to interpolate, analyse and present. The visualization is performed through the post-processor, usually packaged together with the software. Most of these processors allow the user to display three dimension objects in many convenient and colourful ways on the screen. The object can be displayed in the form of wire-frames, group of elements, and group of nodes. The user can rotate, translate and zoom into and out of the objects. Tools to enhance the visual effects are also available, such as shading, lighting and shrinking. Animations and movies can also be produced to simulate the dynamic aspects of a problem. Outputs in the form of tables, text files and x-y plots are also routinely available.

ANSYS software runs to calculate the results of the optimum design. Each case study is based on a set of values for the design variables and the software runs all studies associated with the objectives, functions, and constraints. In the present study, the viewing of the solution results produces an equivalent von-Mises stress, stress intensity factor, strain intensity factor, alternating fatigue stress and fatigue life.

155

5.6 The Cases Studied:

5.6.1 Low Cycle Fatigue Analysis:

In this case study, solutions are provided by selecting the appropriate project model in the analysis system choosing the static structural.

5.6.1.1 Pre-Processing Stage:

During this case study, the main material properties added to the solution types are as follows:

1- Physical properties:

    - Density.

    - Isotropic secant coefficient of thermal expansion.

2- Linear Elastic properties:

    - Young's modulus of elasticity (inserting as table and graph of temperature, young's modulus and poison's ratio).

    - Poisson's ratio.

3- Experimental stress - strain data (inserting as table and graph of uniaxial tension test data).

4- Life:

    - Alternating and mean stress - life data (inserting as table and graph of mean stress, cycles and stresses).

5- Strength properties:

    - Tensile yield strength.

    - Tensile ultimate strength.

A geometrical model of the solid cylindrical samples is created by following the steps below:

1) Create the geometric model by using Solid Works 10.0, especially for complicated models, which is easy having more tools to create models, as the one used in this study; it is shown in Fig. 5.3.

2) Save the models in IGES files format.

3) Import the models into ANSYS Workbench 13.0 software as shown in Fig. 5.4.

A free and mapped mesh is applied to the geometrical model that contains the elements shapes and the mesh patterns employing the tetrahedral element type due to irregular geometric model with the total number of nodes (2913) and the total number of the elements (1651); the meshed model is shown in Fig.5.5.

Figure 5.3 The solid cylindrical geometrical designed model for low cyclic and isothermal fatigue tests created by using Solid Works 10.0 Software.

Figure 5.4 The geometrical model imported in ANSYS Workbench 13 software.
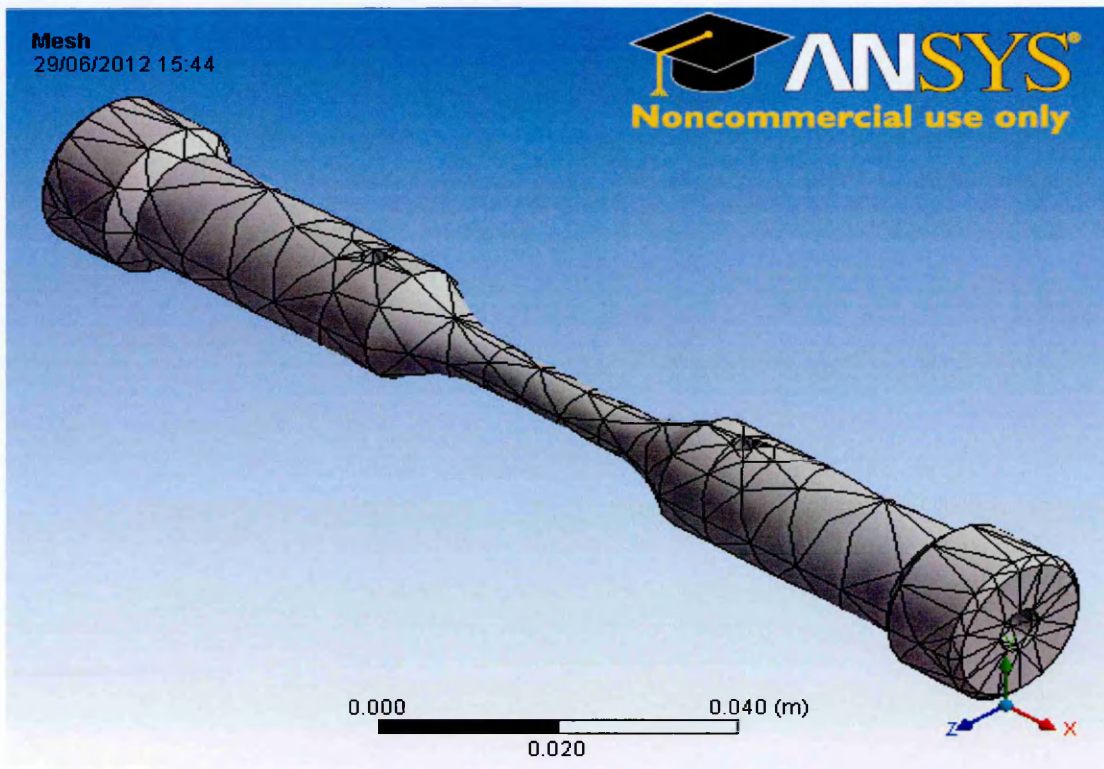
Figure 5.5 The meshing geometrical model of the low cycle fatigue case in the ANSYS Workbench 13 software.

5.6.1.2 Boundary Conditions for the Solution:

The boundary conditions of the low cycle fatigue case are:

1- Constraints:

Applying fixed support (zero displacements in all directions) at one end of the solid cylinder specimen.

2- Mechanical load:

Supplying a tension load which is equalized to the maximum applied stress, which equals($\sigma_{max} = \frac{\Delta\sigma}{1-R}$), in the experimental tests on the gage length of the solid cylinder specimen; it is repeated at different applied stress levels, 100%, 90% and 85% from the ratio of the range stress to the 0.2% yield strength of the material. The settings of the fatigue tool details are described below, where the boundary conditions are shown in Fig. (5.6):

- Fatigue strength factor (Kf) = 1

- Loading type is ratio $R = \frac{\sigma_{min}}{\sigma_{max}} = 0.1$

- Scale factor = 1

- Analysis type is for stress - life.

- Using the mean stress curves by interpolation with input data (Mean stress-Number of cycles-Stress) experimentally generated as S-N curve.

- The applied stress component is equivalent (von-Mises) stress.

- The cyclic load frequency is: 1 cycle = 1 cycle (also one can use 1 cycle = 0.2 second for 5Hz frequency, to find the life in seconds)

5.6.1.3 Post-Processing Stage:

In this case study stage, viewing of the solution results are described as follows:

- Equivalent von-Mises Stress: The maximum estimated equivalent von-Mises stress is shown to occur in the gauge length due to the minimum cross sectional area and

159

maximum applied stress in all applied loads ratio, because of the interaction effects of the stress components in the von-Mises criteria. The estimated equivalent stress at different ratios is shown in Fig.5.7a, b and c, where the per cent is the ratio between the applied stress range and the material yield strength.
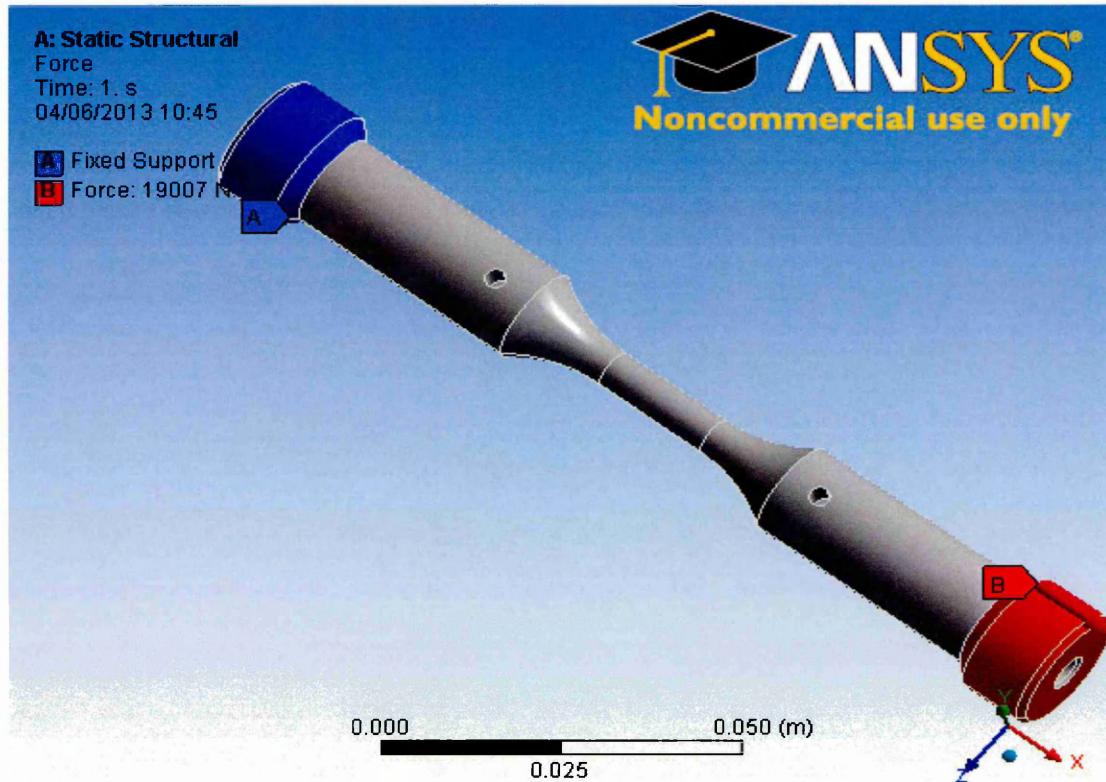
Figure 5.6 The boundary conditions of the low cycle fatigue case at 100% stress range to 0.2% yield stress percent ratio.

- Stress Intensity Factor: The total stress intensity factor is directly affected by the stress and solid cylinder shape factor. The estimated intensity factor in the software employed the equivalent von-Mises stress as it is selected in the boundaries. So, it clearly shows that the pattern of the stress intensity factor is similar to the estimated equivalent stress but it is different in magnitude. The maximum influence occurred along the gauge length, where the distribution for all the simulation is shown in Fig.5.8a, b and c.

160
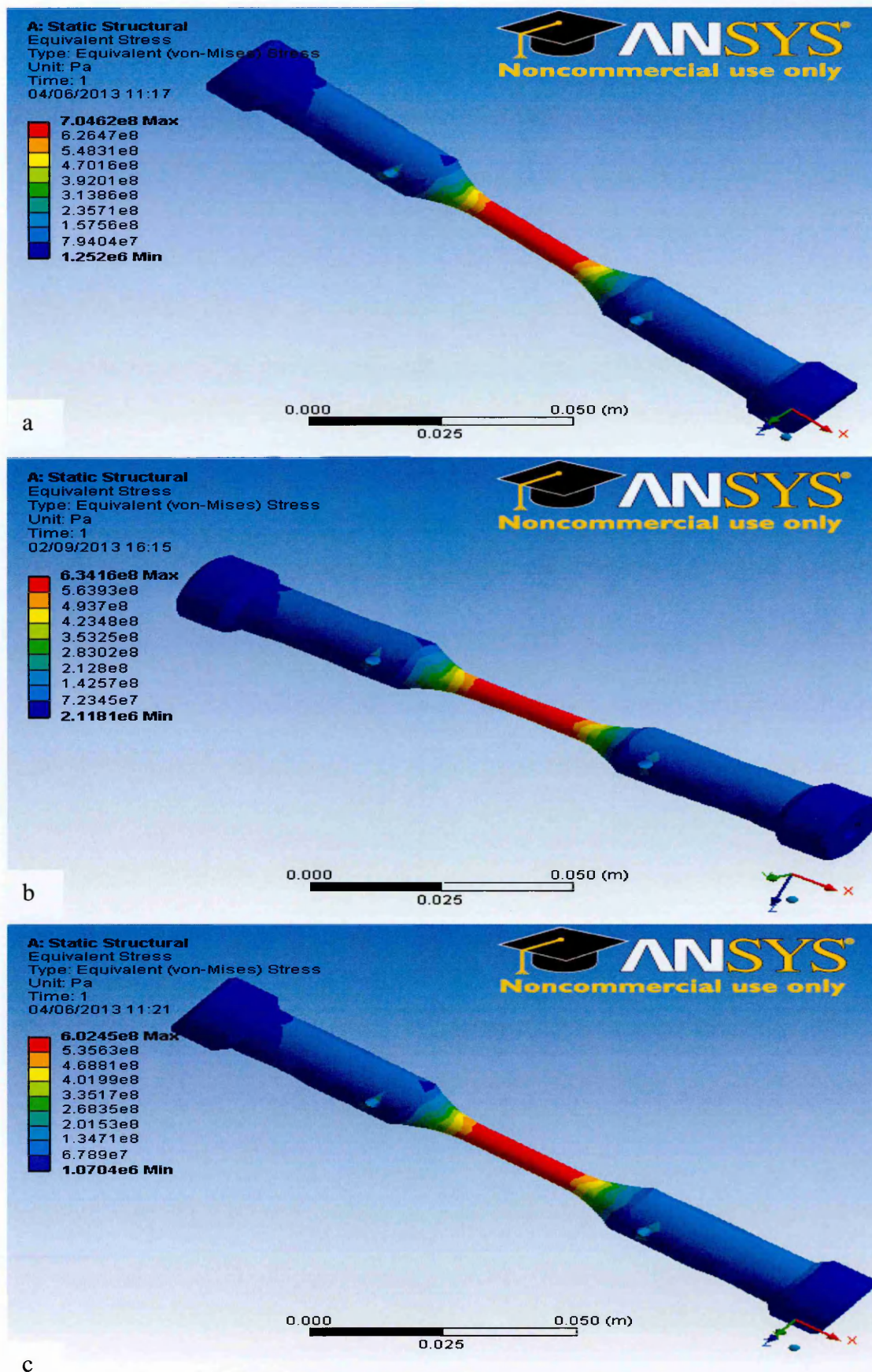
Figure 5.7 The equivalent (von-Mises) stress in low cycle fatigue case due to stress range to 0.2% yield stress ratio, (a) 100% (b) 90% and (c) 85% stress ratio.

161
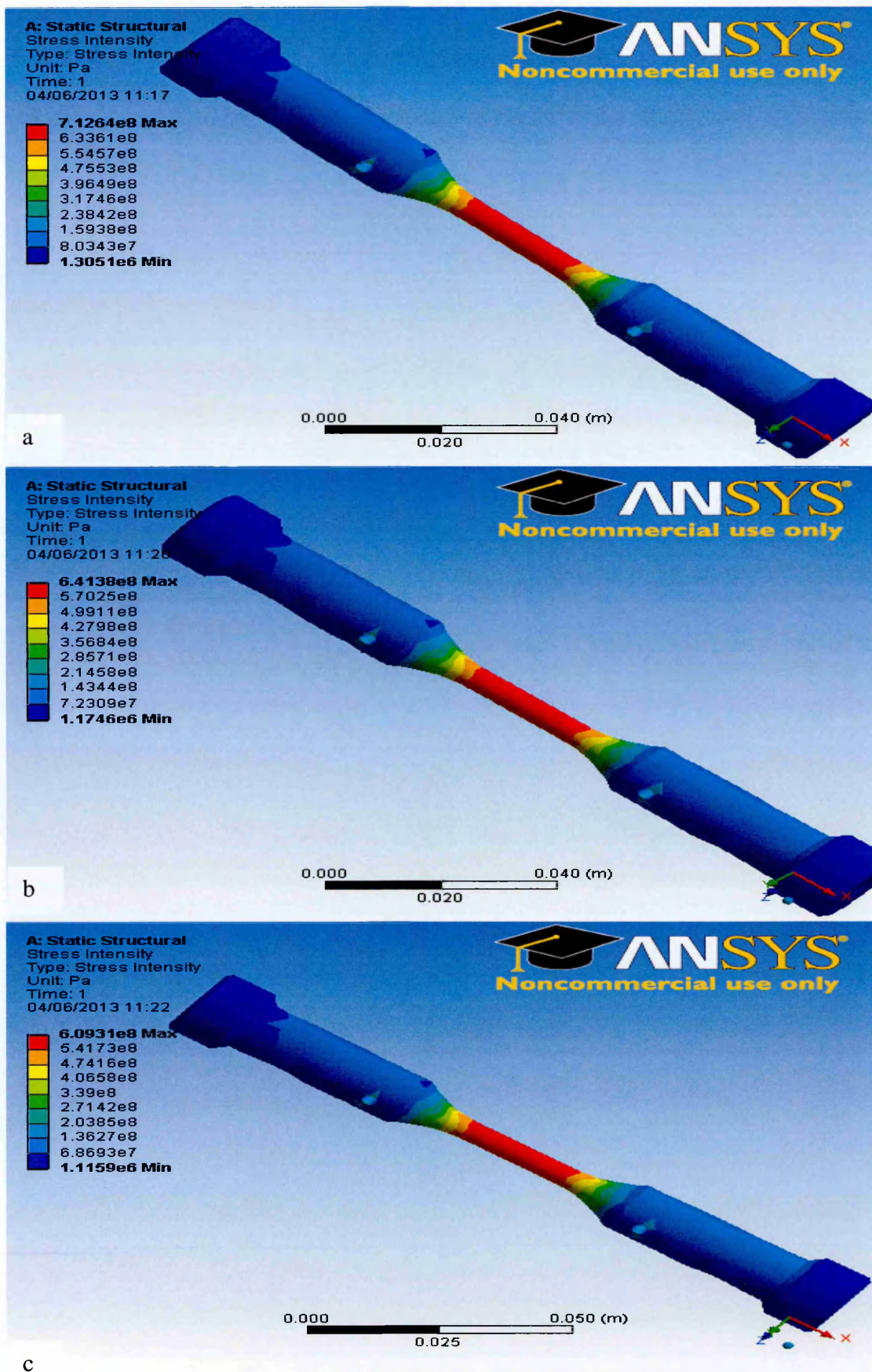
Figure 5.8 The stress intensity factor in low cycle fatigue case at (a) 100% (b) 90% and (c) 85% stress ratio.

- Strain Intensity Factor: The total strain intensity factor patterns are distributed similarly to the stress intensity factor, but in different magnitudes and also the maximum occurred along the gauge length as shown in Fig.5.9a, b and c.
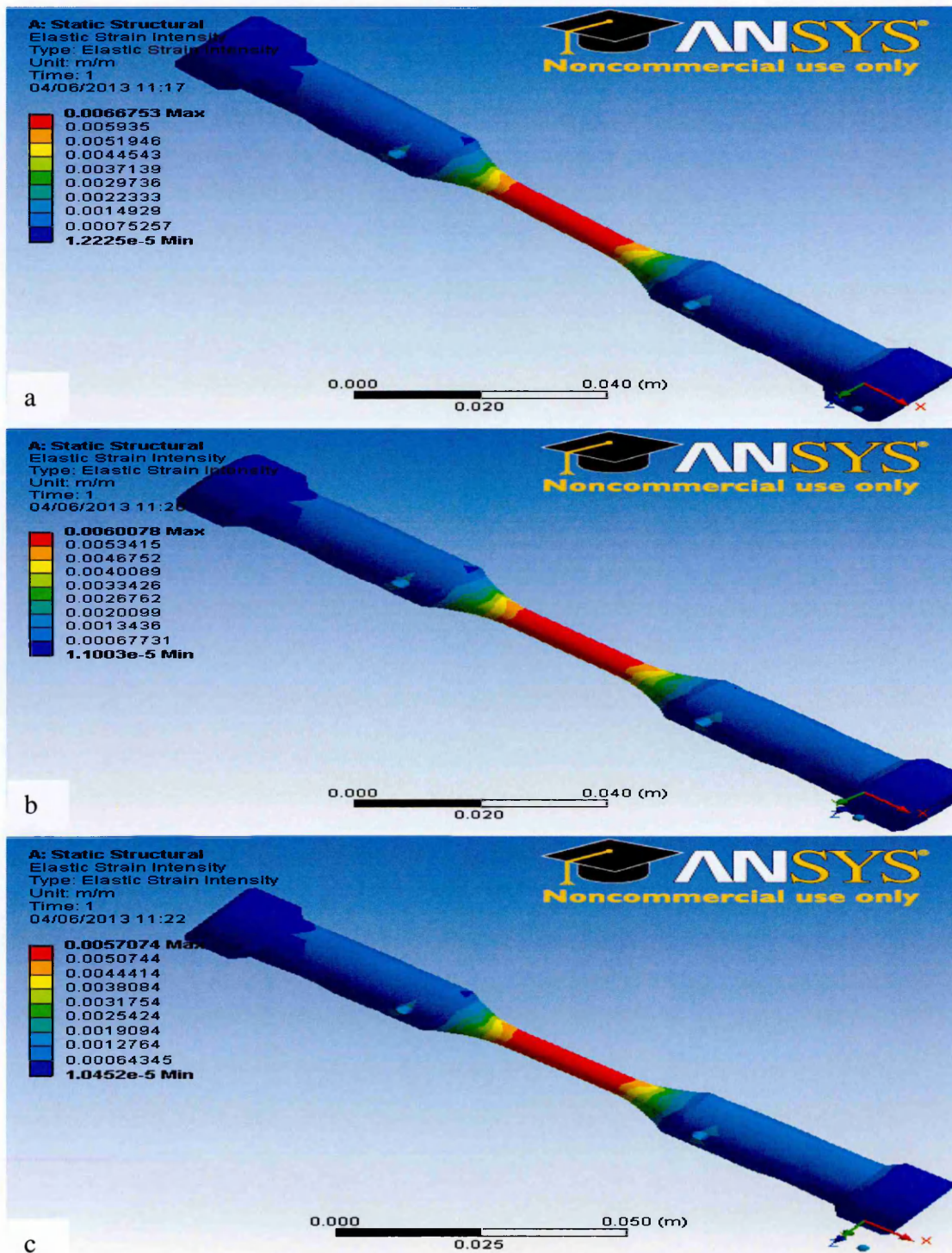
Figure 5.9 The strain intensity factor in the low cycle fatigue case.

- Fatigue Equivalent Alternating Stresses: The equivalent alternating stress depends on the loading ratio and the estimated equivalent von-Mises stress. The finding of the alternating stress is equal to half of the stress range; this is the result of the subtraction of the minimum stress from the maximum where the estimated von-Mises stress is taken as the maximum stress, while the minimum results from the multiplication of the load ratio (R) (used in the fatigue input setting is equal to 0.1) of the maximum stress. Thus, it is higher than the practical alternating stress. The result shows very close values compared to the experimental for all load ratios. For example, at 100% applied stress level, the estimated result is (317MPa) while the experimental value is (302.5MPa) and also the same comparison is valid for the other load ratios and the patterns as shown in Figs. 5.10 to 5.12.
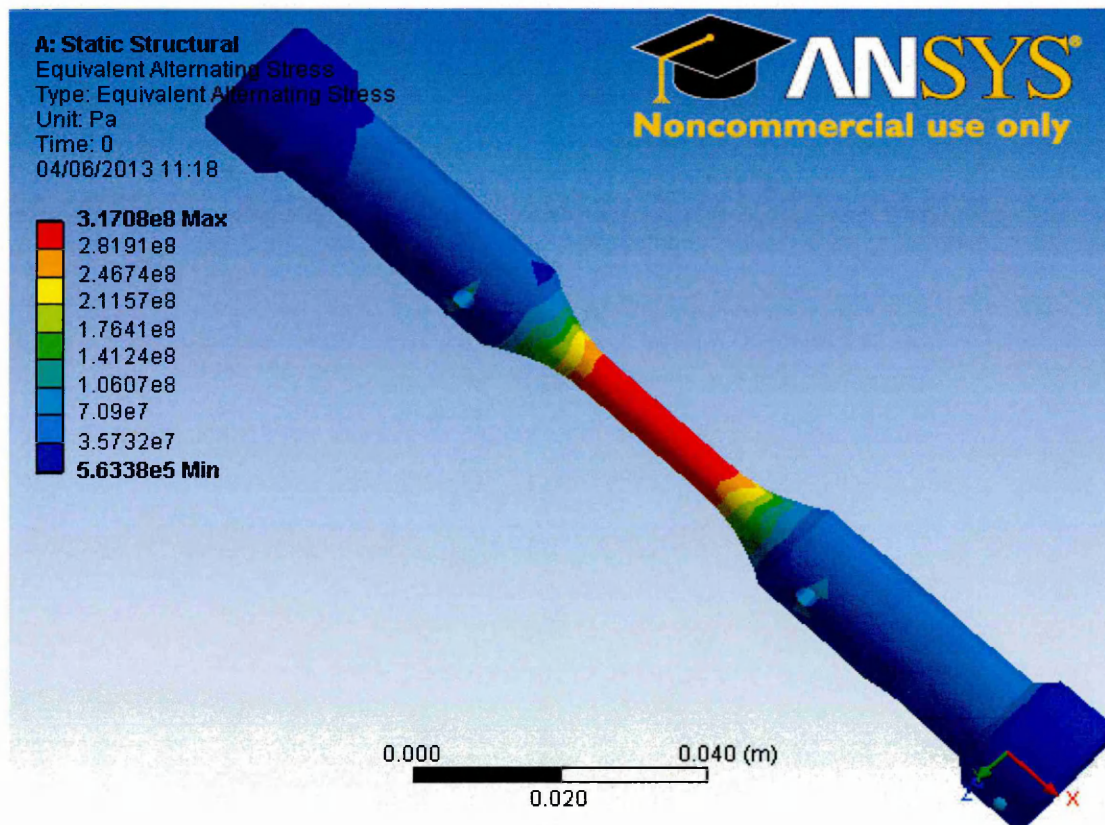
Figure 5.10 The equivalent alternating stress at 100% applied stress level.
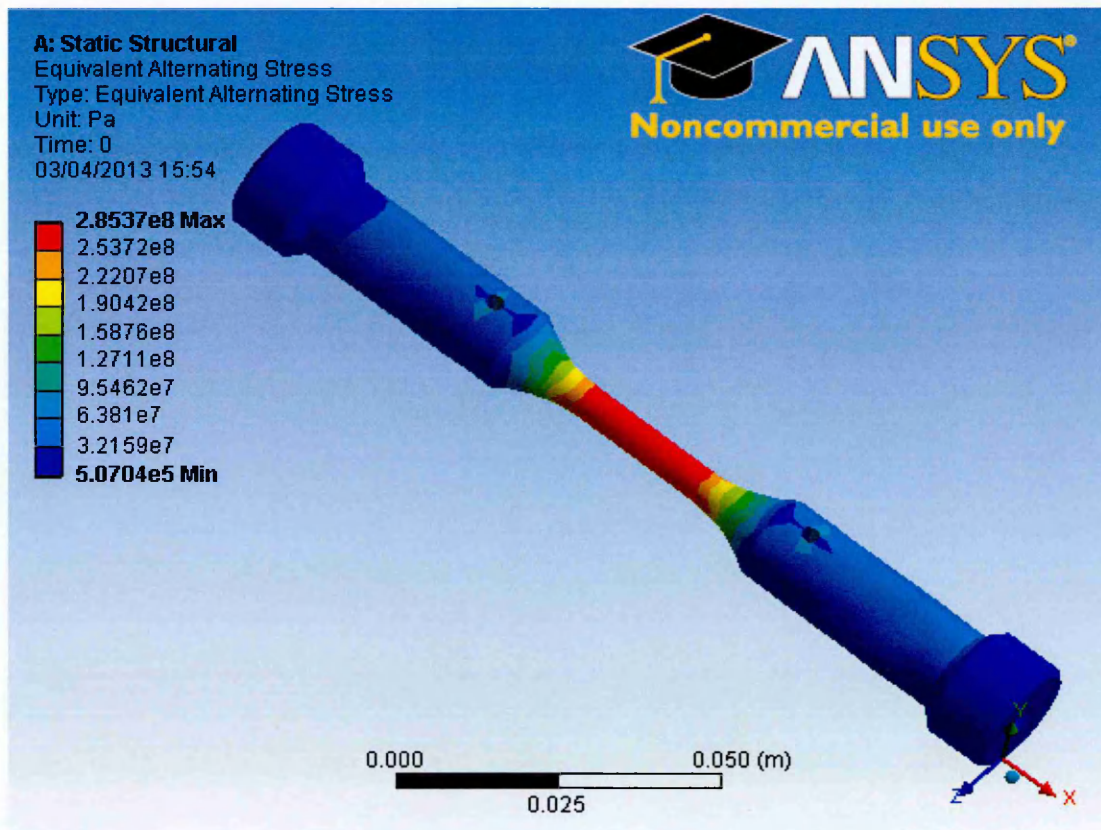
Figure 5.11 The equivalent Alternating stress at 90% applied stress level.
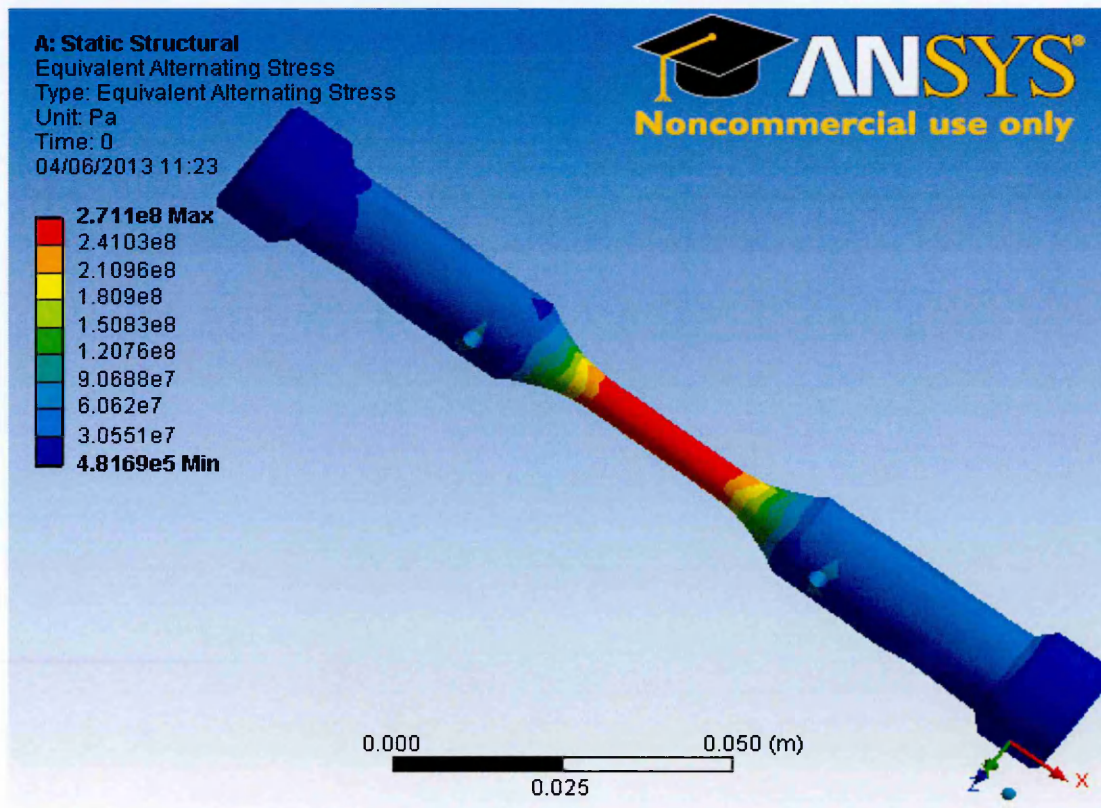
Figure 5.12 The equivalent Alternating stress at 85% applied stress level.

165

- Fatigue Life: The estimated life patterns of the sample under low cycle fatigue at different applied loading are shown in Figs 5.13. to 5.15. From the fatigue tool setting, the maximum applied load employed is the von-Mises stress, which is estimated before. The finding of the fatigue life of the specimen under von-Mises stress results from interpolation with stress range data used as an input data of mean stress-number of cycles-stress, which are used instead of alternating stress because the generated experimental data are made by using stress range and also the estimated von-Mises stress, will be higher than it. To use the alternating stress, we should subject half the maximum applied load. For that reason, at 100% load level from the yield stress, the specimen failed at the minimum life in the input data, because the applied stress is very close to the highest load level in the S-N curve. When the applied load is reduced to 90%, the simulation result shows that the failure life value is the same to the experimental data at the same load which is included in the S-N curve input data and it is the same for 85% level. Also the simulation shows the failure that occurred in the gauge length ends; this is similar to happened experimentally.
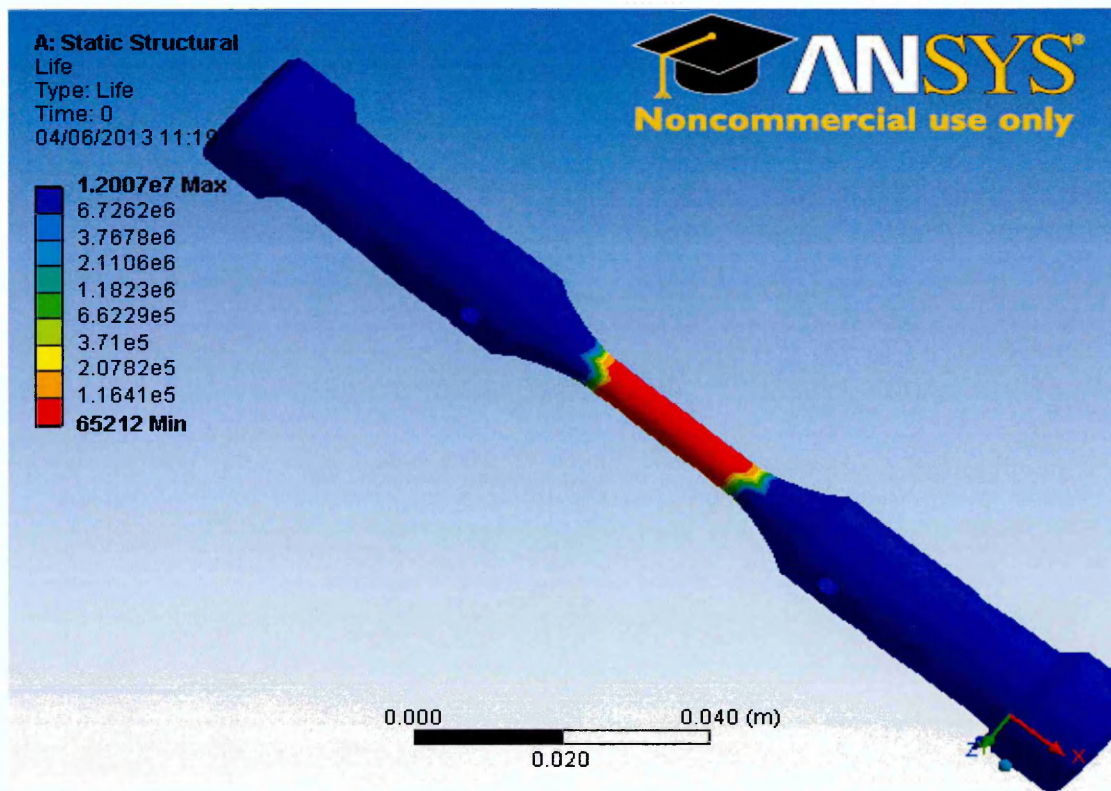
Figure 5.13 The life of 100% applied stress level.

166
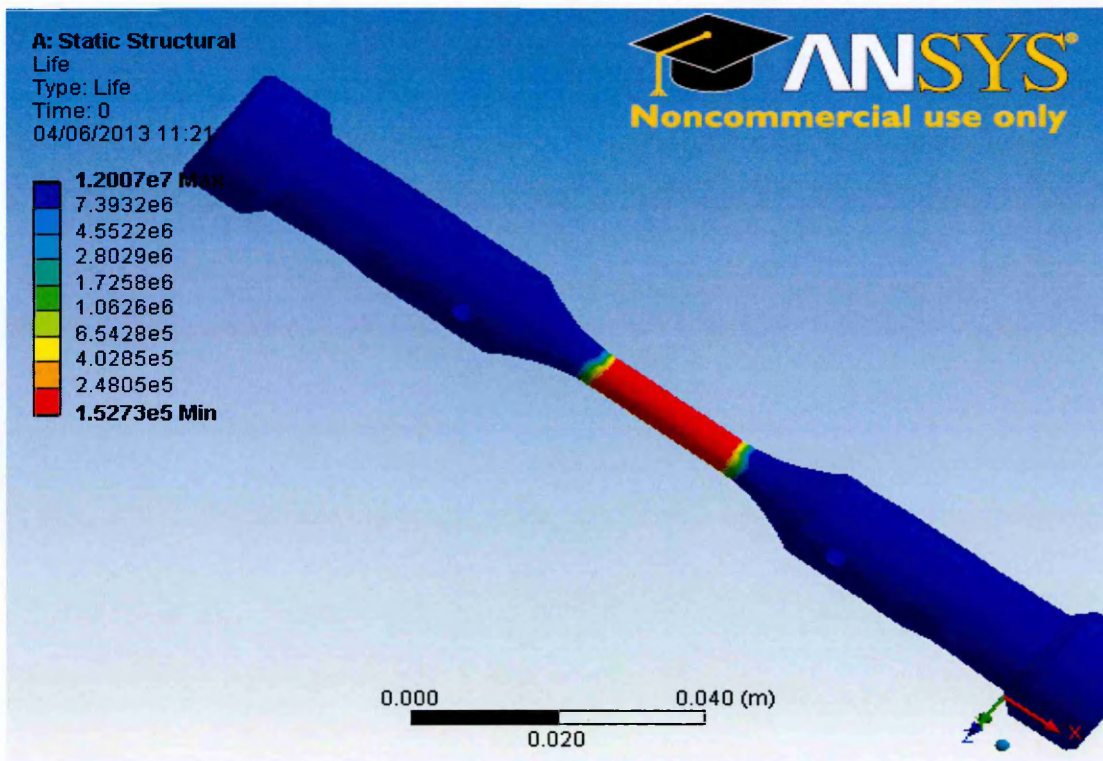
Figure 5.14 The life of 90% applied stress level.
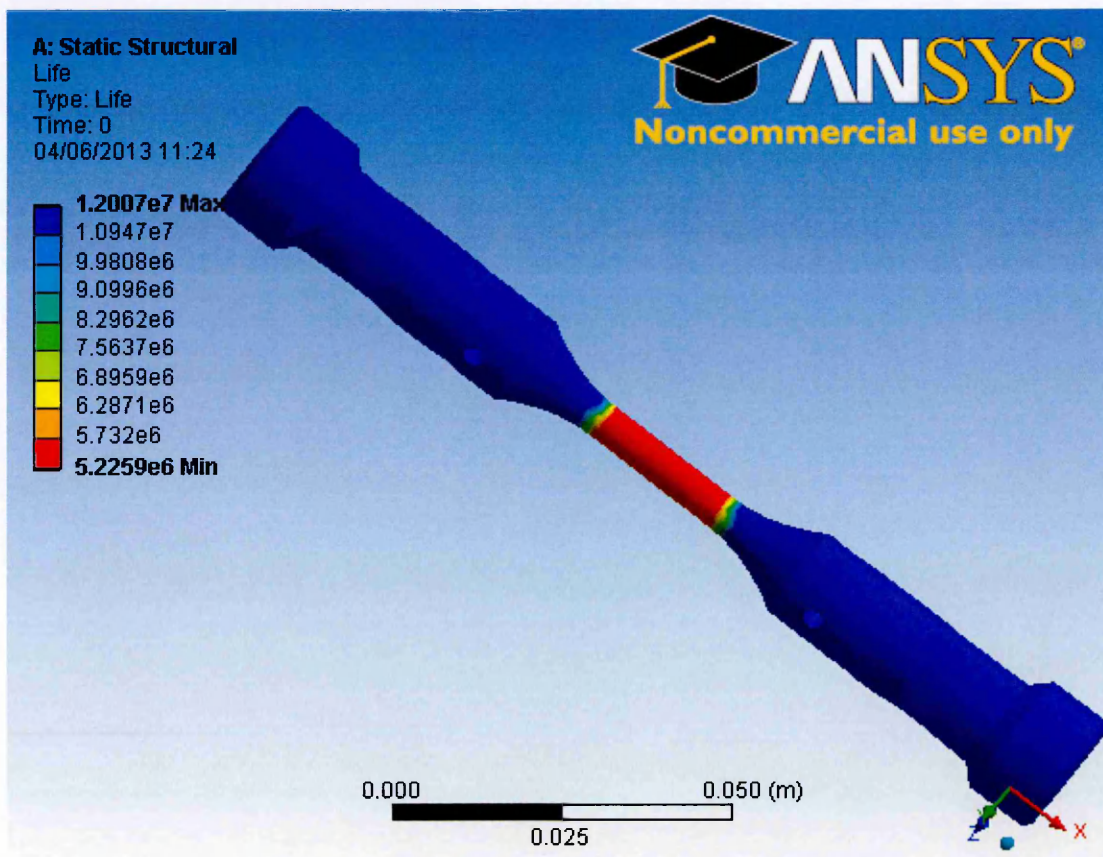
Figure 5.15 The life of 85% applied stress level.

167

5.6.2 Isothermal Fatigue Analysis:

In this study, the solution starts by selecting the type of the project model in the project model in the analysis system through choosing the steady state thermal, combined with thermal stress simulation analysis.

5.6.2.1 Pre-Processing Stage:

The thermal properties are added to the main material structural properties employed in the low cycle fatigue case:

1- Thermal property:

     - Isotropic thermal conductivity.

The creation of the geometrical model of the solid cylindrical samples and the free meshing are the same as in the first case; they are shown in Figs 5.4 and 5.5.

5.6.2.2 Solution and Boundary Conditions Stage:

The thermal boundaries are appended to the employed mechanical loading boundary conditions in the low cyclic fatigue case as detailed below:

1- Steady state thermal loading.

Supplying a selected constant temperature (Tb = 300, 500, 600 °C) at the outer surface of the solid cylinder specimen is shown in Fig 5.16 a, b and c.

5.6.2.3 Post-Processing Stage:

In this case study stage the viewing of the solution results are described by the following:

- **Equivalent von Mises Stress:** The equivalent von-Mises stress obviously occurred in the gauge length section due to the minimum cross sectional area which is reduced with raising the temperature except at 500 °C; this is due to the increment of thermal stress superimposed with the reduction in the applied mechanical stress. The results show a little higher than the experimental applied stress range, except at 300 °C are lower.

168
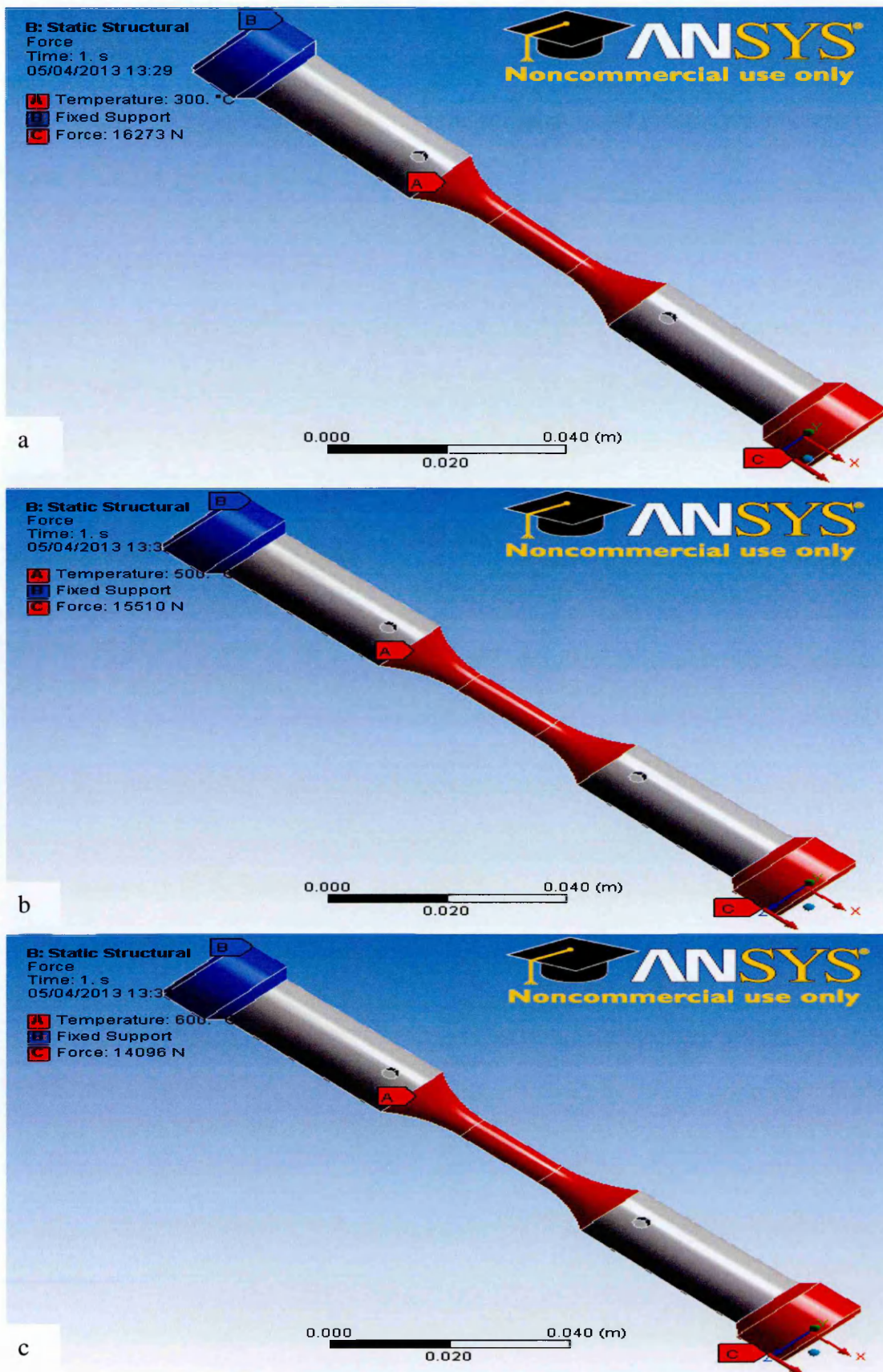
Figure 5.16 The boundary conditions of the isothermal fatigue case at a) 300 °C, b) 500 °C, c) 600 °C supplied temperatures.

Thermal stress is mainly influenced by the modulus of elasticity of the material at the conducted temperature; the total results show the minor effects of the thermal stress. The main effect is indicated by the reduction of the material strength. The effects of the stress concentration in the sharp and holes at the ends of the specimen give a high stress value especially at 600 °C (neglecting viewing it because we focus on the gauge length and realty, the holes made less depth with high curvature). The distribution patterns in different temperatures are shown in Figs. 5.17 to 5.19.

- Stress Intensity Factor: the stress intensity factor depends on the equivalent von-Mises stress. The rise in temperature decreases the stress intensity; this is similar to the estimated equivalent von-Mises stress. The distribution patterns at different temperatures are shown in Figs. 5.20 to 5.22.
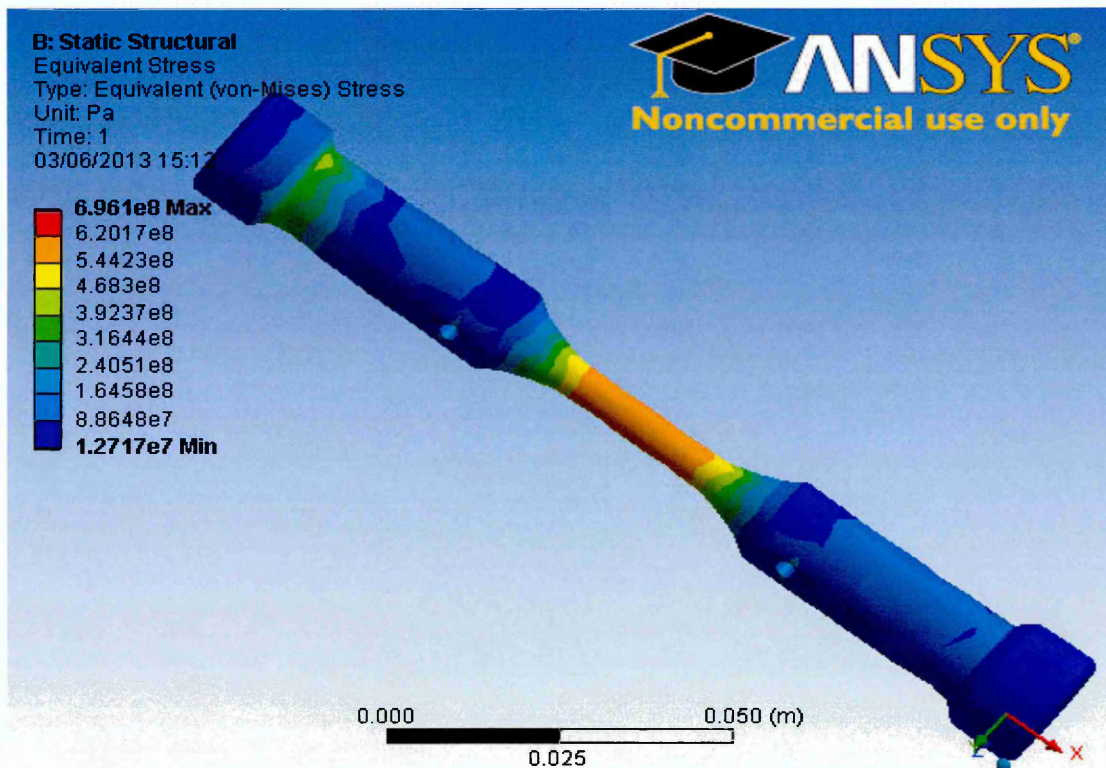
Figure 5.17 The equivalent von-Mises stress of the isothermal fatigue case when 300 °C temperature is supplied.
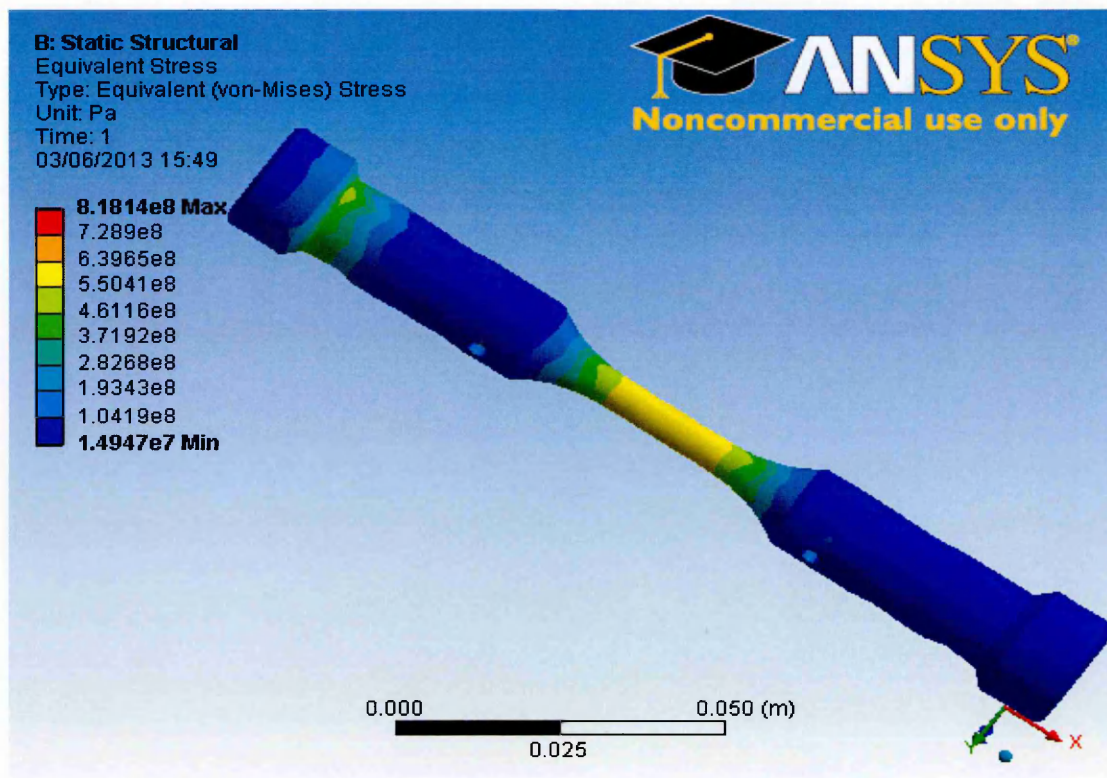
Figure 5.18 The equivalent von-Mises stress of the isothermal fatigue case when 500 °C temperature is supplied.
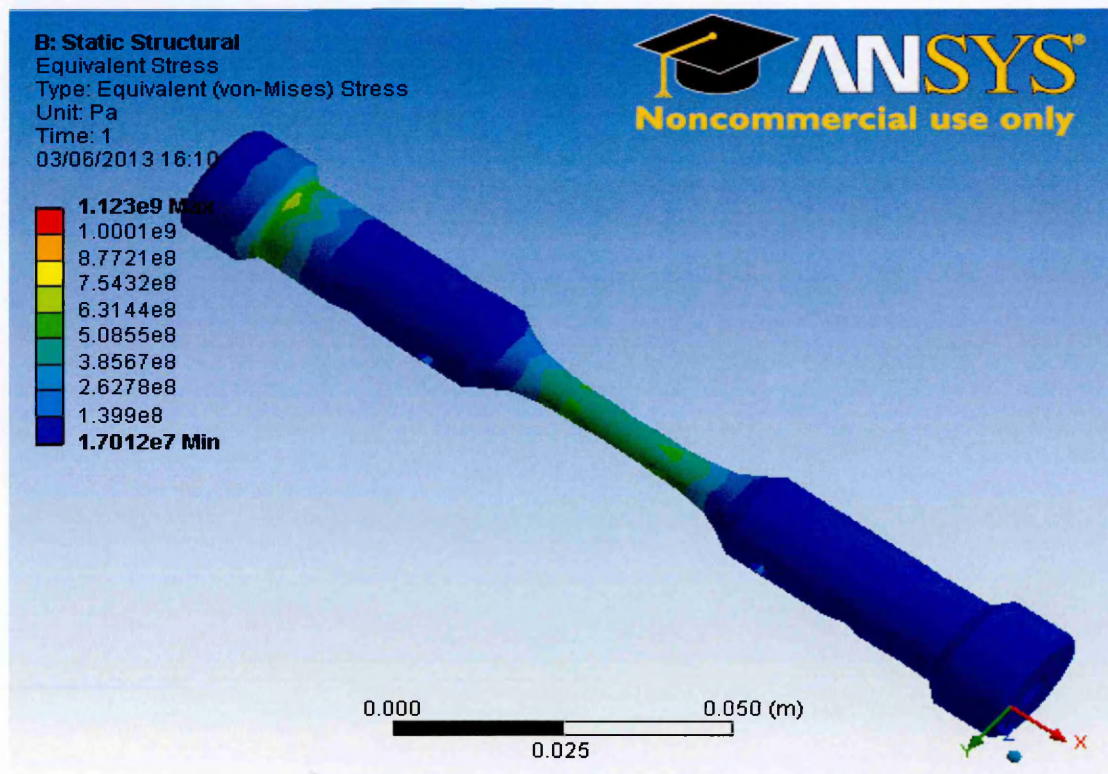
Figure 5.19 The equivalent von-Mises stress of the isothermal fatigue case when 600 °C temperature is supplied.
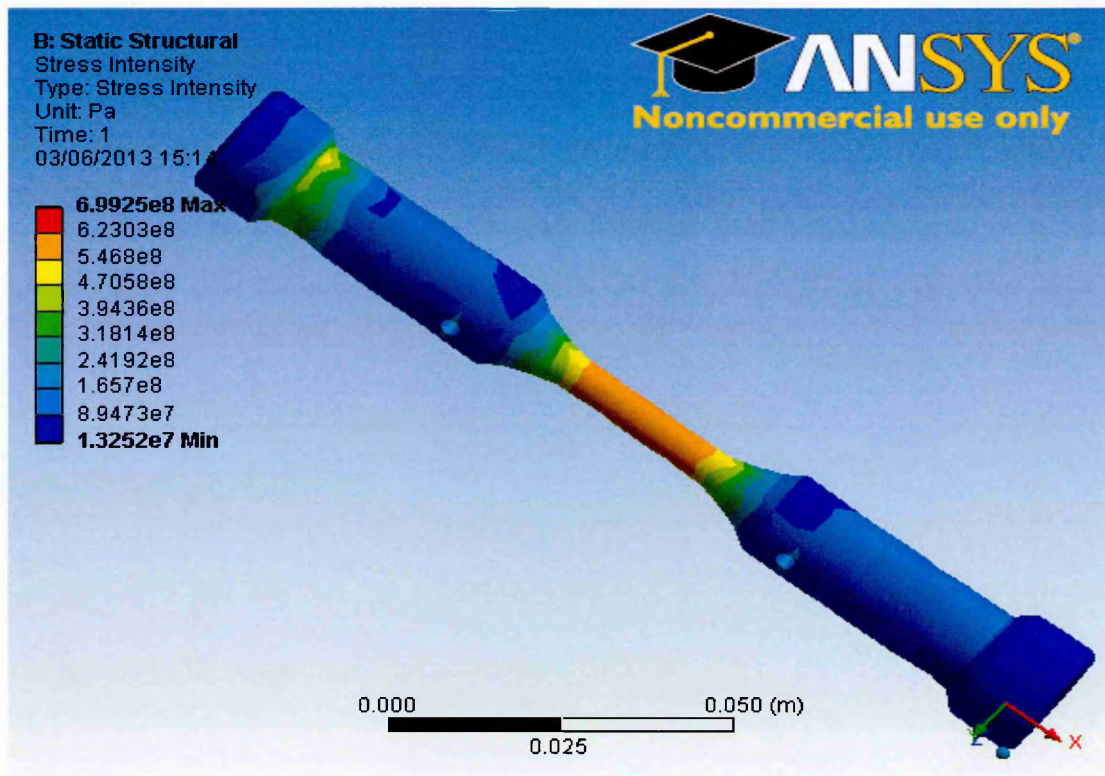
Figure 5.20 The stress intensity factor of the isothermal fatigue case when 300 °C temperature is supplied.
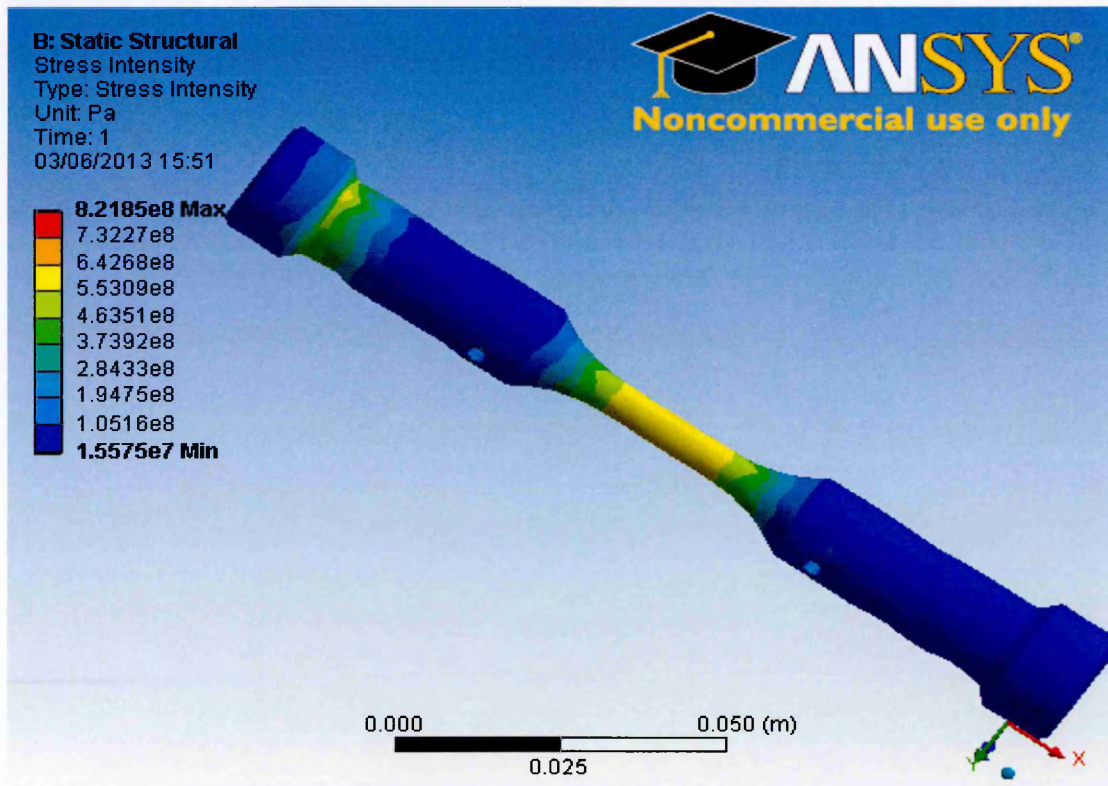
Figure 5.21 The stress intensity factor of the isothermal fatigue case when 500 °C temperature is supplied.
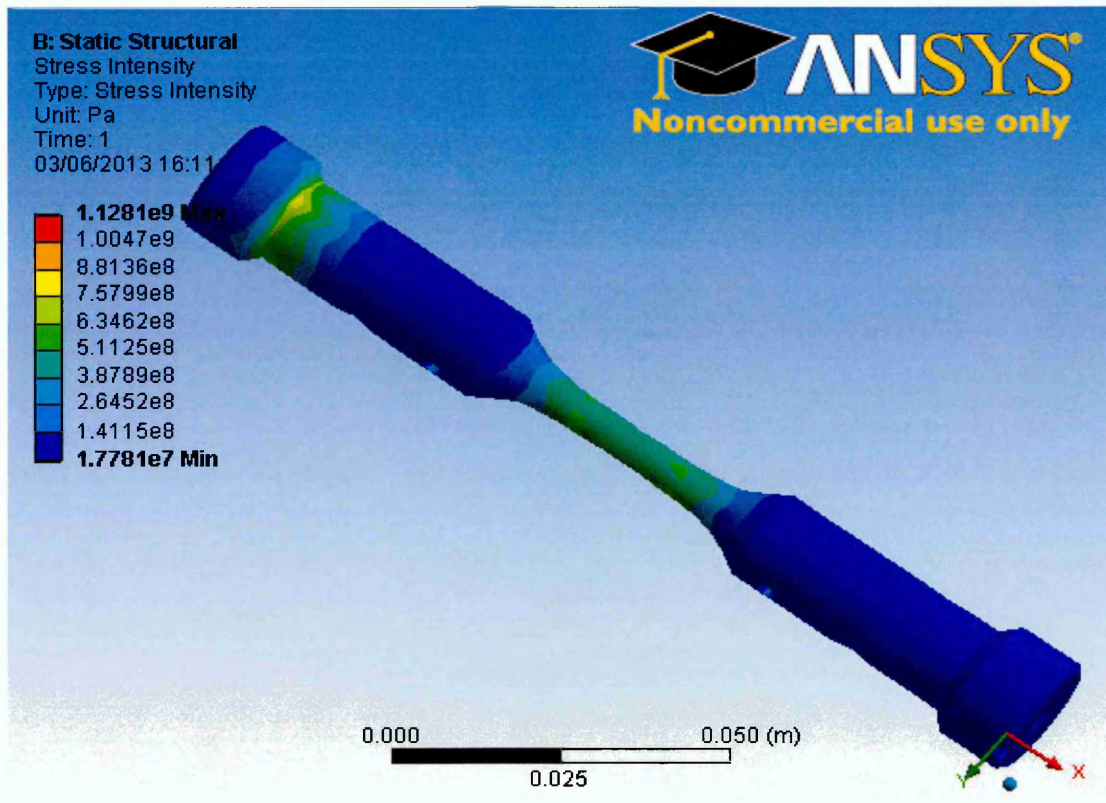
Figure 5.22 The stress intensity factor of the isothermal fatigue case when 600 °C temperature is supplied.

- **Strain Intensity Factor:** the elastic strain intensity factor depends on the stress intensity factor; the two factors are similar in pattern but different in magnitude; the strain is increased with the rise in temperature; it is similar to the theoretical solution and the reduction at 600 °C proportion to thermo-mechanical combined effect, which is very clear caused by the influence of the modulus of elasticity. The distributions in different temperatures are shown in Figs. 5.23 to 5.25.

- **Fatigue Life:** The life of the specimen depends on the combined effects of the applied mechanical load with high temperature. The increase of temperature decreases the strength of the material which leads to a reduction in the supplied mechanical load. The maximum and minimum values of the pattern contour are the highest and lowest input data of the S-N curve, which is generated experimentally at room temperature. This result showed that raising temperature increases the fatigue life in the gauge length of the specimen; also at any temperature the mechanical load supplied is changed due

173

to the tensile yield stress data and to the reduction of the applied load at the conducted temperature which interpolated with nearest value in the S-N input data. This is the reason which explains why the simulation life results are so far from the experimental output data. This is because of the S-N curve input data are generated at room temperature. In order to get acceptable results, we should use the curves at the selected temperature. Also the presentation of the high effects of the stress concentration in the sharp edge nearest to the specimen fixed end is at 600 °C. The distributions of the life in different temperatures are shown in Figs. 5.26 to 5.28.

- **Fatigue Equivalent Alternating Stress:** The equivalent alternating stress estimation results from the half difference between the maximum and minimum loads, conducting the von-Mises load as the maximum stress as mentioned before. So, the increase of temperature decreases alternating stress; this is similar to von-Mises stress. The results show very close values with the applied experimental data. Also the high temperature effects are clear in the sharp edges due to the stress concentration. The results patterns are shown in Figs. 5.29 to 5. 31.
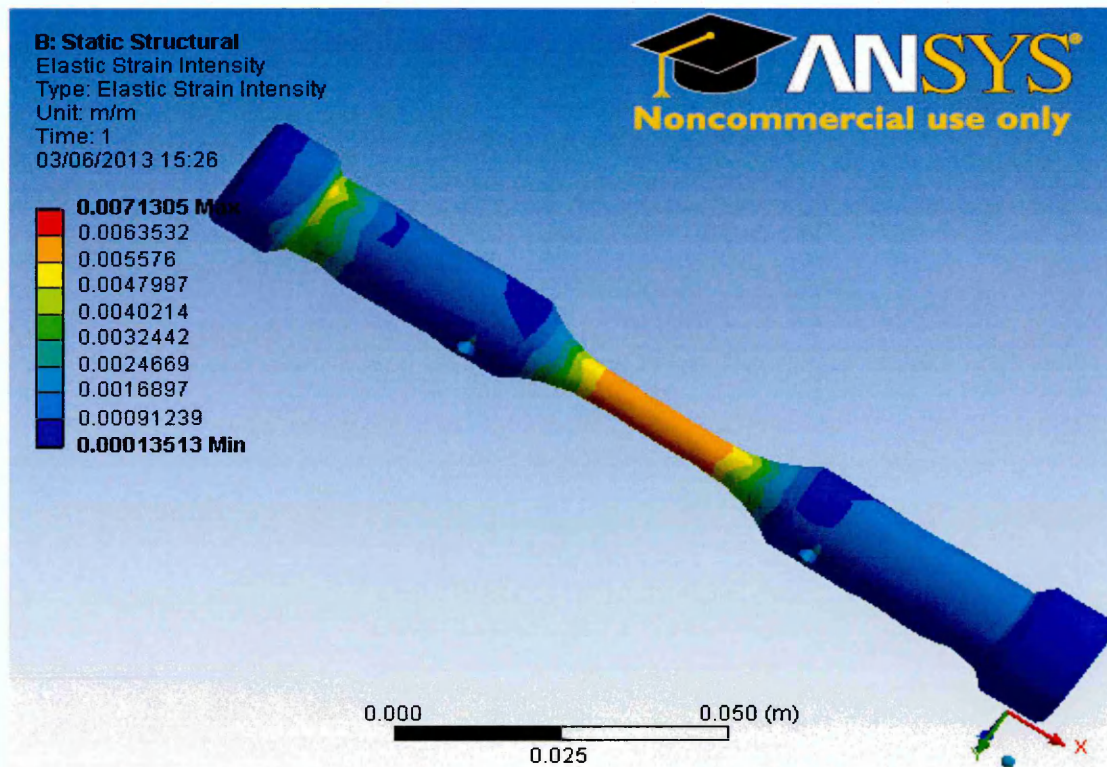
Figure 5.23 The strain intensity factor of the isothermal fatigue case when 300 °C temperature is supplied.

174
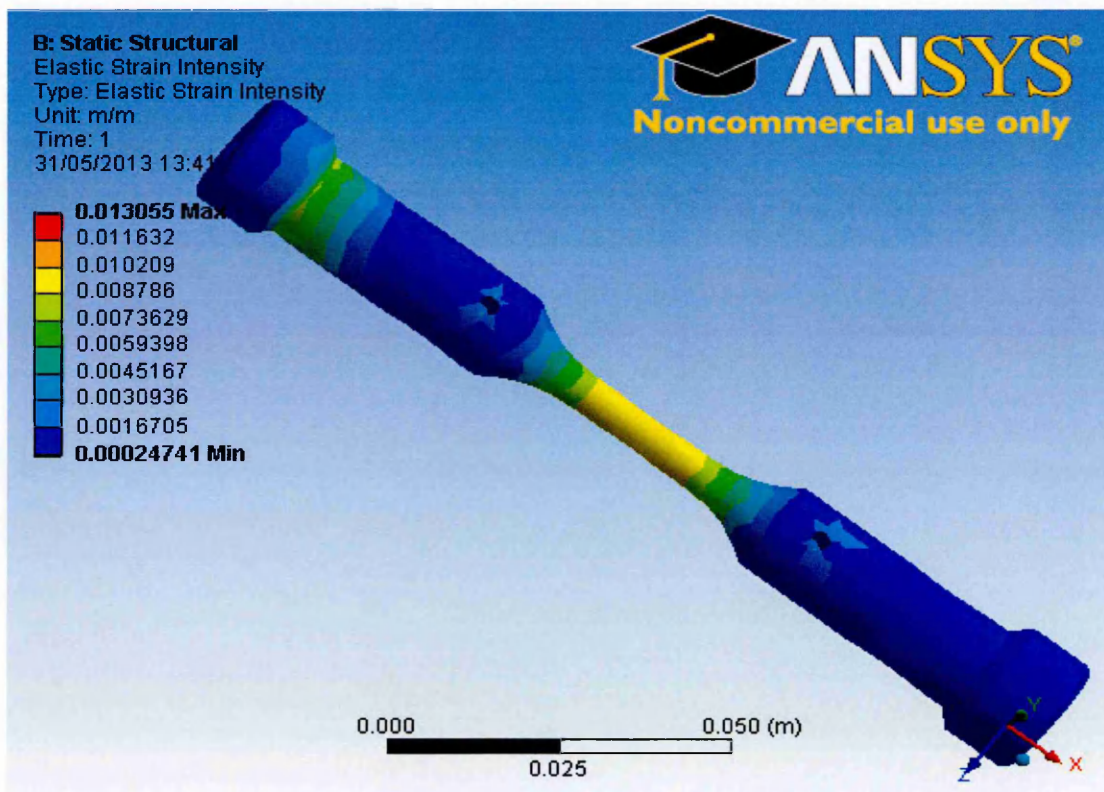
Figure 5.24 The strain intensity factor of the isothermal fatigue case when 500 °C temperature is supplied.
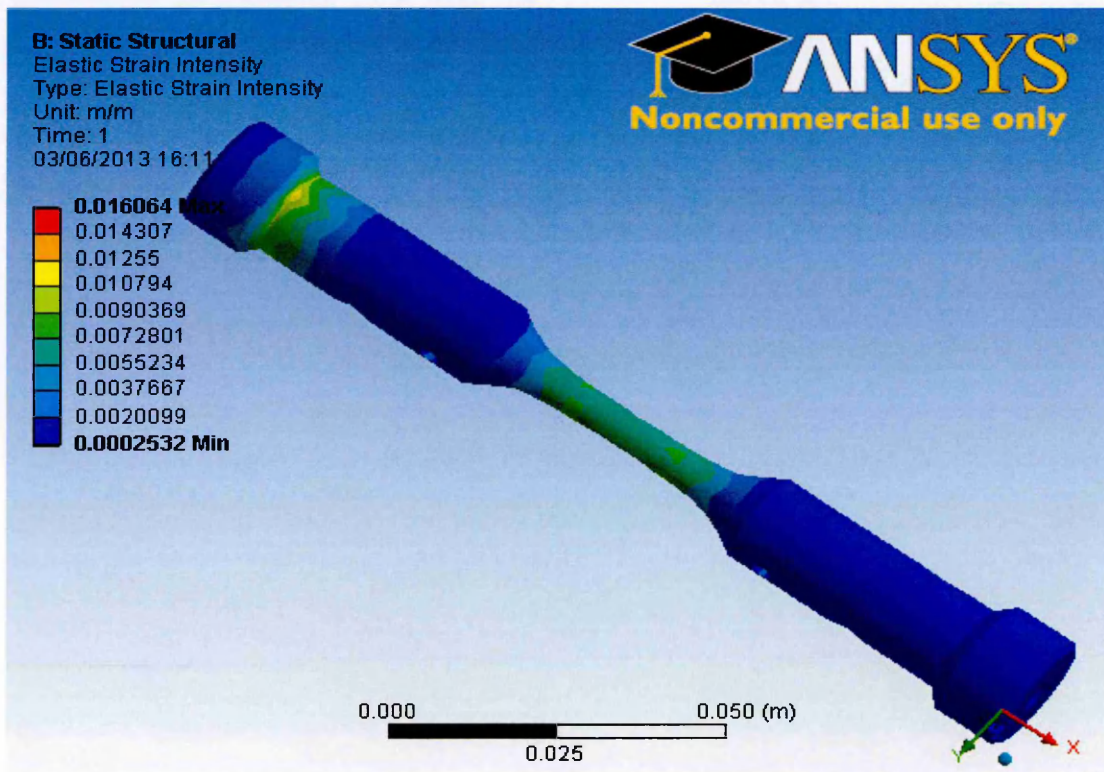
Figure 5.25 The strain intensity factor of the isothermal fatigue case when 600 °C temperature is supplied.
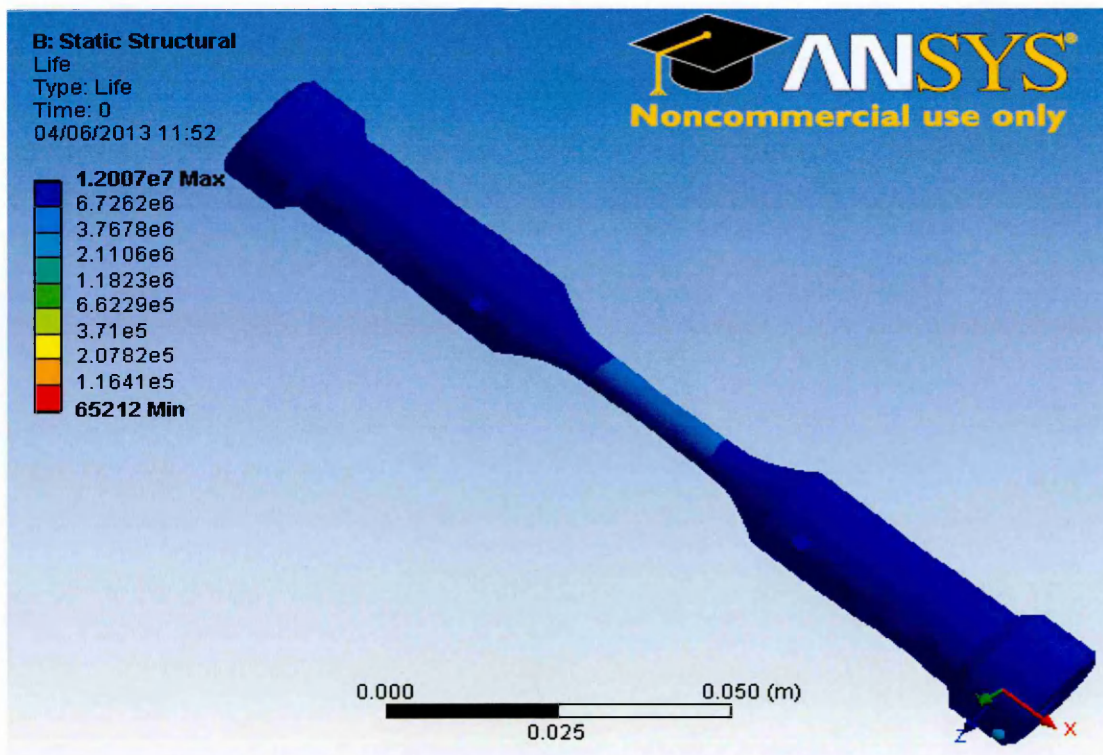
Figure 5.26 The life in seconds of the isothermal fatigue case when 300 °C temperature is supplied.
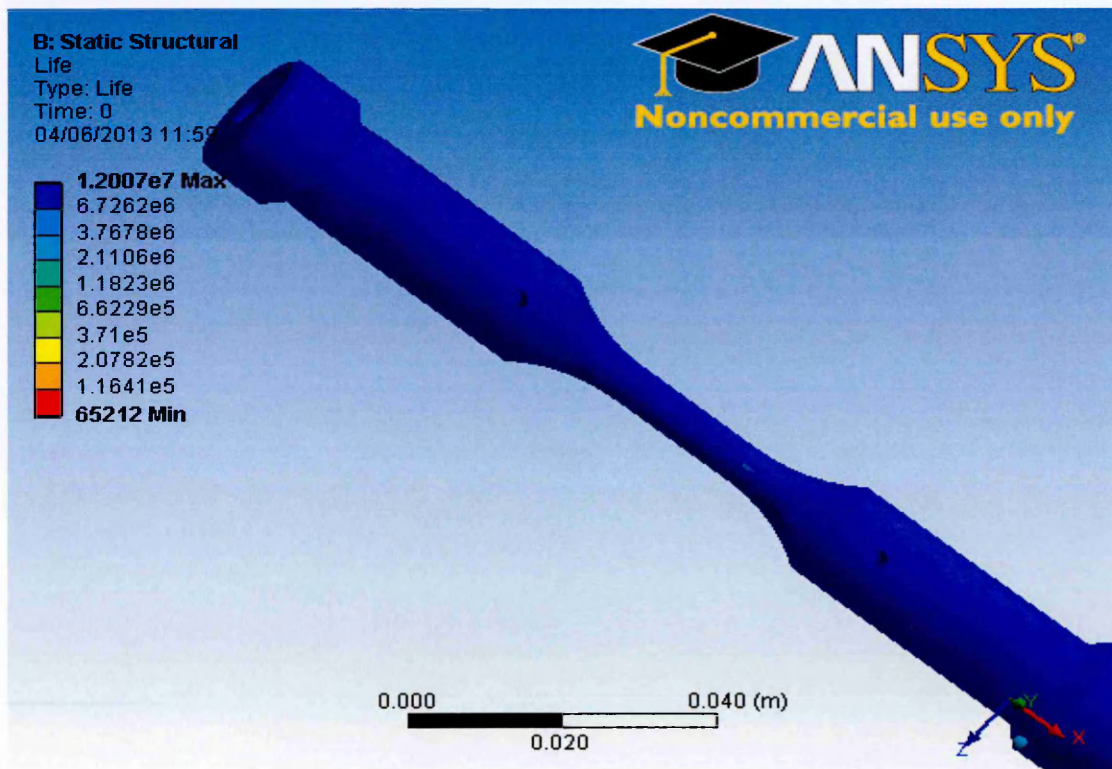
Figure 5.27 The life in seconds of the isothermal fatigue case when 500 °C temperature is supplied.
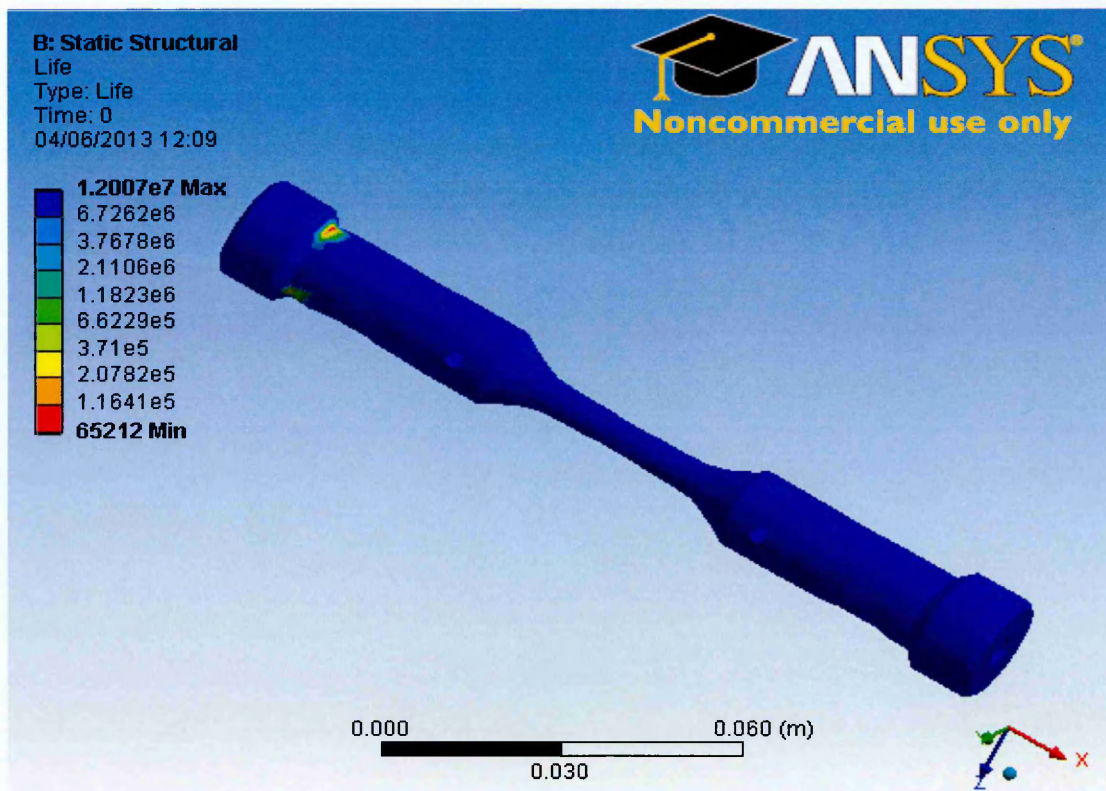
Figure 5.28 The life in seconds of the isothermal fatigue case when 600 °C temperature is supplied.
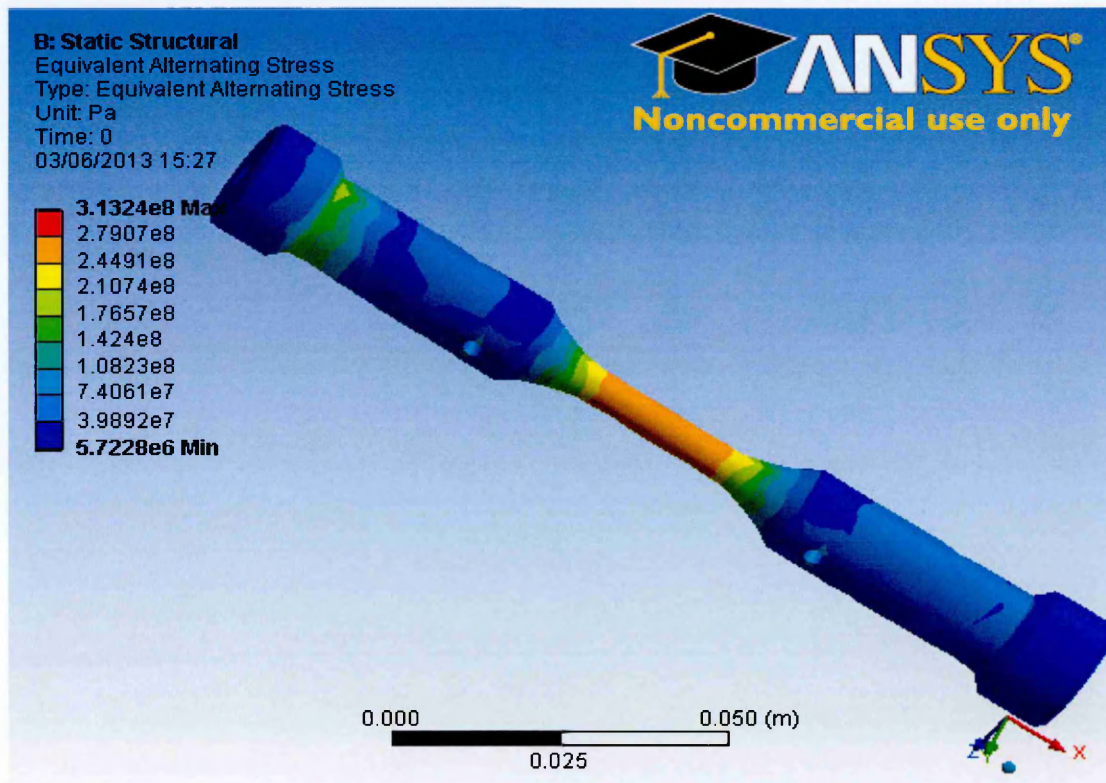
Figure 5.29 The alternative stress of the isothermal fatigue case when 300 °C temperature is supplied.
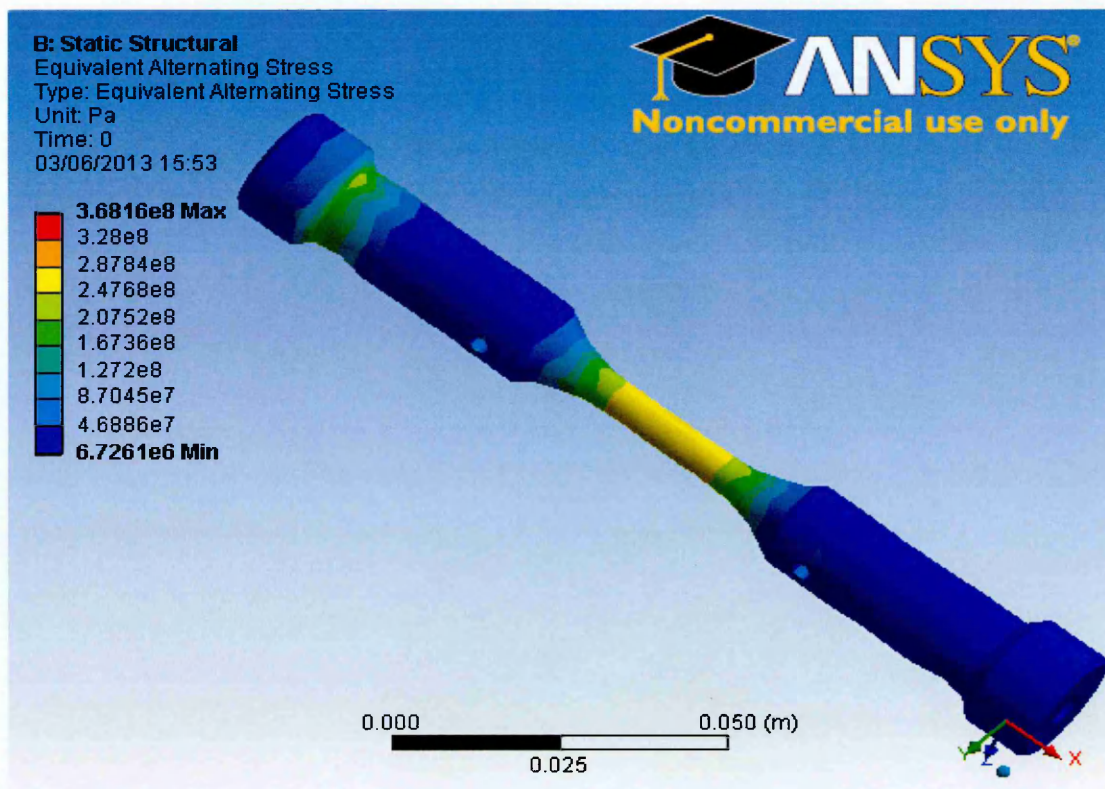
Figure 5.30 The alternative stress of the isothermal fatigue case when 500 °C temperature is supplied.
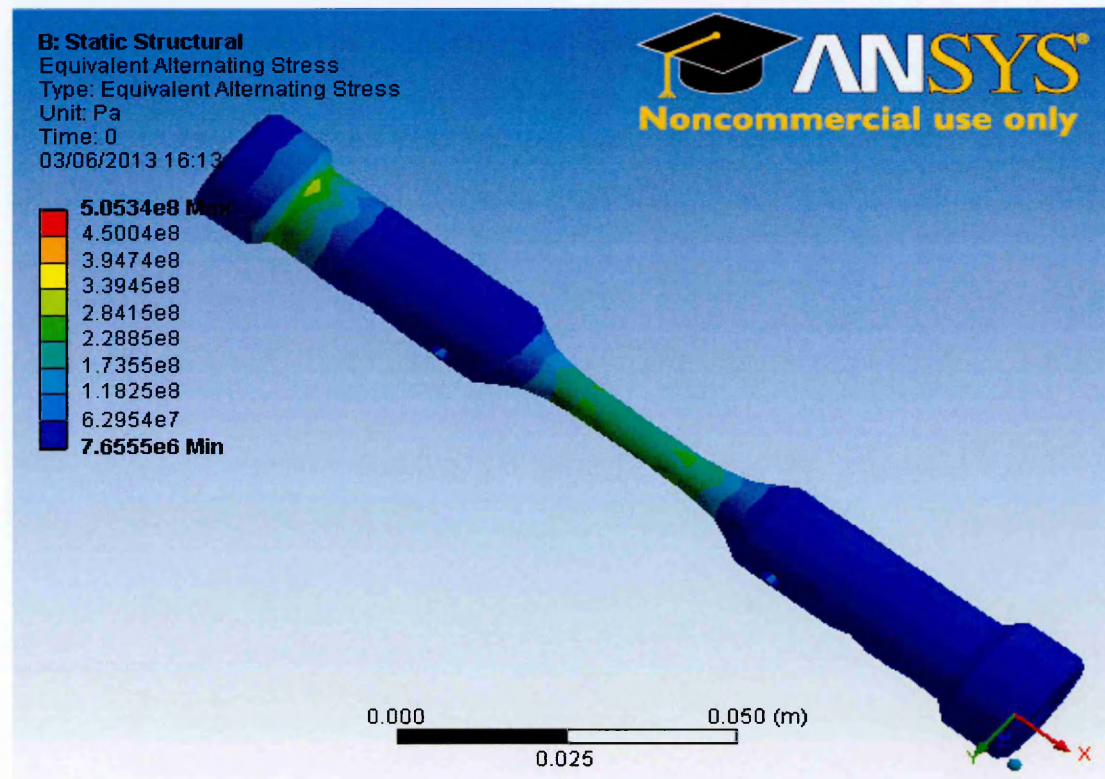
Figure 5.31 The alternative stress of the isothermal fatigue case when 600 °C temperature is supplied.

5.6.3 Thermo-mechanical Fatigue Analysis for Heating and Cooling Shock Cases:

In these two studies, the solution starts by selecting the type transient thermal simulation combined with the thermal stresses analysis.

5.6.3.1 Pre-Processing Stage:

In addition to the main material structural properties used in the low cycle fatigue case, the properties added are:

1- Thermal property:

- Isotropic thermal conductivity.

- Specific heat.

The geometrical shape of the hollow cylindrical model is described by the size boundaries, the inner radius (a = 4 mm), the outer radius (b = 5 mm) and the length (L= 22 mm) established in the ANSYS program to generate the model depending on the standard of the hollow cylinder specimen gauge length as shown in Fig 5.32. The free meshing is used to generate the nodes and the elements automatically employing the hexahedral element type due to the regularly geometric model with the total numbers of nodes of (3501) and the total number of the elements (558) as shown in Fig.5.33.

179
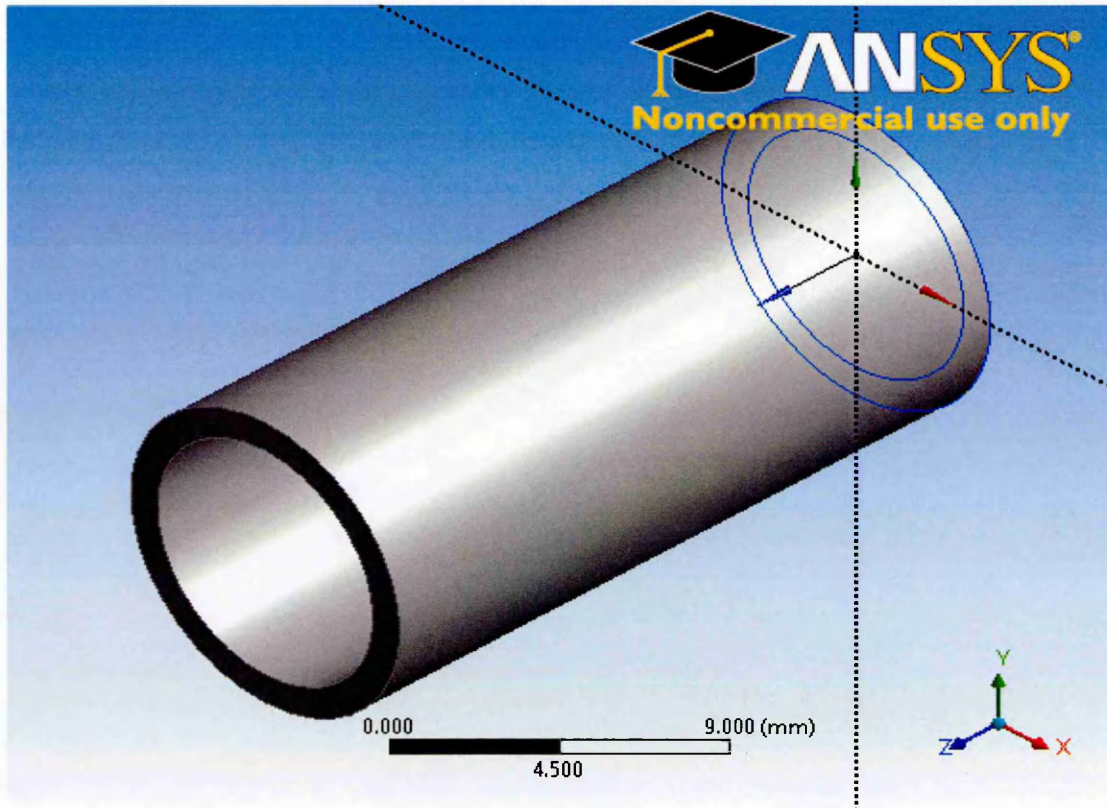
Figure 5.32 The hollow cylinder geometrical model created by ANSYS Workbench 13 Software.
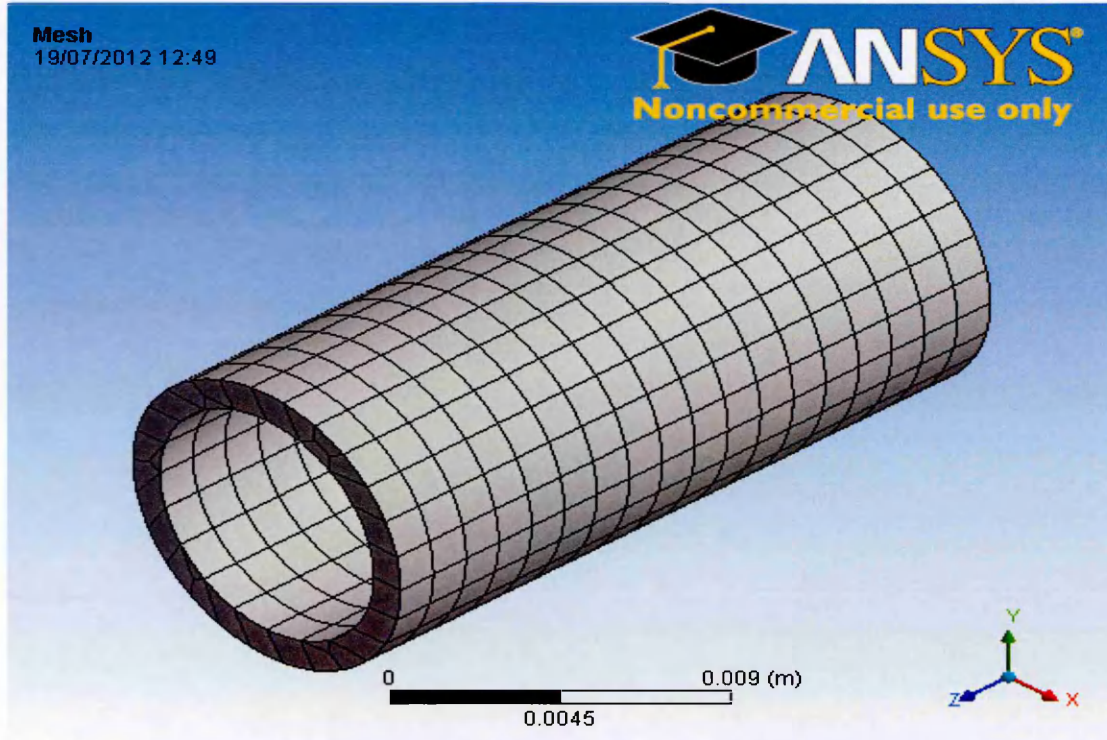
Figure 5.33 The hollow cylinder meshed model created by ANSYS Software.

5.6.3.2 Solution and Boundary Conditions Stage:

In these cases, the boundary conditions are divided into two types: transient thermal and low cycle fatigue boundaries. The thermal boundaries are described for each case as follows:

I- Heating Case:

1- Thermal loading.

Assuming a constant temperature (Ta = 600 °C) at the inner surface and a heat flux (P=10500 W/m2) supplied on the outer surface of the hollow cylinder simulation model, similar to the theoretical study.

2- Fatigue loading.

By fixing support at one end of the hollow cylinder and supplying a load component oriented to the cylinder axis ($F_z = \sigma_{ys}.A$ at $T = 600\,°C$), as shown in Fig. (5.34).

Figure 5.34 The boundary conditions of the heating case.

181

II- Down shock Cooling Case:

1- Thermal loading.

Assuming a constant temperature (Tb = 600 °C) at the outer surface and a forced-air convection cooling $\left(\frac{dT}{dr} = \frac{H}{k} \cdot (T_a - T_{air}) \right)$ on the inner surface of the hollow cylinder simulation model, similar to theoretical case study.

2- Fatigue loading.

By fixing support at one end of the hollow cylinder and supplying a z-axis force component ($F_Z = \sigma_{ys}. A \ at \ T = \ 600 \ °C$), as shown in Fig. (5.35).
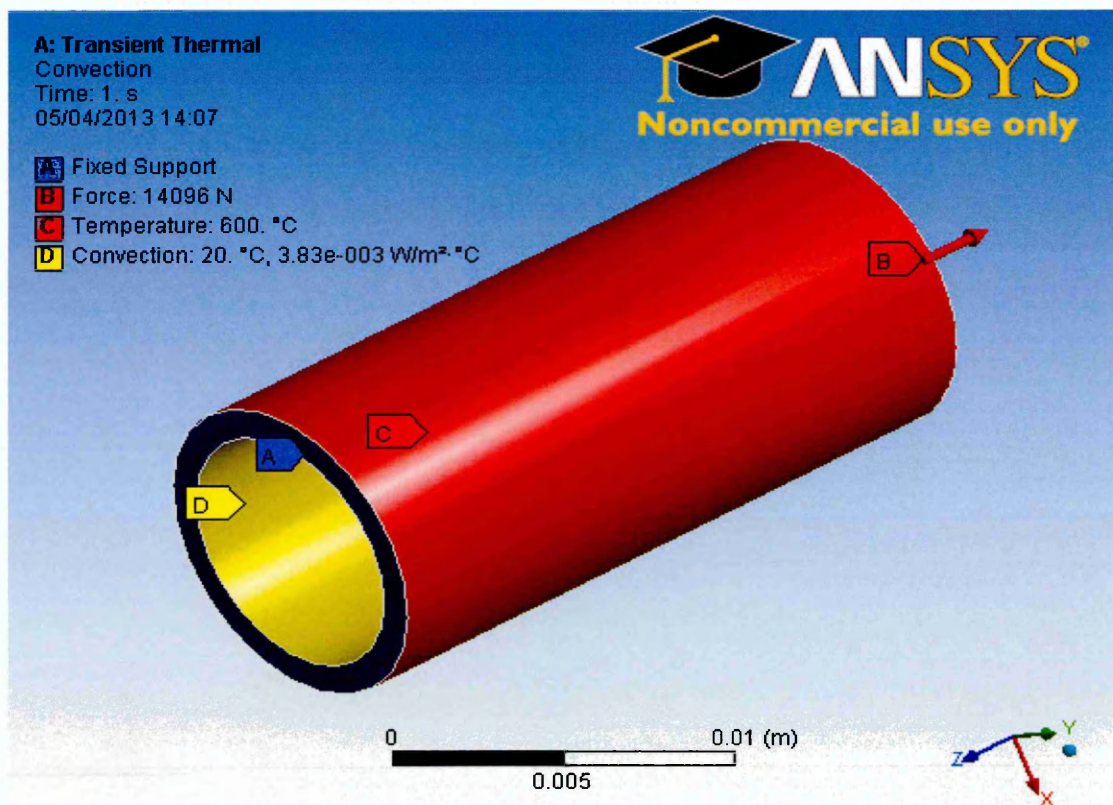
Figure 5.35 The boundary conditions of the down shock cooling case.

182

5.6.3.3 Post-Processing Stage:

In this case study stage, the solution results are described by the following:

- Temperature Distribution: The temperature distribution through the hollow cylinder wall at the selected time in the two cases is very close to the theoretical calculation, especially in the down shock cooling case. The results give a significant indication of the up shock in the heating case and down shock in the cooling case which started in the beginning of the starting time, and then proceeds to steady during the continuous running time; the results are shown in Figs. 5.36 to 5.39.
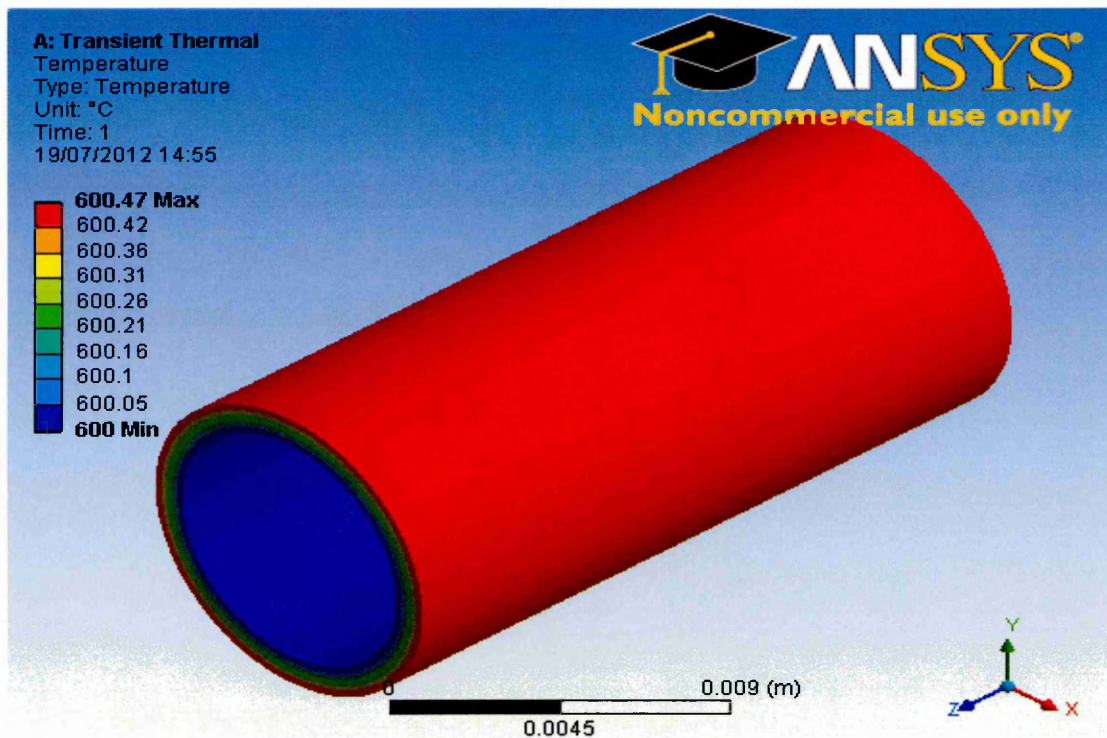
Figure 5.36 The temperature distribution of the heating case through the hollow cylinder wall at 1 sec.
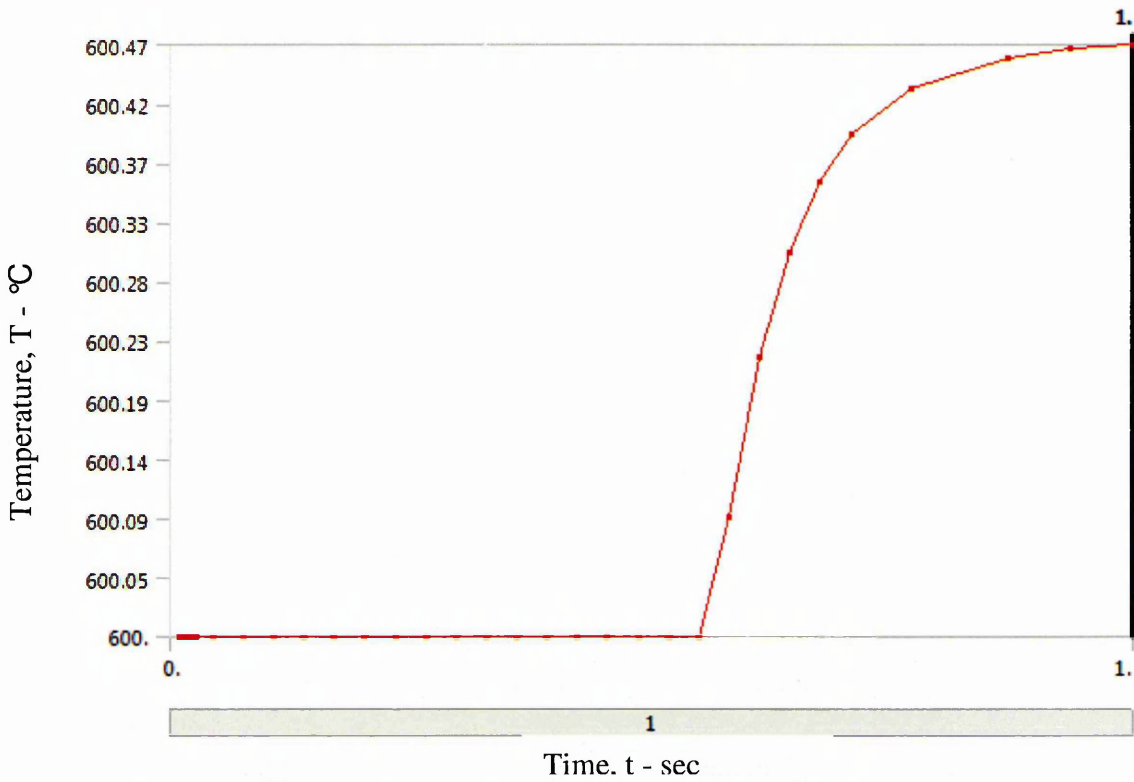
Figure 5.37 The temperature distribution with time through 1 second in the heating case.
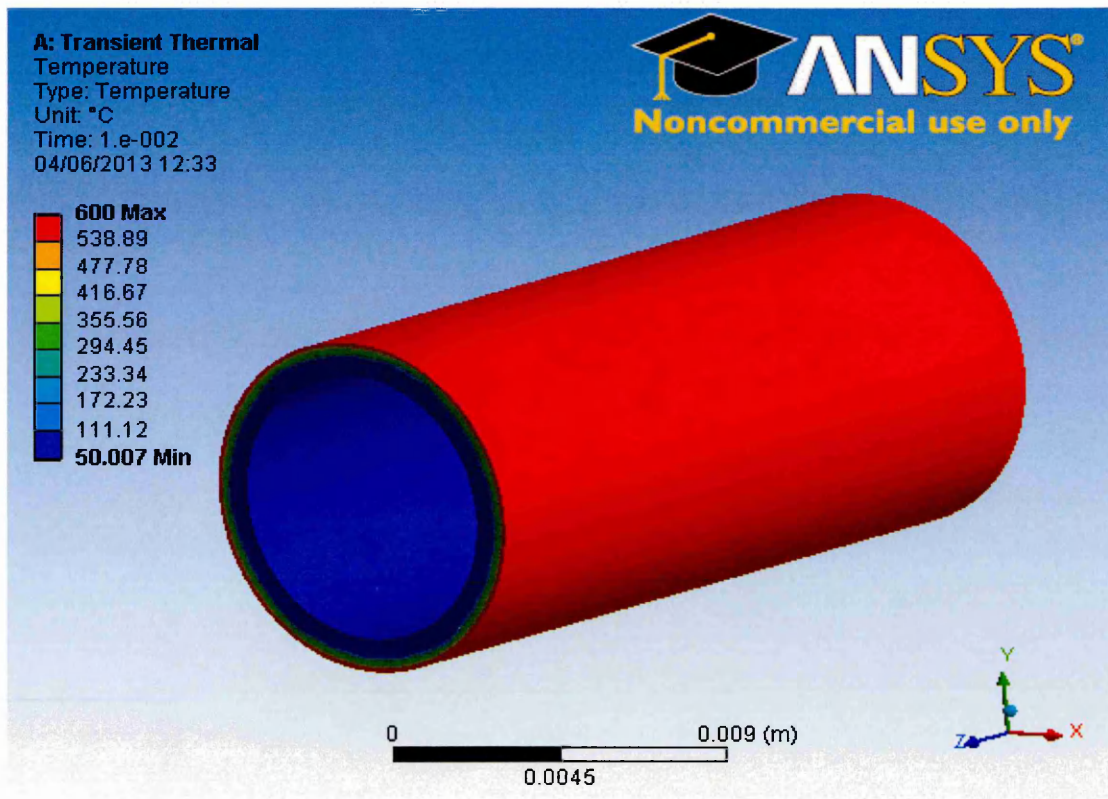
Figure 5.38 The temperature distribution through the hollow cylinder wall at 0.01 sec in the down shock cooling case.
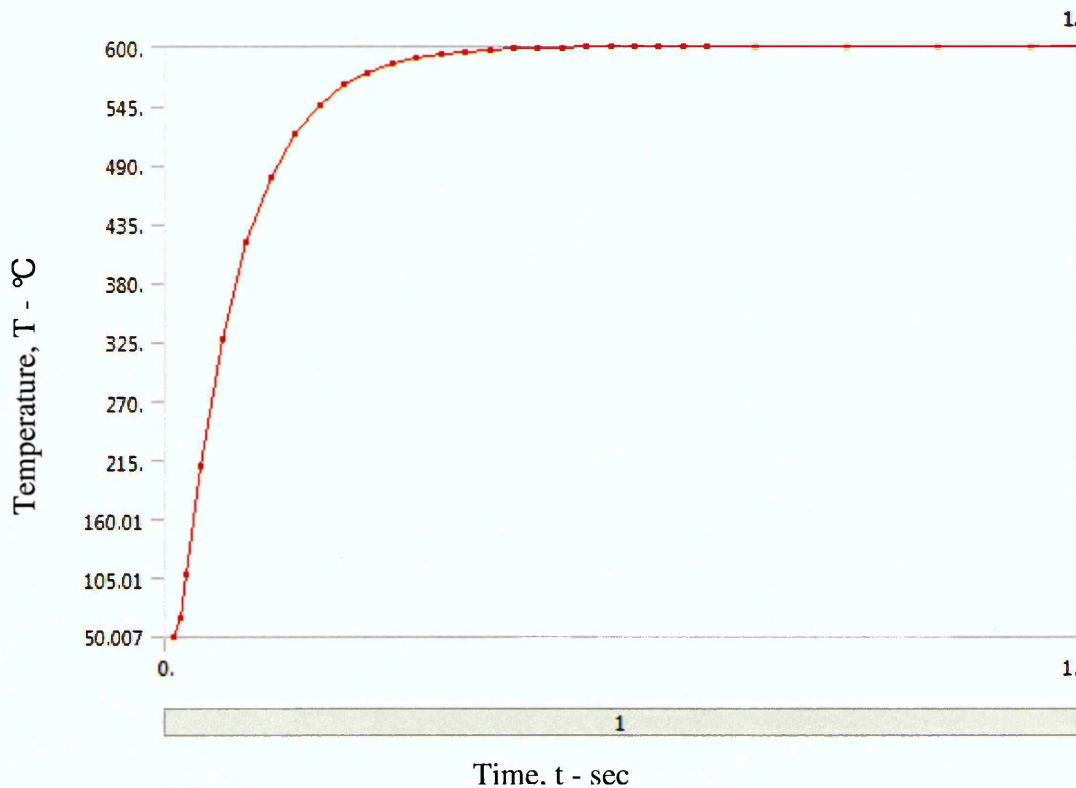
Figure 5.39 The temperature distribution with time through 1 second in the down shock cooling case.

- **Equivalent von-Mises Stress:** The maximum equivalent von-Mises stress in the two cases occurred close to the fixed supported end because of the superimposed effect of thermal and tensile mechanical stresses, which are higher than the ultimate tensile stress at 600 °C; this means that the possibility of failure is takes place in the outer surface of the hollow cylinder estimated at one or fraction of second as a period of time. The von-Mises stress pattern in two cases is approximately similar but in the heating case, it is a resolution of up shock effect. In contrast, the cooling case results from the down shock effect; also they are all related to the maximum temperature 600 °C, but the difference is the timing of the effect; the results are shown in Figs. 5.40 and 5.41.

- **Stress Intensity Factor:** the stress intensity factor depends on the effective stress, the equivalent von-Mises stress and the geometrical shape factor of the hollow cylinder. For that distribution pattern, the stress intensity factor is similar to the equivalent

185

stresses in the two cases but it is obviously different in magnitude; the results are shown in Figs. 5.42 and 5.43.

- **Strain Intensity Factor:** the elastic strain intensity factor mainly depends on the stress intensity factor and the modulus of elasticity, for that the strain pattern is similar to the stress pattern in the two cases; the results are shown in Figs. 5.44 and 5.45.

- **Alternating Fatigue Stress:** the distribution of the alternating stress pattern is apparent; the maximum stress effects are close to the supporting end especially in the outer surface of the hollow cylinder due to the high thermal stress obtained at 600 °C temperature and the difference between the two cases patterns is related to the difference of the opposite supplied action as a heating or down shock cooling loads and the effective periods of time as shown in Figs. 5.46 and 5.47.

- **Fatigue Life:** the fatigue life distribution pattern in the two cases indicates that the possibility of fracture started very close to the supported end, which the maximum equivalent stress obtained from the combined effect of the thermal and mechanical stresses as shown in Figs. 5.48 and 5.49. The fatigue life comparison between the generated experimental isothermal fatigue tests at 600 °C temperature with the two cases of simulation results is highly different, because the S-N curve uploaded in this software input data is generated experimentally at room temperature and this is the main cause of the large gap.
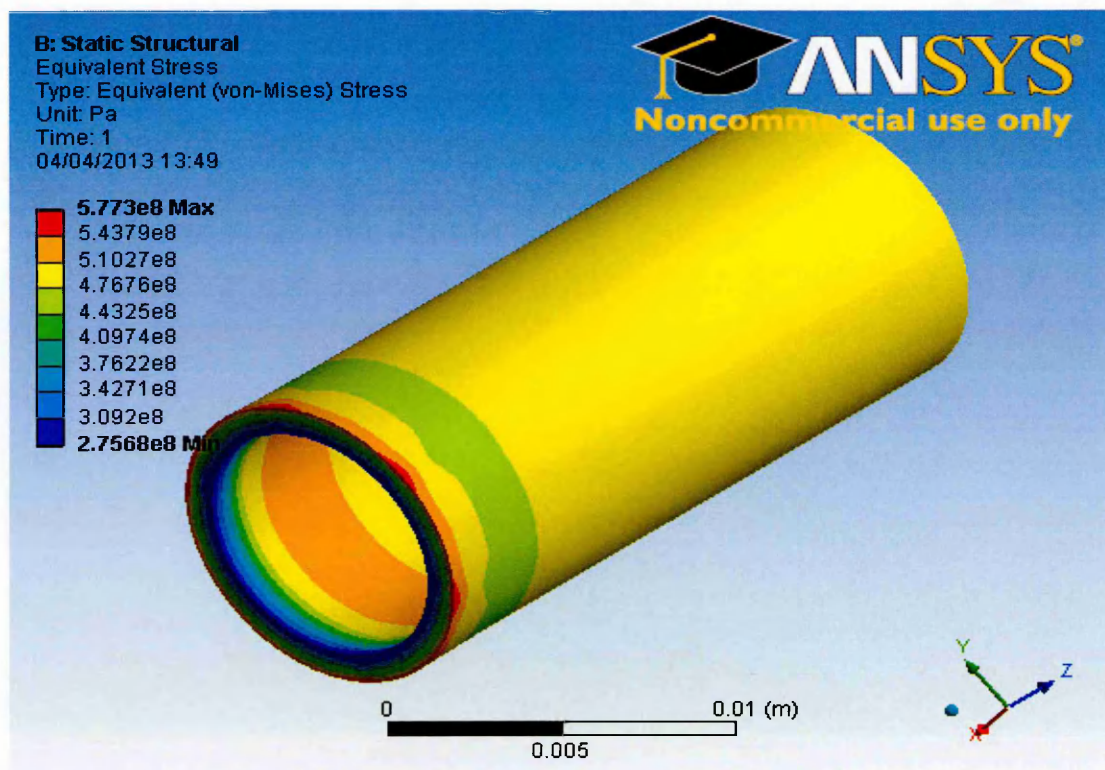
Figure 5.40 The distribution pattern of the equivalent von Mises stress in the heating case.
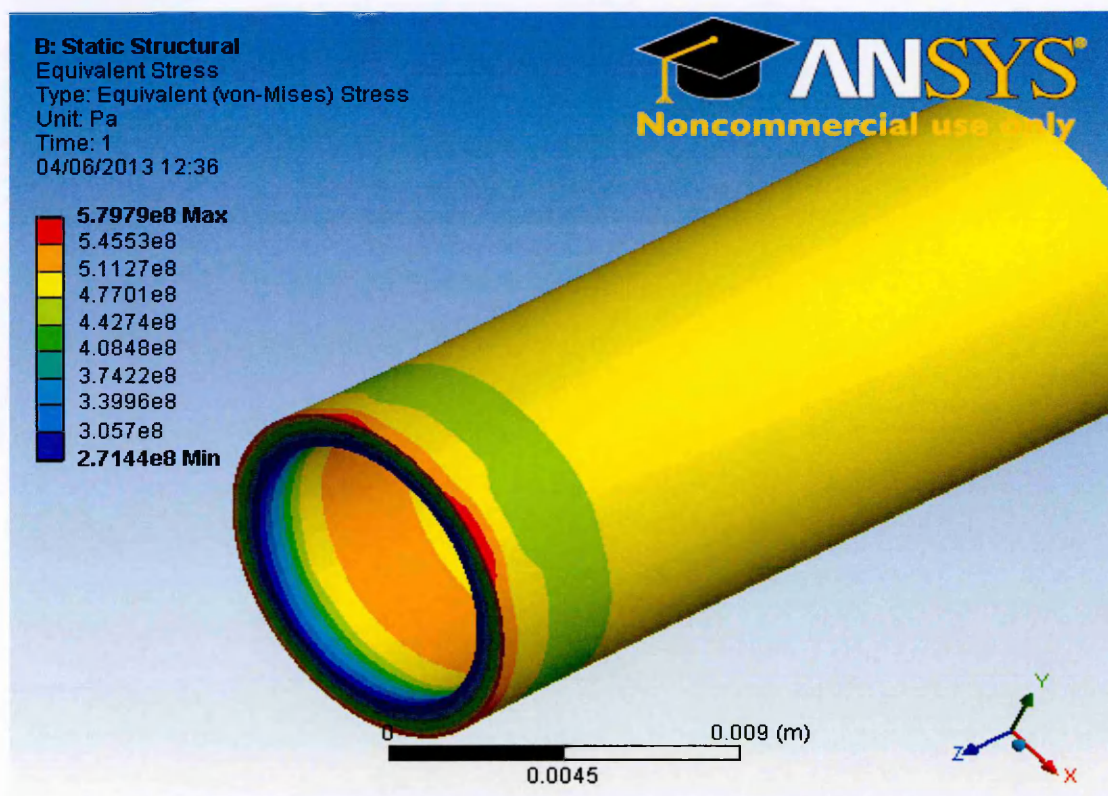
Figure 5.41 The distribution pattern of the equivalent von Mises stress in the down shock cooling case.

187
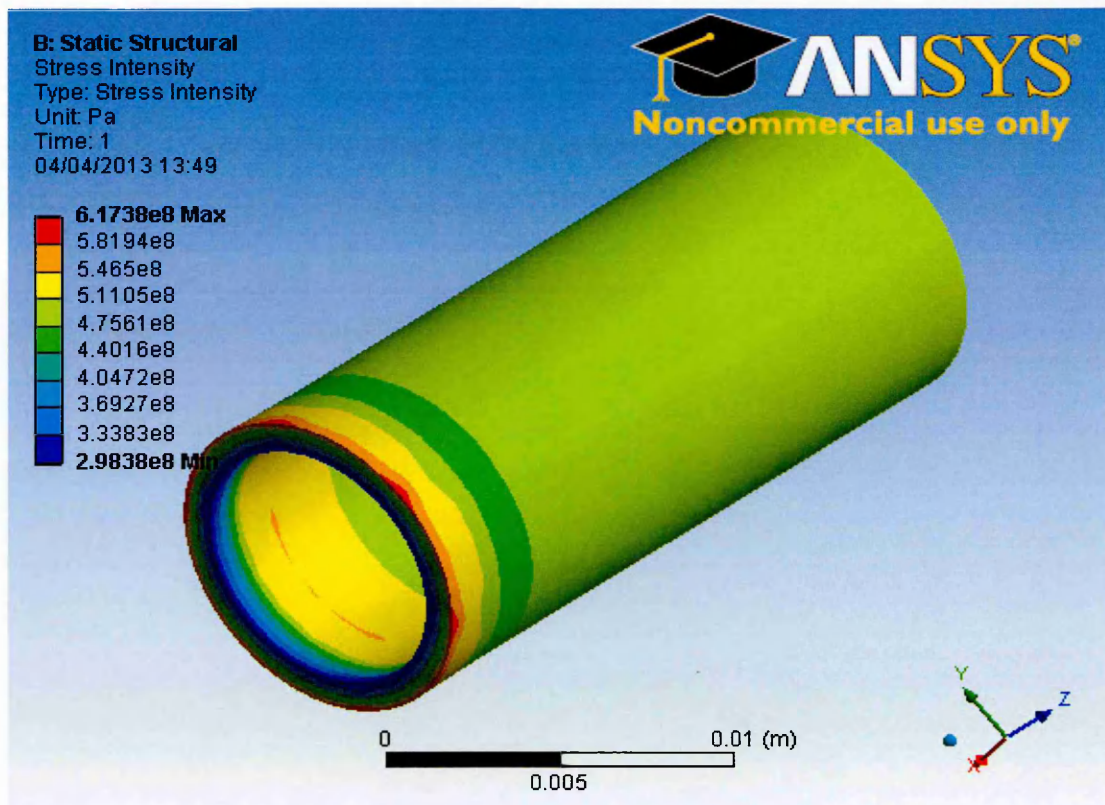
Figure 5.42 The distribution pattern of the stress intensity factor at the heating case.
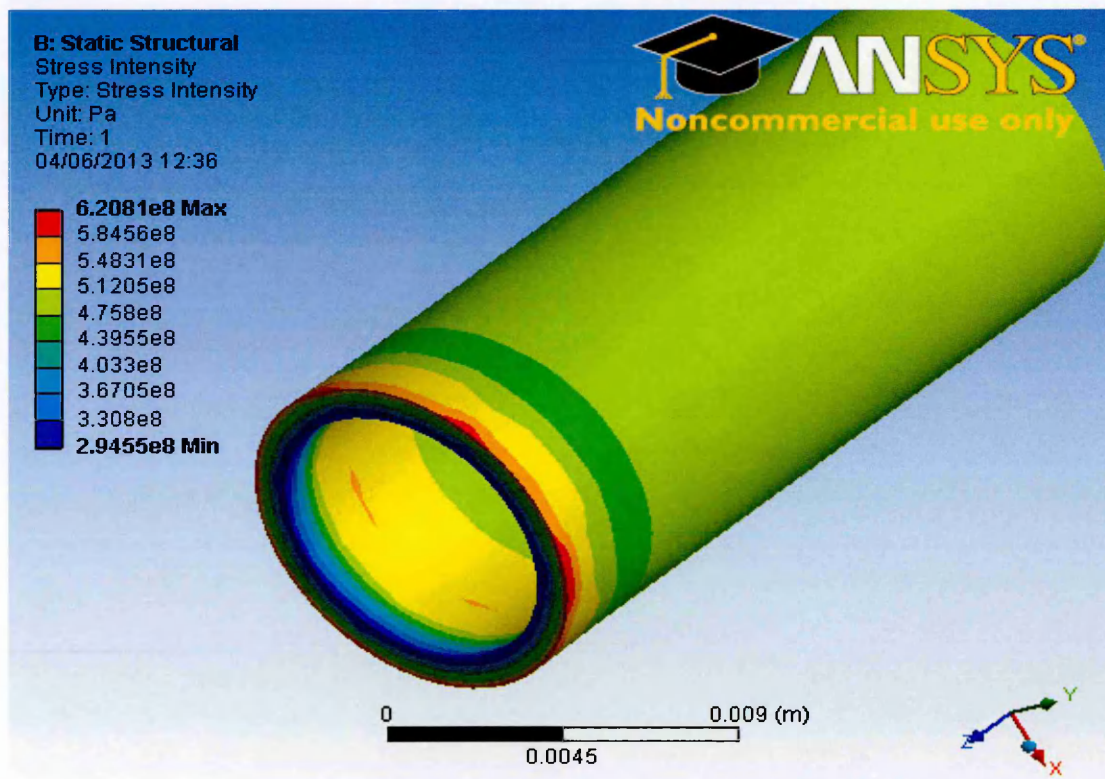
Figure 5.43 The distribution pattern of the stress intensity factor in the down shock cooling case.
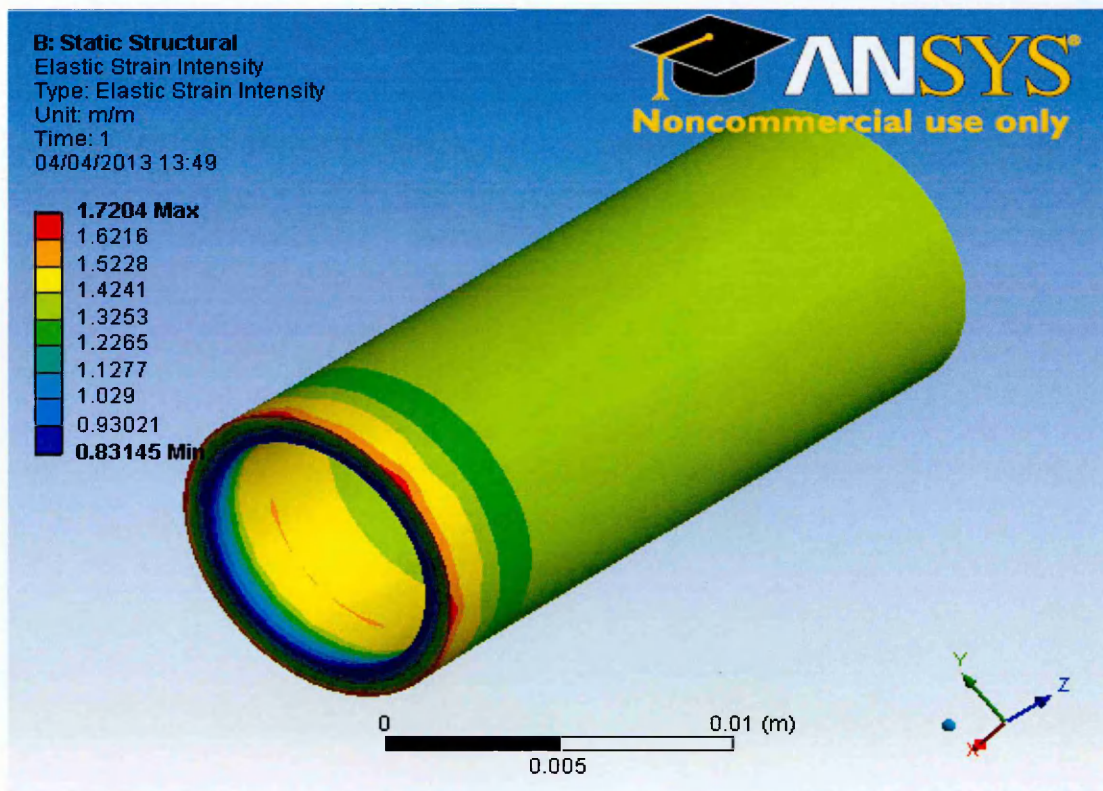
Figure 5.44 The distribution pattern of the strain intensity factor in the heating case.
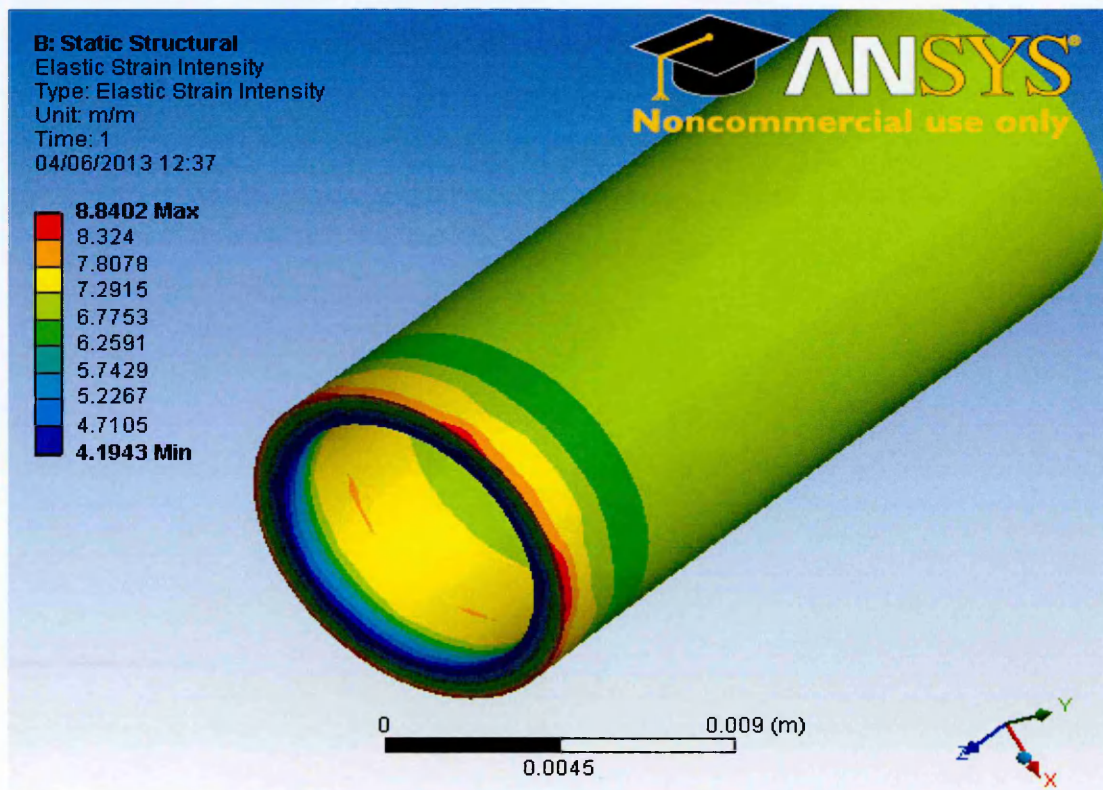
Figure 5.45 The distribution pattern of the strain intensity factor in the down shock cooling case.
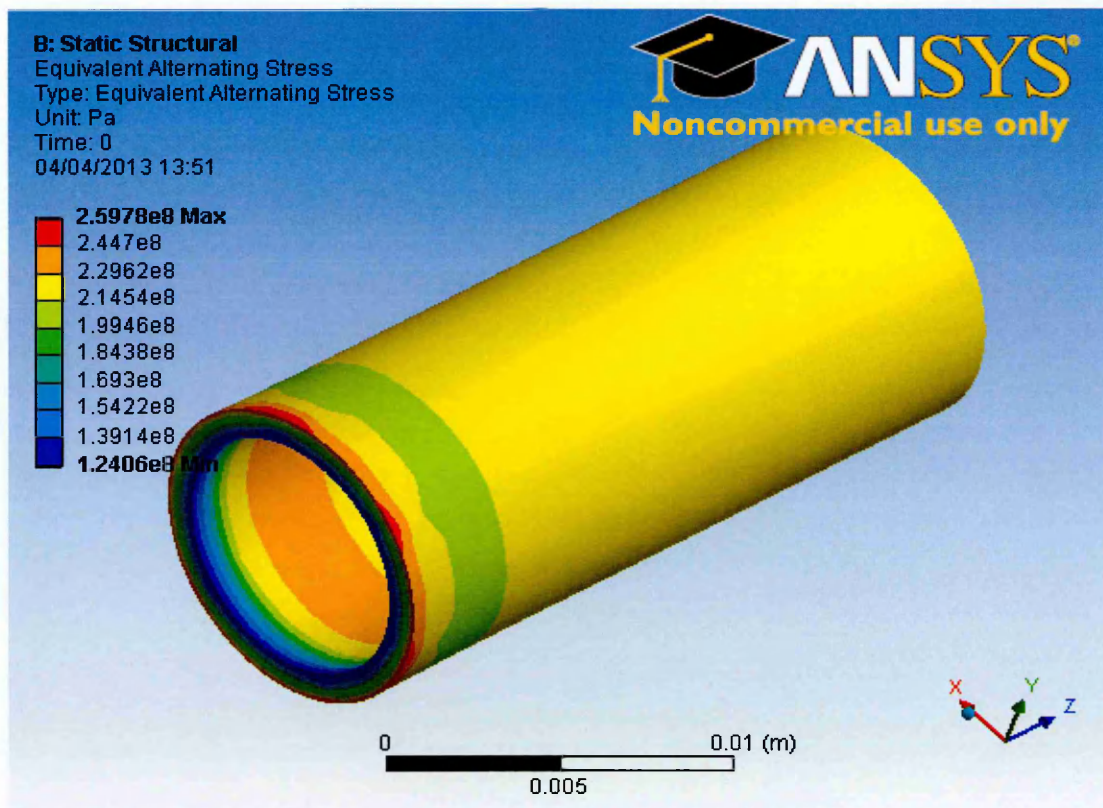
Figure 5.46 The distribution pattern of the alternating stress in the heating case.
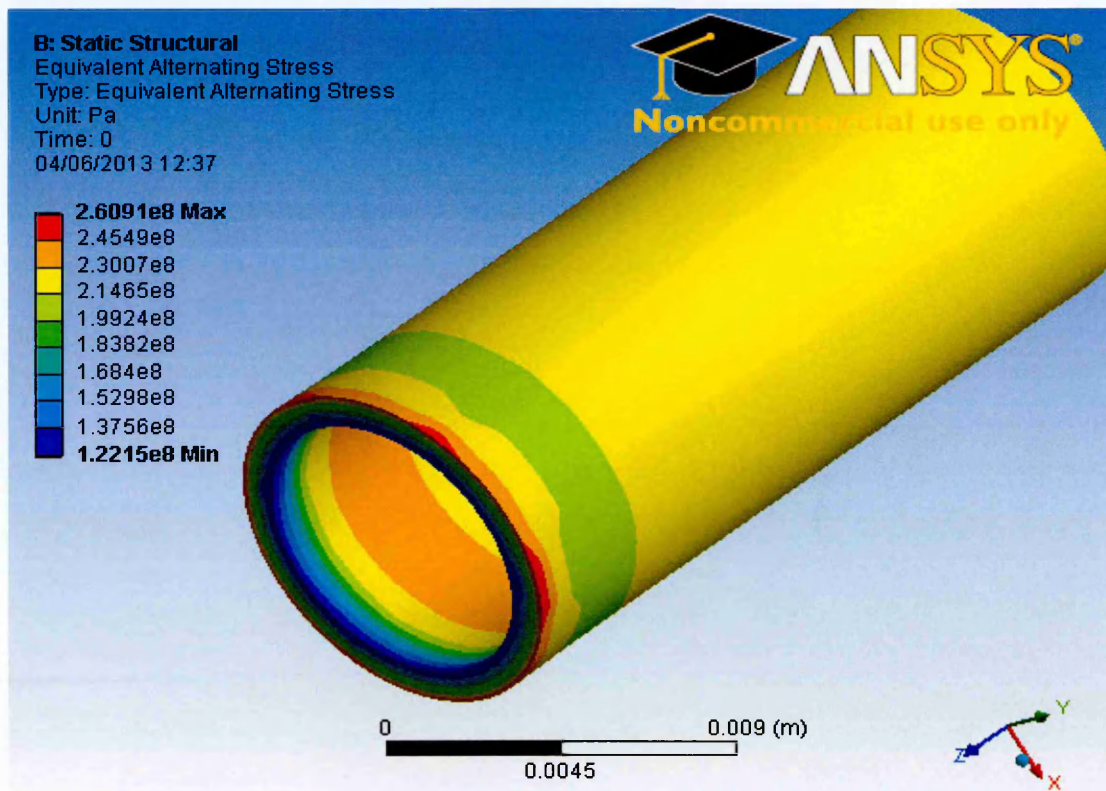
Figure 5.47 The distribution pattern of the alternating stress in the down shock cooling case.

190
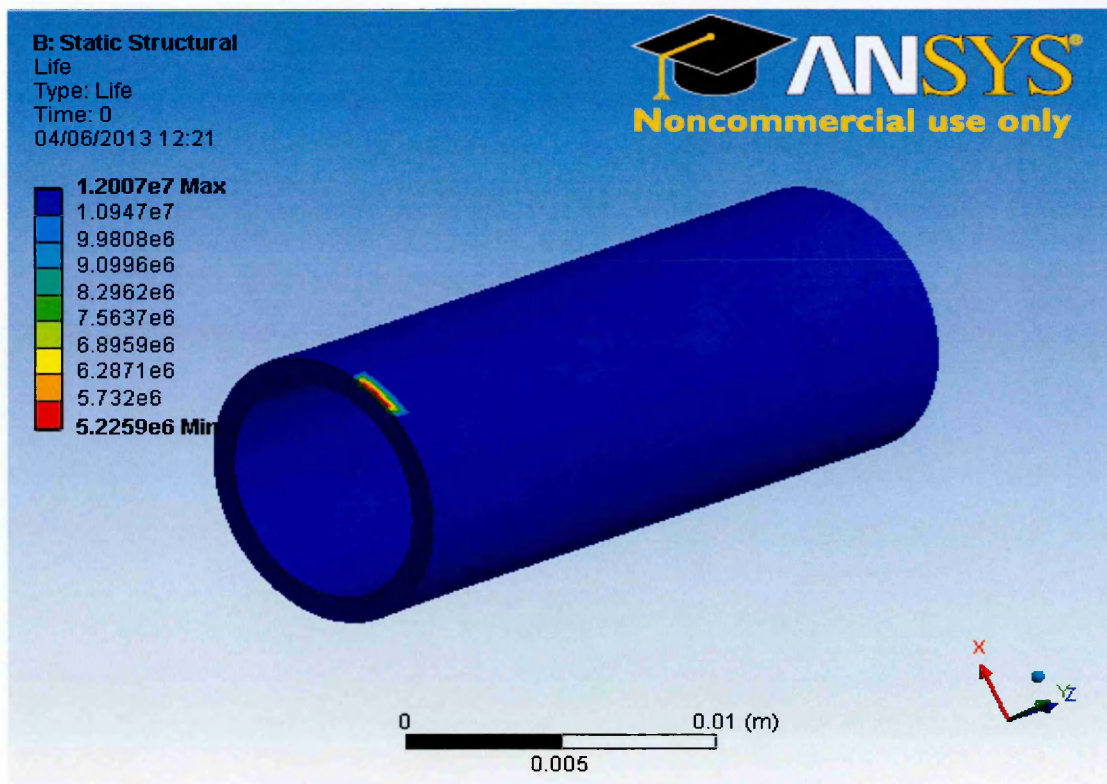
Figure 5.48 The distribution of the fatigue life pattern in the heating case.
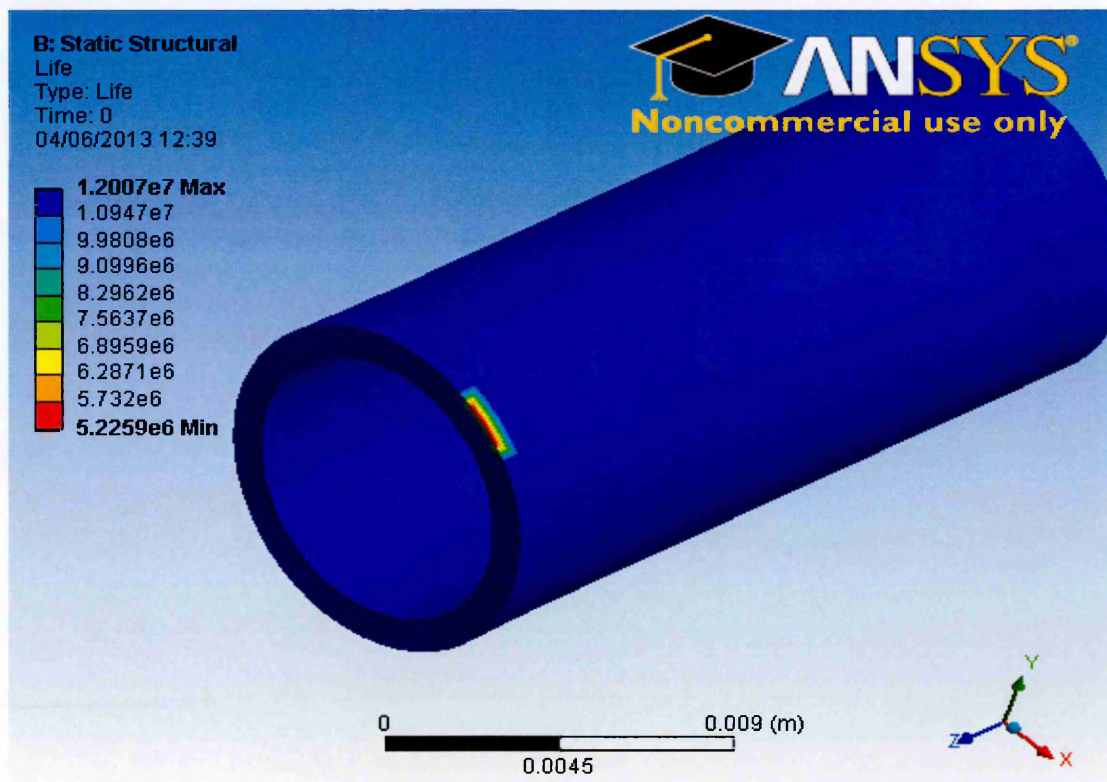
Figure 5.49 The distribution of the fatigue life pattern in the down shock cooling case.

CHAPTER SIX

6- EXPERIMENTAL RESULTS

This chapter outlines the experimental program results obtained during this research study. The presentation of the results falls into two parts: the fatigue stress-life data and the isothermal fatigue data.

6.1 Fatigue Stress–Life Results:

Three sets of fatigue stress-life data, described in Tables 3.5 to 3.7, are collected from different geometrical surface finished samples; they are polished, finely machined and notched (already cracked) types. The fatigue life property results look for a combination of the three types of geometry samples specified by the relation between the applied stresses ranging with the test life expressed by a number of cycles as shown in Fig.6.1. Tests are conducted at room temperature; the applied stress range was equal in magnitude to the yield stress of the material. The notch depth in the cracked specimen is created depending on the standard of the (D/d) ratio of the E602-03, ASTM test method [85]. The results shown in Fig.6.1 are the polished types, the higher strength with a small slope and the threshold stress level are equal to ($\Delta\sigma_{polished}$ = 0.9 σ_{ys}), while the machined type shows low strength; nearly the same slope depends on the surface roughness with a threshold stress level equal to ($\Delta\sigma_{machined}$ = 0.81 σ_{ys}); the effect of the stress concentration is significantly clear in the notched type, which gives a lowest strength with sharp slope and the level equal to ($\Delta\sigma_{notched}$ = 0.22 σ_{ys}).

The behaviour in Fig.6.2 for the AISI 420 martensitic stainless steel material employing the machined samples under low cycle fatigue at room temperature was observed by the DCPD machine in details, showing an initial hardening of the test after the fast elastic extension passes through the plastic zone; it is indicated by an increase in the DCPD machine reading, due to the specimen extension; it is then followed by decelerates to be a flat curve due to the process of strain ageing and cyclic softening of

192

the material that has taking place, until the saturation of the plastic deformation reaches the crack initiation companion with a sharp fast crack growth and specimen failure.
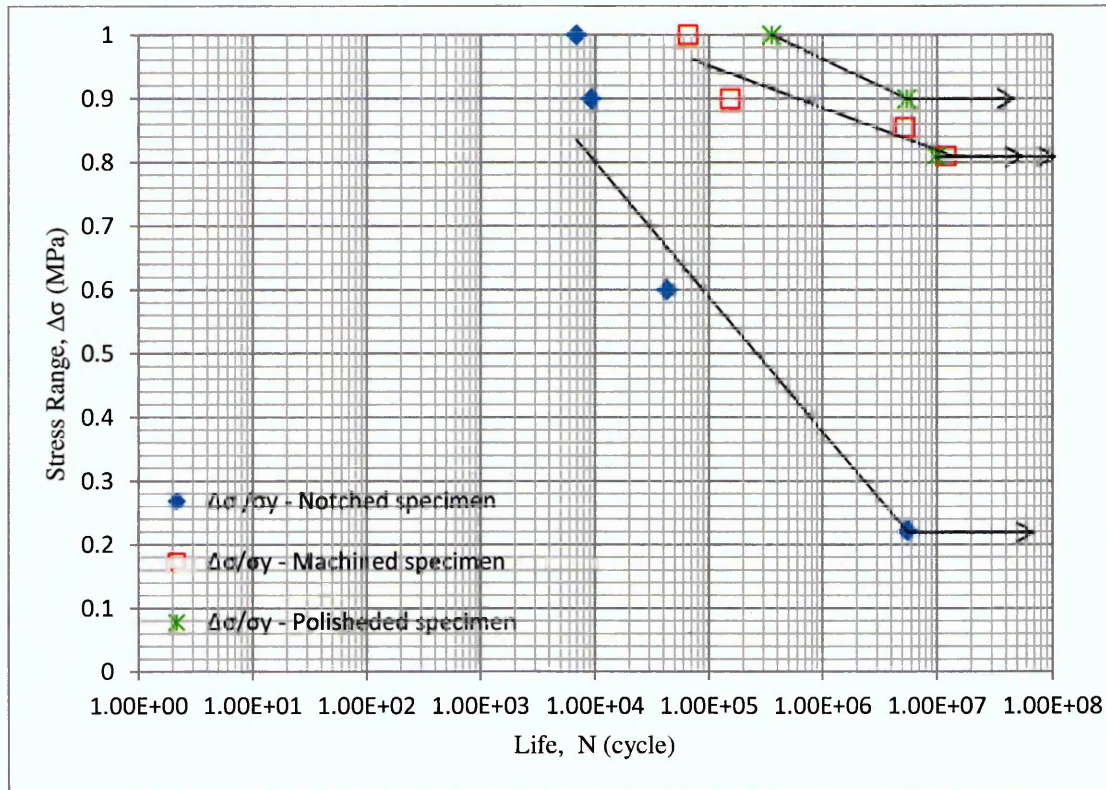
Figure 6.1 The stress range ratio to yield stress versus the number of cycles for different types of specimens.

6.2 Isothermal Fatigue Results:

One of the challenges of this research work was to monitor crack propagation using uncracked solid cylinder specimen under isothermal fatigue instead of the standard cracked combat type (CT) specimen, which is easily used and monitored, besides the small size of the testing section of the sample used in this research project. Nevertheless, an acceptable output data are obtained. The series of isothermal fatigue tests results have been described. Presentations of the properties are summarized in graphical and tabular forms. Results have been divided into parts: a) Material behaviour, and b) Crack growth analysis. The calibration analysis of the data was carried out by calculation method described in Chapter Three.

6.2.1 The Material Behaviour:

Several uniaxial isothermal fatigue tests are conducted on solid cylinder specimen. The tests were carried out at temperature range 300 °C to 600 °C, with one-half of monotonic yield stress or very slightly higher, taking the cyclic stress range at the respective testing temperature. The normalization profiles very clearly show the material characteristics change during the temperature range for isothermal fatigue tests, described by the DCPD machine reading for the specimen extension or crack growth during the isothermal fatigue test life. The behaviour of the material for the machined samples was detailed in Fig.6.2.showing a fast elastic extension due to the combined thermo-mechanical loading effects, observed by the increase of the DCPD machine, followed by hardening superimposed with dynamic strain ageing and softening, through the deceleration of the readings to be flat curves until plastic saturation reaches the crack initiation and the specimen fail. At 400 °C, the flat curve is nearly clear due to the high hardness increase in this temperature. Generally, all the profiles can be divided into three regions: a) thermo-elastic region, b) thermo-plastic region, and c) fatigue crack initiation, growth and fracture region, as shown in Fig.6.2.
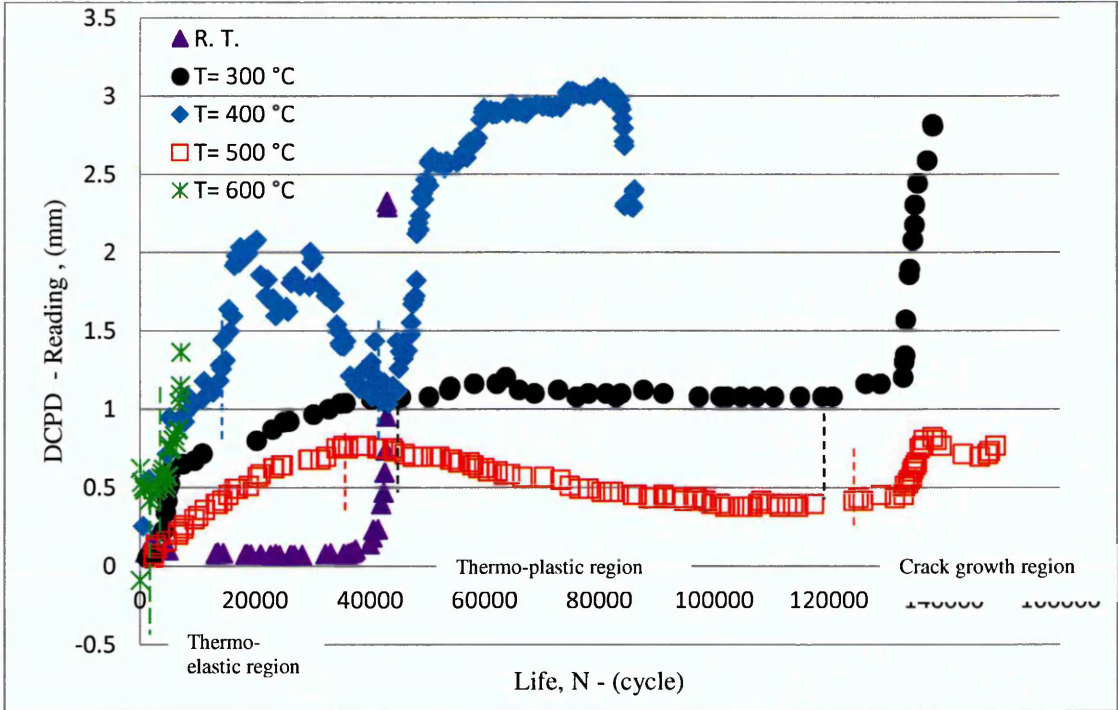
Figure 6.2 The behaviours of the material during the test series at different temperatures.

194

6.2.1.1 Thermo-Elastic Region:

This is a quick extended region that started at the beginning of temperature range and speeded up by applying the cyclic load of the test as a result of softening under load interaction, as shown in Figs.6.3., the fracture surface shows the effect of the increase in temperature by rough surfacing to the gauge length necking. The incremental temperature increased the elastic level or the specimen extension limit of this region, which can be practically indicated by the output grip position of the servo-hydraulic machine display where the range of the extension is between (1.5- 2.9 mm) proportions to total gauge length (20 mm), as for this research specimen at temperature range (300 – 600 °C) respectively. This extension is illustrated clearly in the beginning of the behaviour profile graph in Fig.6.2. This means that the curve level at 600 °C is the highest and at 300 °C, it should be the lowest, but this is affected by the DCPD machine voltage calibration between the testing specimen and the reference sample, which have directly affected the extension levels due to the calibration equation.

6.2.1.2 Thermo-Plastic Region

This is the stage where the material behaviour showed an initial hardening indicated by the decay of the curves, followed by a slow speed extension due to the microstructural changes taking place, which alters the dislocation substructure by strain ageing and dynamic recovery of the material, and also by the ductility caused by the interaction of the applied temperature and mechanical softening. The thermo-plastic region occurs when the material behaviour crosses the elastic zone passing to the plastic due to the loading interaction that reaches plastic saturation, which means getting fully plastic. Finally, the fatigue crack initiation and growth take place till failure and this is indicated by the crack initiation and growth region.

The interaction influence of the thermal and mechanical loading has been obtained by the soft or brittle material microstructure. The strain ageing continues under combined loading reaching fully plastic, which can be indicated by the length of the straight profile of this region in the curve as in Fig.6.2 and also the type of fracture surface observation on the broken sample face as shown in Fig.6.3.
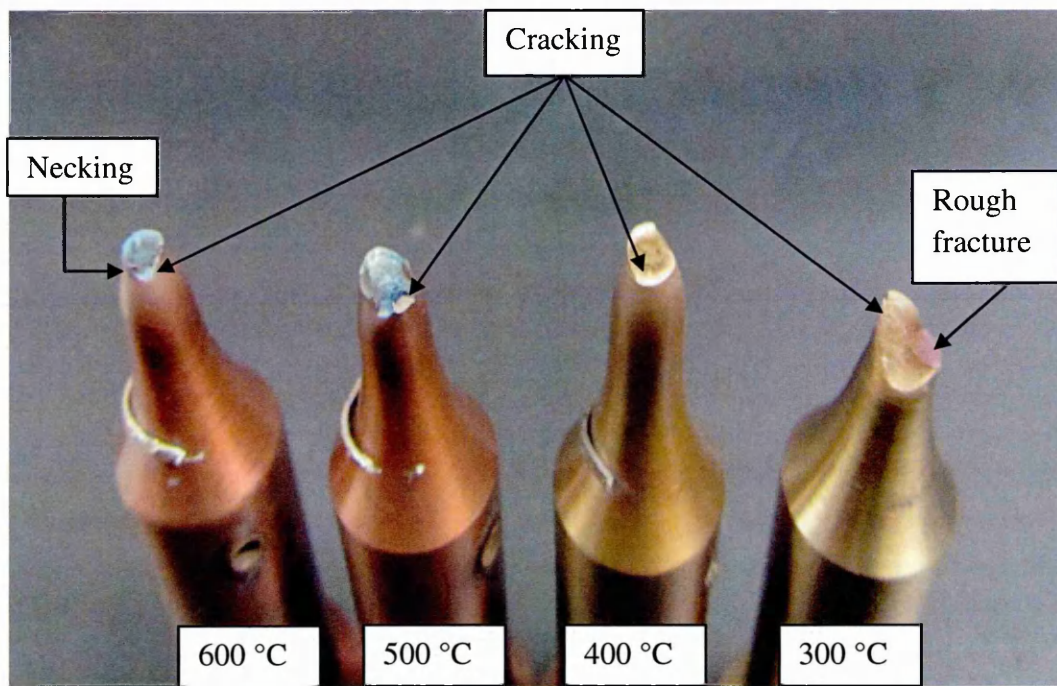
Figure 6.3 The image of the fracture surfaces of the isothermal fatigue test samples.

6.2.1.3 Fatigue Crack Initiation and Growth Region:

The crack initiation and propagation region started at different intervals of lives depending on the fully plastic deformation of the sample material, which is explained by the thermo-plastic region. Four sets of fatigue crack length data are plotted against the test life duration illustrated in Fig.6.4. The tests were carried out under uniaxial fatigue loading at 300 °C to 600 °C temperature ranges, employing electrical monitoring for the crack propagation by using the DCPD machine. The applied stress range employed in the tests is equal to the monotonic yield stress of the material in 300 °C test and the other tests are slightly higher in case of increased hardening levels.

The observations recorded showed that the cracking occurred in the specimen body below the fix end section, especially at 300 °C and 400 °C tests and as a result of hard material fracture obtained in the higher load region while, at the high temperatures, the cracking with slight necking takes place in the middle of the gauge length of the specimen due to softening and cross sectional area reduction. These are clearly illustrated in Fig.6.3. The crack initiation started at different intervals of lives depending on the fully plastic deformation of the specimen material, explained by the

196

end of thermo-plastic region as shown in Fig.6.4. The result shows a sharp slop crack growth with a small crack length and the crack initiation period all reduced by increasing the temperature. At 300 °C, cracking started after the period is extended (7 hours and 43 minutes), 400 °C crack initiation started after 4 hours and 47 minutes and at 600 °C, 24 minutes, except for 500 °C when crack initiation started, after 8 hours and 18 minutes, which is approximately close to the 300 °C test. This can be explained by balancing the combined effect of thermal strain ageing, which is also due to the interaction between the mechanisms of dislocation and the precipitation hardness under high temperature, with the mechanical softening which can be clearly observed at the fractured specimen faces in Fig.6.3.
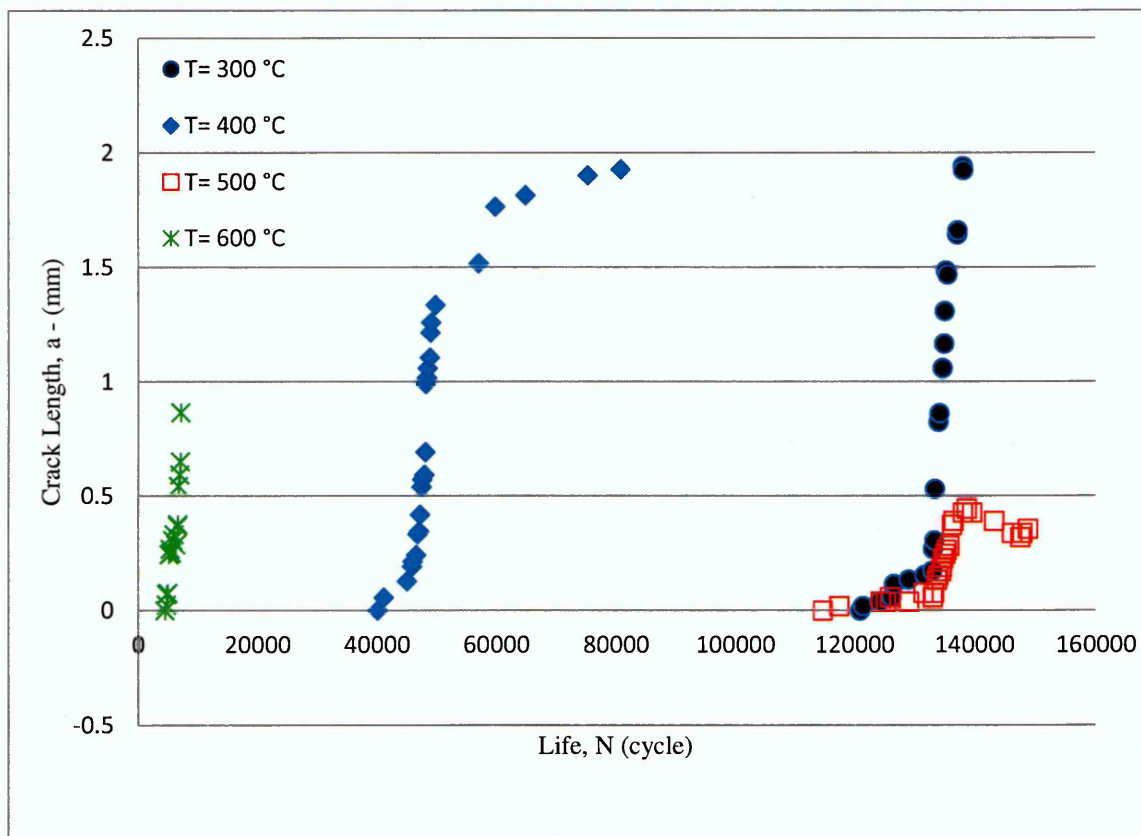
Figure 6.4 The crack length ratio with number of cycles at different temperatures range.

The crack growth can be expressed in three observations, which are illustrated in Fig.6.4. The first is the fast growth indicated by the sharp profile, especially at 300 °C and 400 °C tests, because of the hardness of the material with minimum softening due

to the temperature increase. The crack continuity arrest also occurs at 400 °C test due to the hardness increment caused by the precipitation of the intermetallic carbides. The second observation is the slow growth caused by the interaction of the dislocation (strain ageing) and the hardening behaviour. This is shown by the graduate of slope at 500 °C test. The last observation is the very fast growth due to creep–fatigue interaction. This is obtained at 600 °C test, where the strain ageing of the material is described by the necking of the sample gauge length superimposed by the crack propagation.
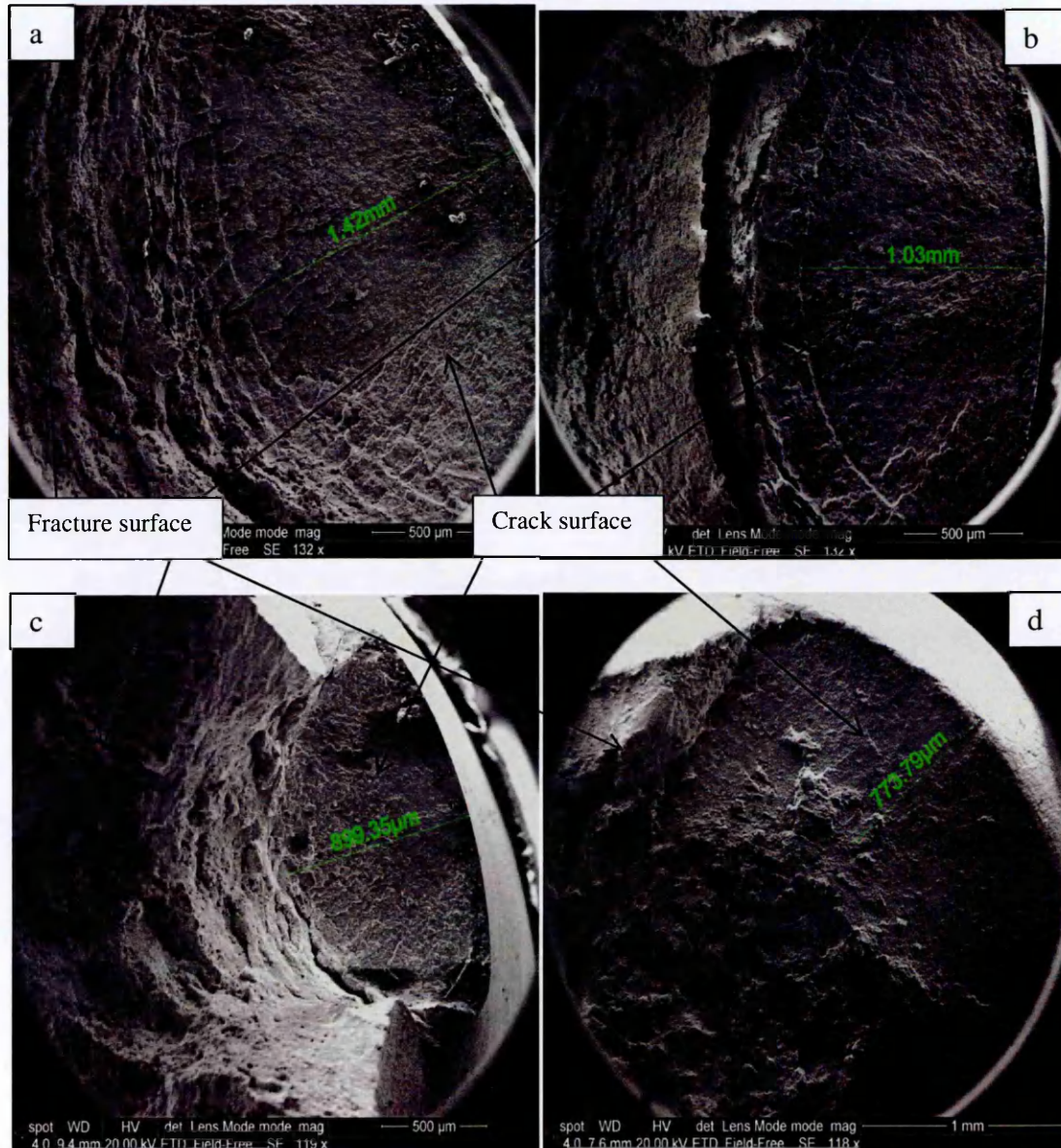
Figure 6.5 The SEM images of the isothermal fatigue crack length at different temperatures, a) at 300 °C, b) at 400 °C, c) at 500 °C and, d) at 600 °C.

The crack length and the microstructure checking are made for the fractured surface by utilizing the scanning electron microscope (SEM) images, to find the real crack length that occurred at specified temperature; it confirmed the accuracy level of the output DCPD machine reading and also the curve fitting calibration calculation; these images are shown in Fig.6.5. In addition, a general fatigue body information ratio is made between the cracks lengths to the original sample diameter of testing at different temperatures as shown in Fig.6.6. These results show that the crack length is reduced with the increase in temperature due to the combined load softening of the material; this means the long crack has a hard fracture and the small has a soft fracture.
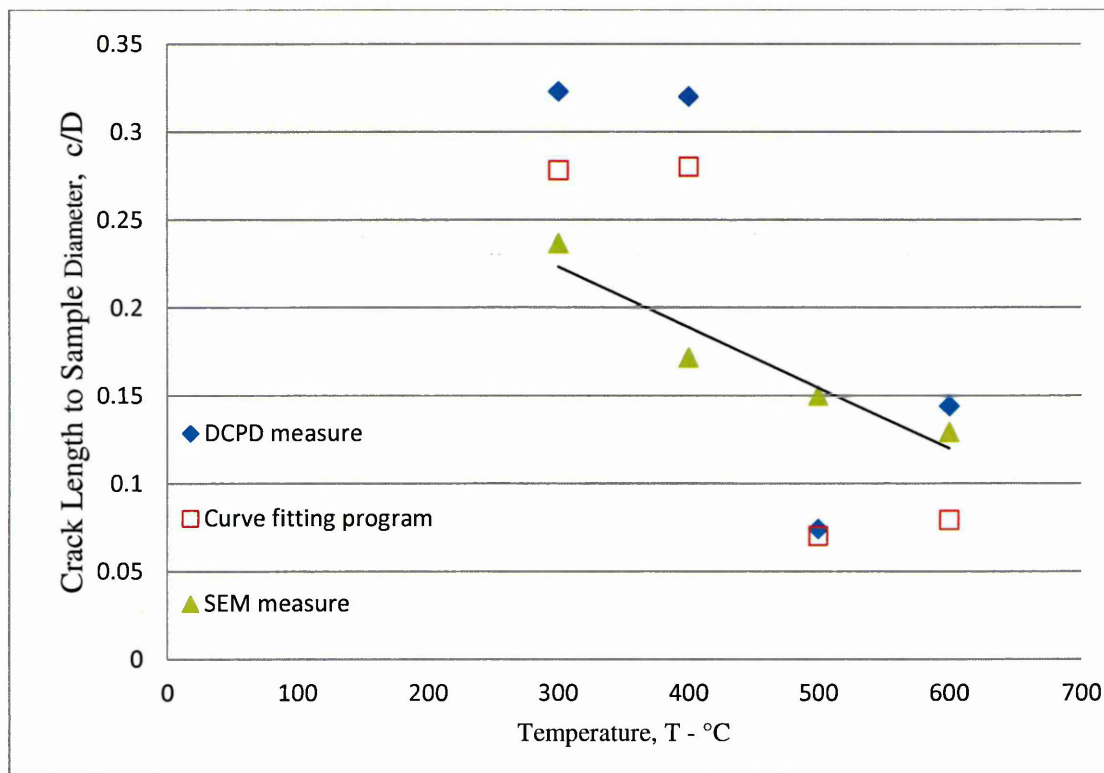
Figure 6.6 The crack length to the sample diameter ratio with temperature.

6.2.2 Fatigue Crack Growth Analysis:

The crack growth results are indicated by the stress or strain intensity and crack growth rate can be obtained by calculating the measured crack length and number of cycles. The crack growth data from a series of isothermal fatigue tests have been analysed and plotted as stress or strain intensity factors range against the crack length,

199

and fatigue crack growth rate $\left(\frac{dc}{dN}\right)$. Tables 6.1 to 6.4 contain the isothermal fatigue tests data, as measured and calibrated crack length and elapsed number of cycles are complied, together with crack growth rate and the stress and strain intensity factors calculated by the modified program discussed in Chapter Three, based on the data reduction technique [90]. Some of the crack growth rates have a negative value due to the continuous reading of the extended fluctuations and these will be neglected in the Log-Log graph.

Table 6.1 Uniaxial isothermal fatigue test data at 300 °C.

Test No.	N cycle	c - Exp. mm	c - cal. mm	ΔK MPa√mm	ΔK$_\epsilon$ √mm	dc/dN mm/cycle
	120960	0				
MIF300	121430	0.019377				
	124145	0.038721				
	126175	0.058031	0.0831	1.53E+02	1.30E-03	1.48E-05
	126560	0.115766	0.0889	1.64E+02	1.40E-03	1.44E-05
	129015	0.134947	0.1286	2.39E+02	2.00E-03	1.93E-05
	131670	0.154095	0.1833	3.43E+02	0.0028	3.82E-05
	132945	0.173211	0.2967	5.66E+02	0.0047	1.08E-04
	133095	0.268326	0.3482	6.71E+02	0.0055	3.45E-04
	133295	0.306158	0.3659	7.07E+02	0.0058	4.82E-04
	133370	0.530719	0.4586	9.04E+02	0.0074	6.57E-04
	133985	0.824267	0.8097	1.77E+03	0.0145	4.96E-04
	134110	0.860542	0.8611	1.91E+03	0.0157	5.00E-04
	134660	1.058617	1.0974	2.70E+03	0.0222	5.38E-04
	134935	1.165744	1.2312	3.24E+03	0.0267	5.00E-04
	135010	1.307745	1.2924	3.53E+03	0.029	4.22E-04
	135210	1.484187	1.3922	4.04E+03	0.0332	5.09E-04
	135485	1.466586	1.3951	4.06E+03	0.0334	1.66E-04
	137115	1.642297	1.6671	5.96E+03	0.049	2.19E-04
	137190	1.65984				
	138055	1.940363				
	138115	1.922819				

Table 6.2 Uniaxial isothermal fatigue test data at 400 °C.

Test No.	N	c - Exp.	c - cal.	ΔK	ΔK_ϵ	dc/dN
	cycle	mm	mm	MPa√mm	√mm	mm/cycle
MIF400	40090	0				
	41115	0.0569				
	45020	0.1278				
	45845	0.1929	0.2053	401.9231	2.10E-03	8.29E-05
	45970	0.2151	0.2097	410.7604	2.10E-03	1.07E-04
	46570	0.2418	0.28	555.053	2.90E-03	1.64E-04
	46770	0.3337	0.2984	5.94E+02	0.0031	2.37E-04
	47045	0.3458	0.3729	7.52E+02	0.0039	3.25E-04
	47185	0.4193	0.441	9.03E+02	0.0047	2.86E-04
	47460	0.5397	0.514	1.07E+03	0.0055	2.75E-04
	47525	0.5711	0.519	1.08E+03	0.0056	3.83E-04
	47935	0.5926	0.6938	1.52E+03	0.0079	6.04E-04
	48085	0.691	0.7664	1.72E+03	0.0089	7.46E-04
	48150	0.9886	0.8533	1.97E+03	0.0102	4.99E-04
	48360	1.0163	1.0302	2.56E+03	0.0132	6.72E-04
	48425	1.0583	1.0432	2.61E+03	0.0135	5.42E-04
	48835	1.1046	1.1678	3.10E+03	0.016	2.46E-04
	48910	1.2132	1.1751	3.13E+03	0.0162	2.40E-04
	49035	1.2581	1.1893	3.19E+03	0.0165	5.07E-05
	49750	1.3338	1.2566	3.50E+03	0.0181	5.51E-05
	57010	1.5159	1.6014	5.65E+03	0.0292	3.55E-05
	59775	1.7635	1.6844	6.38E+03	0.033	2.90E-05
	64860	1.8133				
	75295	1.8991				
	80815	1.9254				

Table 6.3 Uniaxial isothermal fatigue data at 500 °C.

Test No.	N cycle	c - Exp. mm	c - cal. mm	ΔK MPa√mm	ΔK_ϵ √mm	dc/dN mm/cycle
MIF500	114690	0				
	117480	0.0193678				
	124390	0.0386594				
	125200	0.0386594	0.0495	86.5823	0.0011	3.36E-06
	125965	0.0578749	0.0511	89.4495	0.0011	3.54E-06
	129045	0.0386594	0.06	105.2417	0.0013	6.75E-06
	131500	0.0770144	0.0804	141.2734	0.0018	1.81E-05
	133010	0.0578749	0.1192	210.6245	0.0027	3.06E-05
	133225	0.0770144	0.1167	2.06E+02	0.0026	5.53E-05
	133715	0.133978	0.147	2.61E+02	0.0033	7.48E-05
	133990	0.1528144	0.1745	3.11E+02	0.004	8.37E-05
	134415	0.1715754	0.2056	3.68E+02	0.0047	8.26E-05
	134540	0.1902608	0.2189	3.93E+02	0.005	8.32E-05
	134740	0.2274059	0.2317	4.16E+02	0.0053	9.54E-05
	135115	0.2458656	0.2745	4.97E+02	0.0064	1.06E-04
	135330	0.2642503	0.2962	5.38E+02	0.0069	1.00E-04
	135830	0.28256	0.3611	6.65E+02	0.0085	9.60E-05
	136230	0.3729885	0.3995	7.41E+02	0.0095	8.79E-05
	136505	0.3908509	0.4126	7.68E+02	0.0098	6.60E-05
	138070	0.4263534	0.4221	7.87E+02	0.0101	4.67E-06
	138695	0.4439937	0.4105	7.63E+02	0.0098	-6.31E-06
	139585	0.4263534	0.3964	7.35E+02	0.0094	-1.50E-05
	143250	0.3908509	0.3301	6.04E+02	0.0077	-8.50E-06
	146205	0.3370407	0.3284	6.01E+02	0.0077	1.11E-05
	147545	0.3189552				
	147880	0.3370407				
	148845	0.3550518				

Table 6.4 Uniaxial isothermal fatigue test data at 600 °C.

Test No.	N	c - Exp.	c - cal.	ΔK	ΔK$_\epsilon$	dc/dN
	cycle	mm	mm	MPa√mm	√mm	mm/cycle
MIF600	4460	-0.0005				
	4660	0.024				
	4720	0.0716				
	4945	0.0757	0.1325	213.2033	0.0024	2.94E-04
	5170	0.2455	0.2084	339.0271	0.0039	2.69E-04
	5310	0.2685	0.24	392.5215	0.0045	2.29E-04
	5510	0.2525	0.2909	480.1689	0.0055	1.85E-04
	5795	0.3066	0.2917	481.5299	0.0055	7.38E-05
	6015	0.3317	0.3061	506.6833	0.0058	8.34E-05
	6275	0.2885	0.3252	540.147	0.0062	2.10E-04
	6560	0.369	0.3836	644.7232	0.0074	3.96E-04
	6635	0.3765	0.4074	688.1059	0.0079	4.47E-04
	6760	0.5424	0.4762	816.7583	0.0094	7.01E-04
	6960	0.5938				
	7035	0.6508				
	7100	0.865				

6.2.2.1 Stress and Strain Intensity Factors Results:

The calculation of the stress and strain intensity factors was carried out by a traditional approach using experimental crack length data and standard shape function corresponding to the solid cylinder specimen externally cracked under uniaxial fatigue loading.

Figs.6.7 and 6.8 show the stress and strain intensity calibration related to the crack length in a number of isothermal fatigue tests at 300 °C to 600 °C temperature range, which increases with the increase in the crack length and the stress intensity factor decreases with the increase in temperature, except at 400 °C. While, the strain intensity factor curves are bonded between the maximum values at 500 °C and the minimum at 400 °C. The correlation between the theoretical solution and the experimental data

calculation for stress and strain intensity factors find out a convergence in less than 0.5 mm crack length limit, which then diverge with the increase in the crack length, more closely at the stress intensity factor, but the behaviour relation with the increasing temperature is similarly, as shown in Figs. 6.9 and 6.10.
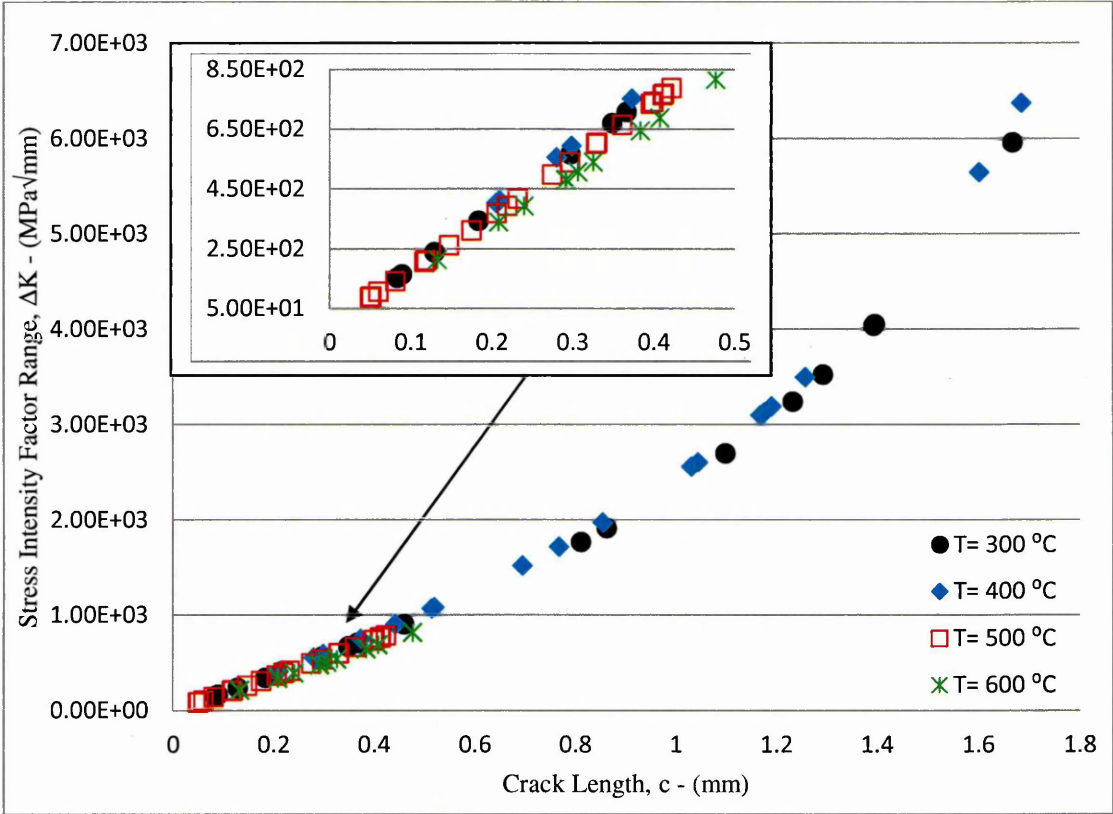
Figure 6.7 The stress intensity factor in relation to the crack length at different temperatures.
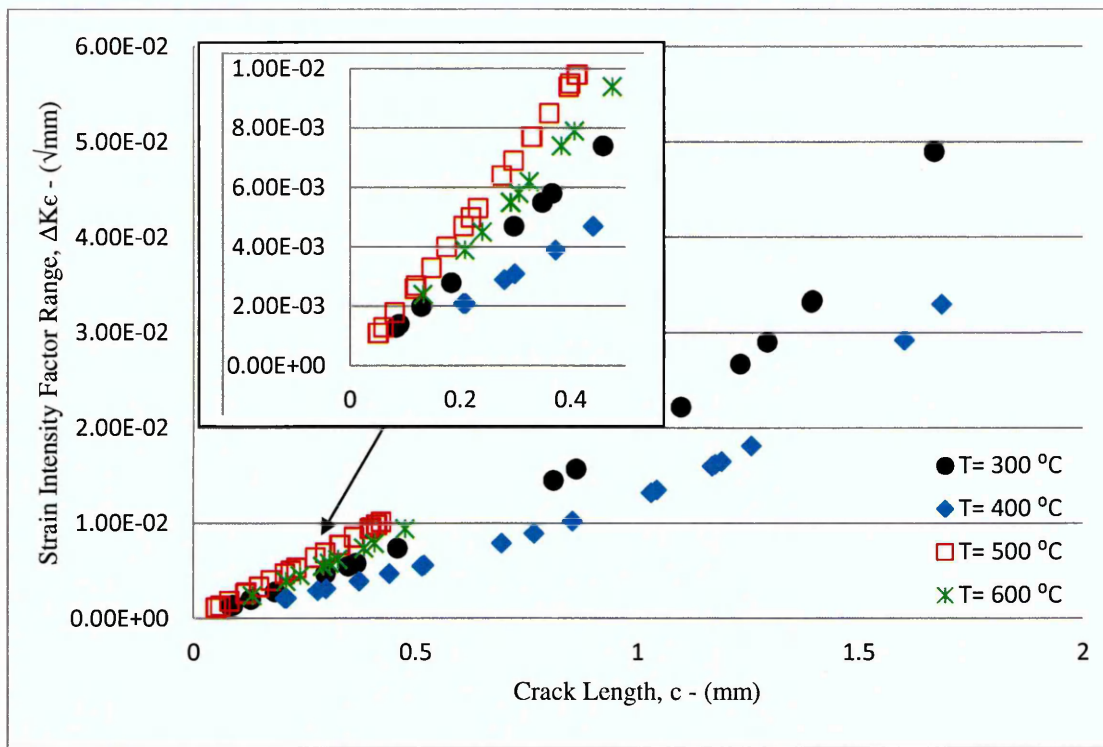
Figure 6.8 The strain intensity factor in relation to the crack length at different temperatures.
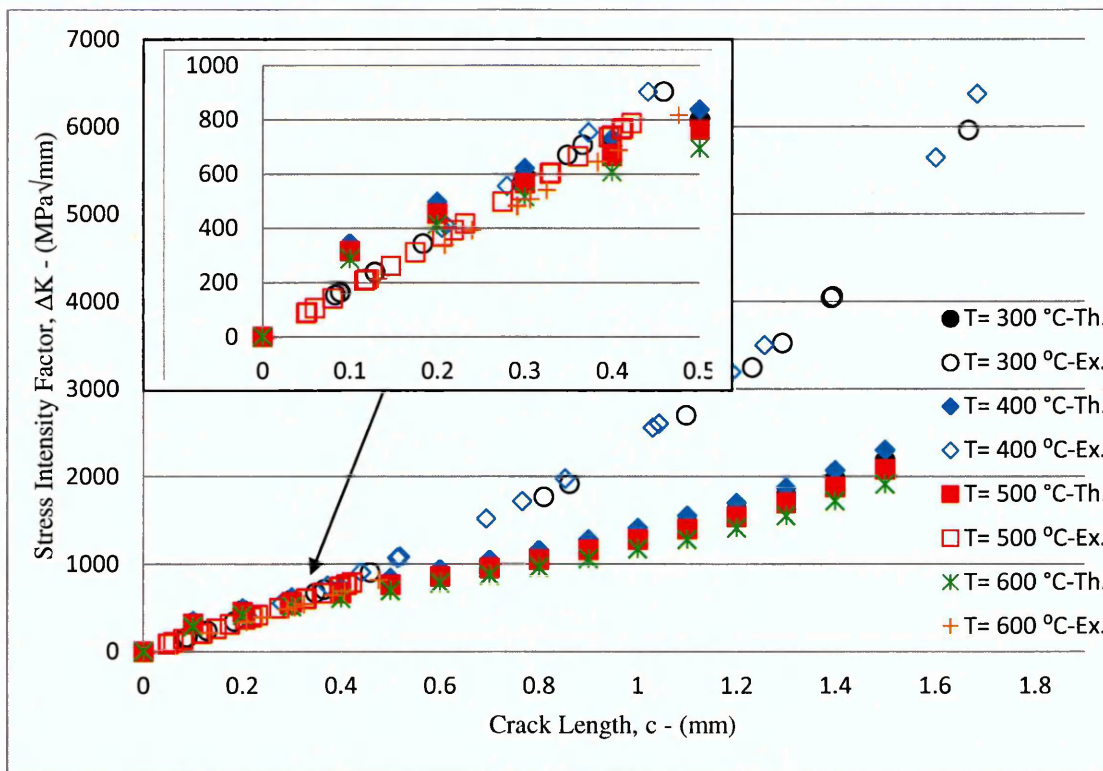
Figure 6.9 The stress intensity factor correlation between theoretical and experimental solutions.

205
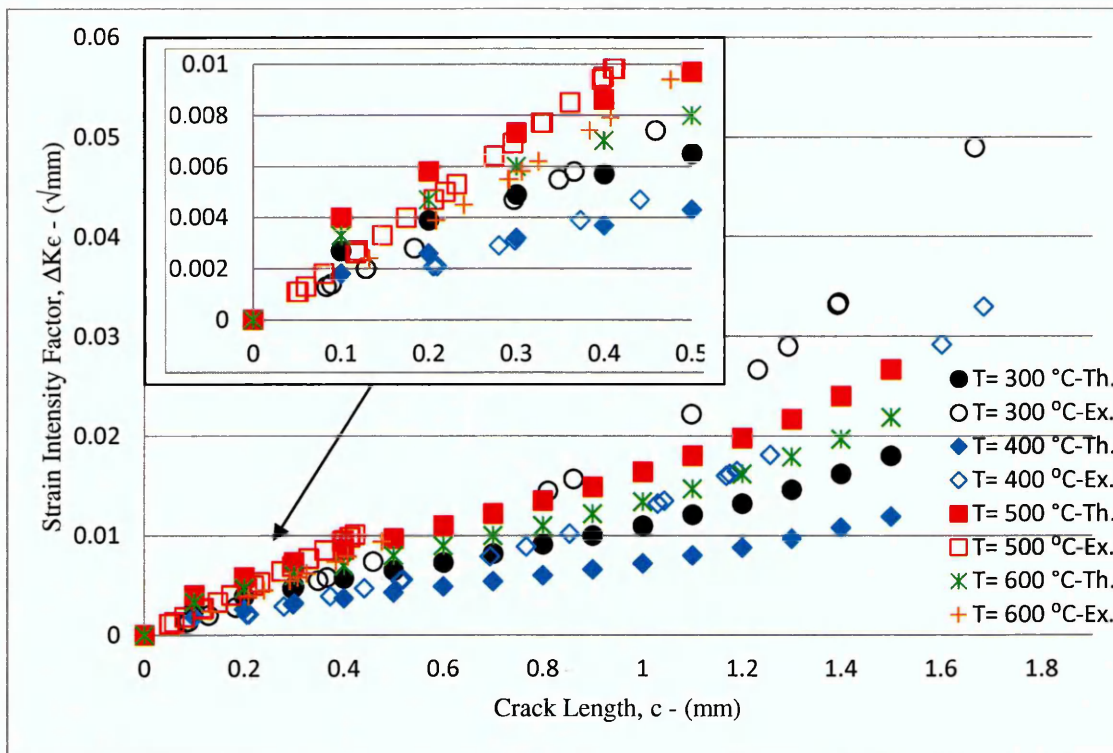
Figure 6.10 The strain intensity factor correlation between theoretical and experimental solutions.

6.2.2.2 Crack Growth Rate Results:

The effect of the elevated temperature on the fatigue crack growth rate in the un-notched fine machined solid cylinder specimen is shown in Figs.6.11 and 6.12. It is described in terms of two rational plots, as crack growth rate (dc/dN) against stress or strain intensity factors. The plots illustrate the influence of the crack growth rate due high temperatures, and the effects of the modulus of elasticity on the crack growth behaviour of the material. Tables 6.1 to 6.4 contain data from series of isothermal fatigue tests at 300 °C to 600 °C temperature range. The crack growth rate and stress or strain intensity factor is calculated by the modified programme in Appendix A, based on the data reduction technique employing the measured crack length and the elapsed number of fatigue cycles.

The results illustrated in Fig.6.11 display the relation between the crack growth rate and the stress intensity factor; the crack rate increases with the increasing temperature. They also show that at 500 °C, the crack rate started quickly due to the softening

obtained by the thermo-mechanical interaction loading; the growth rate at 600 °C is less than that at 500 °C. The profiles show that the crack growth rate against the stress intensity factor at different temperature ranges is bonded between the minimum at 300 °C and the maximum at 500 °C.
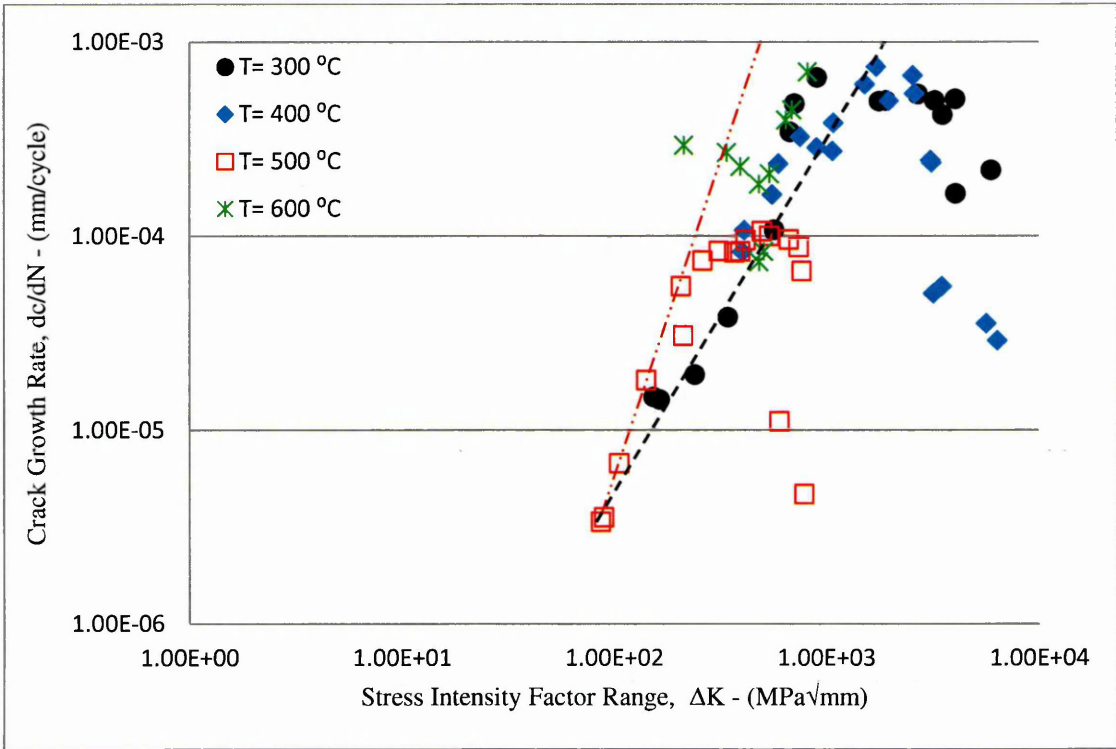
Figure 6.11 The crack growth rate as related to the stress intensity factor range at different temperature levels.

The results in Fig.6.12 show that the relation between the crack growth rate and the strain intensity factor is significantly influenced by the modulus of elasticity, making the results bonded between the maximum at 400 °C and nearly one line of the other temperatures.

The dispersion of the last data right side the dashed line in Figs.6.11 and 6.12, is related to the influence of the crack discontinuity before failure of the material on the crack growth rate calculations, especially at 300, 400 and 500 °C temperature tests.
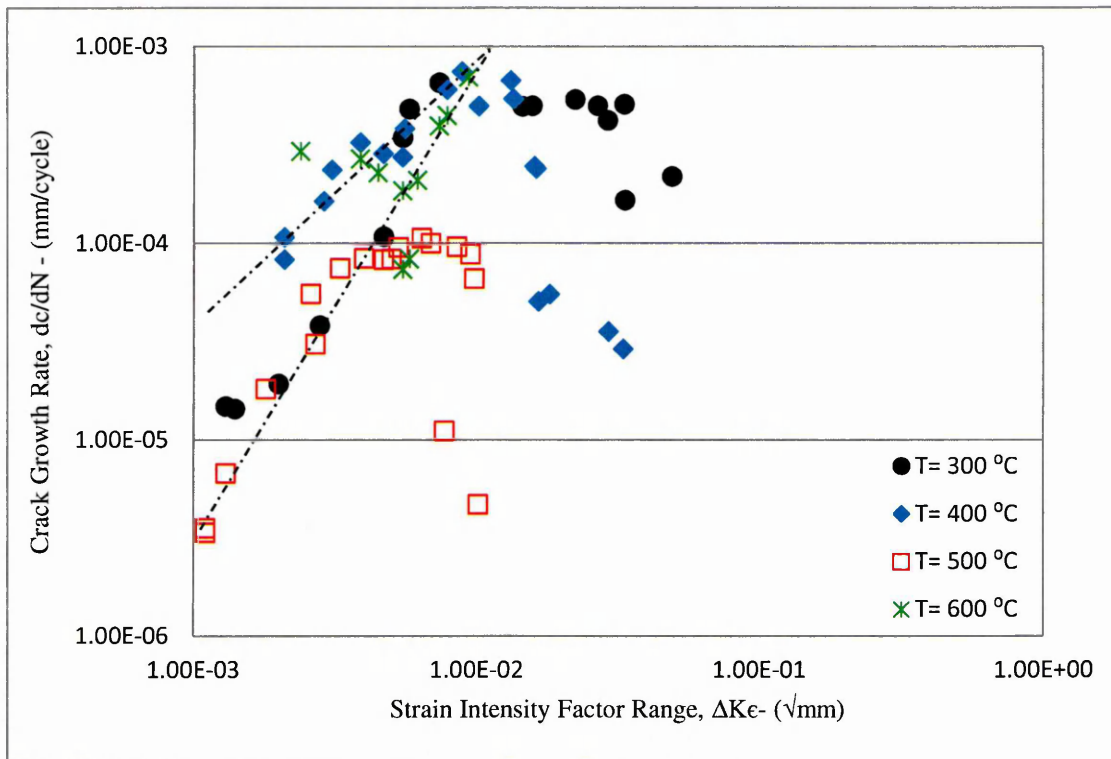
Figure 6.12 The crack growth rate as related to the strain intensity factor range at different temperature levels.

CHAPTER SEVEN

7- DISCUSSION

Many factors affect the material failure mechanism at room and high temperature fatigue. This chapter discusses and analyses the factors discovered in the experimental program results obtained during this research project. It outlines two sections: section one that deals with the analysis of the low cyclic fatigue finding at room temperature and section two that presents the isothermal fatigue findings.

7.1 Low Cyclic Fatigue Analysis:

Low cyclic fatigue tests were carried out at room temperature to assess the fatigue life properties specified by the S–N curves by combining three different geometry specimens: polished, finely machined and notched. The results are shown in Fig.6.1: the highest strength is the polished specimen, while the machined shows low strength and nearly similar slope depending on the surface roughness, and the lowest strength due to the high effects of the stress concentration in the notched specimen. The reason for that is martensitic stainless steel consists of high carbon and chromium material; the increase in this content increases the strength and hardness potential but decreases the ductility and toughness. The large carbides do not enter into the hardening process, but they provide additional abrasion resistance and precipitate from the melt as primary carbides, while the other elements which are added have indirect influence through their control over the phase stability, making the martensitic stainless steel a hard material that tends to be nearly brittle fracture [126]. To confirm this property, the sharp and fast crack growth is observed in the last stage of the material behaviour as shown in Fig.6.2. During a subcritical anneal and hardened structures of type 420, the visible carbides are precipitated, mostly on the grain boundaries [126]. Fournier et al., [23] observed the damage mechanisms taking into account the increased

209

cracks density and the grain size effect on crack initiation causing the shorter cyclic lifetimes of the three different 9–12%Cr martensitic steels.

The behaviour of the material under low cycle fatigue at room temperature for the machined samples in Fig.6.2, shows an initial hardening after fast elastic extension, passing through plastic deformation by cyclic softening until saturation, reaching the crack initiation and specimen fracture. The cause of the hardening is related to the characteristics of structure transformation from body centric cubic martensitic stainless steel to hexagonal closed packed lattice phase type at room temperature. It is closely related to stacking-faults [126]. Faulted material is considered to have surface tension, which tends to pull the partial dislocations together. This configuration is one of relatively high energy. Its formation and stability depends on the magnitude of the surface tension or the stacking-fault energy. The deformation processes involves dislocation slip or, particularly at higher temperatures, climbing cannot readily slip past each other or climbing from one plane to another. In this manner, the work-hardening behaviour or strength of the material can be increased [126]. Similarly, Armas et al., [37] observed the fully annealed AISI 420 initial hardening followed by a saturation stage while carrying out a strain control test at temperatures ranging from room temperature to 823 K. Furthermore, Song et al., [34] revealed the cyclic softening observed at room temperature and at 600 °C related to the cellular structures of dislocations formed in the fatigued specimens at both room and elevated temperatures.

7.2 The Isothermal Fatigue Analysis:

The results of the isothermal fatigue tests show the material is affected by various factors due to cyclic softening, microstructure deformation high temperature, stress and strain intensity factors, fatigue crack growth and creep-fatigue.

7.2.1 Cyclic Softening and Dynamic Strain Ageing:

The behaviour of cyclic softening and dynamic strain ageing results shown in Fig.6.2 has a rapid extension due to the ductility of the material at high temperature and the increase in temperature; this is clear in the first region. The important aspect is to

210

note the thermoplastic region where the material at room and high temperature produces an initial hardening, followed by slow extension until it reaches fully plastic saturation followed by crack initiation and growth eventually reaching the failure of the specimen.

Martensitic stainless steel is one of those that contain more than 11.5% chromium; it has a predominantly austenitic microstructure at elevated temperatures that can be transformed into martensite by suitable cooling at room temperature or as a result of deformation [126]. The compositions of most precipitation-hardening or age-hardening stainless steel are carefully balanced to produce hardening by two separate mechanisms: first, an allotropic transformation of austenite to martensite produced by thermal austenite-condition treatment or by cold working, and the second is the resulting structure giving a simple, low-temperature aging treatment that is hardened by chromium carbide precipitation; it simultaneously tempers the martensite [127].

The experimental observation shows that at 300 °C, the effect of the temperature is not high on the material microstructure behaviour. Thus, the strain ageing obtained by the mechanical softening is more like the thermal effect. This can be designated by the length of the nearly straight curve of this region. A good sign of the mechanical softening effect is the rough fracture surface of the test sample, which is still in the brittle phase, as shown in Fig.6.3. A similar behaviour observation is made by Armas et al., [37] for the same material and by Negesha et al., [45] for other martensitic steels. They demonstrated that the cause of the slower cyclic softening is related to the dynamic strain ageing effects. Zhang et al., [42] also noted that cyclic softening is generally explained by the modification of the dislocation structure and density and/or the carbide morphology, chemical composition and density for hot working martensitic tool steels. On the other hand, Gerard et al., [38] showed that the fatigue damage control depends on the thermally activated plastic strain range mechanisms and the mechanisms which are not thermally activated.

The stainless steel with higher carbon and chromium contents exhibits the higher hardness at any specific tempering temperature. These steels do not soften appreciably until the tempering temperature exceeds 482 °C. Moreover, a secondary hardening occurs when tempering at about 427 °C. Tempering between 538 °C and 760 °C decreases the hardness of these steels considerably [126]. Heating in air can lead to surface decarburizing. The carbon loss may be reduced by heating in a nitrogen

atmosphere. However, that nitrogen may absorb and stabilize the austenite against transformation. The $M_{23}C_6$ carbide begins to nucleate about 482 °C and becomes predominant above 538 °C these carbides tend to be too large to influence strength. Additionally, they are stable enough to significantly reduce the matrix carbon content which remained high during the lower temperature temper treatment. The net effect is the observed drop in hardness [126]. Experimentally, at 400 °C, and due to the high heating rate of the isothermal fatigue test, hardness increased very clearly due to tempering caused by this temperature; this is expressed by the decay of the thermo-plastic region profile after the elastic region; it then continued slowly till fully plastic is formed and the fatigue cracking appears (see Fig.6.2). The short length of the thermo-plastic region is caused by the combined highly applied mechanical load 9% over the yield strength, whilst the ultimate to the yield stress ratio is 20%. The thermal loading effect can be displayed by the partially rough fracture sample face shown in Fig.6.4. The initial hardening was identified by Isfahany et al., [84], that is due to tempering in the range of (400 - 500 °C), the attribution of the secondary hardening phenomenon increased. This is generally associated with the formation of the precipitation of M_7C_3 carbides within martensite lath; the softening occurred when the M_7C_3 carbides started to coarsen and partially transform to $M_{23}C_6$ carbides.

At 500 °C, the interaction balance between the hardening due to the tempering range with the strain ageing and cyclic softening is obtained by the cyclic loading with the high temperature ductility. This strain ageing continues to reach the fully plastic state. This is indicated by the long duration length of the straight profile of this region. The good sign of the high thermal effect can be presented by the smooth fracture sample surface shown in Fig.6.3.

At 600 °C, this is the creep temperature range for the martensitic material [86]. The action of creep-fatigue in this isothermal fatigue test can be observed by the short duration of this region, which is caused by the interaction of the sample straining (necking) and cracking.

7.2.2 High Temperature Effects:

The isothermal fatigue test observations show the influence of the high temperature on the fatigue crack initiation and growth. Increasing temperature leads to surface oxidation, dropping the carbon contains and hardness. The formation of large and stable chromium-carbide precipitation causes the weakness of the grain boundary strength, leading to reduce crack initiation period and fast crack growth. At 300 °C and 500 °C cracking initiation started at long testing duration approximately close intervals, while at 400 °C and 600 °C, the tests are in short intervals. This can be explained by the interaction of the thermal strain ageing between the mechanisms of dislocation and precipitation hardness under high temperature, with mechanical softening, which can be clearly observed by the fractured specimen faces in Fig.6.3.

The crack initiation behaviour is observed; it results from mechanical cyclic softening in the low temperature, indicated by rough fracture surface transmitted to thermal softening and creep-fatigue at the high temperature; this is indicated by necking with small crack length as shown in Fig.6.4.

Martensitic stainless steel is a hard material that softens under cyclic loading; the elevated temperature decreases the strength and increases the flow stress of the plastic deformation. The crack length observed is decreased with the increase in the temperature due to the balance between the hardening and softening of the material, which means passing from the hard to the ductile phase, causing the interaction of the ageing of the second phase particles; it is expressed by the specimen necking and the crack propagation. This is shown more clearly by the scanning electron microscope (SEM) measurement shown in the images Fig.6.5; the longest crack depth is related to the lowest temperature due to the hardness of the material. The crack length of the original sample diameter ratio is related to the temperature as shown in Fig.6.6; it gives significant information to the engineers on the crack limitation for the usage and replacement of design components made from this type of material. Also, the images did not give any evidence of striation at elevated temperature range as tested in this project.

The crack growth is expressed as fast growth indicated by the sharp profile at low temperature; it slows down with increasing temperature till 500 °C due to the interaction of the dislocation (strain ageing) and the hardening behaviour. Latterly, at

high temperature, there is fast growth due to the creep–fatigue interaction. The reasons for that are that the precipitation of $M_{23}C_6$ carbides formation and the effect of the retained austenite significantly reduce the yield strength level at higher temperature [126]. Many investigators [38, 41-47], showed that the cyclic softening of the martensitic steel is increased with increasing temperature. Bernhart et al., [25], found out that the plastic strain amplitude depends on the initial total strain, but the evolution rate is temperature dependent.

7.2.3 Stress and Strain Intensity Factors Analysis:

The calculations of the stress intensity factors are shown in Figs. 6.7. They are directly influenced by the high temperature, which decreases with increasing temperature, where the increase of the temperature decreases the strength of the material. This is for all temperatures except at 400 °C, where the maximum value is due to increase hardness.

Introducing the elastic region by dividing the modulus of the elasticity of the material at the applied temperature with the stress intensity factors is illustrated in Fig.6.8; it is expressed by the strain intensity factor showing the minimum at 400 °C because of the high mechanical loading effects with high modulus of elasticity and the activation of microstructural transformation indicated by the hardening of the material. The maximum strain factor is shown at 500 °C due to the thermal effects indicated by the ductility and strain ageing. This is because the AISI 420 martensitic stainless steel is a high carbon with chromium contents exhibiting secondary hardening when being tempered at about 427 °C due to the precipitation nucleation which decreases the hardness between 538 °C to 760 °C due to the austenite and precipitation transformation [126]. Kanazawa et al., [41], deals with two kinds of martensitic stainless steels (types 403 and 616) at room temperature, 400, 500 and 600 °C. For both materials, they showed that the elastic strain range decreases with increasing test temperature and that the plastic strain range changes to 400 °C but above 400 °C, it increases with temperature.

214

The correlation between empirical estimation and experimental calculation is shown in Figs. 6.9 and 6.10. The values are close at the beginning about 0.5 mm from the crack length but it then diverge due to the combined effect of the cyclic softening of the material with fast crack growth, which could not be displayed in the empirical formulation especially in the geometrical function F(c/r). But the empirical results show the same observation of the effects of the temperature and mechanical loading with experimental finding as the maximum and minimum stress and strain intensity factors magnitudes.

7.2.4 Fatigue Crack Growth Rate:

The increment of the temperature improves the fatigue crack growth rate against the stress intensity factor as shown in Fig.6.11. The discovery of creep-fatigue range at 600 °C causes a reduction of growth rate less than 500 °C. Conversely, at 500 °C, the crack initiation is produced as a combination of cracking and reduction area resulting from the accumulation of softening created by the addition of mechanical cyclic softening with thermal strain ageing during the test period. The observation of the crack growth rate of the material under isothermal fatigue tests shows that it is bonded between the lower bond at 300 °C and the upper bond at 500 °C, because of the transmission from nearly brittle fracture to ductile with increasing temperature.

The variation of the crack growth rate with the strain intensity factor is shown in Fig.6.12, where the fatigue crack growth rate is bonded between the upper bond at 400 °C and the lower bond; it nearly seems to be in line with the other temperatures ranges. This is related to the effects of the modulus of elasticity and additionally to the thermal and mechanical loadings. Kim et al., [13] showed that the fatigue crack growth rates increase with the increase in test temperature: it is expected that the fatigue crack growth mechanism at elevated temperature would change to one similar to the common metallic materials, whereby crack blunting and resharpening is the dominant mechanism and the main reason for the increased crack growth rate at elevated temperature. KUEI-CHANG HSU [51], pointed out that the precipitates would become coarser leading to a decrease in strength and to hardness which is the main reason of the fatigue crack growth increase.

7.2.5 Creep-Fatigue Effect:

Concerning the AISI 420 martensitic stainless steel properties, the creep temperature is 600 °C [86]. The fatigue crack growth test at this temperature gives an indication that creep-fatigue interaction is taking place. The cyclic softening and the strain ageing are very fast in this temperature range due to the microstructure deformation, which is clearly shown by the reduction area (necking) with small crack length on the fracture specimen face Fig.6.3. This is a retained austenite that significantly reduces the yield strength level; another potentially serious reaction can be the later martensitic transformation following tempering. This volume change could lead to cracking [126]. Fourniera et al., [47], studied the fatigue and creep-fatigue tests carried out on 9–12%Cr tempered ferritic–martensitic steels at high temperature. They conclude that the creep-fatigue is affected by the cyclic softening because it is correlated with the decrease in dislocation density and with the sub-grain coarsening. Brnic et al., [86], performed the short-time creep tests for the same AISI 420 martensitic steel; it becomes apparent that the creep strains can be acceptable when the stress level does not exceed 50% of 0.2 per cent offset yield strength. Even if the stress level at the temperature of 600°C is under 20% of 0.2 per cent, the offset yield strength and the creep strain may be acceptable.

CHAPTER EIGHT

8- CONCLUSIONS AND FUTURE WORKS

8.1 Conclusions:

In the present study, three methods of analysis are applied to study the fatigue crack growth rate behaviour of the AISI 420 martensitic stainless steel under high temperature fatigue conditions. This research produce an experimental work under uniaxial stress-controlled fatigue testing at elevated temperatures providing the crack growth rate data, which is less data about this material available due to its high hardness and low toughness properties. The empirical modelling develops a solution based on adding the experimental fatigue applied load to the calculated thermo-elastic-plastic stresses depends on the mechanical properties generated under high temperature tensile tests, giving a good agreement with the experimental work results. Finally, the numerical modelling solution using ANSYS software gives a good agreement with the experimental work results, moreover, with the theoretical solution. The following conclusions are drawn from the research study:

8.1.1 Experimental Study:

The conclusions collected from the experimental work are:

1- The low cycle fatigue life observation of the tested specimens at room temperature shows the highest strength in the polished specimen, while the machined shows low strength and nearly same slope is observed to the polished, and the lowest strength is that of the notched specimen due to the high effect of the stress concentration. That is because AISI 420 martensitic stainless steel is a hard material influenced by the surface roughness condition.

2- The DCPD machine monitoring presented the material behaviour during the isothermal fatigue tests; it is described by three regions. The fast extension started

when supplying the temperature; it is accelerated with applying the cyclic mechanical load, denoted by thermo-elastic region. The hardening interacted with graduate extension denoted by thermo-plastic region. The Final region is the process of crack initiation and propagation until the fracture takes place.

3- The material at room and high temperature produces an initial hardening, followed by slow extension until fully plastic saturation is realized; it is then followed by crack initiation and growth eventually reaching the failure of the specimen, resulting from the dynamic strain ageing occurred from the transformation of austenitic microstructure to martensite and also, the nucleation of precipitation in grain boundaries.

4- The crack growth is represented as a fast rough crack at 300 °C and 400 °C due to hardened phase of the material while it decreases gradually at 500 °C in a ductile phase due to the combined mechanical and thermal softening effects.

5- The general observation of the behaviour of the crack growth for all isothermal fatigue tests, except 600 °C are described as a fast fatigue crack growth at the beginning of cracking followed by crack growth arresting, especially at 400 °C and 500 °C.

6- The effects of increasing temperature decrease the crack initiation period and also the crack length. The crack length ratio to the original diameter gives important information to the engineers to determine the design limitation of the components made from this material.

7- The stress intensity factor increases with crack growth and decreases with increasing temperature, as a result of decreasing the applied mechanical load. It is bonded between 400 °C and 600 °C, due to the hardness increase at 400 °C and the creep-fatigue effects at 600 °C.

8- The increment in temperature increases the fatigue crack growth rate with stress intensity factor and the crack growth rate at 600 °C test temperature less than 500 °C, because the creep-fatigue takes place.

9- The relation of the strain intensity factor with the crack length is significantly influenced by the modulus of elasticity with the temperature and the bond between 400 °C and 500 °C temperatures.

218

10- The relation between crack growth rates against stress intensity factor shows an effective region limited by the lower bond at 300 °C and the upper at 500 °C. Where the lower is obtained by the mechanical softening and the upper by thermal softening.

11- The crack growth rate against stress intensity factor at 500 °C test is observed step down curve caused by the addition of softening under mechanical and thermal loading. This is observed by interaction of cracking and dislocation (necking) of the specimen.

12- The crack growth rate against strain intensity factor is limited between the upper bond at 400 °C and nearly same line for the other temperatures.

13- The creep-fatigue action is significantly noticed in 600 °C isothermal test due to the cyclic softening behaviour of the material caused by the microstructure deformation and retained austenite significantly reduce the yield strength level.

8.1.2 Theoretical Study:

The conclusions collected from the theoretical solutions are:

A-For Isothermal Fatigue Case:

1- The effects of the temperature explained by the von Mises thermal stresses increases with the increase in temperature. The jump of high stress at 400 °C is due to hardness increase in the material; it is indicated by the high modulus of elasticity (E). This effect superimposed by the applied mechanical cyclic stress raises the total combined effects.

2- The effect of the mechanical stress on the combined loading is present as the effective loading rather than the thermal loading.

3- The stress intensity factor calculation shows an increase in temperature which decreases the intensity factor due to reduction of the strength of the material, which is indicated by the reduction of mechanical cyclic loading and the increment of temperature. Except at 400 °C, the increases of both thermal and mechanical stresses give rise to the highest values due to the hardness increase.

4- The strain intensity factor calculation is bonded between the upper bond at 500 °C and the lower at 400 °C temperature, due to the significant influence of the modulus of elasticity of the material at the test temperature.

5- The combination of stress and strain intensity factor theoretical calculations with the experimental output recorded data shows the same behaviour with increasing temperature, and there is a fair correlation between the profiles at the beginning until (0.5 mm) crack length after the divergence increases, due to the combined effect of cyclic softening with fast crack propagation on the behaviour of the material.

B-For Thermal Shock Fatigue Cases:

1- The transient influence of high temperature in the heating or cooling cases for hollow cylinder are taking place suddenly, giving a very high thermal shock stress as a heating or cooling effects, shifting up the combined stress, when applied to a cyclic mechanical load in a fraction of seconds; the recurrence of these shocks cause a fast failure under high thermal shock stress superimposed by mechanical loading.

8.1.3 Numerical Study:

The conclusions collected from the numerical solution are:

1- The expectation of failure position depends on the geometrical shape of the simulated low cyclic and isothermal fatigue models.

2- The low cyclic fatigue simulation shows very close results. These are in agreement with the experimental data in terms of alternative stress and life. For example, in 100% case the estimated alternating stress is equal to (317 MPa), while the experimental is (302.5 MPa) which is very close and for 90% life simulation cases, the possibility of failure value is the same as that of the experimental output data.

3- The isothermal fatigue simulation results show the estimated equivalent von Mises stress and stress intensity factor are reduced with increasing temperature, except at

500 °C. The strain intensity factor increases with increasing temperature similar to the theoretical solution due to the influence of the modulus of elasticity.

4- The estimated alternating stress is very close to the experiment data. While, the difference in life estimation with the experimental output record is related to the input data obtained from the mixture of theoretical physical properties, and the experimental stress-life data, which are generated at room temperature. Also the observation shows minor effects of thermal stress in the simulation on the equivalent von Mises stress.

5- The thermal stresses are increased with increasing the temperature.

6- The transient temperature simulation of the hollow cylinder for heating or cooling cases gives very close temperature distribution results to the theoretical calculations.

7- The failure that occurs in the transient cases is close to the fixed ends; this is because of the increased stresses in this section, rather than the free moving ends. Also, similar results are noted between the two cases; this is related to the 600 °C temperature but the difference is in the timing of the effects.

8.2 Future Works:

Recommendations are made while drawing the conclusion of the three-way solutions for the present study; they can be further elaborated and scrutinized. The following recommendations are made for each of the three solutions.

A- The Experimental Solution Recommendations:

1- The generation of the S-N curve under different temperature levels for the material will be very useful for the model behaviour and assessment.

2- Creep has been discovered in this research at 600 °C with stress range equal to 0.2% yield stress. The search for the minimum load level causing the creep or creep fatigue of the material is a very important indication for the design limitation of designing engineering.

3- One of the effective factors influences the fatigue crack growth at elevated temperature studies. Further studies are required to investigate the effects of oxidation on fatigue crack closure.

4- The manufacturing of the designed thermo-mechanical system is developed in Chapter Three to set a thermal shock testing and thermo-mechanical in and out phase testing by conducting a hollow cylinder specimen.

B- The Empirical Solution Recommendations:

1- The linear integral accumulation technique is used for solving the empirical solution results. The usage of a finite element or difference for solving could improve the results.

2- The temperature is assumed to be one directional effect in this solution. The use of two directional effects can provide more reliable information.

C- The Numerical Solution Recommendations:

1- The employment of the S-N curve data at the selected temperature with different applied mechanical loads will produce a good assessment.

2- The importance of the use of a finite element simulation is to optimize the geometrical design by utilizing the collected material properties data of the experimental testing. The simulation of a real model with more complicated geometry; for example, turbine blade under isothermal fatigue by using the material testing data is also recommended.

REFERENCES

[1] R.L. Klueh, A.T. Nelson,"Ferritic/martensitic steels for next-generation reactors", Journal of Nuclear Materials 371, 2007, 37–52.

[2] R. Viswanathan, J. Nutting, "Advanced heat resistant steels for power generation", IOM Communications Ltd, 1999.

[3] Garden, Mc Evily, Wells, "Fatigue at elevated temperature" American Society for Testing and Materials ASTM STP 520, 1973.

[4] S. S. Marsen, "Thermal stress and Low cycle fatigue" McGraw-Hill,INC,1966.

[5] R.P. SKELTON, "Fatigue at High Temperature", Applied Science Publishers, London, 1983.

[6] Les Pook, "Metal Fatigue, What it is, why it matters", Springer, 2007.

[7] David Broek, "Elementary Engineering Fracture Mechanics", fourth revised edition, Martinus Nijhoff Publishers, 1986.

[8] Tomkins, B. "Fatigue Crack Propagation-Analyses", Philosophical magazine, Vol.18, 155, 1968, pp.1041.

[9] Ellyin, Frenand, "Fatigue Damage, Crack Growth and Life Prediction", springer, 30 Nov. 1996.

[10] Syed T. Hasan, "Analysis of Fatigue Crack Propagation Due to Cyclic Thermal and Mechanical Stresses", PhD Thesis, University of Sheffield, 1990.

[11] Jaap Schijve,"Fatigue of Structures and Materials", Springer, 2009.

[12] P. Bown, C. A. Hippsley, "High Temperature Intergranular Crack Growth in Martensitic 2 ¼ Cr - 1Mo steel",Pergamon Journals Ltd, Acta metall. vol. 36,No.2,pp. 425-439, 1988.

[13] S.W. Kim, A. Kohyama, H.K.Yoon, "Fatigue Crack Growth Behaviour and Microstructure of Reduced Activation Ferritic/Martensitic Steel (JLF-1)", Fusion Engineering and Design, 81,(2006), 1105-1110.

[14] H.L. Ewalds, R.J.H. Wanhill, "Fracture Mechanics", Edward Arnold (Publishers) Ltd, 1984.

[15] C.J. Thomas, R.G.J. Edyvean, R. Brook, "Environmentally Assisted Crack Growth in Martensitic Stainless Steel", Materials science and engineering, 78, (1986), 55-63.

[16] Z. Sun, G. Benoit, C. Moriconi, F. Hamon, D. Halm, F. Hamon, G. He'naff, "Fatigue Crack Propagation Under Gaseous Hydrogen in a Precipitation-Hardened Martensitic Stainless steel", international journal of hydrogen energy, 36,(2011), 8641-8644.

[17] J.I. Shakib , H. Ullmaier, E.A. Little, R.G. Faulkner , W. Schmitz ,T.E. Chung, "Fatigue of DIN 1.4914 Martensitic Stainless Steel in a Hydrogen Environment", Journal of Nuclear Materials, 212-215, (1994) 579-583.

[18] Lin, CK, Fan, WC, Tsai, WJ, "Corrosion Fatigue of Precipitation-Hardening Martensitic Stainless Steel", NATL ASSN CORROSION ENG.,vol.58,11/2002, 904-911.

[19] B. Fournier, M. Sauzay, C. Cae"s, M. Noblecourt, M. Mottot, A. Bougault,V. Rabeau, A. Pineau," Creep–Fatigue–Oxidation Interactions in a 9Cr–1Mo Martensitic Steel. Part I: Effect of Tensile Holding Period on Fatigue Lifetime", International Journal of Fatigue, 30, (2008), 649–662.

[20] B. Fournier, M. Sauzay, C. Cae"s, M. Noblecourt, M. Mottot, A. Bougault,V. Rabeau, A. Pineau, "Creep-Fatigue-Oxidation Interactions in a 9Cr–1Mo Martensitic Steel. Part II: Effect of Compressive Holding Period on Fatigue Lifetime", International Journal of Fatigue, 30, (2008), 663–676.

[21] B. Fournier, M. Sauzay, C. Cae"s, M. Noblecourt, M. Mottot, A. Bougault,V. Rabeau, J. Man, O. Gillia, P. Lemoine, A. Pineau, "Creep–Fatigue–Oxidation Interactions in a 9Cr–1Mo Martensitic Steel. Part III: Lifetime Prediction", International Journal of Fatigue, 30, (2008), 1797–1812.

[22] Kassner, Michael E.," Fundamentals of Creep in Metals and Alloys" second edition, 2009 Elsevier Ltd.

[23] B. Fournier, M. Salvi, F. Dalle, Y. De Carlan, C. Caës, M. Sauzay, A. Pineau," Lifetime Prediction of 9-12%Cr Martensitic Steels Subjected to Creep-Fatigue at High Temperature", International Journal of Fatigue, 32, 2010, 971-978.

[24] Lee Edward, "Correlation of Localised Thermal Shock to Isothermal Biaxial Crack Growth Rates in Thin Plates of AISI 316 Stainless Steel", PhD Thesis, Sheffield Hallam University, 2002.

[25] G. Bernhart, G. Moulinier, O. Brucelle, D. Delagnes, "High Temperature Low Cycle Fatigue Behaviour of a Martensitic Forging Tool Steel", International journal of fatigue, 21, (1999), 179-186.

[26] Lloyd, G. J., "High Temperature Fatigue", Ed. R. P. Skelton, Elsevier Applied Science Publisher, London, 1983, pp.187.

[27] L. L. Faulkner, "Practical Fracture Mechanics in Design", Marcel Dekker, 2005.

[28] Boettner, R. C., Laird, C. and McEvily, A. J., "Trans. AIME", 233, 1965, pp.379.

[29] Solomon, H. D., "J. Mater", 7, 1972, pp.299.

[30] Haigh, J. R. and Skelton, R. P., "Mater. Sci. Eng.", Vol.36, 1978, pp.133.

[31] Les Pook, "Metal Fatigue, What it is, why it matters", Springer, 2007.

[32] A. F. MADAYAG, "Metal Fatigue, Theory and design", John Wiley and sons, 1969.

[33] Dorn, J. E., "Mechanical Behaviour of Materials at elevated temperature", McGraw-Hill, New York, 1961.

[34] X.L. Song, G.X. Yang, S.L. Zhou, H. Fan, S.S. Yang, J.W. Zhu, Y.N. Lin, "Cyclic deformation behaviour and microstructural changes of 12Cr-WMoV martensitic stainless steel at elevated temperature", Material Science and Engineering, Vol. A 483-484, 2008, pp.211-213.

[35] M.L. Roessle, A. Fatemi," Strain-controlled fatigue properties of steels and some simple approximations", International Journal of Fatigue, 22, (2000), 495-511.

[36] J.M. Barsom,"fatigue-crack propagation in steels of various yield strengths", Transaction of the ASME, November, 1971, 1190-1196.

[37] A. F. Armas, M. Avalos, I. Alvarez-Armas, C. Peterson, R. Schmitt,"Dynamic strain ageing evidences during low cycle fatigue deformation in ferritic-martensitic stainless steels", Journal of Nuclear Materials, 258-263, (1998), 1204-1208.

[38] Gerard Degallaix, Suzanne Degallaix, Jacques Foct,"A damage law for predicting the elevated temperature low cycle fatigue life of a martensitic stainless steel", Materials Science and Engineering, 58, (1983), 55-62.

[39] R. Lindau, A. Möslang,"Low cycle fatigue properties of the helium-implanted 12%Cr steel 1.4914(MANET)", Journal of Nuclear materials, 179-181, (1991), 753-756.

[40] R. Lindau, A. Möslang,"Fatigue test on a ferritic-martensitic steel at 420°C: Comparison in situ and postirradiation properties", Journal of Nuclear materials, 212-215, (1994), 599-603.

[41] KENJI KANAZAWA, KOJI YAMAGUCHI, KAZUO KOBAYASHI," The Temperature Dependence of Low Cycle Fatigue Behaviour of Martensitic Stainless Steels", Materials Science and Engineering, 40, (1979), 89 - 96.

[42] Z. Zhang, D. Delagnes, G. Bernhart, "Anisothermal cyclic plasticity modelling of martensitic steels", International Journal of Fatigue, Vol. 24, 2002, pp. 635–648.

[43] Z. Zhang, D. Delagnes, G. Bernhart, " Ageing effect on cyclic plasticity of a tempered martensitic steel", International Journal of Fatigue, 29, 2007,336–346.

[44] ZHANG Zhanping, Delagnes D, and Bernhart G, "Cyclic behaviour and plastic strain memory effect of 55NiCrMoV7 steel under low cycle fatigue", RARE METALS, Vol. 30, Spec. Issue, Mar 2011, p. 443.

[45] A. Nagesha, M. Valsan, R. Kannan, K. Bhanu Sankara Rao, S.L. Mannan, " Influence of temperature on the low cycle fatigue behaviour of amodified 9Cr–1Mo ferritic steel", International Journal of Fatigue, 24,2002, 1285–1293.

[46] B. Fournier, M. Sauzay, A. Pineau, "Micromechanical model of the high temperature cyclic behavior of 9–12%Cr martensitic steels", International Journal of Plasticity, 27, 2011, 1803–1816.

[47] B. Fournier, F. Dalle, M. Sauzay, J. Longour, M. Salvi , C. Caës, I. Tournié, P.-F. Giroux, S.-H. Kim," Comparison of various 9–12%Cr steels under fatigue and creep-fatigue loadings at high temperature", Materials Science and Engineering, A 528, (2011), 6934– 6945.

[48] S.L. Mannan, M. Valsan, "High-temperature low cycle fatigue, creep– fatigue and thermomechanical fatigue of steels and their welds", International Journal of Mechanical Sciences, Vol. 48, 2006, pp.160–175.

[49] Hyeong-Yeon Lee, Se-Hwan Lee, Jong-Bum Kim, Jae-Han Lee," Creep–fatigue damage or a structure with dissimilar metal welds of modified 9Cr–1Mo steel and 316L stainless steel", International Journal of Fatigue, 29, (2007), 1868–1879.

[50] P.BOWEN' and C.A. HIPPSLEY," HIGH TEMPERATURE INTERGRANULAR CRACK GROWTH IN MARTENSITIC 2$r-1Mo STEEL", Acta metall. Vol. 36, No. 2, pp. 425-439, 1988.

[51] KUEI-CHANG HSU and CHIH-KUANG LIN," High-Temperature Fatigue Crack Growth Behavior of 17-4 PH Stainless Steels", METALLURGICAL AND MATERIALS TRANSACTIONS A, 3018—VOLUME 35A, SEPTEMBER 2004.

[52] Shuhei NOGAMI, Yuki SATO and Akira HASEGAWA," Fatigue Life Assessment Based on Crack Growth Behavior in Reduced Activation Ferritic/Martensitic Steel", Journal of NUCLEAR SCIENCE and TECHNOLOGY, Vol. 47, No. 5, p. 457–461, 2010.

[53] Y.C. Lin, S.C. Chen," Effect of residual stress on thermal fatigue in a type 420 martensitic stainless steel weldment", Journal of Materials Processing Technology, 138, (2003), 22–27.

[54] Y.C. Lin , Y.T. Lin, S.C. Chen, Z.R. Liu," Role of retained ferrite on the thermal fatigue cracking resistance in martensitic stainless steel weldment", Materials Science and Engineering, A339, (2003), 133/135.

[55] N. N. Mitrokhovich," Thermal fatigue of low-carbon martensitic steel", Metal Science and Heat Treatment, Vol. 49, Nos. 5 – 6, 2007.

[56] A. Akdogan, A. Koyun," Heat transfer analysis and material behaviour of martensitic steel during thermal cycling process", Materials Science and Technology, 2007, VOL 23, NO 9, 1093.

[57] Peter Hähner, Ernst Affeldt, Tilmann Beak, Hellmuth Klingelhöffer, Malcolm Loveday, Claudia Rinaldi, "Validated code-of-practice for strain-controlled thermo-mechanical fatigue testing", Joint Research centre, European commission, June, 2006.

[58] A. Nagesha, R. Kannan, G.V.S. Sastry, R. Sandhya, Vakil Singh, K. Bhanu Sankara Rao,M.D. Mathew, "Isothermal and thermomechanical fatigue studies on a modified 9Cr–1Mo ferritic martensitic steel", Materials Science and Engineering, A 554, (2012), 95– 104.

[59] Stefan Dietz, Helmuth Netter, Delf Sachau, " Fatigue Life Prediction of a Railway Bogie under Dynamic Loads through Simulation", Vehicle System Dynamics: International Journal of Vehicle Mechanics and Mobility, Vehicle System Dynamics. 29 (1998), pp. 385-402.

[60] Mahmood M. Shokrieh, Roham Rafiee, "Simulation of fatigue failure in a full composite wind turbine blade", Composite Structures, 74, (2006), 332–342.

[61] A. Movaghghar, G. I. Lvov, "A Method of Estimating Wind Turbine Blade Fatigue Life and Damage using Continuum Damage Mechanics", International Journal of DAMAGE MECHANICS, Vol. 21—August 2012.

[62] Mehmet Firat, Recep Kozan, Murat Ozsoy, O. Hamdi Mete, " Numerical modeling and simulation of wheel radial fatigue tests", Engineering Failure Analysis, 16, (2009),1533–1541.

[63] S. Glodez˘ , N. Jezernik, J. Kramberger, T. Lassen, " Numerical modelling of fatigue crack initiation of martensitic steel", Advances in Engineering Software, 41, (2010), 823–829.

[64] Hongxia Yu, I.W. Burgess, J.B. Davison, R.J. Plank, "Numerical simulation of bolted steel connections in fire using explicit dynamic analysis" , Journal of Constructional Steel Research, 64, (2008), 515–525.

[65] Q.J. Yang *, X.Q. Shi, Z.P. Wang, Z.F. Shi, "Finite-element analysis of a PBGA assembly under isothermal=mechanical twisting loading", Finite Elements in Analysis and Design, 39, (2003), 819–833.

[66] F.X. Che and John H.L. Pang, "Thermal Fatigue Reliability Analysis for PBGA with Sn-3.8Ag-0.7Cu Solder Joints" , IEEE, 6/04/2004, 0-7803-8821.

[67] R. A. CLA´ UDIO, C. M. BRANCO, E. C. GOMES, J. BYRNE , G. F. HARRISON, and M. R. WINSTONE, " Fatigue life prediction and failure analysis of a gas turbine disc using the finite-element method", 2004 Blackwell Publishing Ltd., Fatigue Fract. Engng. Mater Struct., 27, 849–860.

[68] P. Revel, D. Kircher , V. Bogard," Experimental and numerical simulation of a stainless steel coating subjected to thermal fatigue", Materials Science and Engineering, A290, (2000), 25–32.

[69] Donald W. Rhymer, W. Steven Johnson, Ripudaman Singh, Richard Pettit," Stress intensity solutions of thermal fatigue induced cracks in a thin plate hot spot using LEFM and finite element analysis", Engineering Fracture Mechanics, 75, (2008), 2826–2841.

[70] Hoai Nam Le, Catherine Gardin," Analytical calculation of the stress intensity factor in a surface cracked plate submitted to thermal fatigue loading", Engineering Fracture Mechanics, 77, (2010), 2354–2369.

[71] Kazunori Shinohara, Qiang Yu, "Evaluation of Fatigue Life of Semiconductor Power Device by Power Cycle Test and Thermal Cycle Test Using Finite Element Analysis", Engineering, 2010, 2, 1006-1018.

[72] Kazunori Shinohara, Qiang Yu," Fatigue life evaluation accuracy of power devices using finite element method", International Journal of Fatigue, 33, (2011), 1221–1234.

[73] Yung-Chuan Chiou, Yi-Ming Jen, Shih-Hsiang Huang," Finite element based fatigue life estimation of the solder joints with effect of intermetallic compound growth", Microelectronics Reliability, 51, (2011), 2319–2329.

[74] J Shang, T H Hyde, and S B Leen," Finite element-based life prediction for high-temperature cyclic loading of a large superplastic forming die", The Journal of Strain Analysis for Engineering Design, 2006, 41: 539.

[75] A.A. Deshpande, S.B. Leen, and T.H. Hyde," Finite Element Prediction of Creep-Plastic Ratchetting and Low Cycle Creep-Fatigue for a Large SPF Tool", Journal of Materials Engineering and Performance,Volume 19(4) June 2010, 452-466.

[76] M.P. Rodriguez, N.Y.A. Shammas,"Finite element simulation of thermal fatigue in multilayer structures: thermal and mechanical approach", Microelectronics Reliability, 4, 2001, 517-523.

[77] C.M. Chen, R. Kovacevic, "Finite element modelling of friction stir welding—thermal and thermomechanical analysis", International Journal of Machine Tools & Manufacture, 43, (2003), 1319–1326.

[78] P. Terriault, F. Viens, V. Brailovski," Non-isothermal finite element modelling of a shape memory alloy actuator using ANSYS", Computational Materials Science, 36, 2006, 397–410.

[79] S.H. Kanga, Y.T. Im," Thermo-elasto-plastic finite element analysis of quenching process of carbon steel", Journal of Materials Processing Technology, 192–193, (2007), 381–390.

[80] P.K. Panda, T.S. Kannan, J. Dubois, C. Olagnon, G. Fantozzi," Thermal shock and thermal fatigue study of alumina", Journal of the European Ceramic Society, 22, (2002), 2187–2196.

[81] A.G. Tomba, A.L. Cavalieri,"Numerical simulation of the thermal shock of alumina disks with different surface finish", Journal of European Ceramic Society, 21,2001,1205-1212.

[82] A. G. Tomba Martinez Æ M. A. Camerucci Æ, A. L. Cavalieri," Thermal stress analysis of cordierite materials subjected to thermal shock", J Mater Sci, (2008), 43:2731–2738.

[83] R.L.Klueh, D.S. Gelles, S. Jitsukawa, A. Kimura, G.R. Odette, B. van der Schaaf, M. Victoria, "Ferritic/martensitic steels - overview of recent results", Journal of Nuclear Materials, 307-311,2002, 455 - 465.

[84] A. Nasery Isfahany, H. Saghafian, G. Borhani," The effect of heat treatment on mechanical properties and corrosion behavior of AISI420 martensitic stainless steel", Journal of Alloys and Compounds, 509, (2011), 3931–3936.

[85] E602-91,"2005 Annual Book of ASTM Standards, Metals test methods and Analytical procedures", volume 03.01.

[86] J. Brnic · G. Turkalj · M. Canadija · D. Lanc., S. Krscanski," Martensitic stainless steel AISI 420—mechanical properties, creep and fracture toughness", Mech Time-Depend Mater, (2011), 15:341–352.

[87] ASTM special technical publication 465," Manual on low cycle fatigue testing", ASTM,1969.

[88] G.Sumner, V. B. Livesey,"Techniques for high temperature fatigue testing", Elsevier applied science publishers Ltd, 1985.

[89] T. V. Venkatasubramanaian , B. A. Unvala,"An AC potential drop system for monitoring crack length", Journal of phys. E:SCI. Instrum., Vol.17,1984.

[90] E647-00,"2005 Annual Book of ASTM Standards, Metals test methods and Analytical procedures", volume 03.01.

[91] Tada, H., Paris, P., Irwin, G. "The stress analysis of cracks handbook", 1985, Del Research Corporation.

[92] H. S. Carslaw and J. C. Jaeger," Conduction of Heat in Solids", second edition, Oxford University press, NewYork,1959.

[93] H. F. Nied and F. Erdogan,"Transient thermal stress problem for a circumferentially cracked hollow cylinder", Journal of Thermal Stresses,6 : 1 – 14, 1983.

[94] H. Cho, G. A. Kardomateas and C. S. Valle," Elastodynamic solution for the thermal shock stresses in an orthotropic thick cylinder shell ", Journal of Applied Mechanics,Vol. 65, March,1998.

[95] Hiromasa Ishikawa," A thermoelastoplastic solution for a circular solid cylinder subjected to heating and cooling ", Journal of Thermal Stresses,1 : 211 – 222, 1978.

[96] J. A. Lopez Molina and M. Trujillo," Thermal stresses in an infinitely long solid cylinder using Green's function and hyperbolic heat equation ", Proceeding of the 2nd WSEAS International conference on Applied and Theroertical Mechanics, Venice, Italy, November, 20 – 22, 2006.

[97] Jun Zhao, Xing A., Yanzheng Li and Yanghui Zhou," Thermal shock resistance of functionally gradient solid cylinders ", Journal of Materials Science and Engineering A 418 (2006), 99 – 110.

[98] Moncef Aouadi,"A generalized thermoelastic diffusion problem for an infinitely long solid cylinder ", International Journal of Mathematics and Mathematical Sciences, vol. 2006,Article ID 25976, pages, 1-15.

[99] V. Radu, N. Taylor and E. Paffumi," Development of new analytical solutions for ealstic thermal stress components in a hollow cylinder under sinusoidal transient thermal loading ", International Journal of pressure vessels and piping 85 (2008), 885 - 893.

[100] G. A. Kardomateas," Transient thermal stresses in cylindriically orthotropic composite tubes ", Journal of Applied Mechanics, June 1989,vol. 56.

[101] G. A. Kardomateas," The initial phase of transient thermal stresses due to general boundary thermal loads in orthotropic hollow cylinder ", Journal of Applied Mechanics, September 1990,vol. 57.

[102] M. Jabbari, S. Sohrabpour and M. R. Eslami," Mechanical and thermal stresses in a functionally graded hollow cylinder due to radially symmetric loads ", International Journal of pressure vessels and piping 79(2002),493 - 497.

[103] M. Jabbari, S. Sohrabpour and M. R. Eslami" general solution for mechanical and thermal stresses in a functionally graded hollow cylinder due to nonaxisymmetric steady-state loads ", Journal of Applied Mechanics, January 2003, vol. 70.

[104] M. A. Ehteram, M. Sadighi and H. Basirat Tabrizi," Analytical solution for thermal stresses of laminated hollow cylinders under transient nonuniform thermal loading ", ISSN 1392 - 1207, MECHANIKA. 2011. 17(1): 30 - 37.

[105] A. M. Clayton," Thermal shock in nuclear reactor ", Progress in nuclear Energy.1983, Vol.12, No. 1,pp. 57 - 83.

[106] S. P. Timoshenko and J. N. Goodier," Theory of Elasticity ", International student edition, McGraw-Hill Book company, 1970.

[107] A. R. Shahani and S. M. Nabavi," Transient thermal stress intensity factors for an internal longitudinal semi-elliptical crack in a thick-walled cylinder ", Journal of Engineering Fracture Mechanics 74 (2007), 2585 - 2602.

[108] I. S. Jones," Impulse response model of thermal striping for hollow cylindrical geometries ", Journal of Theoretical and Applied Fracture Mechanics 43 (2005), 77 - 88.

[109] Rooke, d. P. and cartwright, D. J. ,"Compendium of Stress Intensity Factors", HMSO, London, 1976.

[110] E. Paffumi, K. -F. Nilsson and N. G. Taylor," Thermal frequency response studies of a hollow cylinder subjected to loads of different amplitude and shape", Journal of Nuclear Engineering and design 240 (2010) 1355 - 1362.

[111] E. Paffumi, K. -F. Nilsson and N. G. Taylor," Thermal fatigue cyclic - down shocks on 316L model pipe components", ASME Pressure Vessels and piping Division Conference, Jule 27 - 31, 2008, Chicago, lllinois, USA.

[112] E. Paffumi, K. -F. Nilsson and N. G. Taylor," Simulation of thermal fatigue damage in a 316L model pipe components", International Journal of Pressure Vessels and Piping 85 (2008) 798 - 813.

[113] V. Radu, E. Paffumi, N. G. Taylor and K. -F. Nilsson," A study on fatigue crack growth in the high cycle domain assuming sinusoidal thermal loading", International Journal of Pressure Vessels and Piping 86 (2009) 818 - 829.

[114] HIDEAKI ABE, "Crack growth of craburized materails due to thermal striping in sodium", Journal of Engineering Fracture Mechanics, vol. 55, No. 4, and pp: 679 - 687, 1996.

[115] J.M. Barsom, "Fatigue-crack propagation in steels of various yield strengths", J. Eng. Ind. (Trans. ASME), series B, No. 4, Nov 1971, p1190.

[116] O.C. ZIENKIEWICZ and R.L. TAYLOR, "The finite element method" Fifth edition published by Butterworth-Heinemann, 2000.

[117] David W. Nicholson, "FINITE ELEMENT ANALYSIS Thermomechanics of Solids", second edition by Taylor & Francis Group, LLC, 2008

[118] Nakasone, Y., Yoshimoto, S. and Stolarski, T.A., " Engineering Analysis with ANSYS Software ", Butterworth-Heinemann, 2006.

[119] ANSYS Release 9.0, "ANSYS modelling and meshing guide", ANSYS Inc. Company, November, 2004.

[120] G. R. Liu and S. S. Quek," The Finite Element Method: A Practical Course", Elsevier Science Ltd, First published, 2003.

[121] B. NATH, "Fundamentals of Finite Elements for Engineers", The ATHLONE press, University of London, 1974.

[122] Zhangxin Chen, "The Finite Element Method", World Scientific Publishing Co. Pte. Ltd, 2011.

[123] C. A. BREBBIA AND J. J. CONNOR, "Fundamentals of Finite element Techniques", Butterworth & Co. Ltd, 1973.

[124] Raymond B. and Al Hancq, "Calculating and displaying fatigue results", Ansys Inc., March 29, 2006.

[125] D. Alfred Hancq, "Fatigue analysis in the ANSYs Workbench environment", Ansys Inc., May 2003.

[126] DONALD PECKNER and I. M. BERNSTEIN," Handbook of Stainless Steels", McGraw-Hill Book Company, 1977.

[127] Stephen Lamb, "CASTI Handbook of Stainless Steels and Nickel Alloys", CASTI publications, 1999.

APPENDIX A

MATLAP modified program for data reduction by using seven point incremental polynomial techniques.

The input data are:

N- Number of cycles read from DCPD machine.

a- Crack length read from DCPD machine.

m- Number of data read.

Pmax- Peak cyclic applied load

Pmin- Trough cyclic applied load

```
clear all
N=[---,--- ];
a=[---,---];

m=8;
n=3;
r=3

E=193.36e3
Pmax=600
Pmin=60

delP=Pmax-Pmin
Rratio=Pmin/Pmax

for i=1:n
  No1=i
    Cycle=N(i)
      aMeas=a(i)
end

 p=0

for i=1:(m-2*n)
        i
    I=0
    p=p+1
    p1=p+6

for j=p:p1
    I=I+1
    aa(I)=a(j)
```

```
        nn(I)=N(j)
end
    C1=0.5*(nn(1)+nn(7))
    C2=0.5*(nn(7)-nn(1))

    SX=0
    SX2=0
    SX3=0
    SX4=0

    SY=0
    SYX=0
    SYX2=0

for k=1:7
    k
    X=(nn(k)-C1)/C2
        Y=aa(k)


        SX=SX+X
        SX2=SX2+(X.^2)
        SX3=SX3+(X.^3)
        SX4=SX4+(X.^4)

        SY=SY+Y
        SYX=SYX+(Y*X)
        SYX2=SYX2+(Y*X.^2)
end
    Term1=((SX2*SX4)-(SX3)^2)
    Term2=((SX*SX4)-(SX2*SX3))
    Term3=((SX*SX3)-(SX2)^2)

    Term4=((SYX*SX4)-(SYX2*SX3))
    Term5=((SYX*SX3)-(SYX2*SX2))

    Term6=((SYX*SX4)-(SYX2*SX3))
    Term7=((SX*SYX2)-(SX2*SYX))

    Term8=((SX2*SYX2)-(SX3*SYX))
    Term9=((SX*SYX2)-(SX2*SYX))

    D=7*Term1-SX*Term2+SX2*Term3
    B0=SY*Term1-SX*Term4+SX2*Term5
    B1=7*Term6-SY*Term2+SX2*Term7
    B2=7*Term8-SX*Term9+SY*Term3

    b0=B0/D
    b1=B1/D
    b2=B2/D

    Ymean=SY/7
    rss=0
    tss=0

for k=1:7
    k
```

236

```
        X=(nn(k)-C1)/C2
        YReg=b0+b1*X+b2*X.^2

        rss=rss+(aa(k)-YReg)^2
        tss=tss+(aa(k)-Ymean)^2

end
        r2=1-rss/tss

        dadN(i+n)=(b1/C2)+(2*b2*(nn(4)-C1)/C2^2)

        X=(nn(4)-C1)/C2

        ar=b0+b1*X+b2*X^2

        c=ar/r

        Fc=(1.122-1.302*c+0.988*c^2-0.308*c^3)/(1-c)^1.5

        j=i+n

        delK(j)=delP*Fc*(pi*ar)

        delKE(j)=delK(j)/E

        dadN=dadN(j)
        deltK=delK(j)
        delKE=delKE(j)
        MCC=r2
        aReg=ar
        aMeas=a(j)
        Cycles=N(j)
        No=j
end

for i=m-n+1:m

        No3=i

        EndCycles=N(i)

        Endameasure=a(i)
end
```

The output data are:

dadN- The crack growth rate.

deltK- The stress intensity factor range.

delKE- The strain intensity factor range.

aReg- The regression crack length (measured crack).

Cycles- Number of cycles at the crack length.

APPENDIX B

The Bessel functions are defined by the equations:

$$J_\nu(z) = \sum_{i=0}^{\infty} \frac{(-1)^i \left(\frac{1}{2} z\right)^{\nu+2i}}{i!\ \Gamma(\nu+i+1)} \qquad\qquad (B.1)$$

$$Y_\nu(z) = \frac{J_\nu(z)\cos\nu\pi - J_{-\nu}(z)}{\sin\nu\pi} \qquad\qquad (B.2)$$

Isothermal Temperature Distribution for Solid Cylinder Case:

The details of stresses integrating are given below:

$$\int_0^r r^{n+1}.\,J_n(\lambda_i r)dr = \frac{1}{\lambda_i}.r^{n+1}.J_{n+1}(\lambda_i r) \qquad\qquad (B.3)$$

So, at n = 0.

$$\int_0^r r.J_0(\lambda_i r)\,dr = \frac{1}{\lambda_i} r J_1(\lambda_i r) \qquad\qquad (B.4)$$

And at the outer radius of the solid cylinder, r = b, n= 0;

$$\int_0^b r.J_0\left(r\frac{\xi}{b}\right) dr = \frac{b}{\xi} r J_1\left(r\frac{\xi}{b}\right) \qquad\qquad (B.5)$$

Where; $\xi = \lambda_i.b$ $\qquad\qquad (B.6)$

238

Thermal Shock Temperature Distribution for Hollow Cylinder Case:

In the temperature distribution $T_{(r,t)}$ through the hollw cylinder wall for the two cases in equations (4.3) and (4.6), the constant are given as follows:

I-Heating Case:

$$A_1 = T_a \tag{B.7}$$

$$A_2 = \frac{b\,F}{k} \tag{B.8}$$

$$A_{3i} = -\pi\,e^{-D\lambda_i^2 t}\,.\,\frac{J_1(b\,\lambda_i).\left\{\lambda_i\,T_a\,J_1(b\,\lambda_i) - \dfrac{F.J_0(a\,\lambda_i)}{k}\right\}}{\lambda_i\left(J_0^2(a\,\lambda_i) - J_1^2(b\,\lambda_i)\right)} \tag{B.9}$$

II-Down shock cooling Case:

$$B_1 = T_b \tag{B.10}$$

$$B_2 = -\frac{a\,H}{k}\,(T_a - T_{air}) \tag{B.11}$$

$$B_{3i} = \pi\,e^{-D\lambda_i^2 t}\,.\,\frac{J_0(b\,\lambda_i).\left\{\dfrac{H}{k}\,(T_a - T_{air}).J_0(b\,\lambda_i) - \lambda_i\,T_b\,J_1(a\,\lambda_i)\right\}}{\lambda_i\left(J_1^2(a\,\lambda_i) - J_0^2(b\,\lambda_i)\right)} \tag{B.12}$$

$$H = 5.5 \times 10^{-5}.u^{0.8}.d^{-0.2} \tag{B.13}$$

where:

u - is the flow velocity of forced air.

d- pipe diameter.

The details of stresses integrating are given below:

$$\int_a^b C \ln\frac{r}{a} . r \, dr = C \left\{ \int_a^b r.\ln r . dr - \int_a^b r.\ln a . dr \right\}$$

$$= C \left\{ \left(\frac{r^2}{2}\ln r - \frac{r^2}{4} \right)_a^b - \ln a . \left(\frac{r^2}{2} \right)_a^b \right\} \qquad (B.14)$$

$$\int_a^r C \ln\frac{r}{a} . r \, dr = C \left\{ \int_a^r r.\ln r . dr - \int_a^r r.\ln a . dr \right\}$$

$$= C \left\{ \left(\frac{r^2}{2}\ln r - \frac{r^2}{4} \right)_a^r - \ln a . \left(\frac{r^2}{2} \right)_a^r \right\} \qquad (B.15)$$

Where; C is represented to the constants A2, B2 in the case studies.

$$\int_a^b r.U_0(r\,\lambda_i) \, dr = -\frac{1}{\lambda_i^2}\left[r.\frac{d\,U_0(r\,\lambda_i)}{d\,r} \right]_a^b$$

$$= -\frac{1}{\lambda_i^2}.\left\{ \left[r.\frac{d\,U_0(r\,\lambda_i)}{d\,r} \right]_b - \left[r.\frac{d\,U_0(r\,\lambda_i)}{d\,r} \right]_a \right\} \qquad (B.16)$$

For the Heating Case:

$$U_0(r\,\lambda_i) = J_0(r\,\lambda_i).Y_0(a\,\lambda_i) - Y_0(r\,\lambda_i).J_0(a\lambda_i) \qquad (B.17)$$

$$\left[r.\frac{d\,U_0(r\,\lambda_i)}{d\,r} \right]_{r=b} = \lambda_i.b\,\{ J_1(b\,\lambda_i).Y_0(a\,\lambda_i) - Y_1(b\,\lambda_i).J_0(a\lambda_i) \} \qquad (B.18)$$

$$\left[r.\frac{d\,U_0(r\,\lambda_i)}{d\,r} \right]_{r=a} = \lambda_i.a\,\{ J_1(a\,\lambda_i).Y_0(a\,i) - Y_1(a\,\lambda_i).J_0(a\lambda_i) \} = -\frac{2}{\pi} \qquad (B.19)$$

240

$$\int_a^b r.U_0(r\,\lambda_i)\,dr = \frac{b}{\lambda_i} \cdot \{ Y_1(b\,\lambda_i).J_0(a\lambda_i) - J_1(b\,\lambda_i).Y_0(a\,\lambda_i) \} - \frac{2}{\pi\,\lambda_i^2} \qquad (B.20)$$

and;

$$\int_a^r r.U_0(r\,\lambda_i)\,dr = \frac{r}{\lambda_i} \cdot \{ Y_1(r\,\lambda_i).J_0(a\lambda_i) - J_1(r\,\lambda_i).Y_0(a\,\lambda_i) \} - \frac{2}{\pi\,\lambda_i^2} \qquad (B.21)$$

For the down shock cooling Case:

$$U_0(r\,\lambda_i) = J_0(r\,\lambda_i).Y_1(a\,\lambda_i) - Y_0(r\,\lambda_i).J_1(a\lambda_i) \qquad (B.22)$$

$$\left[r.\frac{d\,U_0(r\,\lambda_i)}{d\,r} \right]_{r=b} = \lambda_i.b \{ J_1(b\,\lambda_i).Y_1(a\,\lambda_i) - Y_1(b\,\lambda_i).J_1(a\lambda_i) \} \qquad (B.23)$$

$$\left[r.\frac{d\,U_0(r\,\lambda_i)}{d\,r} \right]_{r=a} = \lambda_i.a \{ J_1(a\,\lambda_i).Y_1(a\,\lambda_i) - Y_1(a\,\lambda_i).J_1(a\lambda_i) \} = 0 \qquad (B.24)$$

$$\left[r.\frac{d\,U_0(r\,\lambda_i)}{d\,r} \right]_{r} = \lambda_i.r \{ J_1(r\,\lambda_i).Y_1(a\,\lambda_i) - Y_1(r\,\lambda_i).J_1(a\lambda_i) \} \qquad (B.25)$$